

OPTICAL AND ELECTRICAL CHARACTERIZATION OF TITANOSILICATE
ETS-10 THIN FILMS:
PHOTOCHROMISM AND IONIC CONDUCTIVITY

A THESIS SUBMITTED TO
THE GRADUATE SCHOOL OF NATURAL AND APPLIED SCIENCES
OF
MIDDLE EAST TECHNICAL UNIVERSITY

BY
SEZİN GALİOĞLU ÖZALTUĞ

IN PARTIAL FULFILLMENT OF THE REQUIREMENTS
FOR
THE DEGREE OF DOCTOR OF PHILOSOPHY
IN
MICRO AND NANOTECHNOLOGY

JUNE 2015

Approval of the thesis:

**OPTICAL AND ELECTRICAL CHARACTERIZATION OF
TITANOSILICATE ETS-10 THIN FILMS: PHOTOCHROMISM AND IONIC
CONDUCTIVITY**

submitted by **SEZİN GALİOĞLU ÖZALTUĞ** in partial fulfillment of the requirements for the degree of **Doctor of Philosophy in Micro and Nanotechnology Department, Middle East Technical University** by,

Prof. Dr. Gülbin Dural Ünver
Dean, Graduate School of **Natural and Applied Sciences** _____

Prof. Dr. Tayfun Akın
Head of Department, **Micro and Nanotechnology** _____

Assoc. Prof. Dr. Burcu Akata Kurç
Supervisor, **Micro and Nanotechnology Dept., METU** _____

Prof. Dr. A. Macit Özenbaş
Co-Supervisor, **Metallurgical and Materials Eng. Dept., METU** _____

Examining Committee Members:

Assoc. Prof. Dr. Burcu Akata Kurç
Micro and Nanotechnology Dept., METU _____

Assoc. Prof. Dr. Y. Eren Kalay
Metallurgical and Materials Engineering Dept., METU _____

Assoc. Prof. Dr. Ali Çırpan
Chemistry Dept., METU _____

Prof. Dr. Selim Acar
Department of Physics., Gazi University _____

Assist. Prof. Dr. Selis Önel
Department of Chemical Eng., Hacettepe University _____

Date: _____

I hereby declare that all information in this document has been obtained and presented in accordance with academic rules and ethical conduct. I also declare that, as required by these rules and conduct, I have fully cited and referenced all material and results that are not original to this work.

Name, Last Name : Sezin Galioglu Özaltuğ

Signature :

ABSTRACT

OPTICAL AND ELECTRICAL CHARACTERIZATION OF TITANOSILICATE ETS-10 THIN FILMS: PHOTOCHROMISM AND IONIC CONDUCTIVITY

Galioglu Özaltuğ, Sezin

Ph.D., Micro and Nanotechnology Department

Supervisor: Assoc. Prof. Dr. Burcu Akata Kurç

Co- Supervisor: Prof. Dr. A. Macit Özenbaş

June 2015, 211 Pages

Zeolite-type Engelhard titanosilicate (ETS-10) crystals were synthesized by using Ti source of P25 and titanium (IV) isopropoxide. Using different Ti sources resulted in ETS-10 crystals with different particle morphology and particle size. The investigation of the titanosilicate ETS-10 crystals was done by FE-SEM, XRD and Raman analyses. The analyses showed that the samples contain only pure ETS-10 phase without any titanosilicate ETS-4 and quartz phases in our ETS-10 samples.

Ag^+ ions and Ag^0 nanoparticles were incorporated to submicrometer-sized ETS-10 crystals that were synthesized by using Ti source of P25 and characterized by using advanced analytical methods including ICP-OES, XRD, XPS, FE-SEM, TEM, HR-TEM, DR-UV-vis, Raman spectroscopies and N_2 adsorption-desorption technique. Although maintaining of structural integrity of host material had been monitored for Ag^+ -ETS-10, detailed Raman analyses of Ag^0 -ETS-10 samples showed significant changes in the titanate quantum wires of ETS-10 framework depending on the silver

loading. To figure out the role of 1D TiO_3^{2-} quantum wires in the ETS-10 crystals, Ag^+ ions were incorporated into ETS-10 matrix by ion-exchange of extra framework cations (i.e., Na^+ and K^+) to form Ag^+ ion-exchanged ETS-10. Afterwards, partially reversible photochromic behavior of Ag^0 nanoparticle incorporated titanosilicate ETS-10 films was achieved for the first time. The resulting Ag^0 -ETS-10 films and also Ag^+ -ETS-10 crystals had been characterized by ICP-OES, XRD, XPS, FE-SEM, HR-TEM, UV-vis spectroscopies. Partial restoration of color was achieved after second thermal treatment, which implies reversibility of the photochromic process.

In the second part of the current thesis study, different techniques to obtain ETS-10 thin films were deeply investigated by spin-coating and secondary growth methods for the purpose of testing the obtained films in different applications. To attach the silver incorporated ETS-10 particles to the substrate, Ag^+ ion-exchanged ETS-10 crystals were suspended in acetone and coated on regular glass substrates by spin coating method in order to investigate its photochromic property. Further investigation was carried out to obtain firmly attached ETS-10 films on conducting ITO glass and non-conducting α -alumina substrates by using secondary growth of seed crystals. After that, long-range ionic conductivity properties of zeo-type ETS-10 films prepared via secondary growth method was investigated by using impedance spectroscopy for the first time at Central Laboratory, METU. The Na^+ and K^+ ions within the framework of as-synthesized ETS-10 films were ion-exchanged with Li^+ , Ca^{2+} , and Zn^{2+} ions to figure out the effect of cation site occupancy on conduction. The current studies reveal the long-range ionic conductivity of titanosilicate ETS-10 films prepared by secondary growth method for the first time. These results might open new gateways for ion-exchange, fuel cells, and sensor applications.

Keywords: ETS-10, Titanosilicate, Zeo-type materials, Secondary growth, Silver nanoparticles, Thin films, Photochromism, Ionic conductivity, X-ray Photoelectron spectroscopy (XPS), Raman spectroscopy, Impedance spectroscopy.

ÖZ

TİTANYUMSİLİKAT ETS-10 İNCE FİLMLERİNİN OPTİK VE ELEKTRİKSEL KARAKTERİZASYONU: FOTOKROMİZM VE İYONİK İLETKENLİK

Galioglu Özaltuğ, Sezin

Doktora, Mikro ve Nanoteknoloji Bölümü

Tez Yöneticisi: Doç. Dr. Burcu Akata Kurç

Yardımcı Tez Yöneticisi: Prof. Dr. A. Macit Özenbaş

Haziran 2015, 211 Sayfa

P25 ve titanyum (IV) isopropoksit titanyum kaynakları kullanılarak zeo-tip Engelhard titanyumsilikat (ETS-10) kristalleri sentezlenmiştir. Farklı titanyum kaynaklarının kullanılması farklı morfoloji ve parçacık boyutlarında ETS-10 elde edilmesine yol açmıştır. Titanyumsilikat ETS-10 kristallerinin incelenmesi Alan Emisyonlu İkincil Elektron Mikroskobu (FE-SEM), X-Işını Difraktometresi (XRD) and Raman spektroskopisi kullanılarak yapılmıştır. Yapılan analizler göstermiştir ki: örnekler sadece saf ETS-10 fazını içermekte, titanyumsilikat ETS-4 ya da kuartz fazlarını içermemektedir.

P25 titanyum kaynağı kullanılarak mikronaltı ETS-10 parçacıkları, Ag^+ iyonları ve Ag^0 nanoparçacıkları ile katkılılandırıldı ve İndüktif Eşleşmiş Plazma-Optik Emisyon Spektrometresi (ICP-OES), X-Işını Difraktometresi (XRD), X-Işını Fotoelektron Spektroskopisi (XPS), Alan Emisyonlu İkincil Elektron Mikroskobu (FE-SEM), Geçirimli Elektron Mikroskobu (TEM), Yüksek Çözünürlüklü-Geçirimli Elektron Mikroskobu (HR-TEM), Ultraviyole ve Görünür Işık (UV-Vis) Absorpsiyon

Spektroskopisi, Azot Adsorpsiyon-Disorpsiyon tekniđi ve Raman Spektroskopisi gibi ileri analitik teknikleri kullanılarak karakterize edildi. Ayrıntılı Raman analizleri sonucunda, Ag^+ -ETS-10 örneklerinde konak malzemenin yapısal bütünlüğünün bozulmadığı fakat ETS-10'nun yapısındaki titanat kuantum zincirlerinde gümüş yükleme oranlarına bađlı olarak belirgin bir deđişim olduđu gözlenmiştir. ETS-10 kristalleri içerisindeki 1D TiO_3^{2-} kuantum zincirlerinin etkisini anlamak için, Ag^+ iyonları ETS-10 matrisi içine, ana matrisin dışında bulunan katyonlarla (Na^+ and K^+) iyon deđişimi yöntemi kullanılarak yerleştirilmiştir. Daha sonra, yarı geri dönüşümlü fotokromik davranış, Ag^0 nanoparçacık katkılanırılmış ETS-10 filmlerinde ilk defa olarak elde edilmiştir. Elde edilen Ag^0 -ETS-10 filmleri ve aynı zamanda Ag^+ -ETS-10 kristalleri, İndüktif Eşleşmiş Plazma-Optik Emisyon Spektrometresi (ICP-OES), X-Işını Difraktometresi (XRD), X-Işını Fotoelektron Spektroskopisi (XPS), Alan Emisyonlu İkincil Elektron Mikroskobu (FE-SEM), Yüksek Çözünürlüklü-Geçirimli Elektron Mikroskobu (HR-TEM), Ultraviyole ve Görünür Işık (UV-Vis) Absorpsiyon Spektroskopisi kullanılarak karakterize edilmiştir. İkinci ısısal muameleden sonra rengin kısmi geri dönüşümü sağlanmıştır, bu da fotokromik prosesin geri dönüştürebilir olduğunu göstermiştir.

Bu tezin ikinci aşamasında, elde edilen filmleri farklı uygulama alanlarında test etmek amacıyla, döndürerek kaplama ve ikincil büyütme metodları gibi farklı teknikler kullanılmış ve ayrıntısıyla incelenmiştir. Gümüş içeren ETS-10 parçacıklarını alltaşa tutturabilmek için, Ag^+ iyon deđişimi yapılmış ETS-10 kristalleri asetonun içerisinde süspansiyon haline getirilmiştir normal cam alltaşlar üzerinde döndürerek kaplama yöntemi kullanılarak kaplanmış ve fotokromik özellikleri incelenmiştir. İletken ITO cam ve iletken olmayan alfa alumina alltaşlarına sıkı tutunan ETS-10 filmleri elde etmek için, öncül (seed) kristallerin ikincil büyütülmesi metodu kullanılarak kapsamlı araştırmalar yapılmıştır. Daha sonra, ikincil büyütme yöntemi kullanılarak hazırlanan zeo-tip ETS-10 filmlerinin uzun-mesafe iyonik iletkenliği empedans spektroskopisi kullanılarak literatürde ilk defa olarak incelenmiştir. Katyon yerleşim yerlerinin iletkenlik üzerindeki etkilerini anlayabilmek için, sentezlendiğinde ETS-10 filmlerinin yapısında bulunan Na^+ ve K^+ iyonları, Li^+ , Ca^{2+} , ve Zn^{2+} iyonlarıyla deđiştirilmiştir. Bu çalışmalar, ikincil büyütme

yöntemi ile hazırlanan titanyumsilikat ETS-10 filmlerinin uzun-mesafe iyonik iletkenliğini literatürde ilk defa olarak göstermiştir. Bu sonuçlar iyon-değişimi, yakıt-hücreleri ve sensor uygulamaları için yeni kapılar açabilir.

Anahtar Kelimeler: ETS-10, Titanyumsilikat, Zeo-tip malzemeler, İkincil büyütme, Gümüş nanoparçacıkları, İnce filmler, Fotokromizm, İyonik İletkenlik, X-ışını fotoelektron spektroskopisi (XPS), Raman spektroskopisi, İmpedans spektroskopisi.

To my dearest, Emrah
and
To my family

ACKNOWLEDGEMENTS

I would like to express my deepest gratitude to my supervisor Assoc. Prof. Dr. Burcu Akata Kurç, for her excellent guidance, caring, patience, inspiration, and providing me an excellent atmosphere for doing research during my Ph.D. study. Her trust in me has changed all my academic life.

It is great pleasure to thank my co-supervisor Prof. Dr. Macit Özenbaş for his guidance and comments.

I would like to thank to the thesis monitoring committee members Prof. Dr. Selim Acar, Assoc. Prof. Dr. Y. Eren Kalay, Assoc. Prof. Dr. Ali Çırpan, and Assist. Prof. Dr. Selis Önel for their precious comments.

I would like to thank to group members; Berna Ozansoy Kasap, Duygu Kuzyaka, Melda İşler Binay, S. Kaan Kirdeciler for their friendship and helps during my study. All of them calmed me down when I was stressed out, and they helped me sincerely when I was in trouble. I owe my sincere gratitude and special thanks to Dr. İbrahim Çam from whom I learned various subjects. I would like to thank to Seçkin Öztürk, Sedat Canlı, Ali Güzel, İlker Yıldız, Merve Kaplan, Merve Cengiz, Leyla Molu, and Zafer Artvin for their guidance and help in the experiments conducted at Central Laboratory, METU.

The author is most grateful to her family members for supporting her continuously throughout her life unconditionally, to her mother, for raising her with never-ending love, patience and support, to her father, for teaching her the excitement of science and committing his life to his family, to her sisters F. Esin Galioglu and Yeliz

Galioglu and to her brother Mehmet Galioglu, for their love, never-ending patience and support. I love you my dear family!

Special thanks to Nur Coşan Özköse, Mehmet Özköse and Kavi Özköse for their friendship and for reminding me what really matters in life. I would like to thank Esin Soy Yapıcı and Dilek Demir for their friendship. Special thanks to Kadriye Sırçacı for her love, caring and support. It is great pleasure to thank my mother in law Bedriye Sırçacı for her love, patience, caring and support.

Last but not least, I would like to give my endless gratitude to my dearest Emrah Özaltuğ, who supported and motivated me with his love and understanding during the whole period of my study.

I am also appreciative of the financial support that I received for this study through Scientific and Technical Research Council of Turkey (TUBITAK) and European Union project with the project number FP7-PEOPLE-2012-IRSES, 318524, Integrated Nanodevices-NANODEV.

TABLE OF CONTENTS

ABSTRACT	v
ÖZ	vii
ACKNOWLEDGEMENTS	xi
TABLE OF CONTENTS	xiii
LIST OF TABLES	xviii
LIST OF FIGURES	xx
LIST OF ABBREVIATIONS	xxvii
LIST OF SYMBOLS	xxviii
CHAPTERS	
1. INTRODUCTION	1
1.1 Goal and Objectives	4
1.2 Literature Review	4
1.2.1 Zeolites	4
1.2.2 Titanosilicate ETS-10.....	6
1.2.3 Silver Modified Titanosilicate ETS-10	9
1.2.4 Photochromism	13
1.2.4.1 What is Photochromism?	13
1.2.4.2 Photochromic Behavior of Inorganic and Zeo- Type Materials	14
1.2.5 Zeolite and Zeo-Type Films Prepared by using Secondary Growth Method	17
1.2.5.1 Introduction to Secondary Growth Method	17
1.2.5.2 MFI, BEA, LTL, LTA, and FAU Type Zeolite Films Prepared by using Secondary Growth Method	20
1.2.5.2.1 MFI Type Membranes and Films.....	21
1.2.5.2.2 LTA and FAU Type Films.....	23
1.2.5.3 Zeo-Type Films Prepared by using Secondary	

Growth Method	24
1.2.5.3.1 Titanosilicate ETS-4 and ETS-10 Films Prepared by using Secondary Growth Method	25
1.2.6 Ionic Conductivity of Zeolites and Zeo-Type Materials	33
1.2.6.1 General Aspects.....	33
1.2.6.2 Introduction to Impedance Spectroscopy (IS).....	35
1.2.6.2.1 Impedance-Related Functions	40
1.2.6.3 Metal Cation Conduction	40
1.2.6.3.1 Effect of Si/Al Ratio of Zeolites	45
1.2.6.3.2 Effect of Charge - Radius of Extra- Framework Cations	46
1.2.6.3.3 Effect of Hydration State.....	51
1.2.6.4 Metal Cation Conduction of Zeo-Type Materials and Thin Films	52
REFERENCES	59
2. EXPERIMENTAL PROCEDURES	69
2.1 Synthesis of Submicrometer-Sized ETS-10 Crystals	69
2.1.1 Synthesis of Submicrometer-Sized ETS-10 Crystals.....	69
2.1.2 Analytical Procedures and Equipment	70
2.2 Silver Encapsulation of Titanosilicate ETS-10	70
2.2.1 Preparation of Ag ⁺ -ETS-10 and Ag ⁰ -ETS-10 Crystals	70
2.2.2 Analytical Procedures and Equipment	70
2.3 Photochromism.....	71
2.3.1 Preparation of Ag ⁺ -ETS-10 Crystals and Ag ⁰ -ETS-10 Films.....	71
2.3.2 Analytical Procedures and Equipment	73
2.3.3 Testing the Photochromic Activity of Ag ⁰ -ETS-10 Films.....	74
2.4 Preparation of ETS-10 Films by using Secondary Growth Method	75
2.4.1 Preparation of ETS-10 Films.....	75
2.4.2 Analytical Procedures and Equipment	78

2.5 Preparation of ETS-10 Films by using Secondary Growth Method	78
2.5.1 Preparation of ETS-10 Films	78
2.5.2 Preparation of Zeolite Y (FAU) Films	78
2.5.3 Ion-Exchange of Titanosilicate ETS-10 Films.....	80
2.5.4 Analytical Procedures and Equipment	82
2.5.5 Design of Conductivity System	82
REFERENCES.....	85
3. SYNTHESIS OF TITANOSILICATE ETS-10	87
3.1 Synthesis of Submicrometer-Sized ETS-10 Crystals.....	87
3.2 Structural Characterization of Titanosilicate ETS-10 Crystals	90
3.3 Conclusions	92
REFERENCES.....	93
4. EFFECT OF SILVER ENCAPSULATION ON THE LOCAL STRUCTURE OF TITANOSILICATE ETS-10	95
4.1 Inductively Coupled Plasma / Optical Emission Spectrometry (ICP-OES)	96
4.2 X-Ray Diffraction (XRD)	97
4.3 Field Emission - Scanning Electron Microscopy (FE-SEM) and High Resolution-Transmission Electron Microscopy (HR-TEM).....	99
4.4 Diffuse Reflectance - Ultraviolet - Visible (DR-UV-vis) Spectroscopy and Nitrogen Adsorption-Desorption	104
4.5 X-Ray Photoelectron Spectroscopy (XPS)	107
4.6 Raman Spectroscopy	109
4.7 Conclusions	112
REFERENCES	115
5. PHOTOCROMISM.....	117
5.1 Field Emission-Scanning Electron Microscopy (FE-SEM) and High Resolution-Transmission Electron Microscopy (HR-TEM)....	119
5.2 X-Ray Diffraction (XRD)	123
5.3 Ultraviolet-Visible (UV-vis) Spectroscopy.....	124
5.4 X-Ray Photoelectron Spectroscopy (XPS)	128

5.5 Mechanism of Photochromic Process of Titanosilicate ETS-10	
Films.....	135
5.6 Conclusions	137
REFERENCES	139
6. PREPARATION OF ETS-10 FILMS BY USING SECONDARY GROWTH METHOD	141
6.1 Parameters that affect Microstructure of Titanosilicate ETS-10	
Films.....	141
6.1.1 Effect of Seed Concentration and Number of Spin Coating Step	141
6.1.2 Effect of Reaction Time and Substrate Type	147
6.2 Discussion	157
6.3 Conclusions	162
REFERENCES	165
7. IONIC CONDUCTIVITY OF ZEOLITES AND ZEO-TYPE MATERIALS	167
7.1 Measurement Methods	168
7.2 Ionic Conductivity of (Na ⁺ , K ⁺)-ETS-10 and FAU Films.....	169
7.2.1 Ionic Conductivity of Hydrated (Na ⁺ , K ⁺)-ETS-10 and FAU Films.....	172
7.2.2 Ionic Conductivity of Dehydrated (Na ⁺ , K ⁺)-ETS-10 and FAU Films	175
7.2.2.1 Ionic Conductivity of Dehydrated (Na ⁺ , K ⁺)-ETS-10 Films as a Function of Film Thickness.....	179
7.2.3 Ionic Conductivity of Dehydrated M-ETS-10 (where, M = Li ⁺ , Zn ²⁺ , and Ca ²⁺) Films.....	182
7.3 Conclusions	188
REFERENCES	191
8. SUMMARY, CONCLUSION AND FURTHER SUGGESTIONS	193
8.1 Synthesis of ETS-10 Crystals.....	193
8.2 Silver Incorporation into Titanosilicate ETS-10	194
8.3 Photochromism.....	195

8.4 Preparation of ETS-10 Films by using Secondary Growth Method	196
8.5 Ionic Conductivity of Zeolites and Zeo-Type Materials.....	198
8.6 Outlook for the Future Work.....	200
REFERENCES.....	201
APPENDICES	203
Appendix A : Calculation of Activation Energy of ETS-10 Films...	203
CURRICULUM VITAE	207

LIST OF TABLES

TABLES

Table 1.1. The (110)/(001) peak intensity ratios of ETS-4 crystals in samples [80]	28
Table 1.2 Relation between the four basic imittance functions* [87]	40
Table 1.3. Distribution of Na ⁺ ions over the corresponding sites in NaX and NaY [90].	41
Table 1.4. Activation energies (kJ mol ⁻¹) of ionic conduction of monovalent cations in faujasite [93].	45
Table 1.5. Activation energies (kJ mol ⁻¹) for ionic conduction of divalent cations in zeolite X [93].	47
Table 1.6. Typical ionic conductivities and activation energies of dehydrated M ₃ HGe ₇ O ₁₆ , M = K ⁺ , Rb ⁺ and Cs ⁺ [85]	53
Table 1.7. Conductivity and activation energy values of zincosilicate M-VPI-9, where M = K ⁺ , Rb ⁺ , Cs ⁺ , Ca ²⁺ , and Sr ²⁺ [86]	54
Table 2.1. ETS-10 films prepared on ITO glass and α -alumina substrates by using secondary growth method.	77
Table 2.2. ETS-10 and M-ETS-10 (where, M= Li ⁺ , Zn ²⁺ , and Ca ²⁺) films prepared on α -alumina substrates by using secondary growth method.	81
Table 4.1. The ICP-OES-determined Na, K, Ag values (wt. %) and (Na+K+Ag)/Ti ratios in as-synthesized, Ag ⁺ -ETS-10 and Ag ⁰ -ETS-10 samples.	97
Table 5.1. Binding energy of the deconvoluted peaks of the Ti 2p and Ag 3d spectra and the corresponding relative sub-peak area ratios of the films.	134
Table 6.1. Thicknesses of ETS-10 films prepared on ITO glass substrates using secondary growth of seed crystals 7-1S-ITO.	150

Table 6.2. Thickness of ETS-10 films prepared on ITO glass substrates using secondary growth of seed crystals 7-2S-ITO.	153
Table 6.3. Thickness of ETS-10 films prepared on α -alumina substrates using secondary growth of seed crystals 7-2S- α -alumina.	157
Table 6.4. Comparison of ETS-10-film-thickness related to reaction time.	159
Table 7.1. Thickness, activation energy of transport (E_A), and conductivity values at 300, 450 and 500 °C for ETS-10 films.	181
Table 7.2. Thickness, activation energy of transport (E_A), and conductivity values at 300, 450 and 500 °C for partly ion-exchanged M-ETS-10 films, where M = Li ⁺ , Zn ²⁺ , Ca ²⁺	186

LIST OF FIGURES

FIGURES

Figure 1.1. Representative zeolite frameworks, (with pore openings). (a) zeolite A (3D, 4.2 Å); (b) zeolite Y (3D, 7.4 Å);(c) Zeolite L (1D, 7.1 Å); (d) ZSM-5 (silicalite) (2D, 5.3 ×5.6 Å, 5.1 ×5.5 Å) D-dimensions of channel system [3]	5
Figure 1.2. Crystal structure of ETS-10,a) typical truncated bipyramidal morphology of the crystals, which consist of a three-dimensional network of SiO ₂ channels (blue) and TiO ₃ ²⁻ molecular wires (red), b) view along the [1 $\bar{1}$ 0] axis, c) view along the [110] axis, d) a single TiO ₃ ²⁻ molecular wire [5]	6
Figure 1.3. High-resolution electron micrograph of ETS-10 recorded on a JEOL 400 kV electron microscope [9].	7
Figure 1.4. SEM images of the solid products synthesized in the synthesis system of 3.4Na ₂ O:1.5K ₂ O:TiO ₂ :5.5SiO ₂ :180H ₂ O at 230 °C with (a) P25, (b) TiCl ₃ as the Ti sources, respectively [8].	8
Figure 1.5. Proposed mechanisms of ETS-10 crystallization with P25 as the Ti source [8].	9
Figure 1.6. FE-SEM images of (a) as-synthesized ETS-10, (b) Ag ⁺ -exchanged ETS-10 (Ag ⁺ -ETS-10-15); and Ag ⁰ nanoparticle-modified ETS-10 samples with different Ag ⁰ loading levels: (c) Ag ⁰ -ETS-10-3 (i.e., 3 mM AgNO ₃), (d) Ag ⁰ -ETS-10-6 (i.e., 6 mM AgNO ₃), (e) Ag ⁰ -ETS-10-10 (i.e., 10 mM AgNO ₃), and (f) Ag ⁰ -ETS-10-15 (i.e., 15 mM AgNO ₃) [13].	11
Figure 1.7. (a) An example of photochromic smart bispiropyran polymers [37], (b) photochromic materials in sunglasses [38].	14
Figure 1.8. A schematic representation of zeolite crystallization process [48].	18
Figure 1.9. Schematic of secondary (or seeded) growth technique [48]	19

Figure 1.10. Schematic representation of the steps used to fabricate MFI films with <i>b</i> - and <i>a</i> -out-of-plane orientations are shown in the upper and lower panels, respectively [54].	22
Figure 1.11. Schematic illustrations of (A) leaflet-shaped and (B) coffin-shaped Silicalite (framework type MFI) crystals and (C) truncated bipyramidal zeolite beta (framework type BEA) crystals and their channel systems, as well as their respective (D) <i>a</i> -oriented, (E) <i>b</i> -oriented, and (F) <i>a</i> -oriented monolayers. (G to I) Secondary growth on these monolayers produces uniformly oriented films [69].	23
Figure 1.12. (a) Top view of ETS-4 membranes made by secondary growth (200°C, 1 day); (b) structure of ETS-4 (view down the <i>b</i> -axis) and (c) X-ray powder diffractograms of the membrane in different stages in comparison with a randomly oriented ETS-4 powder [81].	27
Figure 1.13. FE-SEM images of ETS-4 seed layer on α -alumina substrate (a) ETS-4 film on α -alumina substrate (b) top view; (c) cross-sectional view [80].	29
Figure 1.14. SEM images of heteroepitaxially grown ETS-10 crystals on ETS-4. (a) View of the (<i>h</i> 00) face of ETS-4 with nucleated submicron crystals of ETS-10; (b) view of the (00 <i>l</i>) face of the ETS-4 crystals; few of the ETS-10 crystals extend over the (<i>h</i> 00) face and start covering the (00 <i>l</i>) faces of ETS-4. A schematic of the early growth process is shown in (c). SEM images of the ETS-4 precursor layer (d), and of the ETS-10/-4 film synthesized by heteroepitaxial growth on the ETS-4 precursor layers after 20 h (e) [78].	30
Figure 1.15. FE-SEM top view (a) and cross-section (b) images of ETS-10 films prepared on the ITO glass substrates using secondary growth of seed layers deposited using 1 dip coating steps. *SL = seed layer, CG = columnar grains [84].	32
Figure 1.16. Ionic conductivity of some solid electrolytes and representative sodium zeolites: NaZSM-5 (Si/Al = 24), NaA (Si/Al = 1), NaX (Si/Al ~ 1.3-1.5), NaY (Si/Al = 5.4), NaZK-5 (Si/Al = 6.5) and NaDY (Si/Al = 350). Concentrated H ₂ SO ₄ is given for comparison [1].	34
Figure 1.17. Excitation and response in IS [88].	36
Figure 1.18. Impedance plane plot (Argand diagram) [89].	37
Figure 1.19. Basic electrical circuit elements [88].	38

Figure 1.20. Typical equivalent RC circuit (a) and its impedance plane plot (b) [88].	38
Figure 1.21. An example of Arrhenius plot.	39
Figure 1.22. Schematic presentation of the faujasite structure with the cation sites SI, SI', SII', SII, and SIII occupied by monovalent cations. While (a) indicates the cation sites, (b) is drawn with the respective Na^+ radius to point out the size relationships [90].	42
Figure 1.23. Modulus spectra of the imaginary part M'' vs. $\log f$ of NaX [92].	43
Figure 1.24. Illustration of the conductivity processes and the corresponding potential profile in faujasite indicating the different activation energies of the high-frequency (HF) and the low-frequency (LF) process [90].	44
Figure 1.25. Activation energy as a function of the $\text{SiO}_2/\text{Al}_2\text{O}_3$ ratio for different alkali cations in zeolite ZSM-5 [94].	46
Figure 1.26. Plots of the activation energy for ionic conduction as a function of the univalent cation radius for synthetic faujasites. a) Y-types ($\text{Si}/\text{Al} \sim 2.5\text{-}5$): ■ [16], ◇ [17], + [18], ▲ [16], ○ [19]. b) X-types ($\text{Si}/\text{Al} \sim 2.5\text{-}5$): X [20], + [21], ○ [19], ● [22], ■ [23], ▲ [24], ☼ [25], □ [26], + [27], ◇ [16], ▣ [28]. Plot (a) also contains data for the barriers for M^{2+} conducting ions (M^{2+}NaY mixed forms). The Li-, Rb-, Tl- and CsY forms retain a small amount of the initial Na ions. The lines are guides for the eyes [1].	49
Figure 1.27. Plot of the activation energy for ionic conduction as a function of the univalent cation radius for A-types. ☼ [16], ● [29], □ [25], ○ [26], ■ [27]. The lines are guides for the eyes [1].	50
Figure 1.28. The displacement of various sized cations from the plane of a six membered oxygen ring, XX' represents the plane of the ring. Cations larger than sodium are displaced along the axis ZZ' toward the center of a large cage [97] (left); ionic radius values of cations (right) [93,112-114].	50
Figure 1.29. Arrhenius plot of Na-Y for the HF process at 1013 hPa Ar. For comparison, the slopes for activation energies of 40 and 70 kJ mol^{-1} , respectively, are shown [96].	51
Figure 1.30. Plots of activation energy trends for Li^+ , Na^+ , and K^+ exchanged zeolite membrane, commercial micrometer-sized, submicrometer- sized, and nano-sized	

zeolites. (The error bars were only done on the Na ⁺ -exchanged version of the sample and obtained from repeat of three independent measurements) [120].	56
Figure 1.31. Proposed model for the interaction of DMMP with cations inside the supercage: cation mobility was facilitated by the re-orientation of the DMMP molecules [120].	57
Figure 2.1. Cross-sectional FE-SEM image of films.	72
Figure 2.2. Photograph of conductivity system at Central Laboratory, METU.	82
Figure 2.3. Photograph of furnace and tubular quartz system at Central Laboratory, METU.	84
Figure 3.1. Framework connectivity of ETS-10.	88
Figure 3.2. FE-SEM image of submicrometer-sized ETS-10 crystals.	89
Figure 3.3. XRD pattern of submicrometer-sized ETS-10 crystals.	90
Figure 3.4. Raman spectra of submicrometer-sized ETS-10 crystals.	91
Figure 4.1. Illustration of the growth mechanism for Ag ⁰ NPs synthesized using NaBH ₄ as proposed by Polte et al [1].	96
Figure 4.2. X-ray diffraction (XRD) patterns of (a) ETS-10, (b) Ag ⁺ -ETS-10-(5 wt. %), (c) Ag ⁺ -ETS-10-(10 wt. %), (d) Ag ⁺ -ETS-10-(15 wt. %), (e) Ag ⁰ -ETS-10-(5 wt. %), (f) Ag ⁰ -ETS-10-(10 wt. %), (g) Ag ⁰ -ETS-10-(15 wt. %).	98
Figure 4.3. Field emission scanning electron microscopy FE-SEM images of (a) ETS-10, (b) Ag ⁰ -ETS-10-(5 wt. %), (c) Ag ⁰ -ETS-10-(10 wt. %), (d) Ag ⁰ -ETS-10-(15 wt. %).	100
Figure 4.4. Transmission electron microscopy (TEM) image of (a) Ag ⁰ -ETS-10-(5 wt. %), (b) Ag ⁰ -ETS-10-(10 wt. %), (c) Ag ⁰ -ETS-10-(15 wt. %).	101
Figure 4.5. (a) and (b) High-resolution TEM (HR-TEM) images of Ag ⁰ -ETS-10-(10 wt. %) in different magnifications, (c) HR-TEM image of Ag ⁰ -ETS-10-(10 wt. %) along [110] direction.	103
Figure 4.6. Nitrogen adsorption-desorption isotherms of ETS-10 (black) and Ag ⁰ -ETS-10-(10 wt. %) (red).	105
Figure 4.7. Diffuse reflectance-UV-vis spectra (in terms of Kubelka-Munk function) of ETS-10 (black), Ag ⁰ -ETS-10-(5 wt. %) (red), Ag ⁰ -ETS-10-(10 wt. %) (blue), Ag ⁰ -ETS-10-(15 wt. %) (olive).	106

Figure 4.8. (a) XPS survey scan of Ag ⁰ -ETS-10-(10 wt. %), (b) high resolution Ag 3d spectra of, (1) Ag ⁺ -ETS-10-(5 wt. %), (2) Ag ⁺ -ETS-10-(10 wt. %), (3) Ag ⁺ -ETS-10-(15 wt. %), (4) Ag ⁰ -ETS-10-(5 wt. %), (5) Ag ⁰ -ETS-10-(10 wt. %), (6) Ag ⁰ -ETS-10-(15 wt. %).	108
Figure 4.9. Raman spectra of ETS-10 (a), Ag ⁺ -ETS-10-(5 wt. %) (b), Ag ⁺ -ETS-10-(10 wt. %) (c), Ag ⁺ -ETS-10-(15 wt. %) (d).	109
Figure 4.10. Raman spectra of ETS-10 (a), Ag ⁰ -ETS-10-(5 wt. %) (b), Ag ⁰ -ETS-10-(10 wt. %) (c), Ag ⁰ -ETS-10-(15 wt. %) (d).	111
Figure 5.1. Photograph of (a) Ag ⁺ -ETS-10 films, (b) I-Ag ⁰ -ETS-10 films, (c) 116-LT-ETS-10 films, (d) 5h-II-Ag ⁰ -ETS-10 films.	118
Figure 5.2. Photograph of (a) 90-LT-ETS-10 films, (b) 100-LT-ETS-10 films, (c) 116-LT-ETS-10 films.	119
Figure 5.3. Field emission scanning electron microscopy (FE-SEM) images of (a) I-Ag ⁰ -ETS-10 films, (b) 116-LT-ETS-10 films, (c) 5h-II-Ag ⁰ -ETS-10 films, high resolution transmission electron microscopy (HR-TEM) images of (d) I-Ag ⁰ -ETS-10 films, (e) 116-LT-ETS-10 films, (f) 5h-II-Ag ⁰ -ETS-10 films.	121
Figure 5.4. X-ray diffraction (XRD) patterns of (a) ETS-10 (black), (b) I-Ag ⁰ -ETS-10 films (red), (c) 116-LT-ETS-10 films (blue), (d) 5h-II-Ag ⁰ -ETS-10 films (green).	123
Figure 5.5. UV-vis spectra of (a) ETS-10 (black), I-Ag ⁰ -ETS-10 films (red), 116-LT-ETS-10 films (blue), 5h-II-Ag ⁰ -ETS-10 films (green), (b) I-Ag ⁰ -ETS-10 films (black), 90-LT-ETS-10 films (red), 100-LT-ETS-10 films (blue), 116-LT-ETS-10 films (green).	126
Figure 5.6. I-Ag ⁰ -ETS-10 films (black), 116-LT-ETS-10 films (red), 3h-II-Ag ⁰ -ETS-10 films (blue), 5h-II-Ag ⁰ -ETS-10 films (green).	127
Figure 5.7. X-ray photoelectron spectroscopy (XPS) high resolution Ag 3d spectra of (a) I-Ag ⁰ -ETS-10 films, (b) 116-LT-ETS-10 films, (c) 5h-II-Ag ⁰ -ETS-10 films.	130
Figure 5.8. X-ray photoelectron spectroscopy (XPS) high resolution Ti 2p spectra of (a) I-Ag ⁰ -ETS-10 films, (b) 116-LT-ETS-10 films, (c) 5h-II-Ag ⁰ -ETS-10 films.	132

Figure 5.9. (a) Comparison between the position of the Fermi level of silver nanoparticles consisting of 20 atoms (~ 0.9 nm) and band gap energy of the ETS-10, (b) The silver nanoparticles consisting of 20 atoms that place within the ETS-10 pores.	136
Figure 6.1. Cross sectional FE-SEM images of seed layers (a) 5-1S-ITO, (b) 7-1S-ITO, and (c) 7-2S-ITO.	142
Figure 6.2. Top-view FE-SEM image of ETS-10 films (a) 5-1S-4h-ITO, (b) 5-1S-10h-ITO and (c) cross-sectional FE-SEM image of 5-1S-4h-ITO.	143
Figure 6.3. FE-SEM images of (a) bare α -alumina substrate, ETS-10 seed layers on α -alumina substrates (b) 7-1S- α -alumina and (c) 7-2S- α -alumina.	146
Figure 6.4. AFM images of bare (a) ITO glass and (b) α -alumina substrates.	146
Figure 6.5. FE-SEM images of ETS-10 films (a) cross section of 7-1S-2h-ITO and top-view of (b) 7-1S-2h-ITO, and (c) 7-1S-24h-ITO.	148
Figure 6.6. FE-SEM images of ETS-10 films prepared via secondary growth method (a) top-view of 7-1S-4h-ITO and cross section of, (b) 7-1S-4h-ITO, (c) 7-1S-6h-ITO, (d) 7-1S-8h-ITO.	149
Figure 6.7. XRD patterns of (a) ETS-10 crystals in the powder form and ETS-10 films (b) 7-1S-2h-ITO, (c) 7-1S-4h-ITO, (d) 7-1S-6h-ITO, (e) 7-1S-8h-ITO, (f) 7-1S-10h-ITO.	151
Figure 6.8. Top-view FE-SEM image of 7-2S-4h-ITO.	152
Figure 6.9. FE-SEM images of ETS-10 films prepared via secondary growth method (a) and (d) cross section view of 7-2S-10h-ITO, (b) 7-2S-4h-ITO, and (c) 7-2S-6h-ITO.	153
Figure 6.10. XRD patterns of (a) ETS-10 crystals in the powder form and ETS-10 films (b) 7-2S-2h- α -alumina, (c) 7-2S-4h- α -alumina, (d) 7-2S-6h- α -alumina, (e) 7-2S-8h- α -alumina, (f) 7-2S-10h- α -alumina.	154
Figure 6.11. Top-view FE-SEM images of ETS-10 films prepared via secondary growth method, (a) 7-2S-2h- α -alumina, (b) 7-2S-4h- α -alumina, (c) 7-2S-6h- α -alumina and (d) 7-2S-10h- α -alumina.	155
Figure 6.12. Cross section FE-SEM images of ETS-10 films prepared via secondary growth method, (a) 7-2S-4h- α -alumina, (b) 7-2S-6h- α -alumina, (c) 7-2S-8h- α -alumina and (d) 7-2S-10h- α -alumina	156

Figure 6.13. Comparison of ETS-10-film-thickness related to reaction time, (a) ETS-10 films prepared on ITO glass substrates using secondary growth of 7-1S-ITO seed crystals, (b) ETS-10 films prepared on ITO glass substrates using secondary growth of 7-2S-ITO seed crystals, (c) ETS-10 films prepared on α -alumina substrates using secondary growth of 7-2S- α -alumina seed crystals.	158
Figure 6.14. (a) Top-view FE-SEM image of 5-1S-4h-ITO, (b) Schematic view adapted from [15].	161
Figure 7.1. Representation of (a) ETS-10 film and gold electrodes, (b) active area of the film where conductivity is measured.	169
Figure 7.2. XRD pattern of zeolite Y films prepared via secondary growth method.	171
Figure 7.3. (a) Top-view and (b) cross-section FE-SEM images of zeolite Y films prepared on α -alumina substrates via secondary growth method.	171
Figure 7.4. Arrhenius plot of conductivity for (Na,K)-ETS-10 films prepared by 8h-reaction, the inset figure is adapted from Yoon et al. [11].	173
Figure 7.5. Arrhenius plot of conductivity for Na-Y films prepared by 12h-reaction.	174
Figure 7.6. Argand diagram (plot of imaginary part of the impedance Z'' versus real part of the impedance Z' plotted parametrically as a function of frequency) of ETS-10 film prepared by 6h reaction.	175
Figure 7.7. Arrhenius plots of ionic conductivities for (a) (Na,K)-ETS-10 film prepared by 6h reaction ($E_A = 50.1 \pm 0.6 \text{ kJ mol}^{-1}$) and (b) NaY film ($E_A = 38.4 \text{ kJ mol}^{-1}$).	177
Figure 7.8. Arrhenius plots of ionic conductivities for (black) pressed pellets of powder ETS-10 (data was taken from literature [13]), (red) pressed pellets of powder zeolite X (data was taken from literature [13]), (blue) 4h-(Na,K)-ETS-10, (pink) 6h-(Na,K)-ETS-10, (green) 8h-(Na,K)-ETS-10, (purple) 10h-(Na,K)-ETS-10.....	180
Figure 7.9. Arrhenius plots of ionic conductivities for (a) (Na,K)-6h-ETS-10, (b) Li-6h-ETS-10, (c) Zn-6h-ETS-10, and (d) Ca-6h-ETS-10 films.	183
Figure 7.10. Relationship of activation energy (E_A) with cation radius (r) within the as-synthesized (Na,K)-6h-ETS-10 and partly ion-exchanged M-6h-ETS-10 films, where $M = \text{Li}^+$, Ca^{2+} , and Zn^{2+}	184

LIST OF ABBREVIATIONS

XRD	X-ray Diffraction
FE-SEM	Field Emission-Scanning Electron Microscopy
XPS	X-ray Photoelectron Spectroscopy
EDX	Energy Dispersive X-ray
EPMA	Electron Microprobe Analysis
HR-TEM	High Resolution-Transmission Electron Microscopy
TEM	Transmission Electron Microscopy
UV-vis Spectroscopy	Ultraviolet-visible Spectroscopy
ICP-OES	Inductively Coupled Plasma/Optical Emission Spectrometry
IS	Impedance Spectroscopy
ITO	Indium Tin Oxide
TCO	Transparent Conductive Oxide
ETS-10	Engelhard Titanosilicate-10
ETS-4	Engelhard Titanosilicate-4
FAU	Faujasite, Zeolite X and Y
NaBH ₄	Sodium Borohydride
AgNO ₃	Silver Nitrate
TiCl ₃	Titanium(III) Chloride
P25	Degussa Titanium Dioxide

LIST OF SYMBOLS

σ	Conductivity
E_A	Activation Energy

CHAPTER 1

INTRODUCTION

Engelhard titanosilicate (ETS-10) is a relatively new class of microporous crystalline material (pore dimensions: 4.9 Å and 7.6 Å) where its Ti substituted silica matrix is composed of Si in tetrahedral and Ti in octahedral coordination. The building units of ETS-10 are uniquely arranged to form 1-D TiO_3^{2-} quantum wires (i.e., -Ti-O-Ti-O-Ti-) that are effectively separated from each other by the silica matrix.

Ag^0 nanoparticles stabilized by titanosilicate (ETS-10) framework were synthesized by following a simple two step procedure involving the incorporation of Ag^+ ions into ETS-10 matrix via ion-exchange with extra framework Na^+ and K^+ cations followed by their reduction with sodium borohydride (NaBH_4) in aqueous medium all at room temperature. Ag^0 nanoparticles dispersed in the ETS-10 matrix were collected as powders and characterized by using advanced analytical methods including ICP-OES, XRD, XPS, FE-SEM, TEM, HR-TEM, DR-UV-vis, Raman spectroscopies and N_2 adsorption-desorption technique. Overall result show the formation of Ag^0 nanoparticles dispersed within the framework of ETS-10 without causing alteration in ETS-10 lattice and mesopore formation. The changes in the local titanate (TiO_3^{2-}) structure of ETS-10 resulting from the incorporation of Ag^+ ions and formation of Ag^0 nanoparticles within the titanosilicate framework were extensively studied on Ag^+ -exchanged and Ag^0 -nanoparticles-containing samples, separately. Although maintaining of structural integrity of host material had been monitored for Ag^+ -ETS-10, detailed Raman analyses of Ag^0 -ETS-10 samples showed significant changes in the titanate quantum wires of ETS-10 framework depending on the silver loading. Total collapse of these units was observed in the Ag^0 -ETS-10 samples with high silver loading (15 wt. % Ag^+).

First of all ETS-10 crystals were synthesized without impurity and collected in the powder form. Then, effect of silver encapsulation in the local titanate (TiO_3^{2-}) structure of ETS-10 was studied extensively. After that, to show role of 1-D TiO_3^{2-} quantum wires in the ETS-10 crystals, Ag^+ ions were incorporated into ETS-10 matrix by ion-exchange of extra framework cations (i.e., Na^+ and K^+) to form Ag^+ ion-exchanged ETS-10 and the partially reversible photochromic behavior of Ag^0 nanoparticle incorporated titanosilicate ETS-10 films was achieved for the first time. The colored (i.e., activated state) and colorless (i.e., bleached state) forms of the photochromic system of Ag^0 nanoparticle incorporated ETS-10 films were achieved through thermal reduction and exposure to visible laser at 532 nm wavelength, respectively. The resulting Ag^0 -ETS-10 films and also Ag^+ -ETS-10 crystals have been characterized by ICP-OES, XRD, XPS, FE-SEM, HR-TEM, UV-vis spectroscopies. Partial restoration of color was achieved after second thermal treatment, which implies reversibility of the photochromic process. The relationship of ETS-10's unique structural formation along with the integration of Ag^0 nanoparticles within its matrix and its subsequent photochromic property was shown for the first time.

For use in advanced applications such as molecular separation, photocatalysis, fuel cells, sensors etc., zeolites and zeo-type crystals should be supported on a substrate. Therefore, several reports exist in the literature about preparation of thin films of these materials on various substrates due to their potential use in advanced application areas. Investigations on the formation of zeo-type ETS-10 thin films on transparent conductive oxide (TCO) substrates were conducted by our group during my master thesis study. One of our objectives was to enhance the film formation methods in order to obtain continuous, well-intergrown ETS-10 films with columnar grain structure. ETS-10 films (average thicknesses 1.3 - 4.3 μm) were prepared on the ITO glass and α -alumina substrates using secondary growth of ETS-10 multilayers. After secondary growth, the films showed a columnar grain microstructure. The prepared films were strongly attached to the ITO glass and α -alumina substrates. The following parameters affecting the microstructure of the ETS-10 films were investigated:

- Concentration of ETS-10 seed crystals,
- Number of spin coating step,
- Reaction time of secondary growth,
- Type of substrate.

In the last part of my thesis study, the thicknesses of ETS-10 films prepared on non-conducting α -alumina substrates were altered from 2.0 - 4.3 μm through changing reaction time of the secondary growth method. A system design was done and impedance spectroscopy was used to study the long-range ionic conductivity of microporous titanosilicate ETS-10 films in the temperature range of 25 to 500 $^{\circ}\text{C}$. The semicircles in the complex (Z' vs. $-Z''$) plane as a function of frequency were plotted for each sample. The activation energies were reported for different thicknesses of the films. ETS-10 films prepared using secondary growth was found to have a lower activation energy for ion conduction and higher dc conductivity than that of ETS-10 powder samples reported in the literature (*Wei et al., J. Phys. Chem. B* 2006, 110, 13728), $50.1 \pm 0.6 \text{ kJ mol}^{-1}$ (0.5 eV) compared to 58.5 kJ mol^{-1} (0.6 eV). Furthermore, Na^+ ions within the framework of ETS-10 film were ion-exchanged with Li^+ , Ca^{2+} , and Zn^{2+} ions to figure out effect of cation site occupancy on conduction. The following parameters affecting the long-range ionic conductivity of the ETS-10 films were studied:

- Hydration state,
- Grain boundary structure (i.e., intergrown film),
- Cation site occupancy.

The current study shows ionic conductivity properties of titanosilicate ETS-10 films prepared by secondary growth method comprehensively for the first time which may be important for ion-exchange, fuel cells, and sensor applications.

1.1. Goal and Objectives

The goal of this study is first to successfully obtain ETS-10 in powder and thin film forms for the purpose of investigating its unknown optical and electrical properties. The objectives to achieve this goal can be summarized as follows:

- To synthesize titanosilicate ETS-10 crystals without impurity,
- To incorporate silver ions and silver nanoparticles into titanosilicate ETS-10 crystals and explore the effect of silver encapsulation on the local structure of titanosilicate ETS-10,
- To explore photochromic behavior of silver nanoparticle incorporated titanosilicate ETS-10 films prepared through spin-coating method,
- To prepare films of titanosilicate ETS-10 on conductive ITO glass and non-conducting α -alumina substrates through secondary growth method and alter the thickness of the ETS-10 films by changing secondary growth reaction parameters,
- To obtain as-synthesized $(\text{Na}^+, \text{K}^+)\text{-ETS-10}$ and ion-exchanged M-ETS-10 (where, M: Li^+ , Zn^{2+} , and Ca^{2+}) films that were grown by secondary growth method and explore the electrical properties by using impedance spectroscopy.

1.2 Literature Review

1.2.1 Zeolites

Zeolites are complex materials that can be considered as an assembly of two subsystems: the covalently bonded and negatively charged aluminosilicate framework and, ionically bonded exchangeable cations (lattice gas with occupational disorder). Bonding energies are ~ 2.5 eV for the framework atoms and approximately ~ 1 eV for extraframework cations [1]. The number of extraframework cations is related to the Si/Al ratio of zeolite since the cations neutralize the charge of zeolite

due to negatively charged AlO_4^- tetrahedron. The extraframework cations (i.e., typically Na^+) can be replaced by desired cations (i.e., Ag^+ , Cu^{2+} , Ca^{2+} , Li^+ , Fe^{3+}) by ion-exchange method, that is, simply by stirring zeolite powder in aqueous solution containing molten salts. Zeolites have wide range of application areas such as, molecular sieving, petrochemical processing, detergent technology, gas sensors, ion-exchange of radioactive chemical elements, etc. [1]

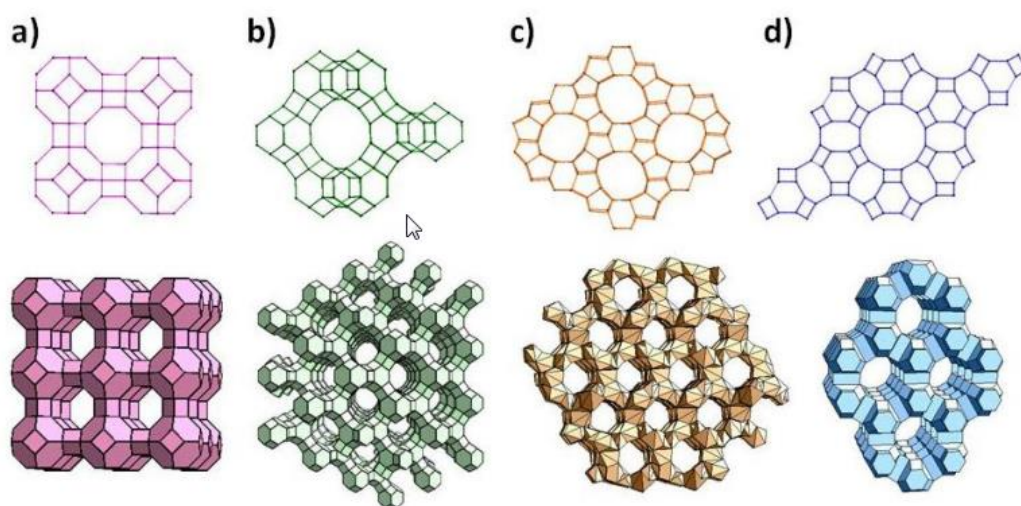


Figure 1.1. Representative zeolite frameworks, (with pore openings). (a) zeolite A (3D, 4.2 Å); (b) zeolite Y (3D, 7.4 Å); (c) Zeolite L (1D, 7.1 Å); (d) ZSM-5 (silicalite) (2D, 5.3 × 5.6 Å, 5.1 × 5.5 Å) D-dimensions of channel system [3].

Zeolites are aluminosilicates with well-defined pore and/or channel structures. Zeolites can be synthesized with different chemical compositions and framework types. 225 zeolite framework types have been approved by the Structure Commission of the International Zeolite Association (IZA-SC) [2]. Figure 1.1 displays the framework structure of four frequently used zeolites: zeolite A (Framework type: LTA), zeolite Y and X (Framework type: FAU), zeolite L (Framework type: LTL), ZSM-5 (Framework type: MFI) [3].

1.2.2 Titanosilicate ETS-10

Engelhard titanosilicate (ETS-10) is a synthetic microporous (pore dimensions; 4.9 Å and 7.6 Å) crystalline material with a framework built of corner-sharing TiO_6 octahedra and SiO_4 tetrahedra linked through bridging oxygen atoms [4]. It comprises monatomic, linear, orthogonal, non-intersecting, semiconducting 1D TiO_3^{2-} quantum wires with a diameter of 0.67 nm (Figure 1.2) [5].

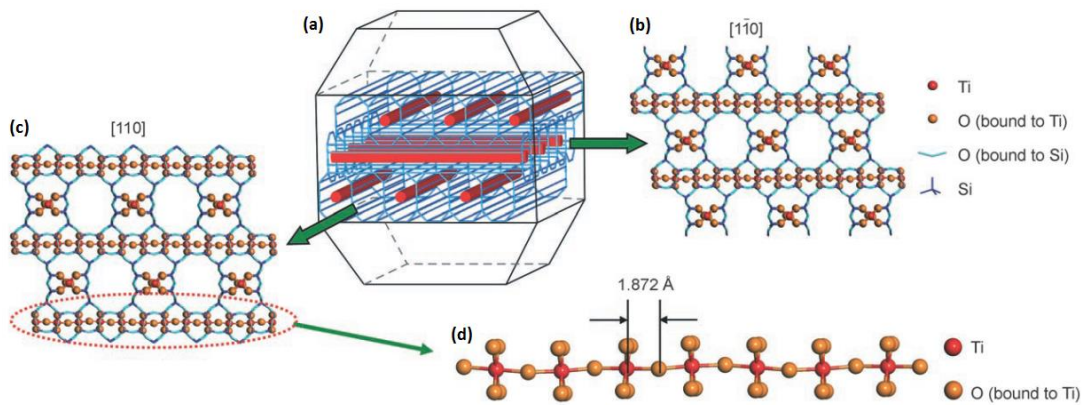


Figure 1.2. Crystal structure of ETS-10, a) typical truncated-bipyramidal morphology of the crystals, which consist of a three-dimensional network of SiO_2 channels (blue) and TiO_3^{2-} molecular wires (red), b) view along the $[1\bar{1}0]$ axis, c) view along the $[110]$ axis, d) a single TiO_3^{2-} molecular wire [5].

Two-dimensional surface nucleation is proposed for growth of ETS-10 crystals [6-8]. In this growth model, ETS-10 crystals grow via “layer-by-layer” crystal growth mechanism, where multiple surface nuclei form and propagate on the square crystal facets [7]. Adjacent layers of Ti wires in ETS-10 are orthogonal to each other and stacked layer by layer [8]. The TiO_3^{2-} wires are broken at random points in ETS-10 crystals due to defects, which are hypothesized to occur where multiple spreading

surface nuclei meet to form a new layer on top of a previous layer (layer-by-layer ETS-10 crystal growth mechanism) [7]. The pore system contains 12-membered rings and displays a considerable degree of disorder due to different stacking sequences, which causes broadening of the ETS-10 pores up to 2 nm (Figure 1.3) [9, 10].

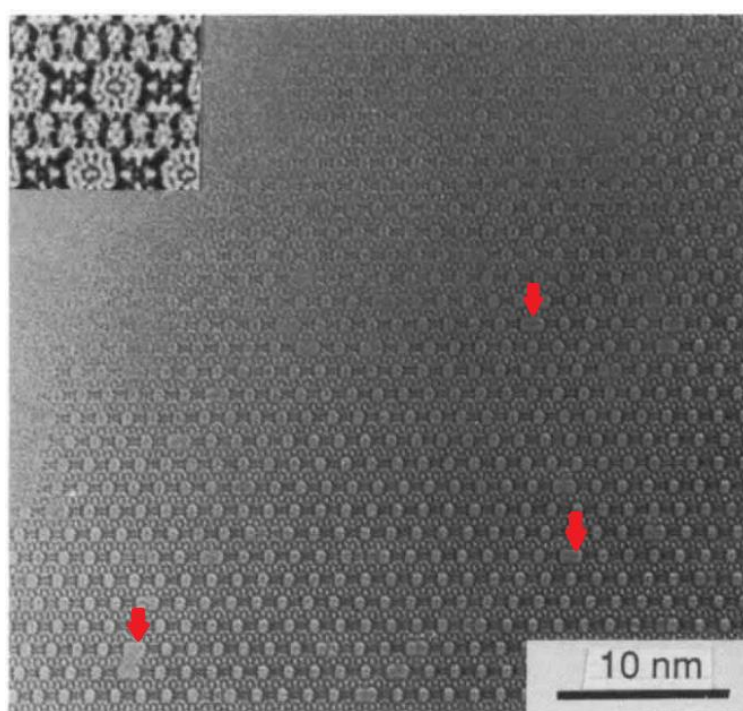


Figure 1.3. High-resolution electron micrograph of ETS-10 recorded on a JEOL 400 kV electron microscope [9].

Synthesis of titanosilicate ETS-10 is very sensitive to source materials, pH of synthesis gel, contents of water, Na^+ and K^+ ions in the synthesis gels, $\text{SiO}_2/\text{TiO}_2$ molar ratios, and temperature on the crystallization of ETS-10 [8]. The use of different titanium sources leads to the formation of ETS-10 crystals with different phase purity, particle morphology, and particle size (Figure 1.4) [11]. ETS-10 crystals synthesized in the synthesis system of

$3.4\text{Na}_2\text{O}:1.5\text{K}_2\text{O}:\text{TiO}_2:5.5\text{SiO}_2:180\text{H}_2\text{O}$ at $230\text{ }^\circ\text{C}$ with (a) P25, (b) TiCl_3 as the Ti sources were shown in Figure 1.4, respectively [8]. The crystals displayed bipyramid morphology when P25 was used as Ti source; whereas, they showed truncated bipyramid morphology when TiCl_3 was used. Different morphology of the crystals was explained by different rates of nucleation and crystal growth as Ti sources were altered [8].

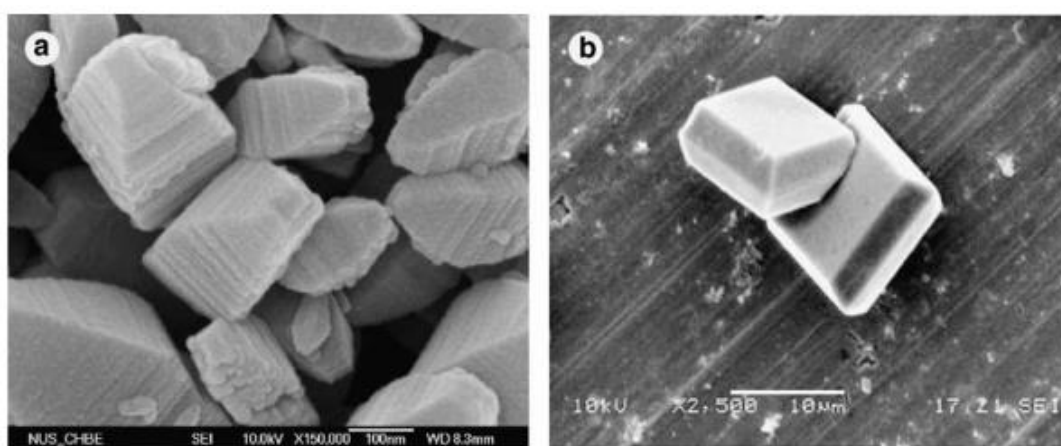


Figure 1.4. SEM images of the solid products synthesized in the synthesis system of $3.4\text{Na}_2\text{O}:1.5\text{K}_2\text{O}:\text{TiO}_2:5.5\text{SiO}_2:180\text{H}_2\text{O}$ at $230\text{ }^\circ\text{C}$ with (a) P25, (b) TiCl_3 as the Ti sources, respectively [8].

Silicate species were formed in solution and highly dispersed P25 fine particles were interacted with them to create hydrous silica-titania gels under the mediation of OH^- ions (Figure 1.5) [8]. Ti atoms in P25 are six-coordinated and they act as a structure-directing agent which leads to rapid nucleation. As a result, a large number of small crystallites with an excellent bipyramid morphology as shown in Figure 1.4-a was obtained since ETS-10 microcrystallites were quickly formed in the silica-titania gels via a direct structure reconstruction. In the case of TiCl_3 , the coordination number for Ti is different, which results in a decreased rate of nucleation and crystal growth

leading to smooth and larger crystals with a truncated bipyramid morphology (Figure 1.4-b) [8].

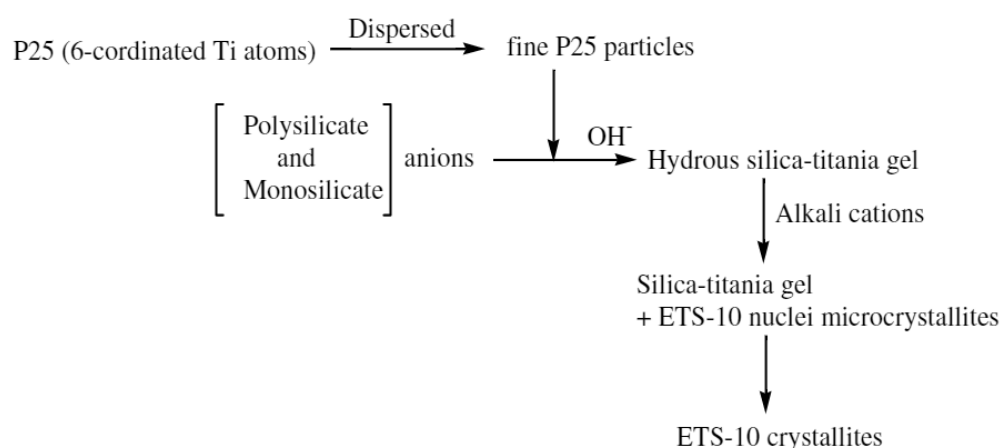


Figure 1.5. Proposed mechanisms of ETS-10 crystallization with P25 as the Ti source [8].

It is also known that if one waits long enough given that there are enough nutrients and synthesis time, ETS-10 crystals will evolve to be bipyramid-like crystals as shown in Figure 1.4-a. This fact is correlated with the “layer-by-layer” crystal growth mechanism of ETS-10 (i.e., two-dimensional surface nucleation) (*vide supra*) [6-8].

1.2.3 Silver Modified Titanosilicate ETS 10

ETS-10 is a very unique material in photocatalysis due to its monatomic, linear, orthogonal, non-intersecting, and semiconducting -Ti-O-Ti-O-Ti- chains. A recent report has drawn the attention on examining the local structure of ETS-10 [12]. Although this semiconductor electronic behavior coupled with the ordered

microporous structure makes ETS-10 an important photocatalytic material, its band gap energy limits activity of ETS-10 in the photocatalytic reactions [13].

The incorporation of metal cations or nanoparticles into ETS-10 matrix seems to be one of the possible solutions to extent its activity to visible region [4,13-17]. The previous studies on this issue have mostly focused on the use of Ag^0 nanoparticles as guest materials to host ETS-10 framework (Figure 1.6) [4,13-17]. The enhancement in the photocatalytic activity by the presence of Ag^0 nanoparticles has been explained by electron trap property of metallic silver that removes electrons from the irradiated semiconductor surface through the formation of Schottky barrier through electron transfer from the TiO_2 conduction band to metallic silver particles at the interface to reduce the electron-hole recombination, and thus increase the photocatalytic activity [18,19]. Additionally, Ag^0 nanoparticles can also create a strong local electric field through the locality of nanoparticles due to surface plasmon resonance, which can be tuned by controlling the size and morphology of Ag^0 nanoparticles [20-22].

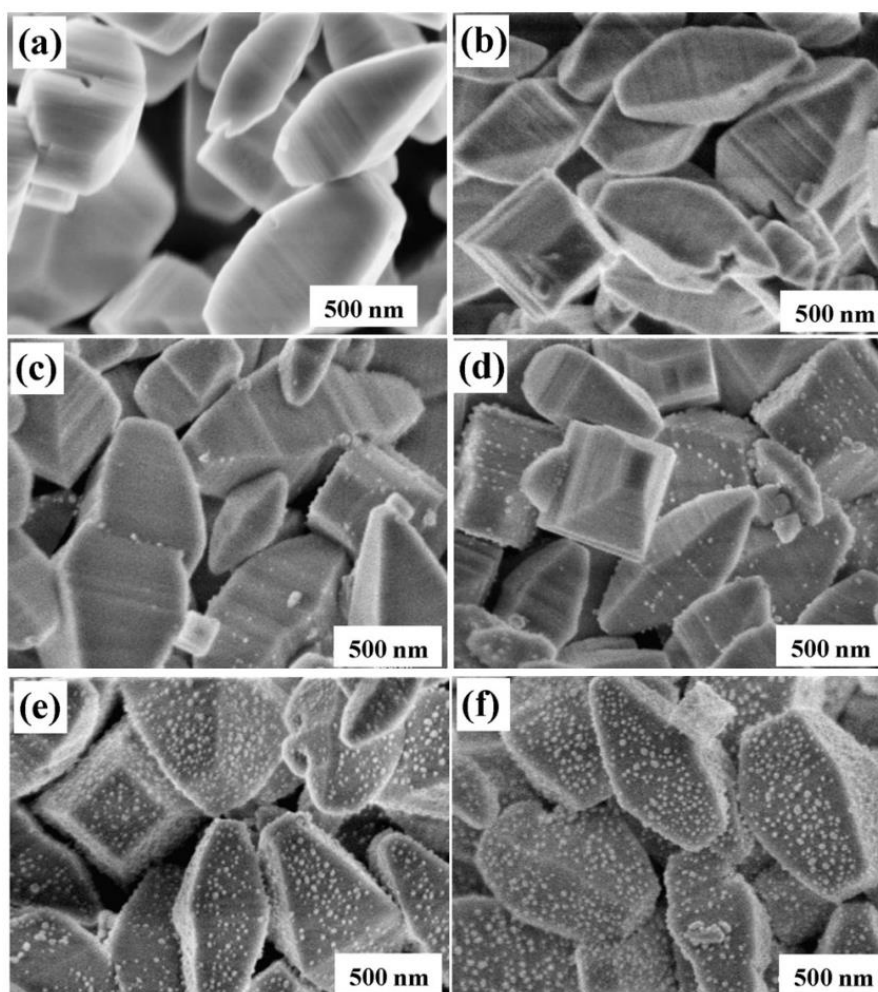


Figure 1.6. FE-SEM images of (a) as-synthesized ETS-10, (b) Ag^+ -exchanged ETS-10 (Ag^+ -ETS-10-15); and Ag^0 nanoparticle-modified ETS-10 samples with different Ag^0 loading levels: (c) Ag^0 -ETS-10-3 (i.e., 3 mM AgNO_3), (d) Ag^0 -ETS-10-6 (i.e., 6 mM AgNO_3), (e) Ag^0 -ETS-10-10 (i.e., 10 mM AgNO_3), and (f) Ag^0 -ETS-10-15 (i.e., 15 mM AgNO_3) [13].

As a common feature, all of the previously reported Ag^0 nanoparticles in ETS-10 systems [4,13-17], except the one by Lv et al. [16], have been obtained by the protocols that involve thermal reduction [4,14,17], dihydrogen reduction [13,15] or photoreduction [15] of Ag^+ -exchanged-ETS-10 sample. Unfortunately, these protocols require high temperature treatment, which may cause migration of large part of the guest metal atoms out of the cavities of ETS-10. Expectedly, the

formation of large sized bulk silver on the surface of ETS-10 crystals has been reported in all of these aforementioned studies [4,13-17]. A recent study [16] has reported the efforts to prepare Ag^0 nanoparticles-ETS-10 system to investigate its bacterial activity towards microorganisms, such as *Escherichia coli*. The synthesis protocol reported involves the reduction of silver ion-exchanged ETS-10 by borohydride. However, the reduction has been applied under in-situ conditions in concentrated solution, without removing support free Ag^+ cations so that large size Ag^0 agglomerates have been formed on the surface of ETS-10, as observed by XRD and TEM even at low silver loadings. Moreover, the paper has not reported the changes in the local structure of ETS-10 induced by the ion-exchange of Ag^+ ions and their chemical reduction. In this context, the reduction of Ag^+ ion exchanged in ETS-10 by using chemical reduction methods under mild conditions (at room temperature under air) can play a significant role in the formation of small size Ag^0 nanoparticles encapsulated in the host matrix. The previous literature studies have shown that the preparation of small sized unagglomerated nanoparticles of Rh^0 [23], Ru^0 [24], Au^0 [25], Os^0 [26], Ni^0 [27], and Cu^0 [28] confined within the framework of zeolite-Y have been achieved by using sodium borohydride (NaBH_4) [23-28] resulting in the reduction of M^{n+} -exchanged-zeolite ($n = +2$ or $+3$) at room temperature.

In the current thesis study, we report the preparation of Ag^0 nanoparticles within the framework of ETS-10 (Ag^0 -ETS-10) following an established method, which involves the incorporation of Ag^+ ions into ETS-10 matrix by ion-exchange with extra framework ETS-10 cations (Na^+ and K^+) forming Ag^+ -ETS-10 and their reduction within ETS-10 matrix with sodium borohydride in aqueous medium at room temperature. In comparison with the methodology by Lv et al., [16] support free Ag^+ cations have been washed out from the material by simple centrifugation before reduction. Thus, the borohydride reduction was applied only to Ag^+ ion-exchanged-ETS-10 in more dilute solutions. The resulting Ag^0 nanoparticle incorporated ETS-10 framework were isolated as solid powder and characterized by ICP-OES, XRD, XPS, FE-SEM, TEM, HR-TEM, DR-UV-vis, Raman spectroscopies and N_2 adsorption-desorption technique. The study also includes

the results obtained from investigation of the changes in the local structure of ETS-10 upon its modification by Ag^+ ion-exchange and following chemical reduction plus the extent of destruction as a function of silver loading.

1.2.4 Photochromism

Silver doped titania has been studied extensively as a photochromic inorganic material. For reversible photochromic reactions, electron-hole (e^- - h^+) pairs generated by electronic transition must react with each reactant in every cycle. For instance, in the structure of Ag^0 nanoparticle incorporated TiO_2 , electronic transition is generated through UV radiation and the created e^- - h^+ pairs initiate several reactions for reversible photochromic process [29-34].

The Ag^0 nanoparticles incorporated into the insulating silica matrix were found not to exhibit photochromism, whereas semiconductor TiO_2 is needed for electron transport [29]. Microporous zeolites are insulators (i.e., wide bandgap materials). Therefore, insulating silica matrix should not contribute to electronic transition in the case of microporous titanasilicate ETS-10. Instead, TiO_3^{2-} quantum wires (i.e., Ti-O-Ti-O-Ti) are considered to be responsible for the electronic transition. Accordingly, photochromic behavior of Ag^0 nanoparticle incorporated titanasilicate ETS-10 films was studied to show role of 1-D TiO_3^{2-} quantum wires in the ETS-10 crystals for the first time (Chapter 5).

1.2.4.1 What is Photochromism?

Photochromism is defined as a light-induced reversible change of color [35]. “It is a reversible transformation of a single chemical species being induced in one or both directions by electromagnetic radiation between two states having different distinguishable absorption spectra. The radiation changes may be induced by UV (ultraviolet), visible and IR (infrared) radiation. Reversibility of the process is an important criterion” [35]. The most famous applications are smart windows [36] and

sunglasses (Figure 1.7). Transmittance of these glasses is changed in relation to the intensity of the solar radiation.

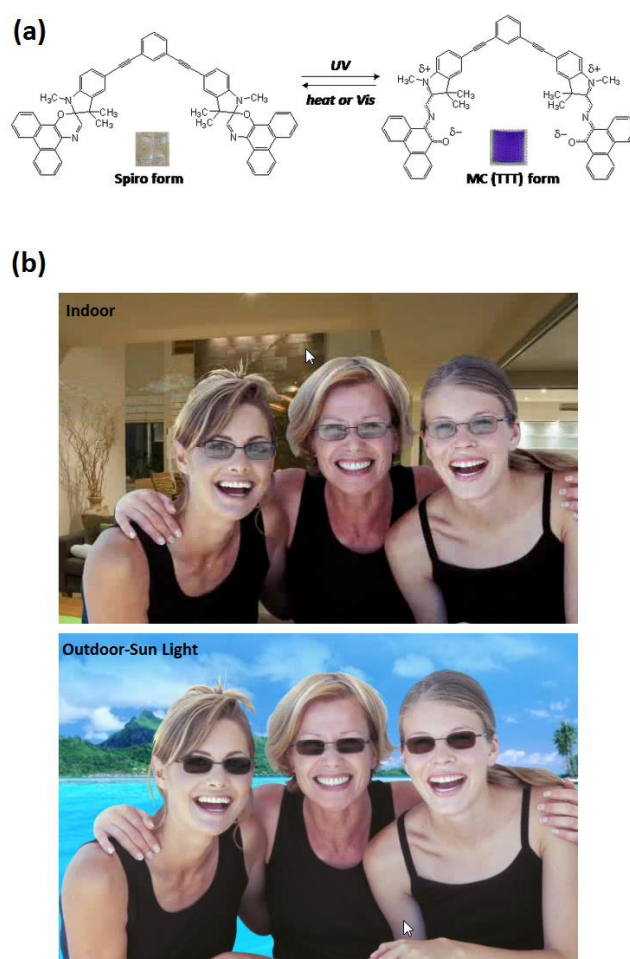


Figure 1.7. (a) An example of photochromic smart bispiropyran polymers [37], (b) photochromic materials in sunglasses [38].

1.2.4.2 Photochromic Behavior of Inorganic and Zeo-Type Materials

Up to now, photochromic properties of organic materials such as spirooxazine, chromene derivatives [39], and azobenzene [40] have been most systematically

examined. However, the number of inorganic materials known to display photochromism is limited. The most explored thin-film inorganic photochromic materials are the transition metal oxides WO_3 , NiO , and MoO_3 [41,42], which have also been investigated for applications in electrochromic devices [43] that show a reversible color change when a small DC voltage is applied.

Recently, silver doped titania has been studied extensively by the group of Prof. Tatsuma as a promising photochromic inorganic material [29-32], where electrons at the valence band of TiO_2 are excited upon UV irradiation, chemical or thermal means to the conduction band and then are used to reduce Ag^+ ions into Ag^0 nanoparticles. The formed Ag^0 nanoparticles interact with visible light through their surface plasmon resonance and their electrons move towards the conduction band of TiO_2 , which results in the oxidation of Ag^0 nanoparticles into Ag^+ ions. The design of new hierarchical composite materials, such as silver nanoparticle incorporated TiO_2 matrixes that are used as porous templates for silver nanoparticle growth were investigated for photochromic applications. In such systems, the interest has usually been into mesoporous TiO_2 films with high surface area and controlled porosity [44].

In such porous matrixes, although TiO_2 films are used as templates for the reduction of silver nanoparticles, the role of TiO_2 has been discussed to particularly identify the necessity of these units in the visible light-induced oxidation process of silver nanoparticles [29]. Afterwards, the requirement of TiO_2 with its semiconducting property was indeed shown to facilitate photo-oxidation of Ag^0 into Ag^+ . The Ag^0 nanoparticles in an insulating silica matrix were found not to exhibit photochromism, showing the ultimate evidence of the electron transport path via TiO_2 [29].

Engelhard titanosilicate ETS-10 is a relatively new class of microporous crystalline material (pore dimensions: 4.9 Å and 7.6 Å) where its Ti substituted silica matrix is composed of Si in tetrahedral and Ti in octahedral coordination [45]. The building units of ETS-10 are uniquely arranged to form 1-D TiO_3^{2-} quantum wires (i.e., -Ti-O-Ti-O-Ti-) that are effectively separated from each other by the silica matrix [9] and have band gap energy, which was shown to be related to the length of the crystals

along [110] direction [5]. ETS-10 is a unique nanoporous material in the sense that there are no molecular nanowires or nanorods that are embedded in a chemically inert large-band-gap medium identical to ETS-10.

Each TiO_3^{2-} quantum wire incorporates two negative charges, which are compensated by extra framework charge-balancing cations Na^+ and K^+ . Existence of extra framework cations creates an opportunity to incorporate any desired cation (i.e., Ag^+) into the ETS-10 matrix by ion-exchange. It was previously shown that it is possible to create Ag^0 nanoparticles by the reduction of Ag^+ ions within the ETS-10 matrix opening the possibility to use this unique material in different applications [46]. Although ETS-10 has been stated to be an alternative inorganic material for different optical applications with its above mentioned unique properties [47], there is still a lot of room to examine this material in different applications. Accordingly, photochromic behavior of silver nanoparticle loaded ETS-10 can be considered due to 1-D quantum-confined form of titania (i.e., TiO_3^{2-} quantum wires) that run in the crystal in *a* and *b* directions and exchangeable extra framework charge-balancing cations (i.e., Na^+ and K^+) in the as-synthesized materials as indicated by the ETS-10 stoichiometry $(\text{Na,K})_2\text{TiSi}_5\text{O}_{13}$ [45].

In the present thesis study, we report the partially reversible photochromic behavior of Ag^0 -ETS-10 films for the first time. The unique combination of TiO_3^{2-} quantum wires within the silica matrix forming ETS-10 structure raised the possibility to investigate the possible photochromic behavior of Ag^0 nanoparticle incorporated ETS-10 films and the possible role of these quantum wires in the photochromic mechanism. This is the first study in which the relationship of this unique structural formation in ETS-10 along with the integration of Ag^0 nanoparticles within its matrix is accompanied by its subsequent photochromic property.

1.2.5 Zeolite and Zeo-Type Films Prepared by Secondary Growth Method

1.2.5.1 Introduction to Secondary Growth Method

Zeolites are microporous crystalline aluminosilicates, containing TO_4 tetrahedra (T = Si, Al) with O atoms connecting neighboring tetrahedra. The extra negative charge of alumina tetrahedra is compensated by extraframework cations (typically Na^+) to obtain neutral zeolite framework. The extraframework cations can be ion-exchanged with desired cations (i.e., Ag^+ , Li^+ etc.). The rings formed from T and O atoms generate interconnected cages or channels, which have dimensionalities of one to three depending on the structure.

The synthesis of zeolite can be altered by physical effects such as stirring, aging, and order of source material addition since the synthesis of zeolite contains complex process due to “presence of numerous soluble species, an amorphous phase, polymerization and depolymerization reactions” [48]. Various processes are taking place in the medium, containing “nucleation of various structures, crystallization as well as dissolution of metastable phases”. It has been observed that as crystallization process gets started, the gel is converted to crystals very quickly, which indicates that nucleation is “rate-limiting step”. The synthesis process cannot be oversimplified to nucleation and crystallization steps. Minimum four subsystems were proposed: “(a) formation of simple and polymeric aluminosilicates, (b) aggregation of these complexes to form embryo, (c) nucleation as aggregate formation with a well ordered core (primary particles), and (d) aggregation of primary particles via oriented aggregation” (Figure 1.8) [48].

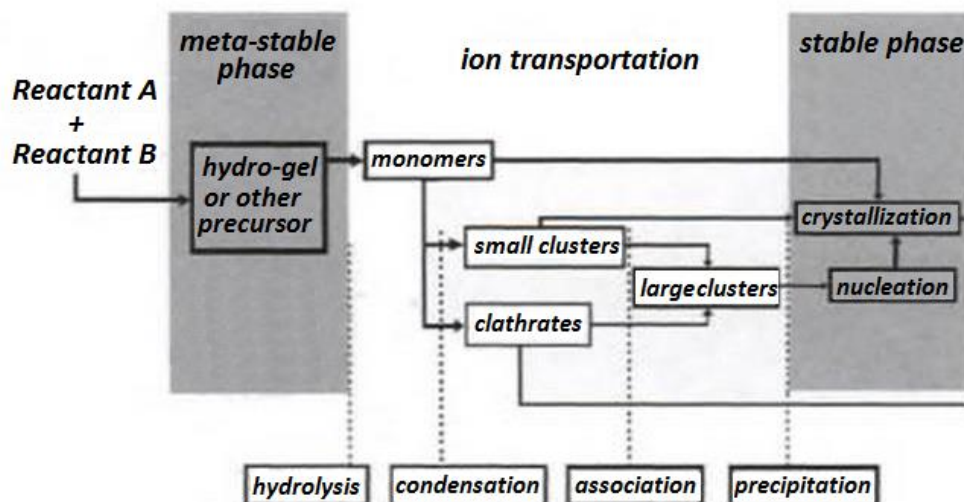


Figure 1.8. A schematic representation of zeolite crystallization process [48].

The seeded growth method is not only applied to zeolite synthesis but also to zeolite film/membrane growth. The secondary growth method is a seeded growth method. The studies about seeded growth showed that adding seed crystals stimulates nucleation due to creation of small fragments that act as nucleation sites [48]. Direct growth of seed crystals was not observed, and instead new populations of crystals were initiated by addition of seed crystals. Furthermore, crystallization time was reduced when seed crystals were added into the synthesis gel [48]. The advantages explained above can be applied to the film/membrane synthesis in the secondary growth method. Instead of adding crushed seed crystal into the gel, seed crystals can be coated on a substrate by using colloidal suspension of zeolite crystals (Figure 1.9). Seed crystals can either be coated randomly or preferentially oriented by using different coating techniques, such as dip/spin coating, direct attachment and direct *in-situ* synthesis methods. Hydrothermal synthesis is carried out to grow continuous zeolite film/membrane (i.e., secondary growth). Nucleation and growth steps are decoupled in the secondary growth method providing an opportunity to control microstructure, orientation and thickness of the zeolite film [48]. The composition of the secondary growth gel can be altered to obtain preferred crystallographic

orientation of film/membrane since different growth rates are initiated in different directions with altered compositions (i.e., different reactant concentrations).

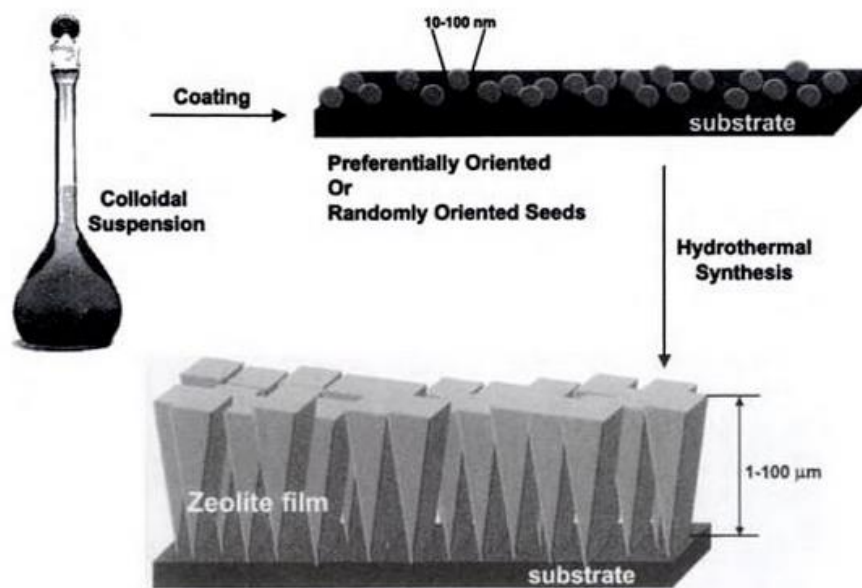


Figure 1.9. Schematic of secondary (or seeded) growth technique [48].

Degree of crystal intergrowth is influenced by changes in “morphology and crystallographic orientation” of the film/membrane. For instance, higher degree of crystal intergrowth is obtained in a membrane when the crystals possess a comparatively high in-plane growth rate than out-of-plane growth rate [48]. It is crucial to adjust the relative growth rates between the “in-plane” and “out-of-plane” directions to preserve the orientation of the seed layer when secondary growth of preferentially oriented seed crystals is conducted. “Columnar-shaped grains” with loose grain boundaries will be obtained if the growth rate throughout the out-of-plane direction is too large. However, if the growth rate throughout the out-of-plane direction is too slow, nutrition on the top of the seed layer will initiate the creation of “twins or randomly deposited nuclei” during the secondary growth. The “twins or

randomly deposited nuclei” grow faster than the original seeds and form “dense layer” with other orientation(s); therefore, orientation of the seed layer cannot be maintained [49]. When appropriate growth conditions are adjusted, the formation of “twins or nuclei” can be restricted since nutrients are consumed by the out-of-plane growth, while simultaneously “intercrystalline gaps” can be closed by the in-plane growth [49].

Inorganic zeolite membranes have several advantages such as shape selectivity, temperature stability and solvent resistance [50]. The ingredients of liquid or gaseous mixtures can be separated (i.e., sieved) depending on their molecular size by zeolite membranes. The most crucial parameter to achieve this molecular sieving is production of pinhole- and crack-free zeolite membranes. Several studies in the literature have been focused on production of continuous and crack-free zeolite membranes and special attention is given to MFI and LTA type membranes (*vide infra*).

1.2.5.2 MFI, BEA, LTL, LTA, and FAU Type Zeolite Films Prepared by using Secondary Growth Method

Formation of “zeolite membranes” has been studied for various zeolite framework types [51-53]. However, reproducibility and adjustability of membrane microstructure (i.e., thickness, texture, grain size, degree of orientation) have been restricted. Two main methods: *in-situ* and secondary growth can be considered in the synthesis of MFI membranes [54]. In the *in-situ* method, hydrothermal synthesis of substrate is directly conducted in the presence of alkaline zeolite precursors. In appropriate synthesis conditions, nucleation and growth of zeolite crystals occur on the support to form a continuous zeolite film. Meanwhile, reactions that occur in the solution contribute to the film formation by depositing nuclei and crystals on the surface. The preferred orientation of films strongly depends on the nucleation and growth phenomena in the *in-situ* methods, which makes it difficult to obtain uniformly oriented zeolite films. The secondary growth consists of two steps:

random or oriented precursor (seed) layer formation and secondary growth of this precursor layer.

Tsapatsis et al. proposed the use of colloidal zeolite suspensions for precursor (seed) layer formation followed by “secondary growth” for zeolite membrane formation. Tsapatsis et al. used this method to form zeolite films and membranes of various framework types: LTL [55], MFI [56], and LTA [57, 58].

1.2.5.2.1 MFI Type Membranes and Films

The xylene isomers are extensively used as industrial solvents and precursors in the petrochemical industry; therefore, the separation of them is demanded. MFI membranes are widely used for separating xylene isomers, because the pore size of the MFI framework permits *p*-xylene (kinetic diameter ca. 5.8 Å) to permeate comparatively faster, where the bulkier *o*- and *m*-xylene (kinetic diameters ca. 6.8 Å) permeate at a considerably lower rate [54]. The present technology in petrochemical industry consumes energy to apply fractional crystallization, adsorption in a simulated moving bed, and distillation [54]. However, separation of xylene isomers by membranes offers better advantages. It has been showed that the separation performances of MFI membranes are intimately related to the microstructural characteristics and orientation of the films.

Tsapatsis et al. comprehensively investigated secondary growth, microstructure, permeation and separation properties of preferentially *a*- (i.e., *a*-out-of-plane orientation, that is, with the 5.1 x 5.5 Å zigzag channels of MFI perpendicular to the substrate), *b*- (i.e., *b*-out-of-plane oriented, with the 5.6 x 5.4 Å straight pore of MFI perpendicular to the substrate), *c*-oriented and randomly oriented membrane and films [49, 54, 59-67].

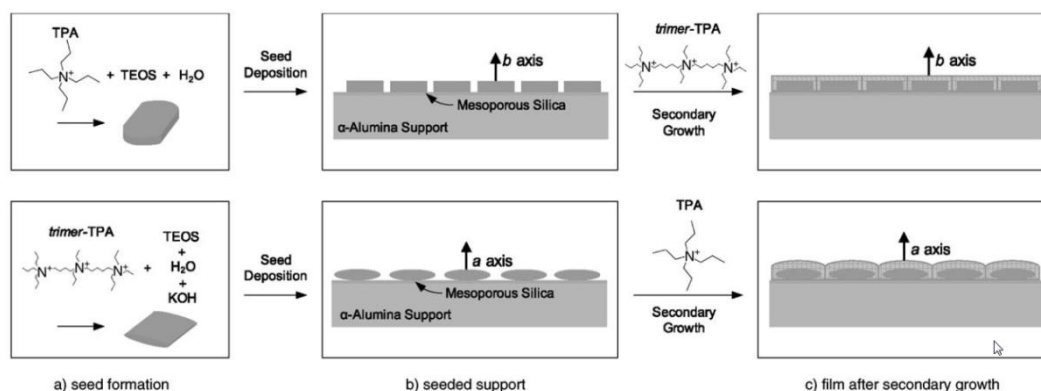


Figure 1.10. Schematic representation of the steps used to fabricate MFI films with *b*- and *a*-out-of-plane orientations are shown in the upper and lower panels, respectively [54].

a-Oriented MFI zeolite membranes were produced by using secondary growth of an *a*-oriented seed layer (Figure 1.10). However, *p*-/*o*-xylene separation performance of the membrane was poor due to cracks and grain boundary defects. Accordingly, different method was applied for the *a*-oriented membrane production [62]. The separation of *n*-/*i*-butane and *p*-/*o*-xylene was low compared to *b*-oriented MFI membranes.

Yoon et al. used “dry gel” for secondary growth of *a*- and *b*-oriented silicalite-1 (framework type MFI) film [68] and semisolid gel for the production of zeolite beta (framework type BEA) film for the first time [69] (Figure 1.11).

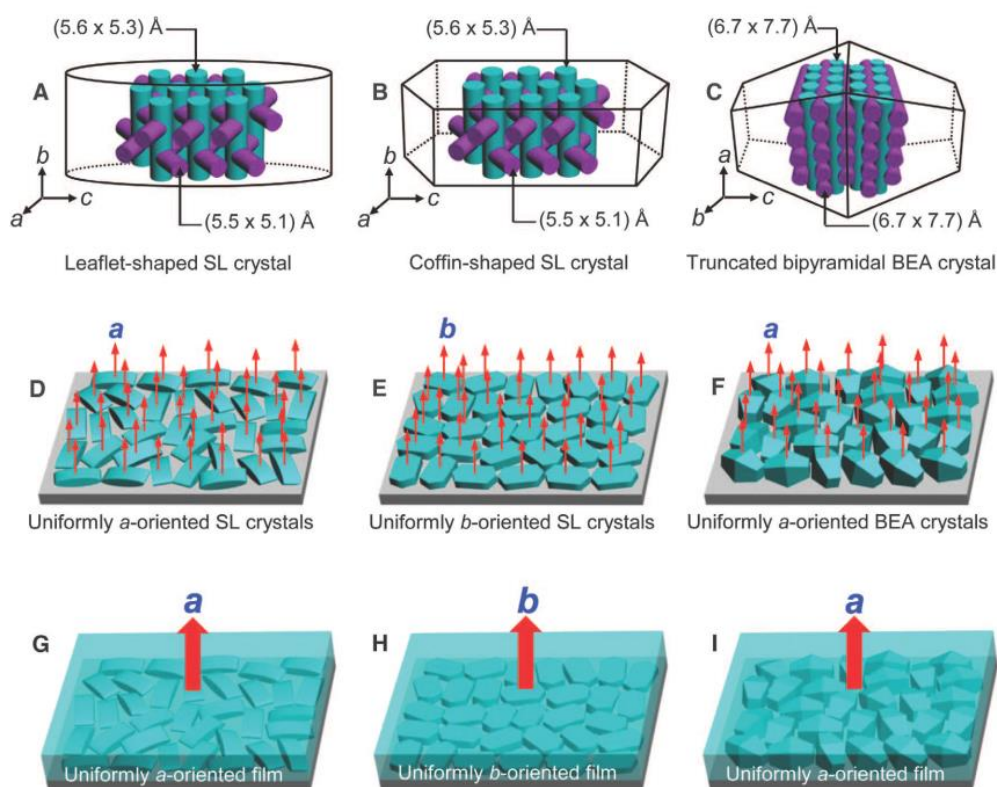


Figure 1.11. Schematic illustrations of (A) leaflet-shaped and (B) coffin-shaped Silicalite (framework type MFI) crystals and (C) truncated bipyramidal zeolite beta (framework type BEA) crystals and their channel systems, as well as their respective (D) a-oriented, (E) b-oriented, and (F) a-oriented monolayers. (G to I) Secondary growth on these monolayers produces uniformly oriented films [69].

1.2.5.2.2 LTA and FAU Type Films

Tsapatsis et al. studied the production of defect-free zeolite A films by using electrostatic deposition technique for seed layer formation. In this technique, positively or negatively charged crystals can be suspended and used to prepare uniformly adsorbed and well-adhered seed layer on oppositely charged substrates [57].

Mintova et al. proposed an excellent idea to use ultrathin (i.e., 65, 470 and 980 nm) zeolite A films on quartz crystal microbalances in humidity sensing [70]. The sensitivity of the zeolite A films were investigated in terms of film thickness at different water vapor concentrations. The produced sensors represented high sensitivity, good reversibility, and long life at low water levels.

Faye et al. investigated sorption properties of zeolite Faujasite films on carbon fibers [71] and zeolite hybrid films on aluminum alloys for space decontamination [72]. Their objective was production of materials that avoid organic contamination of satellites in low earth orbit. The properties of FAU film, i.e., hydrophilicity, prepared on carbon fiber was altered by changing reaction parameters.

1.2.5.3 Zeo-Type Films Prepared by using Secondary Growth Method

The relative easiness and flexibility of secondary growth method provides an advantage not only to produce membrane/film of zeolites but also various types of porous materials. Stoeger et al. studied production of *c*-out-of-plane-oriented cobalt substituted silicoaluminophosphate (CoSAPO-5) and aluminophosphate (AlPO₄-5) membranes by using secondary growth method [73-75]. AlPO₄-5 (framework type AFI) is a type of microporous material with 1D cylindrical pores aligned parallel to the *c*-axis, which contains AlO₄ and PO₄ tetrahedra forming a 12-membered ring framework. SAPO-5 (framework type AFI) is isostructural to AlPO₄-5 with a framework substitution of silicon. They suggested that the produced film can be used in “catalysis, sensor design, and host-guest assemblies” [73].

Tsapatsis et al. [76] and Mintova et al. [77] investigated production of microporous metal organic framework (MMOF) membranes, which are novel crystalline materials containing metal ions with organic linkers, by applying secondary growth method.

1.2.5.3.1 Titanosilicate ETS-4 and ETS-10 Films Prepared by using Secondary Growth Method

In order to be able to use zeolites and zeo-type materials in applications like molecular sieving, fuel cells, sensors, optoelectronic devices, they should be prepared in the film form. The preferred orientation of the well-defined pores and channels of zeolites and zeo-type materials can be adjusted by secondary growth method, which affects transport, optical and electronic properties of the films [78]. Furthermore, it has been shown that grain boundary structure of the MFI type films can be altered by changing preferred orientation of the film, which in turn affects entire performance of membranes [54, 62].

There are some advantages of zeo-type microporous Engelhard titanosilicate (i.e., ETS-4 and ETS-10) membranes compared to conventional zeolite membranes: (i) there is no need to use expensive structure directing agents which leads to application of calcination step that usually forms defects in the films; (ii) the films are generally prepared under comparatively mild pH conditions (i.e., ~ 10 -11 vs. ~ 12 -13), decreasing the chemical attack on the substrate surfaces; (iii) the existence of TiO_6 octahedra- SiO_4 tetrahedra oxides provides a possibility to make framework substitution such as aluminum, gallium, zirconium, tin etc. In this way, the catalytic and adsorption properties of the microporous titanosilicate membranes can be adjusted [79].

Engelhard titanosilicate ETS-4 is a microporous crystal with a pore size of 3-4 Å, which can be used for separation applications. The framework of ETS-4 comprises TiO_6 octahedra and SiO_4 tetrahedra with monatomic quantum $\cdots \text{Ti-O-Ti-O-Ti} \cdots$ wires that run in the *b*-direction [80]. The pore channel system of ETS-4 is also oriented in the *b*-direction. Therefore, it is crucial to form preferentially *b*-out-of-plane oriented (i.e., eight membered ring channels of ETS-4 oriented perpendicular to the substrate) ETS-4 membrane for both conventional and novel applications. Tsapatsis et al. reported production of ETS-4 membrane on porous titania supports for the first time in 2000 [81]. First, *in-situ* hydrothermal synthesis of seed layer was

applied and then secondary growth of the seed layer was conducted. The pervaporation experiments, involving separation of the constituents a mixture of two liquids by selective permeation by means of a semipermeable membrane, using 1:1 water/ethanol mixtures was applied to ETS-4 membranes at room temperature and 50 °C. It was found that the flux of water through ETS-4 membranes was similar or higher than that through all zeolite A, X, and Y membranes [81]. Although they found on kind of titanosilicate type impurity (i.e., GTS-1) in their bulk synthesis of ETS-4, the impurity was not detected on the membrane. The relatively increased reflections were the (110), (020), and (221) in XRD patterns, which indicates the membranes produced were highly oriented (Figure 1.12).

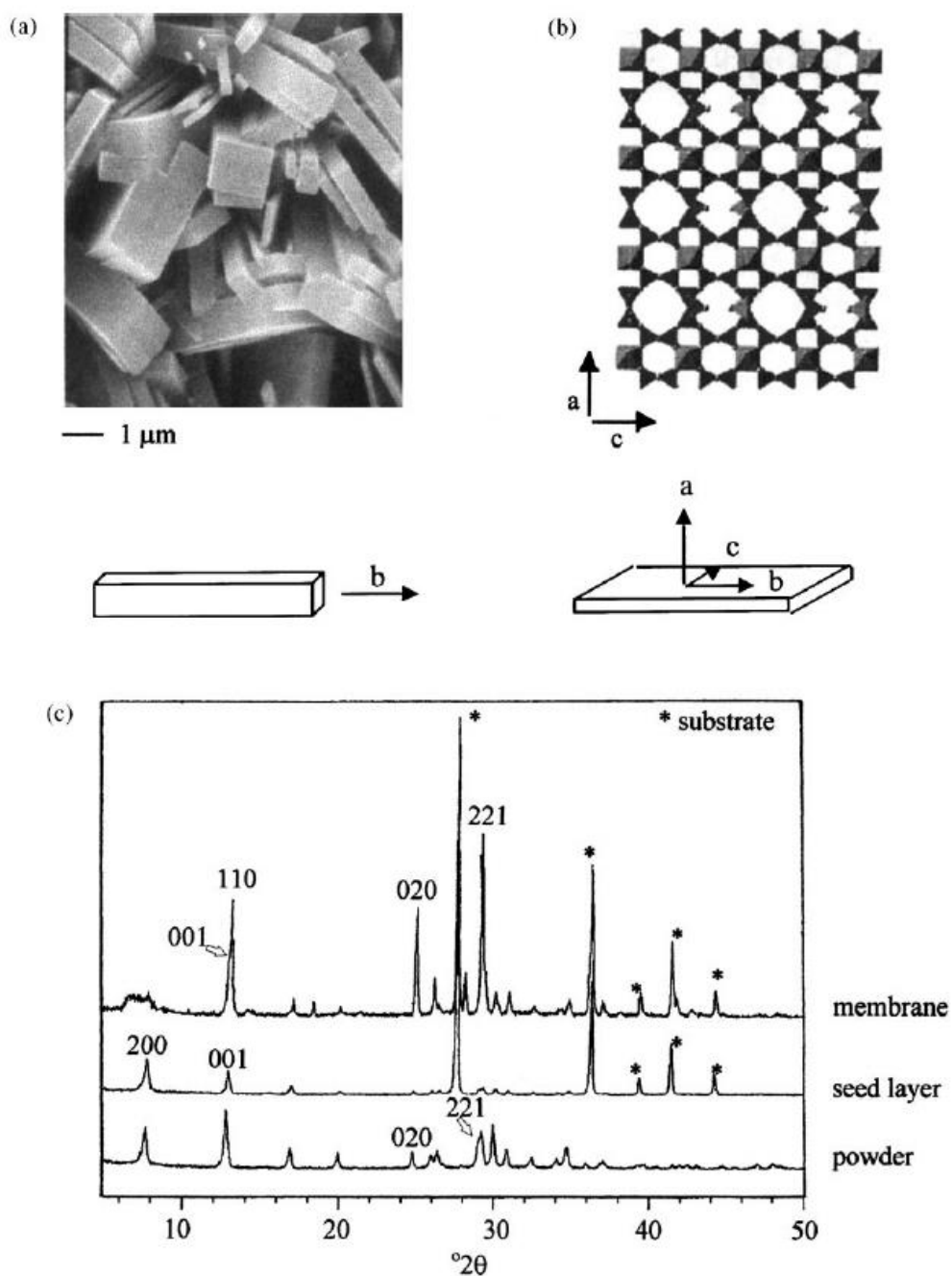


Figure 1.12. (a) Top view of ETS-4 membranes made by secondary growth (200°C, 1 day); (b) structure of ETS-4 (view down the b -axis) and (c) X-ray powder diffractograms of the membrane in different stages in comparison with a randomly oriented ETS-4 powder [81].

Yilmaz et al. studied oriented growth of polycrystalline ETS-4 films on porous and α -alumina for the first time in 2006 [80] and on titania [82] substrates. Seed layer was synthesized hydrothermally on the substrate directly, then, secondary growth of seed layer was conducted to form preferentially oriented, continuous ETS-4 membranes (Figure 1.13). The XRD results (i.e., (110)/(001) peak intensity ratio) showed that, both the synthesized ETS-4 seed layer (with thicknesses $\sim 4 \mu\text{m}$) and membrane (with thicknesses $\sim 11 \mu\text{m}$) was *b*-out-of-plane oriented (Table 1.1).

They proposed that in the production of oriented zeolite/zeotype films by secondary growth method, secondary growth conditions must fulfil the following requirements: (i) growth rate should be faster than nucleation rate; (ii) anisotropic growth rates of crystal faces should be the fastest throughout the direction of desired film orientation [82]. Usually, clear/dilute solutions that have low supersaturation levels are applied for sufficient decoupling nucleation from crystal growth. On the other hand, these solutions essentially diminish the rates of both processes, resulting in films with intercrystalline gaps. Therefore, to obtain oriented continuous film multiple secondary growth steps should be applied [82]. The synthesis mixture with a long induction period used by Yilmaz et al. provided better secondary growth conditions since it better decouples nucleation from crystal growth during that period [82].

Table 1.1. The (110)/(001) peak intensity ratios of ETS-4 crystals in samples synthesized in this study [80].

Sample type	(110)/(001) peak intensity ratio*
Ground bulk ETS-4	1.2 \pm 0.2
ETS-4 seed layers on titania substrate	$\ll 1$
ETS-4 film on titania substrate	3.2 \pm 0.2
ETS-4 seed layers on α -alumina substrate	2.8 \pm 0.3
ETS-4 film on α -alumina substrate	3.8 \pm 0.3

*Obtained by deconvolution of the peaks.

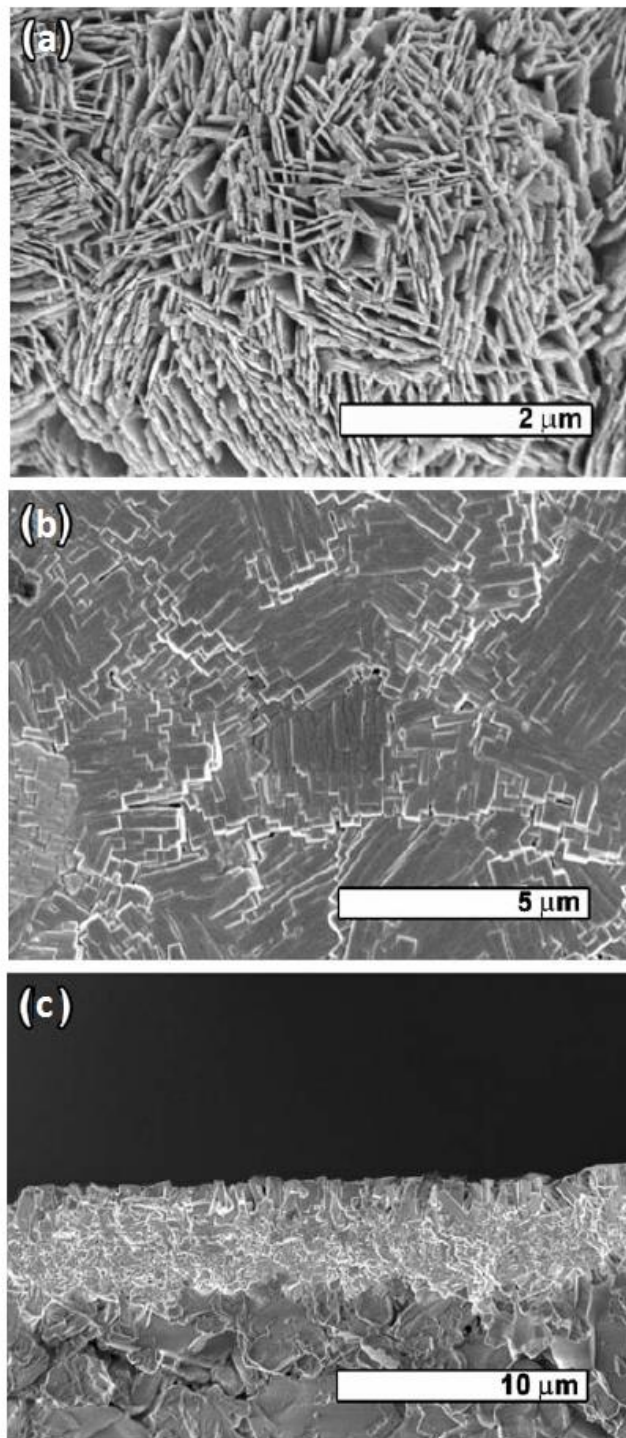


Figure 1.13. FE-SEM images of ETS-4 seed layer on α -alumina substrate (a) ETS-4 film on α -alumina substrate (b) top view; (c) cross-sectional view [80].

Jeong et al. applied heteroepitaxial growth to fill the gap between oriented needles of titanosilicate ETS-4 with preferentially oriented titanosilicate ETS-10 (Figure 1.14) [78].

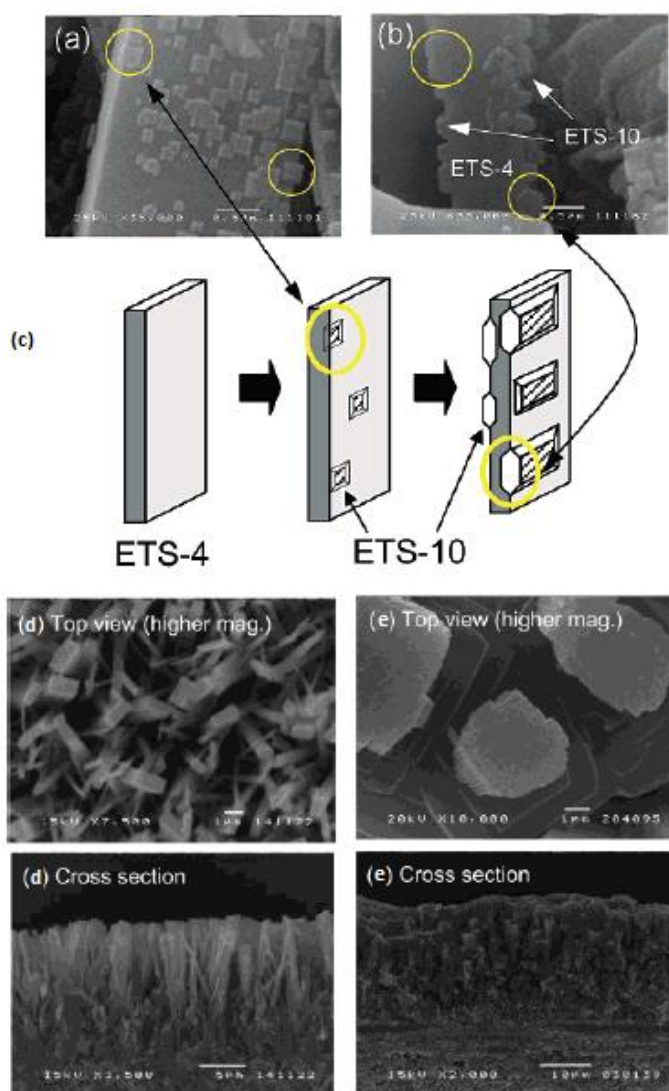


Figure 1.14. SEM images of heteroepitaxially grown ETS-10 crystals on ETS-4. (a) View of the ($h00$) face of ETS-4 with nucleated submicron crystals of ETS-10; (b) view of the ($00l$) face of the ETS-4 crystals; few of the ETS-10 crystals extend over the ($h00$) face and start covering the ($00l$) faces of ETS-4. A schematic of the early growth process is shown in (c). SEM images of the ETS-4 precursor layer (d), and of the ETS-10/-4 film synthesized by heteroepitaxial growth on the ETS-4 precursor layers after 20 h (e) [78].

To calculate preferred orientation of the film the following equation was used [78].

$$CPO_{200/105} = [(I_{200}/I_{105})_D - (I_{200}/I_{105})_B] / (I_{200}/I_{105})_B \quad (1.1)$$

where, I is the integrated intensity of the corresponding reflection, ETS-10 (B) powders and ETS-10/-4 film (D). The film showed strong orientation, that is, crystallographic preferred orientation i.e., ($CPO_{200/105}$) of the film was higher than 50.

Titanosilicate ETS-10 membranes (with thicknesses $\sim 5 \mu\text{m}$) were produced by Santamaria et al. on commercial tubular supports made of α -alumina (with pore sizes 1900 and 3000 nm) and of stainless steel with (pore size 500 nm) through secondary growth method [79]. The synthesis parameters (i.e., reaction time, temperature and seeding step) were examined. 5 wt. % of ETS-10 seeds (~ 500 nm) suspended in water and α -alumina support was immersed in it for 45 min. and dried at 110°C . The seed coverage was sufficient to obtain fully intergrown ETS-10 membrane. The produced membranes were tested in pervaporation experiments at 150°C to separate water/ethanol mixtures; as a result, moderate water/alcohol separation factors were achieved [79].

Non-porous and cylindrical optical fiber support was dip coated in an ethanol suspension containing 5 wt. % of ETS-10 (i.e., size ~ 500 nm) crystals and secondary growth of seed crystals was conducted by Sacco et al. to use them in photocatalytic applications [83]. The surface modification of optical fiber was done through partially hydrolyzed tetraethyl orthosilicate (TEOS). When there is higher light usage in optical fiber reactors, higher degradation of contaminants is obtained (i.e., higher photocatalytic efficiency) since the fibers transmit and distribute light to photocatalyst attached on the surface of fibers. Zeolite/zeotype materials have high surface area and adsorption capacity; thus, using them as photocatalysts provides advantages to increase photocatalytic efficiency. They concluded that the film growth achieved by epitaxial growth of the seed crystals.

In my master thesis, partial $a(b)$ -out-of-plane oriented ETS-10 thin films (average thickness $\sim 1.50 - 1.75 \mu\text{m}$) were produced on the ITO glass substrates using secondary growth of ETS-10 seed crystals [84]. The ITO glass substrates were dip coated in an ethanol suspension of 5 wt. % ETS-10 (i.e., size $\sim 500 \text{ nm}$) for seed layer production. The produced films were displayed a columnar grain microstructure and preferred orientation (Figure 1.15). The equation 1.1 was used to calculate preferred $a(b)$ -out-of-plane orientation of the films produced by secondary growth method by using XRD data obtained for each film. The most $a(b)$ -out-of-plane oriented film was obtained by using single dip-coating step (i.e, $\text{CPO}_{200/105}$ values were 31 ± 2 , 28 ± 3 , and 15 ± 4 for the films applied single, double and triple dip-coating step, respectively) [84].

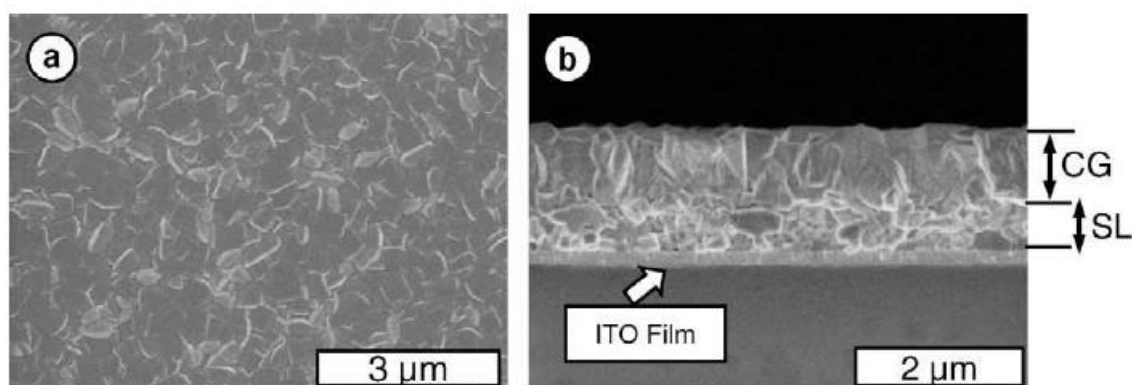


Figure 1.15. FE-SEM top view (a) and cross-section (b) images of ETS-10 films prepared on the ITO glass substrates using secondary growth of seed layers deposited using 1 dip coating steps. *SL = seed layer, CG = columnar grains [84].

As can be seen from the literature, zeolite and zeo-type films/membranes are typically used in catalysis or separation applications. Various type of application areas showed that preferred-oriented, defect- and crack-free intergrown films/membranes are superior to the randomly oriented films/membranes. The advantages of titanosilicate materials are discussed above. However, limited studies

exist in the literature about production of ETS-10 film/membrane. ETS-10 films were produced on conductive ITO glass substrates for the first time by our group [84]. In the current thesis study, defect- and crack- free intergrown ETS-10 films/membranes with columnar grain structure were produced on ITO glass and α -alumina substrates and secondary growth parameters were investigated comprehensively. The production of well-intergrown and well-adhered titanosilicate ETS-10 films on ITO glass and α -alumina substrates led us to investigate conductivity of ETS-10 for the first time in the scope of the current thesis study (Chapter 7).

1.2.6 Ionic Conductivity of Zeolites and Zeo-Type Materials

1.2.6.1 General Aspects

Ionic conductivity and a number of dielectric relaxation of zeolites (*vide infra*), display an obvious dependence on the: (i) size and charge of cations; (ii) structural positioning of cations (i.e., density: absolute number and relative partition in coordination site groups); (iii) mobility of the cations since the strength of the electrostatic interactions is identified by these parameters [1]. The conductivity values of the dehydrated zeolites can be located in the middle range (i.e., $\sim 10^{-6}$ S cm⁻¹ for zeolite X) with respect to the typical solid state electrolytes such as two-dimensional strong electrolyte Na⁺ β -alumina (i.e., $\sim 10^{-1}$ S cm⁻¹) Figure 1.16 [1]. Two reasons are proposed for the low (or middle range) conductivity of zeolites: (i) the electrostatic interaction between negatively charged framework of zeolites and extraframework cations is strong, which hinders ion migration; (ii) the size of channels or cages of the zeolites is so large that the mobile ions are trapped on the walls of the channels or cages that have sites with relatively high potential energy depths; therefore, the cations become partly immobilized [85].

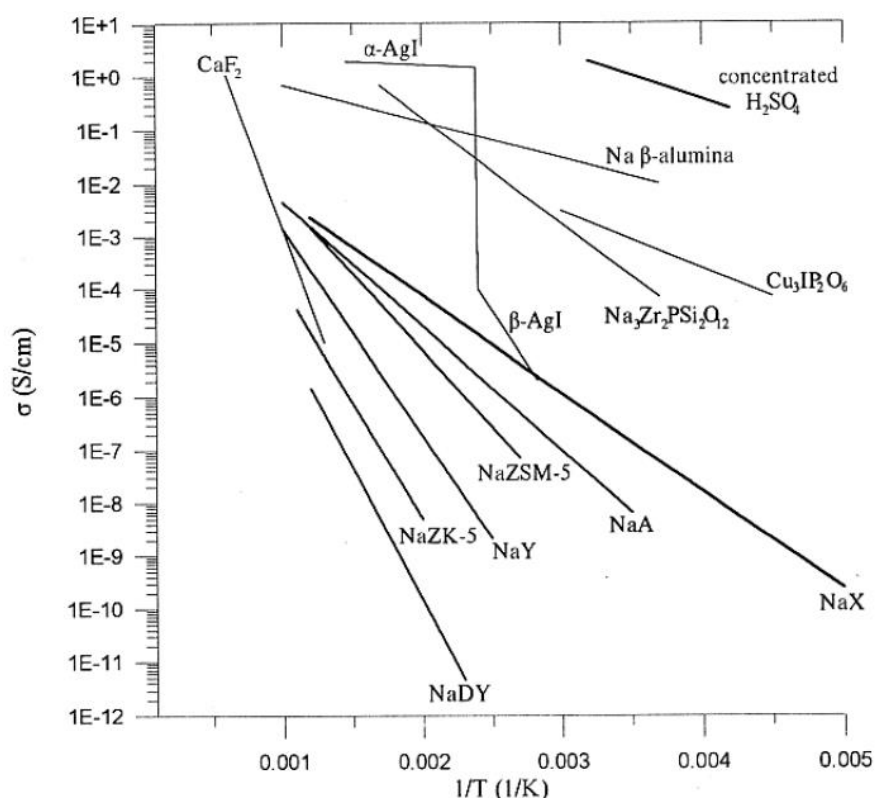


Figure 1.16. Ionic conductivity of some solid electrolytes and representative sodium zeolites: NaZSM-5 (Si/Al = 24), NaA (Si/Al = 1), NaX (Si/Al ~ 1.3-1.5), NaY (Si/Al = 5.4), NaZK-5 (Si/Al = 6.5) and NaDY (Si/Al = 350). Concentrated H₂SO₄ is given for comparison [1].

The synthetic and natural zeolites and zeo-type materials, with various extra-framework cations, have been examined by using impedance spectroscopy in the presence of absorbates or in dehydrated form to investigate electrical conductivity and dielectric properties of them [85-122]. Generally at the frequency range of (10 Hz - 10 MHz) ionic conductivity is dominated by extra-framework cation jumps between sites located at the same or different zeolite cages. Understanding ionic conductivity and dielectric properties of zeolites and zeo-type materials is crucial for catalysis, fuel cells, sensors and also for evaluating zeolites as solid electrolytes [86].

1.2.6.2 Introduction to Impedance Spectroscopy (IS)

“Impedance Spectroscopy (IS) is a powerful method of characterizing many of the electrical properties of materials and their interfaces with electronically conducting electrodes. It may be used to investigate the dynamics of bound or mobile charge in the bulk or interfacial regions of any kind of solids or liquid material: ionic, semiconducting, mixed electronic-ionic, and even insulators (dielectrics)” [87]. The impedance can be defined as frequency dependent resistance to current flow of a circuit element (resistor, capacitor, inductor, etc.). Impedance:

$$Z(\omega) = V(\omega) / I(\omega) \quad (1.2)$$

where, $V(\omega)$ is frequency-dependent potential and $I(\omega)$ is frequency-dependent current. The ratio between potential V and current I is resistance defined by Ohm’s Law.

$$R = V / I \quad (1.3)$$

where resistance R is the impedance at the limit zero frequency. An ideal resistor obeys Ohm’s Law at all current and voltage levels. The resistance value is not changed with alternating current. The ac current and voltage signals are in phase with each other through the ideal resistor. However, the real systems are much more complicated with respect to ideal resistors. Impedance is not restricted by the properties explained for the ideal resistor above.

An electric field can interact with a solid. The interaction leads to a purely real (dc) conductivity σ ,

$$i = \sigma E \quad (1.4)$$

The *long-range conductivity* of materials is investigated [87]. Although IS is theoretically complex and expensive and complex data analysis is required for

quantification, it is widely used for analysis of electrochemical cells since: (i) the information content of IS is much higher than dc techniques or single frequency measurements; (ii) it provides information on the capacitive behavior of the system; (iii) it can distinguish between two or more electrochemical reactions taking place; (iv) time-dependent data can be obtained; (v) it is useful on insulating (i.e., high resistance) materials such as paints and coatings; (vi) it is non-destructive [87,88].

Electrochemical impedance is obtained by measuring the response and computing the impedance at each frequency when a small sinusoidal perturbation (i.e., sinusoidal potential) of fixed frequency is applied. The measurement is repeated for a wide range of frequencies, then, the data is plotted and analyzed. The cell response to sinusoidal perturbation is pseudo-linear, which means the current response $I(t) = I_m \sin(\omega t + \theta)$ to a sinusoidal potential $V(t) = V_m \sin(\omega t)$, involving the single frequency $\nu \equiv \omega/2\pi$, is a sinusoid at the same frequency but shifted in phase (i.e., θ) (Figure 1.17). Phase shift is zero for purely resistive behavior [87].

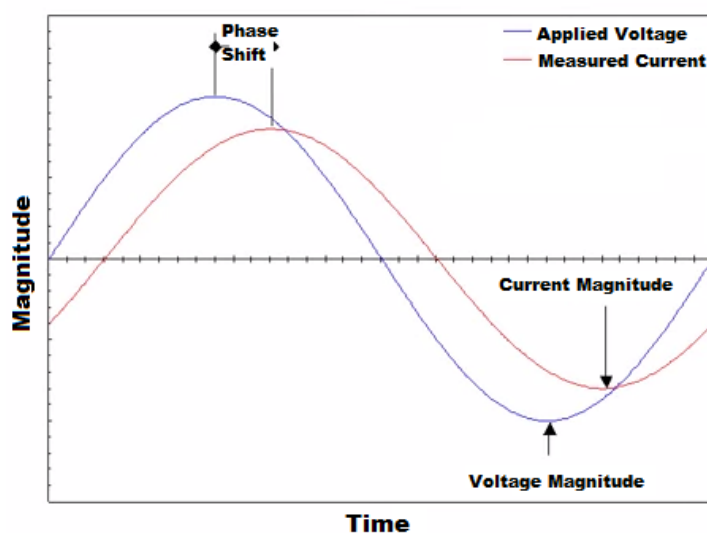


Figure 1.17. Excitation and response in IS [88].

Impedance Z is a more general concept than resistance since it deals with phase shift. “The magnitude and direction of a planar vector of axes can be expressed by the vector sum of the components a and b along the axes, that is, by the complex number $Z = a + jb$. The imaginary number $j \equiv \sqrt{-1} \equiv \exp(j\pi/2)$ indicates an anticlockwise rotation by $\pi/2$ relative to the axis. Thus, the real part of Z , a , is in the direction of the real axis x , and the imaginary part b is along the y axis. An impedance $Z(\omega) = Z' + jZ''$ is such a vector quantity can be plotted as shown in Figure 1.18 (i.e., Impedance plane plot) ” [87]. The impedance can be represented as a vector of length $|Z|$ on the impedance plane plot.

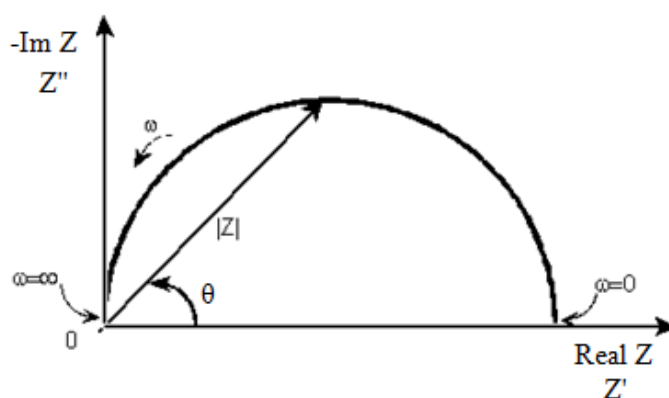


Figure 1.18. Impedance plane plot (Argand diagram) [89].

The value of resistance and capacitance of the samples can be determined through modeling of the electrochemical cell by fitting it to an *equivalent circuit model*. To reveal electrochemical behavior of the samples, electrical circuits having components such as resistors, capacitors and inductors are used in the modeling procedure. The corresponding changes of the components are recorded that give insight into behavior of the electrochemical cell. A real response is in-phase (0°) with the excitation. An imaginary response is $\pm 90^\circ$ out-of-phase (Figure 1.19).

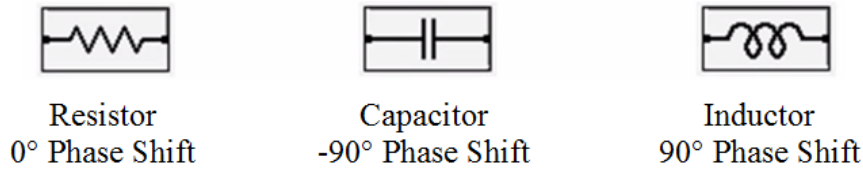


Figure 1.19. Basic electrical circuit elements [88].

A typical model for ion transport through a grain powdered material is the parallel combination of a resistor and capacitor (Figure 1.20). Any material-electrode system in a measuring cell has capacitance $C_g \equiv C_\infty = C_1$ and a bulk resistance $R_b \equiv R_\infty = R_1$ in parallel with it [87]. The conductivity of the sample is calculated using the low frequency intercept of the semicircle with the Z' (i.e., Real Z) axis.

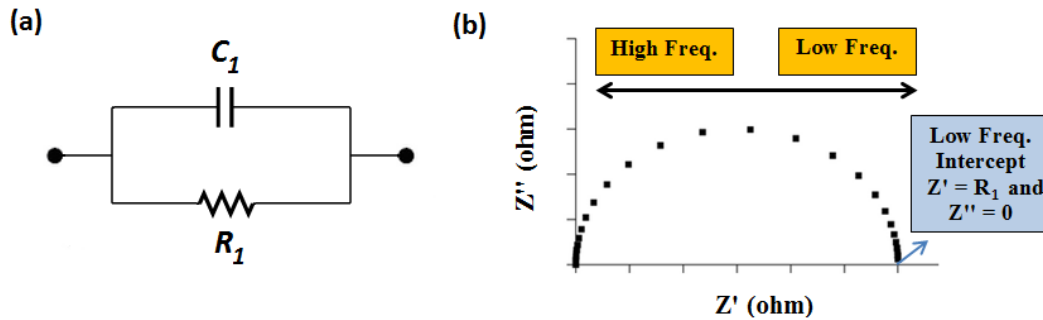


Figure 1.20. Typical equivalent RC circuit (a) and its impedance plane plot (b) [88].

It is proposed that σ obeys the Arrhenius law (i.e., equation 1.7). When impedance data are collected as a function of temperature, activation energy for transport (i.e., dc activation energy), E_A , can be calculated by fitting conductivity data to equation (1.7), where k is Boltzmann's constant, E_A is the activation energy, σ is the conductivity, σ_0 is the pre-exponential factor, and T is the temperature in Kelvin

[86]. A plot of $\ln(\sigma T)$ versus $1/T$, which is called Arrhenius plot, gives a straight line having a slope of $-E_A/k$ (Figure 1.21).

$$\sigma = (\sigma_0 / T) \exp (-E_A / kT) \quad (1.7)$$

Conductivity can be found from the equation below,

$$\rho = RA/\ell \quad (1.8)$$

$$\sigma = 1/\rho \quad (1.9)$$

where, ρ is resistivity, R is the electrical resistance of the material (measured in ohms, Ω , from impedance spectroscopy, low frequency intercept of the semicircle), ℓ is the length of the piece of material (measured in centimeters, cm), A is the cross-sectional area of the specimen (measured in square centimeters, cm^2) and σ is the conductivity ($\Omega^{-1} \text{cm}^{-1}$).

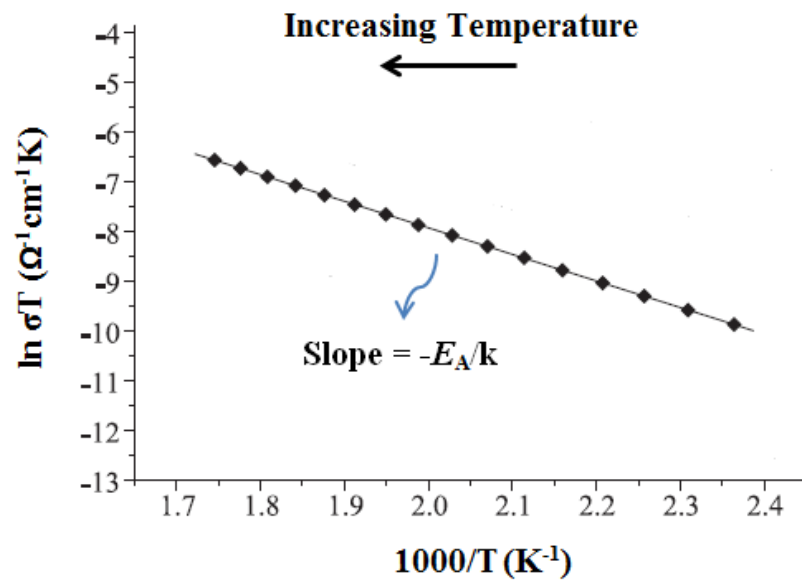


Figure 1.21. An example of Arrhenius plot.

1.2.6.2.1. Impedance-Related Functions

Impedance is a complex quantity and is only real when $\theta = 0$ and thus $Z(\omega) = Z'(\omega)$, that is, for purely resistive behavior. There are three imittance functions which are related to impedance, that is, admittance Y , modulus M , and complex dielectric constant ϵ (Table 1.2).

Table 1.2 Relation between the four basic imittance functions* [87].

	M	Z	Y	ϵ
M	M	μZ	μY^{-1}	ϵ^{-1}
Z	$\mu^{-1}M$	Z	Y^{-1}	$\mu^{-1}\epsilon^{-1}$
Y	μM^{-1}	Z^{-1}	Y	$\mu\epsilon$
ϵ	M^{-1}	$\mu^{-1}Z^{-1}$	$\mu^{-1}Y$	ϵ^{-1}

* $\mu \equiv j\omega C_e$, where C_e is the capacitance of the empty cell.

“The admittance is $Y \equiv Z^{-1} \equiv Y' + jY''$. The other two quantities are usually defined as modulus function $M = j\omega C_e Z = M' + jM''$ and the complex dielectric constant or dielectric permittivity $\epsilon = M^{-1} \equiv Y/(j\omega C_e) \equiv \epsilon' - j\epsilon''$. In these expression $C_e \equiv \epsilon_0 A / \ell$ is the capacitance of the empty measuring cell of electrode area A and electrode separation length ℓ . The quantity ϵ_0 is the dielectric permittivity of free space, 8.854×10^{-12} F/m [87]”.

1.2.6.3 Metal Cation Conduction

Faujasite X and Y, Linde type A, Beta, Mordenite and ZSM-5 were the generally examined zeolites in the literature. Effect of Si/Al ratio of zeolite, charge-radius of the extraframework cations, hydration state of zeolite, sorption of adsorbate on conductivity have been investigated comprehensively for more than thirty years. In

zeolites the conductivity is frequency dependent $\sigma(\omega) = \sigma_0 + A_{\text{const}} \omega^n$ where σ_0 is the frequency independent or dc part of the conductivity and ω^n with $\omega = 2\pi\nu$ expresses its frequency dispersion [90]. Zeolites have energetically different sites or paths for the mobile ions. The structure and Si/Al ratio of zeolite are important parameters in terms of conductivity since they affect the crystallographic positions and distributions of the cations. The cation-sub system is accepted as an interacting lattice gas with occupational disorder, because the number of available lattice sites is much higher than the number of charge compensating cations per unit cell [91].

For instance, zeolite X and Y, commercially used catalysts, belong to the faujasite type crystallographic structure with different Si/Al ratios, which is 1.23 for NaX and 2.43 for NaY. The cation site occupancy is directly related to the Si/Al ratio as can be seen from Table 1.3. NaX (Si/Al = 1) has a higher number of occupied cation sites per unit cell that increase the cation-cation interaction (Figure 1.22.) [90].

Table 1.3. Distribution of Na^+ ions over the corresponding sites in NaX and NaY [90].

	Si/Al ratio	SI	SI'	SII'	SII	SIII	Na^+ per unit cell
Max. sites	-	16	32	32	32	48	-
NaX	1	~3	32	0	32	8 (18 ^a)	86
NaY	2	6	~20	0	32	0	56

^aCalculated as the sum of all possible sites.

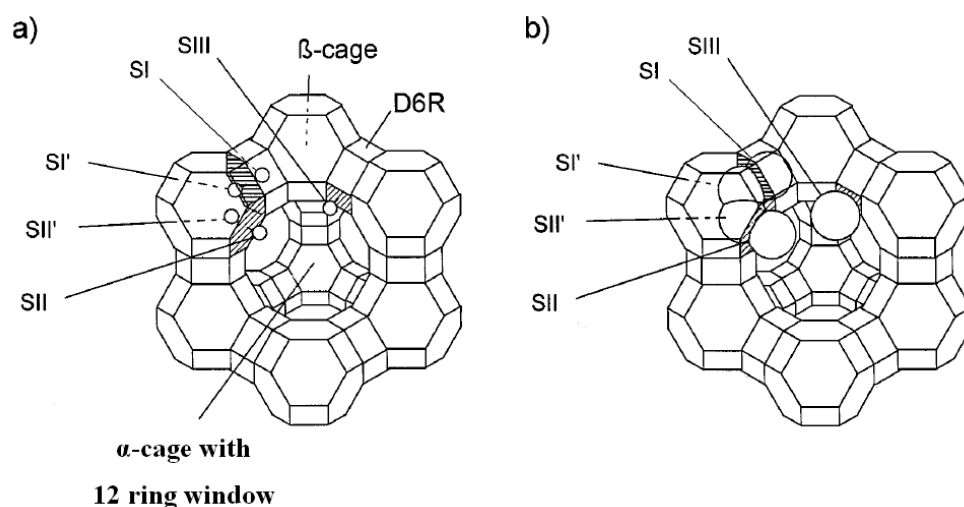


Figure 1.22. Schematic presentation of the faujasite structure with the cation sites SI, SI', SII', SII, and SIII occupied by monovalent cations. While (a) indicates the cation sites, (b) is drawn with the respective Na^+ radius to point out the size relationships [90].

The activation energy of the charge transport (E_A), reflection of electrostatic binding energy, is a complex quantity depending on: (i) the electrostatic interaction (coulombic factor) between the negatively charged framework and the mobile cations; (ii) repulsive cation-cation interaction of neighboring cation sites; (iii) sterical effects caused by the relative size of the ions; (iv) the narrowest site in the conduction path of cations [1, 90].

Simon et al. made an excellent explanation of a *local dipolar relaxation* and a *long-range charge carrier transport* (i.e., DC conductivity) in faujasitic zeolites by using modulus spectra [90]. The *relaxation mode* related to the semicircle observed (i.e., Z' vs. Z'') is a characteristic feature of several types of ion-conducting zeolites. The cations can move along the pore and channel structure due to well defined crystal structure of zeolites. The relaxation mode is ascribed to the motion of mobile cations by hopping diffusion along the pore and channel structure of the zeolite when electric field is applied. Ion hops and subsequent coupled relaxation of the surrounding neighborhood lead to *dielectric absorption* in ionic conductors [90]. As mentioned in

the section 3.5.2.1, there are four imittance functions (i.e., impedance Z , admittance Y , modulus M , and complex dielectric constant ϵ). Representation of data with each function can give insight into the processes occurring within the investigated system. For example, when modulus spectra (i.e., M'' vs. $\log \nu$) is plotted, two well individual relaxation modes (i.e., high frequencies and low frequencies) can be observed easily, which are generally covered in the Argand diagram (i.e., Z' vs. Z'') (Figure 1.23.). In high and low frequency mode, the relaxation times of the cation movements are separate. When the temperature is at 100 °C, a second peak is distinctly noticed at high frequency in NaX that shift to higher frequency upon an increased temperature [92].

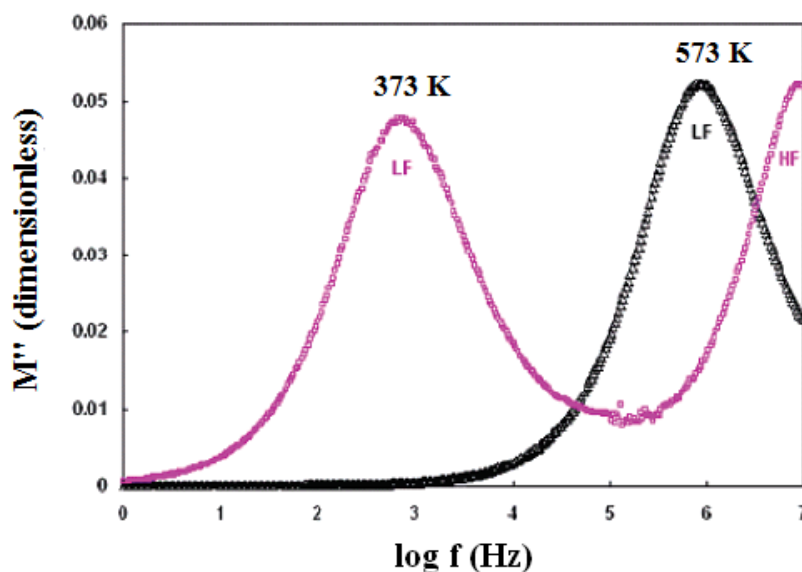


Figure 1.23. Modulus spectra of the imaginary part M'' vs. $\log f$ of NaX [92].

The high-frequency (HF) process is attributed to a local movement of Na^+ ions within the α -cages [90]. The cations located on the equilibrium site SII can move by thermally activated hopping towards SIII to a new potential minimum at SII (Figure 1.24). As mentioned above, the dipole moment created between fixed charge of the

anionic framework and the positive charge of the mobile cations changes with this movement. The equilibrium of *attractive cation-lattice* and of *repulsive cation-cation* interaction determines the potential energy of a given lattice site since the binding energy between cation and lattice is of electrostatic nature. NaX and NaY have same faujasitic crystal structure but different Si/Al ratios changing the number of cations per unit cell as can be seen in Table 1.3. Accordingly, the activation energy of both processes (i.e., HF and LF) is lower in NaX with respect to NaY. In HF process $E_A = 41 \pm 3$ and 72 ± 3 kJ mol⁻¹ (i.e., 0.4 and 0.8 eV) for NaX and NaY, respectively; while in LF process $E_A = 68 \pm 3$ and 80 ± 3 kJ mol⁻¹ (i.e., 0.7 and 0.8 eV) for NaX and NaY, respectively. This can be ascribed to the decrease of the potential energy at the corresponding cation sites due to the cation-cation repulsion [90]. The low-frequency (LF) process is ascribed to the cation movement of *long-range order* which contributes to the dc conductivity. The cations pass the 12 ring windows between neighboring α -cages (Figure 1.24) [90].

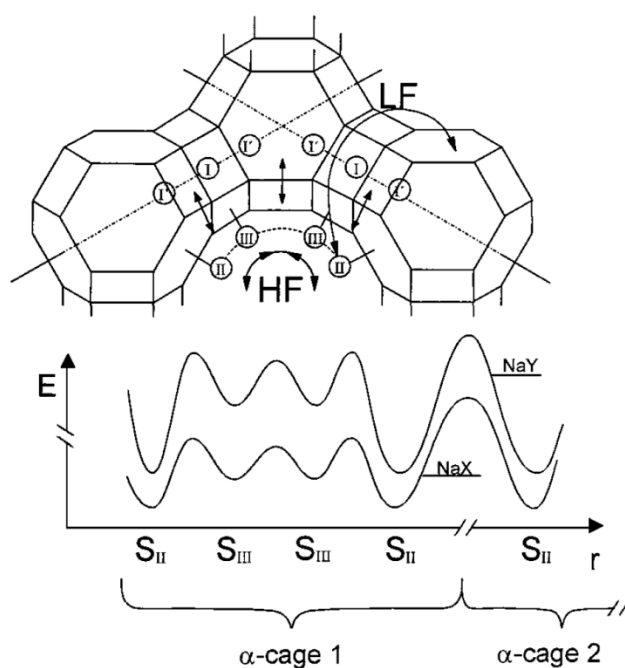


Figure 1.24. Illustration of the conductivity processes and the corresponding potential profile in faujasite indicating the different activation energies of the high-frequency (HF) and the low-frequency (LF) process [90].

1.2.6.3.1 Effect of Si/Al Ratio of Zeolites

The Si/Al ratio of zeolite is a crucial parameter for ion conduction as mentioned above. Several studies were conducted to show the effect of Si/Al ratio on different types of zeolites, i.e., Faujasite X and Y, mordenite, ZSM-5 etc. [1,90,93,94,95]. As a general trend, the activation energy increases with increasing Si/Al ratio, indicating the mainly electrostatic nature of the cation/lattice interaction [1, 90, 93].

Mortier et al. studied the effect of Si/Al ratio and ion radius on the activation energy for monovalent cations of faujasitic zeolite (Table 1.4) [93]. They found that the activation energy decreases with increasing ionic radius of monovalent cations (Li^+ , Na^+ , and K^+) and increases with increasing $\text{SiO}_2/\text{Al}_2\text{O}_3$ ratio.

Table 1.4. Activation energies (kJ mol^{-1}) of ionic conduction of monovalent cations in faujasite [93].

$\text{SiO}_2/\text{Al}_2\text{O}_3$	1.25	3.4	5	5.8
Li^+	72.3		90.3	
Na^+	52.3	55.2	74.2	79.4
K^+	54.7	53.9	54.9	64.8
Rb^+	67.4	61.9	67.3	70.6
Cs^+	55.5	58.0		
Ag^+	54.0			

Buckley et al. studied the effect of $\text{SiO}_2/\text{Al}_2\text{O}_3$ ratios (80, 272, 400, 1000, and 2000) on the activation energy of ZSM-5 ion-exchanged with Li^+ , Na^+ , and K^+ and found the same trend: the activation energy decreased with increasing ionic radius (Li^+ , Na^+ , and Cs^+) and increased with increasing $\text{SiO}_2/\text{Al}_2\text{O}_3$ ratio (Figure 1.25) [94].

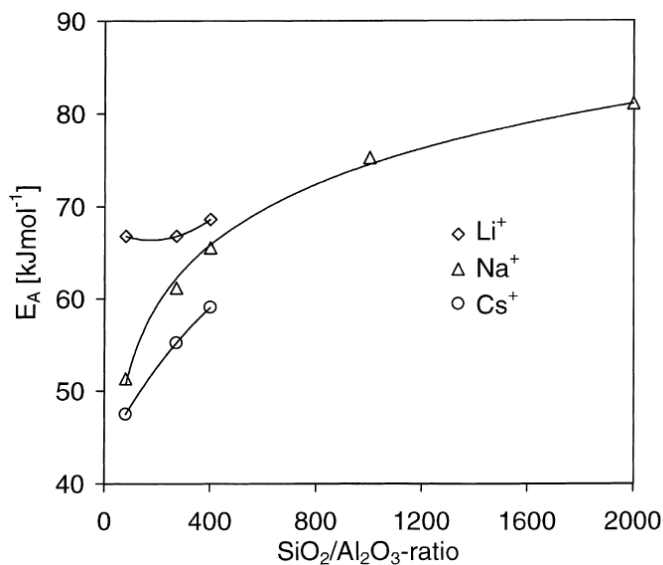


Figure 1.25. Activation energy as a function of the SiO₂/Al₂O₃ ratio for different alkali cations in zeolite ZSM-5 [94].

1.2.6.3.2 Effect of Charge-Radius of Extra-Framework Cations

As explained above, coulombic interaction between lattice and cation is affected by the size of the ions. The coulombic attraction decreases between the counter ion and its site as the cation becomes larger; therefore, the activation energy E_A decreases with increasing univalent-cation radius (r) for many Y-type faujasites (Figure 1.26-a). Due to the additional *intercationic repulsion terms* for comparatively large cations (i.e., Rb⁺, Cs⁺) see Figure 1.28, deviations from this trend have been observed [1,96].

The activation energies of divalent cation-exchanged zeolite X and Y increased with increasing ionic radius (Figure 1.26 and Table 1.5) [1, 93, 97, 96]. The two sites of negative charge in the lattice are associated with each divalent cation [97]. The activation energy of calcium ion would be expected to have twice the activation energy of sodium ion from electrostatic considerations. Since the calcium ion place between two relatively widely separated negative charges, the bond strength

diminishes significantly. The sharp increase in E_A with increasing cation size indicates the greater ease of bonding to two crystallographically separated sites for the larger, more polarizable cations [97].

Table 1.5. Activation energies (kJ mol^{-1}) for ionic conduction of divalent cations in zeolite X [93].

	Ionic radius^a (pm)	E_A
Mg²⁺	72	84.4
Zn²⁺	75	94.4
Cd²⁺	95	95.3
Ca²⁺	100	97.3
Cu²⁺	72	108.7 \pm 15

^aIonic radii for coordination number 6.

The activation energy E_A increases with increasing univalent-cation radius (r) for X-type faujasites as can be seen from Figure 1.26 (i.e., opposite trend with respect to Y-type faujasites). The number of cations in zeolite X is higher compared to zeolite Y. Accordingly, this trend is attributed to the more pronounced *cation-cation repulsions* [1]. Furthermore, the Freeman et al. showed that cation position in zeolite Y and X is displaced when the cation size increases [97]. Sodium ion is small enough to place itself in the plane and probably in the center of a six-membered oxygen ring. However, larger cations must be located out of the plane of the ring and further into the adjacent cavity (Figure 1.28). The coulombic interaction decreases with increasing cation radius, which can be seen in the $E_A(r)$ behaviour going from Li^+ to Na^+ ions for zeolite A (Figure 1.27). However, the motion of the cation is restricted when the channel size approaches the cation dimension (i.e., *steric hindrance*). The increasing activation energy with increasing cation size (i.e., K^+ and Rb^+) indicates the steric hindrance [1]. In the case of small pore zeolites, such as zeolite A,

analcime, sodalite, offretite, cancrinite the steric hindrance dominates over the coulombic factor in defining values of the thermodynamic parameters for cation migration [97,98,99].

In all type of zeolites (i.e., zeolite X, Y and A), Li^+ -forms have high activation energy and subsequently low conductivity values (Figure 1.26 and Figure 1.27). The small-sized Li^+ ions can penetrate into the tetrahedral structure and form covalent bonds with the tetrahedral oxygens [1, 97], which cause a strong interaction with anionic framework. As a result, the total energy barrier for ion migration includes an additional term, i.e., *disassociation energy* [1].

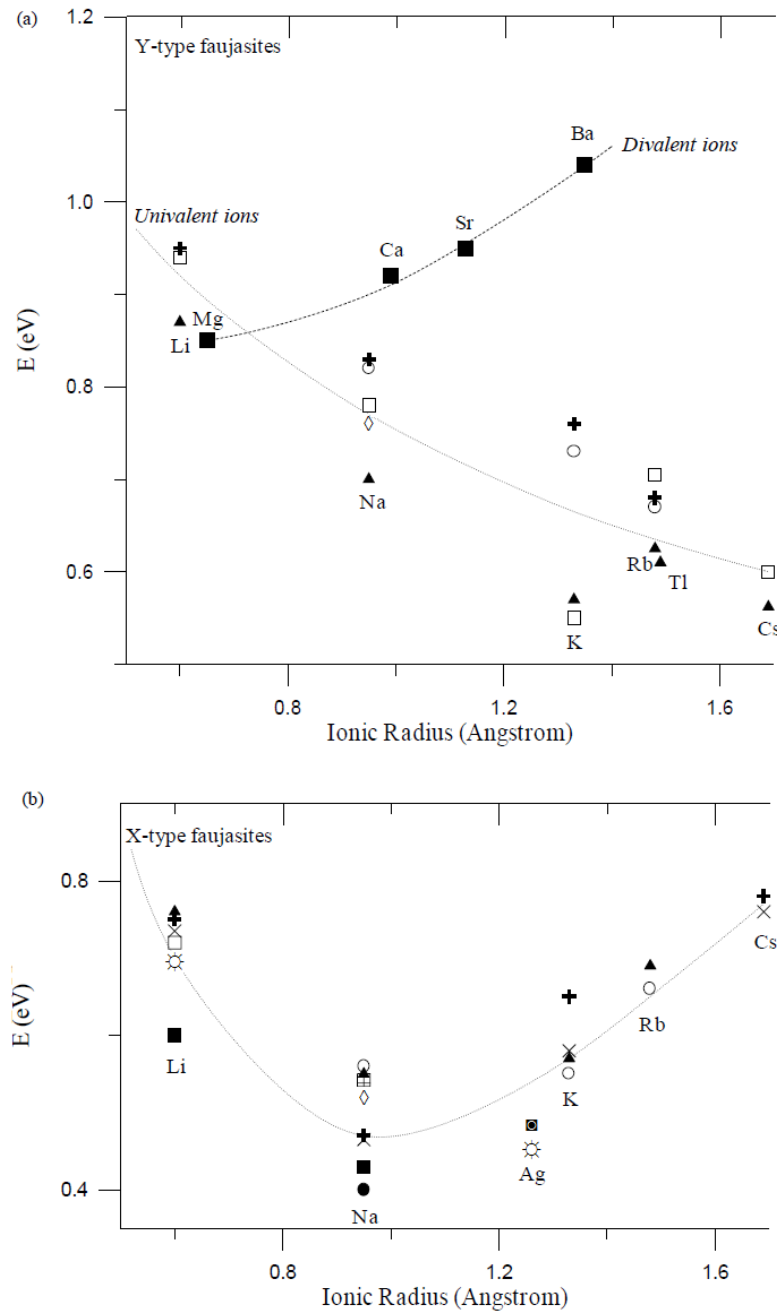


Figure 1.26. Plots of the activation energy for ionic conduction as a function of the univalent cation radius for synthetic faujasites. a) Y-types (Si/Al \sim 2.5-5): ■ [16], ◇ [17], + [18], ▲ [16], ○ [19]. b) X-types (Si/Al \sim 2.5-5): X [20], + [21], ○ [19], ● [22], ■ [23], ▲ [24], ☼ [25], □ [26], + [27], ◇ [16], ▣ [28]. Plot (a) also contains data for the barriers for M^{2+} conducting ions (M^{2+} NaY mixed forms). The Li-, Rb-, Tl- and CsY forms retain a small amount of the initial Na ions. The lines are guides for the eyes [1].

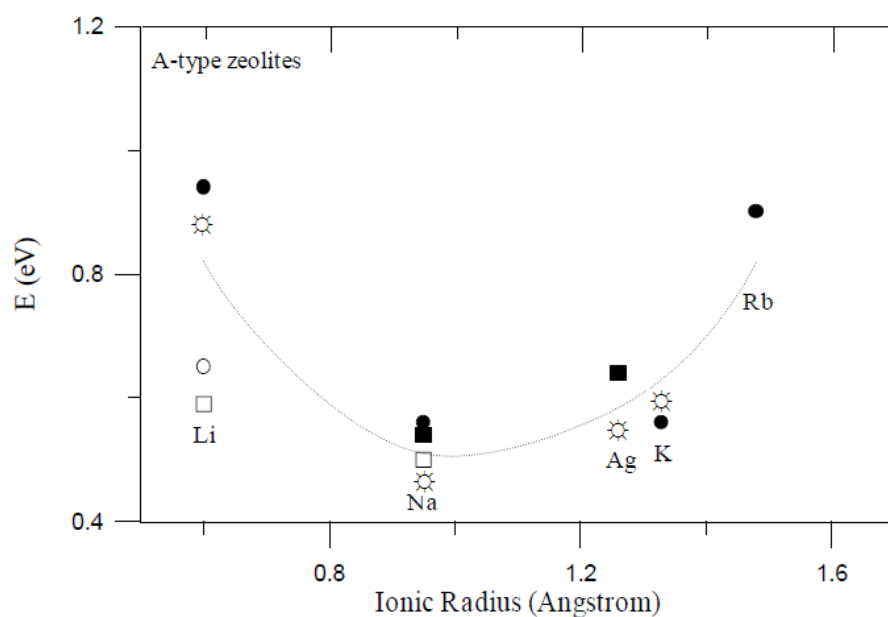
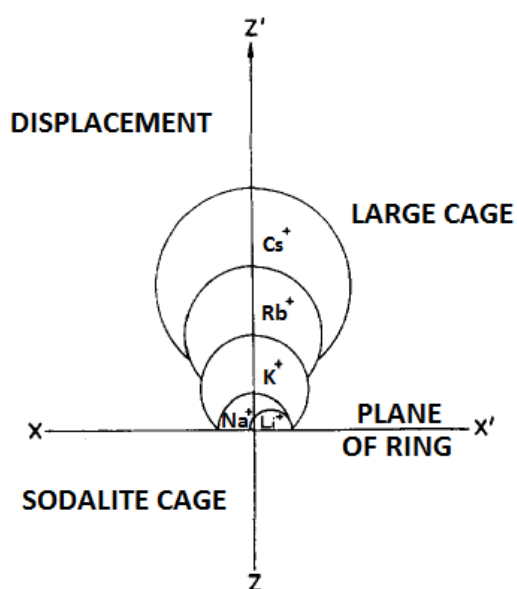


Figure 1.27. Plot of the activation energy for ionic conduction as a function of the univalent cation radius for A-types. ☼ [16], ● [29], □ [25], ○ [26], ■ [27]. The lines are guides for the eyes [1].



Ions	Ionic Radius (pm)	Ref.
Li^+	68	[113]
Na^+	97	[112]
K^+	133	[113]
Rb^+	147	[113]
Cs^+	167	[112]
Mg^{2+}	72	[93]
Zn^{2+}	75	[93]
Ca^{2+}	100	[93]
Sr^{2+}	112	[114]
Ba^{2+}	134	[114]

Figure 1.28. The displacement of various sized cations from the plane of a six membered oxygen ring, XX' represents the plane of the ring. Cations larger than sodium are displaced along the axis ZZ' toward the center of a large cage [97] (left); ionic radius values of cations (right) [93,112-114].

1.2.6.3.3 Effect of Hydration State

The sorption of various molecules on a zeolite affects state of cations and conductivity of the zeolite. It was found that the electrical conductivity of zeolites increases when there is water adsorption (i.e., hydrated samples) [96,115]. In the hydrated state, the cations are coordinated by water molecules, leading to a weaker interaction with the negatively charged lattice. Thus, the probability to move through the lattice is increased, i.e., the conductivity increases with the degree of hydration [96] (Figure 1.29).

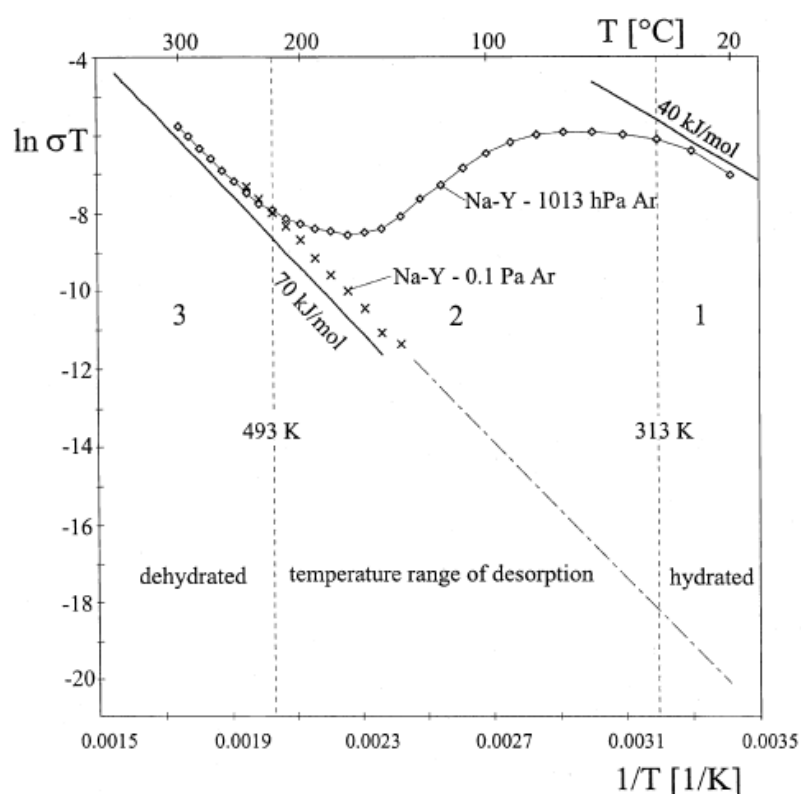


Figure 1.29. Arrhenius plot of Na-Y for the HF process at 1013 hPa Ar. For comparison, the slopes for activation energies of 40 and 70 kJ mol⁻¹ (i.e., 0.4 and 0.7 eV), respectively, are shown [96].

Chabanis et al. have studied the influence of adsorbed water on the conductivity, and the relaxation mechanisms of the exchanged cations of Faujasite NaX (Si/Al = 1.3) by using impedance spectroscopy [116]. The activation energy (0.9 - 0.58 eV) was affected from hydration state of the zeolite indicating their influence on the conduction process. The analysis revealed two relaxation domains: “low-frequency” and “high frequency” relaxations. Abdoulaye et al. have studied the conductivity of Faujasite NaY (Si/Al = 2.12) as a function of hydration state by using impedance spectroscopy [117]. The conductivity was attributed to the migration of cations in large cages. Two relaxation domains were detected due to the movement of cations of sites III' and II. Abdoulaye et al. have also compared the conductivity of Faujasite NaX and NaY [118]. They showed that the dc conductivity was related to the migration of the exchangeable cations over “large distances” with activation energies varying from 0.58 to 0.9 eV for NaX and from 0.61 to 0.85 eV for NaY, which was attributed to possessing different number of exchangeable (i.e., mobile) cations.

For metal cations, solvation such as H₂O cation mobility is enhanced; therefore, potential barrier for ionic mobility is decreased since coordination of the cations by water molecules results weaker binding of the hydrated cations to the anionic framework of zeolite.

1.2.6.4 Metal Cation Conduction of Zeo-Type Materials and Thin Films

Zeolites are promising material to be used as an ion conductor due to well defined pores and mobile exchangeable cations which have been tested for many years. However, conductivity of zeolites is low (or middle range) with respect to the other ionic conductors. Two reasons are proposed: (i) the electrostatic interaction between negatively charged framework of zeolites and extraframework cations is strong, which hinders ion migration; (ii) the size of channels or cages of the zeolites is so large that the mobile ions are trapped on the walls of the channels or cages that have sites with relatively high potential energy depths; therefore, the cations become partly immobilized [85]. Therefore to improve ionic conductivity of zeo-type materials, the ion-channel size should be matched and the interaction between the

anionic framework and the cations should be diminished. To investigate these effects, ionic conductivity of zeo-type crystalline materials has been examined [85,86,92].

Feng et al. investigated the ionic conductivity of hydrated and dehydrated microporous zeo-type sodium hydrogen germanate in the temperature range of 25 - 550 °C by using impedance spectroscopy [85]. The activation energies for ion conduction in dehydrated $M_3HGe_7O_{16}$, $M = K^+$, Rb^+ , and Cs^+ , were found to be 0.69, 0.64, and 0.48 eV, respectively (Table 1.6). The decreasing activation energy with increasing cationic radius was ascribed to the decrease of the Coulombic attraction between the cations and the negatively charged mixed tetrahedral-octahedral (GeO_4 - GeO_6) anionic framework structure.

Table 1.6. Typical ionic conductivities and activation energies of dehydrated $M_3HGe_7O_{16}$, $M = K^+$, Rb^+ and Cs^+ [85].

Sample	Conductivity, ($\Omega\text{ cm}$) ⁻¹				E_A , eV
	200 °C	300 °C	400 °C	500 °C	
$K_3HGe_7O_{16}$	1.8×10^{-6}	3.3×10^{-5}	2.3×10^{-4}	8.7×10^{-4}	0.69
$Rb_3HGe_7O_{16}$	7.2×10^{-6}	9.3×10^{-5}	5.0×10^{-4}	2.1×10^{-3}	0.64
$Cs_3HGe_7O_{16}$	1.1×10^{-4}	6.8×10^{-4}	2.0×10^{-3}	8.9×10^{-3}	0.48

McKeen et al. studied the long-range ionic conductivity of mono- (i.e., Li^+ , Na^+ , K^+ , Rb^+ , and Cs^+) and divalent (i.e., Mg^{2+} , Ca^{2+} , and Sr^{2+}) cation-exchanged zeo-type zincosilicate VPI-9 ($Si/Zn = 4.0$) comprehensively by using impedance spectroscopy and compared with faujasite M-X, where $M = Li^+$, Na^+ , K^+ , Rb^+ , Cs^+ , Mg^{2+} , Ca^{2+} , and Sr^{2+} [86,119]. They showed that X-ray crystallinity of Li-, Na-, Mg-VPI-9 disappeared upon vacuum dehydration at 450 °C. However, all crystalline M-VPI-9 materials showed greater conductivities than M-X, with the exception of K-X ($1.6 \times$

10^{-3} S/cm at 450°C). K-, Rb-,Cs- Ca- and Sr-VPI-9 remained crystalline and exhibited conductivities of 1.7×10^{-4} , 3.5×10^{-4} , 4.9×10^{-4} , 2.3×10^{-6} and 7.7×10^{-7} S/cm respectively, at 450 °C and activation energies of 0.72, 0.64, 0.69, 0.88 and 0.91 eV, respectively, in the temperature range of 150 - 450 °C. VPI-9 was interesting in terms of its ability to transport divalent cations (i.e., Ca^{2+} and Sr^{2+}), which was 4 orders of magnitude greater than Ca- and Sr-X zeolites (i.e., $\sim 10^{-10}$ S/cm at 400 °C) (Table 1.7).

Table 1.7. Conductivity and activation energy values of zincosilicate M-VPI-9, where M = K^+ , Rb^+ , Cs^+ , Ca^{2+} , and Sr^{2+} [86].

Sample	Conductivity, S/cm	E_A , eV
	450 °C	150-450 °C
K-VPI-9	1.7×10^{-4}	0.72
Rb-VPI-9	3.5×10^{-4}	0.64
Cs-VPI-9	4.9×10^{-4}	0.69
Ca- VPI-9	2.3×10^{-6}	0.88
Sr- VPI-9	7.7×10^{-7}	0.91

There is only one study about conductivity of pressed pellets of zeo-type titanosilicate ETS-10 to the best of our knowledge [92]. Wei et al. investigated and compared ion transport of the titanosilicate ETS-10, Cu^{2+} ion-exchanged ETS-10 and zeolite X by using impedance spectroscopy. Activation energies for conduction were 58.5 and 66.8 kJ mol^{-1} (i.e., 0.6 and 0.7 eV, respectively) for Na-ETS-10 and NaX, respectively. However, the dc conductivity and ion hopping rate for Na-ETS-10 were also lower than NaX attributed to its high cation site occupancy. The cation site occupancy was decreased through Cu^{2+} ion-exchange and Cu-ETS-10 was found to have both lower activation energy and higher ionic conductivity than CuX. They concluded that ETS-10 has more facile transport of higher valence cations with

respect to zeolite X that have the highest ionic conductivity among the other zeolites, which may be important for ion-exchange, environmental remediation of radionucleotides, and nanofabrication.

Dutta et al. made comprehensive study about ionic conductivity of zeolite Y in the form of pressed pellets and zeolite Y membrane prepared through secondary growth method, and also, impedance based zeolite Y sensors to detect DMMP (*vide infra*) [120-122]. They studied the effect of crystallite size on ionic conductivity of alkali metal ion-exchanged faujasitic zeolites with morphologies varying from a zeolite membrane, micrometer-sized, submicrometer, and nanoparticles by using impedance spectroscopy (Figure 1.30) [120]. The conductivity of zeolite Y membrane prepared through secondary growth method was investigated for the first time, which is crucial in the scope of the current thesis. They investigated the effect of Si/Al ratios and exchangeable cations (i.e., Li^+ and K^+). Activation energies increased with increasing Si/Al ratio for the membrane, commercial micrometer, submicrometer, nano, and synthetic micrometer zeolite with Si/Al ratios of 2.58, 2.5, 1.75, 1.68, and 1.48 have E_A of 93, 83, 78, 66, and 51 kJ mol^{-1} (i.e., 1, 0.9, 0.8, 0.7 and 0.5 eV), respectively. With lower Si/Al ratios as there are more cations within the framework and the cation-cation repulsion facilitates motion. The activation energies as a function of ion exchanging cation followed the order $\text{Li}^+ > \text{Na}^+ > \text{K}^+$.

They investigated effect of *grain boundaries* on the low-frequency ($10^4 - 10^5$ Hz), long-range ionic conduction of zeolites for the first time by applying surface derivatization to the particles, that is, the surface hydroxyl groups were converted to $-\text{OSiH}(\text{CH}_3)_2$, and then during sample preparation, the organic groups were burnt off, leaving a single layer of Si-O-Si on the zeolite surface. The effect on E_A was size-dependent: (i) activation energy did not change for micron sized zeolite; (ii) increased from 78 to 83 kJ mol^{-1} (i.e., 0.8 to 0.9 eV) for submicrometer sized zeolite; (iii) increased 66 to 81 kJ mol^{-1} (i.e., 0.7 to 0.8 eV) for nanosized zeolite upon surface derivatization. E_A increased significantly as the zeolite reached to the nanoscale due to more defective intergrain boundaries contributing to the higher E_A [120].

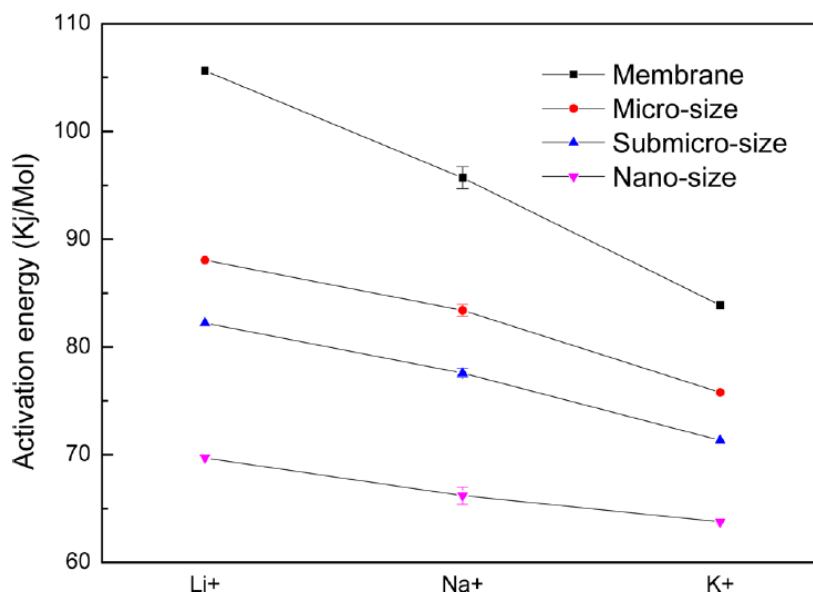


Figure 1.30. Plots of activation energy trends for Li^+ , Na^+ , and K^+ exchanged zeolite membrane, commercial micrometer-sized, submicrometer-sized, and nano-sized zeolites. (The error bars were only done on the Na^+ -exchanged version of the sample and obtained from repeat of three independent measurements) [120].

In 2010 Dutta et al. investigated the effect of Dimethylmethylphosphonate (DMMP, with length of 5.71 Å), a simulant for the highly toxic organophosphate nerve agent Sarin (GB), on the ionic conductivity of zeolite Y by using impedance spectroscopy. They designed an impedance based zeolite NaY sensor (i.e., at temperature 320 °C) for detecting ppm level of DMMP at a single frequency of 3000 Hz [121]. The ionic conductivity of NaY increased in the presence of 20-100 ppm of DMMP. They proposed a mechanism that involves the binding of the sodium cation with the phosphonate group of DMMP that results in facilitated inter cage motion of the cation as shown in Figure 1.31.

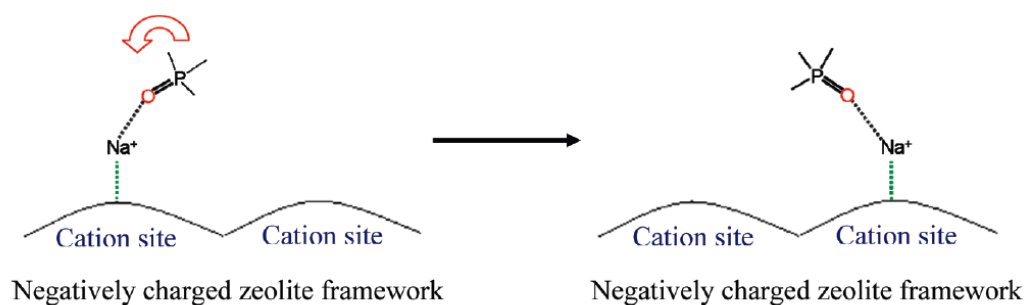


Figure 1.31. Proposed model for the interaction of DMMP with cations inside the supercage: cation mobility was facilitated by the re-orientation of the DMMP molecules [120].

In 2012 Dutta et al. tried to improve the impedance spectroscopy based sensing of DMMP on zeolites by applying two strategies: (i) cerium oxide (CeO_2) was coated on the zeolite surface to neutralize acidic groups that may cause the decomposition of DMMP, and results in better sensor recovery; (ii) zeolite Y membrane was used that have connected supercages of much longer length scales with respect to pressed pellets [122]. The zeolite membranes showed higher sensitivity to DMMP; however, recovery of the device was considerably slower than pressed zeolite pellets. They proposed that the near-surface regions of the zeolites are responsible for the signals in the case of pressed pellet type sensors while diffusion of DMMP occurs within the microstructure of zeolite membranes.

As mentioned above only Dutta et al. studied “film” form of zeolites in conductivity measurements instead of pressed pellets. They proposed that use of zeolite membrane will improve response of sensors and lead to design miniaturized sensors [3]. In the current thesis study, long-range ionic conductivity of zeo-type titanosilicate ETS-10 films prepared via secondary growth method was investigated. A system design (See Section 2.5.5) was carried out to study ionic conductivity of microporous titanosilicate ETS-10 films in the temperature range of 25 to 500 °C by using impedance spectroscopy. The Na^+ and K^+ ions within the framework of as-

synthesized ETS-10 films were ion-exchanged with Li^+ , Ca^{2+} , Zn^{2+} ions to figure out effect of cation site occupancy on conduction. The following parameters affecting the long-range ionic conductivity of the ETS-10 films were studied: (i) hydration state; (ii) grain boundary structure; (iii) cation site occupancy. This study shows long-range ionic conductivity properties of titanosilicate ETS-10 films prepared via secondary growth method comprehensively for the first time which may be important for ion-exchange, fuel cells, and sensor applications.

REFERENCES

- [1] I.M. Kalogeras, A. Vassilikou-Dova, “Electrical Properties of Zeolitic Catalysts”, Defect and Diffusion Forum, 164, 1998, 1-36.
- [2] WEB: “Zeolite Framework Types”, <http://izasc.biw.kuleuven.be/fmi/xsl/IZA-SC/ft.xsl>, 15.04.2015.
- [3] Y. Zheng, X. Li, P.K. Dutta, “Exploitation of Unique Properties of Zeolites in the Development of Gas Sensors”, Sensors, 12, 2012, 5170-5194.
- [4] S.M. Kuznicki, US Patent 4, 853, 2002, 1989.
- [5] N.C. Jeong, M.H. Lee, K.B. Yoon, “Length-Dependent Band-Gap Shift of TiO_3^{2-} Molecular Wires Embedded in Zeolite ETS-10”, Angew. Chem. Int. Ed. 46, 2007, 5868-5872.
- [6] Z. Ji, B. Yilmaz, J. Warzywoda, A. Sacco Jr., “Hydrothermal Synthesis of Titanosilicate ETS-10 using $\text{Ti}(\text{SO}_4)_2$ ”, Micropor. Mesopor. Mater. 81, 2005, 1 - 10.
- [7] Z. Ji, J. Warzywoda, A. Sacco Jr., “Synthesis and Morphological Control of Large Titanosilicate ETS-10 Crystals”, Micropor. Mesopor. Mater. 109, 2008, 1 - 11.
- [8] L. Lv, F. Su, X.S. Zhao, “A Reinforced Study on the Synthesis of Microporous Titanosilicate ETS-10”, Micropor. Mesopor. Mater. 76, 2004, 113 - 122.
- [9] M.W. Anderson, O. Terasaki, T. Ohsuna, A. Philippou, S.P. MacKay, A. Ferreira, J. Rocha, S. Lidin, “Structure of the Microporous Titanosilicate ETS-10”, Nature, 367, 1994, 347 - 351.
- [10] P.D. Southon, R.F. Howe, “Spectroscopic Studies of Disorder in the Microporous Titanosilicate ETS-10”, Chem. Mater. 14, 2002, 4209 - 4218.
- [11] R. Xu, W. Pang, J. Yu, Q. Huo, J. Chen, “Chemistry of Zeolites and Related Porous Materials”, Wiley, Singapore, 2007.
- [12] N.C. Jeong, H. Lim, H. Cheong, K.B. Yoon, Angew. Chem. Int. Ed. 50 (2011) 8697.
- [13] Z. Ji, M.N. Ismail, D.M. Callahan Jr., E. Pandowo, Z. Cai, T.L. Goodrich, K.S. Ziemer, J. Warzywoda, A. Sacco Jr., Appl. Catal. B: Environ. 102 (2011) 323.

- [14] S.M. Kuznicki, A. Anson, A. Koenig, T.M. Kuznicki, T. Haastrup, J. Phys. Chem. C 111 (2007) 1560.
- [15] G. Agostini, S. Usseglio, E. Groppo, M.J. Uddin, C. Prestipino, S. Bordiga, A. Zecchina, P.L. Solari, C. Lamberti, Chem. Mater. 21 (2009) 1343.
- [16] L. Lv, Y. Luo, W.J. Ng, X.S. Zhao, Micropor. Mesopor. Mater. 120 (2009) 304.
- [17] M. Shi, C.C.H. Lin, L. Wu, C.M.B. Holt, D. Mitlin, S.M. Kuznicki, J. Nanosci. Nanotechnol. 10 (2010) 8448.
- [18] G. Zhao, H. Kozuka, T. Yoko, Thin Solid Films 277 (1996) 147.
- [19] N. Sobana, M. Muruganadham, M.J. Swaminathan, J. Mol. Catal. A. Chem. 258 (2006) 124.
- [20] S.A. Maier, H.A. Atwater, J. Appl. Phys. 98 (2005) 101.
- [21] K. Awazu, M. Fujikami, C. Rockstuhl, J. Tominaga, H. Murukami, Y. Ohki, N. Yoshida, T. Watanabe, J. Am. Chem. Soc. 130 (2008) 1676.
- [22] Y. Ohka, T. Tatsuma, T. Fujii, K. Naoi, C. Niwa, Y. Kubota, A. Fujisihma, Nat. Mater. 2 (2003) 29.
- [23] S. Çalışkan, M. Zahmakıran, S. Özkar, Appl. Catal. B : Environ. 93 (2010) 387.
- [24] M. Zahmakıran, Y. Tonbul, S. Özkar, J. Am. Chem. Soc. 132 (2010) 6541.
- [25] M. Zahmakıran, S. Özkar, Mater. Chem. Phys. 121 (2010) 359.
- [26] M. Zahmakıran, S. Akbayrak, S. Özkar, Dalton Trans. 39 (2010) 7521.
- [27] M. Zahmakıran, T. Ayvalı, S. Akbayrak, S. Çalışkan, D. Çelik, S. Özkar, Catal. Tod. 170 (2011) 76.
- [28] M. Zahmakıran, F. Durap, S. Özkar, Int. J. Hyd. Energ. 35 (2010) 187.
- [29] K. Kawahara, K. Suzuki, Y. Ohko, T. Tatsuma, Phys. Chem. Chem. Phys. 7, 2005, 3851-3855.
- [30] Y. Ohko, T. Tatsuma, T. Fujii, K. Naoi, C. Niwa, Y. Kubota, A. Fujishima, Nat. Mater. 2, 2003, 29 - 31.
- [31] K. Naoi, Y. Ohko, T. Tatsuma, J. Am. Chem. Soc. 126, 2004, 3664 - 3668.
- [32] K. Naoi, Y. Ohko, T. Tatsuma, Chem. Commun. 10, 2005, 1288 - 1290.
- [33] L. Nadar, R. Sayah, F. Vocanson, N. Crespo-Monteiro, A. Boukenter, S. Sao Joao, N. Destouches, Photochem. Photobiol. Sci. 10, 2011, 1810 - 1816.
- [34] A. Kafizas, C.W. Dunnill, I.P. Parkin, Phys. Chem. Chem. Phys. 13, 2011, 13827 - 13838.

- [35] H. Dürr, H. Bouas-Laurent, Photochromism: Molecules and Systems, Elsevier BV Press, The Netherlands, 2003.
- [36] C. Bechinger, S. Ferrere, A. Zaban, J. Sprague, B.A. Gregg, Nature 383, 1996, 608-610.
- [37] WEB: GB7 Report: Design, Synthesis, and Photochromism Studies of Photo-Switchable Bispiropyran Polymers”, <https://acswebcontent.acs.org/prfar/2009/reports/P10382.html>, 13.05.2015.
- [38] WEB: Corning Glass&Ceramics, Photochromism, 13.05.2015, http://www.corning.com/ophthalmic/products/educational_info/photochromism.aspx.
- [39] S.V. Paramonov, V. Lokshin, O.A. Fedorova, J. Photochem. Photobiol. C: Photochemistry Reviews. 12, 2011, 209 - 236.
- [40] M.E. Moustafa, M.S. McCready, R.J. Puddephatt, Organometallics 31, 2012, 6262 - 6269.
- [41] G. Leftheriotis, S. Papaefthimiou, P. Yianoulis, Sol. Energy Mater. Sol. Cells 83, 2004, 115 - 124.
- [42] A. Gavriluk, U. Tritthart, W. Gey, Sol. Energy Mater. Sol. Cells 9, 2011, 1846-1851.
- [43] S.K. Deb, Sol. Energy Mater. Sol. Cells 92, 2008, 245 - 258.
- [44] L. Bois, F. Chassagneux, Y. Battie, F. Bessueille, L. Mollet, S. Parola, N. Destouches, N. Toulhoat, N. Moncoffre, Langmuir 26(2), 2010, 1199 - 1206.
- [45] S.M. Kuznicki, U.S. Patent 5, 011, 591, 1991.
- [46] S. Galioğlu, M. Zahmakıran, Y.E. Kalay, S. Özkar, B. Akata, Micropor. Mesopor. Mater. 159, 2012, 1 - 8.
- [47] C. Lamberti, Micropor. Mesopor. Mater. 30, 1999, 155 - 163.
- [48] S.M. Aurbach, K.A. Carrado, P.K. Dutta, “Handbook of Zeolite Science and Technology”, Marcel Dekker, Inc., 2003, p. 21, 22, 37, 869, 870.
- [49] Z. Lai, M. Tsapatsis, J.P. Nicolich, “Siliceous ZSM-5 Membranes by Secondary Growth of *b*-Oriented Seed Layers”, Adv. Funct. Mater. 14(7), 2004, 716 - 729.
- [50] J. Caro, M. Noack, P. Kolsch, R. Schafer, “Zeolite Membranes - State of their Development and Perspective”, Micropor. Mesopor. Mater. 38, 2000, 3 - 24.
- [51] J.G. Tsikoyiannis, W.O. Haag, "Synthesis and Characterization of a Pure Zeolitic Membrane", Zeolites, 12, 1992, 126.

- [52] E. R. Geus, J. E. Marcel, H. Bekkum, "Synthesis and Characterization of Zeolite (MFI) Membranes on Porous Ceramic Supports," J. Chem. Sci. Faraday Trans., 88, 1992, 3101.
- [53] Bakker, W. J. W., F. Kapteijn, J. Poppe, and J. A. Moulijn, "Permeation Characteristics of a Metal-Supported Silicalite-1 Zeolite Membrane", J. Memb. Sci., 117, 1996, 57.
- [54] J. Choi, S. Ghosh, Z. Lai, M. Tsapatsis, "Uniformly *a*-Oriented MFI Zeolite Films by Secondary Growth", Angew. Chem. Int. Ed. 45, 2006, 1154 - 1158.
- [55] M.C. Lovallo, M. Tsapatsis, T. Okubo, "Preparation of an Asymmetric Zeolite L Film," Chem. Mat., 8, 1996, 1579.
- [56] M.C. Lovallo, M. Tsapatsis, "Preferentially Oriented Submicron Silicalite Membranes", AIChE J., 42, 1996, 3020.
- [57] L.C. Boudreau, J.A. Kuck, M. Tsapatsis, "Deposition of Oriented Zeolite A Films: *in-situ* and Secondary Growth", J. Memb. Sci. 152, 1999, 41 - 59.
- [58] L. C. Boudreau, M. Tsapatsis, "A Highly Oriented Thin Film of Zeolite A", Chem. Mat., 9, 1997, 1705.
- [59] G. Xomeritakis, A. Gouzinis, S. Nair, T. Okubo, M. He, R.M. Overney, M. Tsapatsis, "Growth, Microstructure, and Permeation Properties of Supported Zeolite (MFI) Films and Membranes Prepared by Secondary Growth", Chemical Engineering Science 54, 1999, 3521-3531.
- [60] A. Gouzinis, M. Tsapatsis, "On the Preferred Orientation and Microstructural Manipulation of Molecular Sieve Films Prepared by Secondary Growth", Chem. Mater., 10, 1998, 2497 - 2504.
- [61] G. Xomeritakis, S. Nair, M. Tsapatsis, "Transport Properties of Alumina-supported MFI Membranes made by Secondary (Seeded) Growth", Micropor. Mesopor. Mater. 38, 2000, 61-73.
- [62] E. Kim, J. Choi, M. Tsapatsis, "On Defects in Highly *a*-oriented MFI Membranes", Micropor. Mesopor. Mater. 170, 2013, 1 - 8.
- [63] Z. Lai, M. Tsapatsis, "Gas and Organic Vapor Permeation through *b*-Oriented MFI Membranes", Ind. Eng. Chem. Res. 43, 2004, 3000 - 3007.

- [64] G.T. P. Mabande, S. Ghosh, Z. Lai, W. Schwieger, M. Tsapatsis, "Preparation of *b*-Oriented MFI Films on Porous Stainless Steel Substrates", *Ind. Eng. Chem. Res.* 44, 2005, 9086 - 9095.
- [65] J. Choi, S. Ghosh, L. King, M. Tsapatsis, "MFI zeolite membranes from *a*- and randomly oriented Monolayers" *Adsorption* 12, 2006, 339 - 360.
- [66] Won Cheol Yoo, Jared A. Stoeger, Pyung-Soo Lee, Michael Tsapatsis, and Andreas Stein, "High-Performance Randomly Oriented Zeolite Membranes Using Brittle Seeds and Rapid Thermal Processing", *Angew. Chem. Int. Ed.* 49, 2010, 8699 - 8703.
- [67] T. Lee, J. Choi, M. Tsapatsis, "On the Performance of *c*-Oriented MFI Zeolite Membranes Treated by Rapid Thermal Processing", *Journal of Membrane Science* 436, 2013, 79 - 89.
- [68] T.C.T. Pham, T.H. Nguyen, K.B. Yoon, "Gel-Free Secondary Growth of Uniformly Oriented Silica MFI Zeolite Films and Application for Xylene Separation", *Angew. Chem. Int. Ed.* 52, 2013, 8693 - 8698.
- [69] T.C.T. Pham, H. S. Kim, K. B. Yoon, "Growth of Uniformly Oriented Silica MFI and BEA Zeolite Films on Substrates", *Science*, 334, 2011, 1533-1538.
- [70] S. Mintova, S. Mo, T. Bein, "Humidity Sensing with Ultrathin LTA-Type Molecular Sieve Films Grown on Piezoelectric Devices", *Chem. Mater.* 13, 2001, 901 - 905.
- [71] A. Jakob, V. Valtchev, M. Soudard, D. Faye, "Synthesis of Faujasite Films on Carbon Fibers and Characterization of Their Sorption Properties", *Ind. Eng. Chem. Res.* 49, 2010, 5616 - 5624.
- [72] N. Lauridant, T.J. Daou, G. Arnold, H. Nouali, J. Patarin, D. Faye, "Zeolite Hybrid Films for Space Decontamination", *Micropor. Mesopor. Mater.* 172, 2013, 36 - 43.
- [73] J.A. Stoeger, M. Palomino, K.V. Agrawal, X. Zhang, G.N. Karanikolos, S. Valencia, A. Corma, M. Tsapatsis, "Oriented CoSAPO-5 Membranes by Microwave-Enhanced Growth on TiO₂-Coated Porous Alumina", *Angew. Chem. Int. Ed.* 51, 2012, 2470 - 2473.
- [74] J.A. Stoeger, C.M. Veziri, M. Palomino, A. Corma, N.K. Kanellopoulos, M. Tsapatsis, G.N. Karanikolos, "On Stability and Performance of Highly *c*-Oriented

Columnar $\text{AlPO}_4\text{-5}$ and CoAPO-5 Membranes”, *Micropor. Mesopor. Mater.* 147, 2012, 286 - 294.

[75] G.N. Karanikolos, J.W. Wydra, J.A. Stoeger, H. Garcia, A. Corma, M. Tsapatsis, “Continuous *c*-Oriented $\text{AlPO}_4\text{-5}$ Films by Tertiary Growth”, *Chem. Mater.* 2007, 19, 792 - 797.

[76] R. Ranjan, M. Tsapatsis, “Microporous Metal Organic Framework Membrane on Porous Support Using the Seeded Growth Method”, *Chem. Mater.* 21, 2009, 4920 - 4924.

[77] X. Zou, F. Zhang, S. Thomas, G. Zhu, V. Valtchev, S. Mintova, “ $\text{Co}_3(\text{HCOO})_6$ Microporous Metal-Organic Framework Membrane for Separation of CO_2/CH_4 Mixtures”, *Chem. Eur. J.* 17, 2011, 12076 - 12083.

[78] H. Jeong, J. Krohn, K. Sujaoti, M. Tsapatsis, “Oriented Molecular Sieve Membranes by Heteroepitaxial Growth”, *J. Am. Chem. Soc.* 124, 2002, 12966 - 12968.

[79] Z. Lin, J. Rocha, A. Navajas, C. Tellez, J. Coronas, J. Santamaria, “Synthesis and Characterization of Titanosilicate ETS-10 Membranes”, *Micropor. Mesopor. Mater.* 67, 2004, 79 - 86.

[80] B. Yilmaz, K.G. Shattuck, J. Warzywoda, A. Sacco Jr., “Controlling Crystal Orientation in Microporous Titanosilicate ETS-4 Films by Secondary Growth Method”, *J. Mater. Sci.*, 41, 2006, 3135 - 3138.

[81] C.M. Braunbarth, L.C. Boudreau, M. Tsapatsis, “Synthesis of ETS-4/ TiO_2 Composite Membranes and their Pervaporation Performance”, *J. Membrane Sci.* 174, 2000, 31 - 42.

[82] B. Yilmaz, K.G. Shattuck, J. Warzywoda, A. Sacco, Jr., “Oriented Growth of ETS-4 Films Using the Method of Secondary Growth”, *Chem. Mater.* 18, 2006, 1107 - 1112.

[83] Z. Ji, J. Warzywoda, A. Sacco Jr., “Titanosilicate ETS-10 Thin Film Preparation on Fused Silica Optical Fibers”, *Micropor. Mesopor. Mater.* 101, 2007, 279 - 287.

[84] S. Galioğlu, M.N. Ismail, J. Warzywoda, A. Sacco Jr., B. Akata, “Preparation and Microstructural Characterization of Oriented Titanosilicate ETS-10 Thin Films on Indium Tin Oxide Surfaces”, *Micropor. Mesopor. Mater.*, 131, 2010, 401 - 406.

- [85] S. Feng, M. Greenblatt, "Preparation, Characterization, and Ionic Conductivity of Novel Crystalline, Microporous Germanates, $M_3HGe_7O_{16} \cdot xH_2O$, $M = NH_4^+, Li^+, K^+, Rb^+, Cs^+$; $x = 4 - 6.2$ ", Chem. Mater. 1992, 4, 462-468.
- [86] J.C. McKeen, M.E. Davis, "Conductivity of Mono- and Divalent- Cations in Microporous Zincosilicate VPI-9", J. Phys. Chem. C, 2009, 113, 9870-9877.
- [87] Evgenij Barsoukov, J. Ross Macdonald, "Impedance Spectroscopy: Theory, Experiment, and Applications", John Wiley & Sons, Inc., 2nd Edition, 2005.
- [88] WEB: "Introduction to Electrochemical Impedance Spectroscopy", <https://www.youtube.com/watch?v=FCHvYfxxmfc>, 23.03.2015.
- [89] WEB: "Basics of Electrochemical Impedance Spectroscopy", http://www.gamry.com/App_Notes/EIS_Primer/EIS_Primer.htm, 23.03.2015.
- [90] U. Simon, U. Flesch, "Cation-Cation Interaction in Dehydrated Zeolites X and Y Monitored by Modulus Spectroscopy", J. Porous Mater. 1999, 6, 33-40.
- [91] C. Rodriguez, M.T. Perez-Meldonado, J. de la Cruz, M.E. Fientes, Solid State Ionics 95, 231 (1997).
- [92] T. Wei, H.W. Hillhouse, "Ion Transport in the Microporous Titanosilicate ETS-10", J. Phys. Chem. B 2006, 110, 13728-13733.
- [93] W.J. Mortier, R.A. Schoonheydt, "Surface and Solid State Chemistry of Zeolites", Prog. Solid State Chem. 16 (1985) 1-125.
- [94] R.G. Buckley, J.L. Tallon, J.F. Clare, Solid State Ion. 28-30 (1988) 245.
- [95] M. Pamba, G. Maurin, S. Devautour, J. Vanderschueren, J. C. Giuntini, F. Di Renzo, F. Hamidi, "Influence of framework Si/Al ratio on the Na^+ /mordenite interaction Energy", Phys. Chem. Chem. Phys., 2000, 2, 2027-2031.
- [96] U. Simon, M.E. Franke, "Electrical Properties of Nanoscaled Host/Guest Compounds", Micro. Meso. Mater. 41 (2000) 1-36.
- [97] D. C. Freeman and D. N. Stamires, "Electrical Conductivity of Synthetic Crystalline Zeolites", Chem. Phys. 35 (1961), 799-806.
- [98] G. Kelemen, G. Schon, J. Mater. Sci. 27 (1992), p. 6036.
- [99] G. Kelemen, W. Lortz, G. Schon, J. Mater. Sci. 24 (1989) 333.
- [100] R.A Schoonheydt, Proc. 5th Int. Conf. on Zeolites, (Ed. L. V. C. Rees), Heyden, London, (1980), p. 242.

- [101] P. Nischwitz, P. Amels and F. Fetting, "Studies on the Ionic Conductivity of Zeolitic Solids", *Solid State Ionics* 73 (1994), p. 105.
- [102] F. J. Jansen and R. A. Schoonheydt, *J. Chem. Soc. Faraday Trans. I* 69 (1973), p. 1338.
- [103] B. J. H. Jackson and D. A. Young, *Trans. Faraday Soc.* 63 (1967), p. 2246.
- [104] E. Krogh Andersen, I. G. Krogh Andersen, J. Metcalf-Johansen, K. E. Simonsen and E. Skou, "The Ionic Conductivity of Alkalimetal-Zeolite X", *Solid State Ionics* 28-30 (1988), p. 249.
- [105] P. Pissis and D. Daoukaki-Diamanti, "Dielectric Studies of Molecular Mobility in Hydrated Zeolites", *J. Phys. Chem. Solids* 54 (1993), p. 701.
- [106] R. A. Schoonheydt and J. B. Uytterhoeven, "Electrical Conductivity Study on Synthetic Faujasites Type X And Y", *Clay Minerals* 8 (1969), p. 71.
- [107] F. Fetting, E. Galei and P. Kredel, *Ger. Chem. Eng.* 7 (1984), p. 32.
- [108] N. Petranovic and M. Susic, *J. Chem. Soc. Faraday I* 75 (1991), p. 2083.
- [109] J. Kjaer and E. Skou, "The Effect of Adsorbates on the Ionic Conductivity of Zeolites", *Solid State Ionics* 40/41 (1990), p. 121.
- [110] N. Cvjeticanin, S. Mentus and N. Petranovic, "Electric conductivity of Na and Ag forms of A and X zeolites. The effect of cluster formation on the conductivity", *Solid State Ionics* 47 (1991), 111-115.
- [111] G. Jones, "Dielectric Studies of Zeolite Systems", *J. Chem. Soc. Faraday I* 71, 1975, 2085-2096.
- [112] G. Sethia, R.S. Somani, H.C. Bajaj, "Sorption of Methane and Nitrogen on Cesium Exchanged Zeolite-X: Structure, Cation Position and Adsorption Relationship", *Ind. Eng. Chem. Res.*
- [113] WEB: "Sorption of CO, CH₄, and N₂ on Alkali and Alkaline Earth Metal Ion Exchanged Zeolite-X", Chapter 2, http://shodhganga.inflibnet.ac.in:8080/jspui/bitstream/10603/8402/8/08_chapter%202.pdf, 06.04.2015.
- [114] G. Sethia, R.S. Somani, H.C. Bajaj, "Adsorption of Carbon monoxide, Methane and Nitrogen on Alkaline Earth Metal Ion Exchanged Zeolite-X: Structure, Cation Position and Adsorption Relationship", *Electronic Supplementary Material (ESI) for RSC Advances*, 2015.

- [115] D. Vucelic , N. Juranic, “The Effect of Sorption on the Ionic Conductivity of Zeolites”, J. Inorg. Nucl. Chem., 1976, 38, 2091-2095.
- [116] G. Chabanis, A. Abdoulaye, J. C. Giuntini, J. V. Zanchetta, F. Di Renzo, J. Vanderschueren, “Dielectric properties of an NaX Zeolite as a Function of the Hydration State”, J. Chem. Soc., Faraday T rans., 1997, 93(22), 4085 - 4090.
- [117] A. Abdoulaye, G. Chabanis, J. C. Giuntini, J. Vanderschueren, J. V. Zanchetta, F. Di Renzo, “Dielectric Properties of a Faujasite Y as a Function of the Hydration State”, J. Phys. Chem. B 1997, 101, 1831-1836.
- [118] A. Abdoulaye, J.V. Zanchetta, F. Di Renzo, J.C. Giuntini, J. Vanderschueren, G. Chabanis, “Dielectric properties of Faujasites: Comparison between types X and Y during Dehydration”, Micropor. Mesopor. Mater. 34 (2000) 317 - 325.
- [119] J.C. McKeen, “Proton and Ion Conductivity in Microporous Materials”, PhD Thesis, California Institute of Technology Pasadena, CA, 2009.
- [120] M. Severance, Y. Zheng, E. Heck, P.K. Dutta, “Influence of Crystallite Size on Cation Conductivity in Faujasitic Zeolites”, J. Phys. Chem. A 2013, 117, 13704-13711.
- [121] X. Li, P.K. Dutta, “Interaction of Dimethylmethylphosphonate with Zeolite Y: Impedance-Based Sensor for Detecting Nerve Agent Simulants”, J. Phys. Chem. C, 2010, 114, 7986-7994.
- [122] J.Zhang, X. Li, J. White, P.K. Dutta, “Effects of Surface and Morphological Properties of Zeolite on Impedance Spectroscopy-Based Sensing Performance”, Sensors 2012, 12, 13284-13294.

CHAPTER 2

EXPERIMENTAL PROCEDURES

2.1 Synthesis of Titanosilicate ETS-10

All commercially obtained compounds were used as received: AgNO_3 , NaBH_4 , TiO_2 (P25, 76 wt. % anatase and 24 wt. % rutile, Degussa), NaSiO_2 were obtained from Sigma-Aldrich. NaCl (99.0 %), KCl (99.0 %), and H_2SO_4 (96.5 %) were received from J.T. Baker. Deionized water was distilled by water purification system (Milli-Q system). All glassware and Teflon coated magnetic stir bars were cleaned with acetone, followed by copious rinsing with distilled water before drying in an oven at 100 °C.

2.1.1 Synthesis of Submicrometer-Sized ETS-10 Crystals

ETS-10 crystals were synthesized by using the molar composition of 3.4 Na_2O : 1.5 K_2O : TiO_2 : 5.5 SiO_2 : 150 H_2O [1]. In this preparation, NaCl and KCl were dissolved in deionized water in a bottle. After dissolving these components, sodium silicate solution was added and hand-shaken for 5 min, forming the Si precursor solution. For preparation of the Ti precursor solution, H_2SO_4 was added to deionized water in another bottle. To this, P25 TiO_2 was added and hand-shaken for 5 min. After both precursor solutions were hand-mixed, the Ti precursor solution was poured into the Si precursor solution. The resulting mixture (white, viscous “gel”) was hand-shaken for 5 min. After measuring the pH (pH = 10.6 - 10.8) using a Hanna pH meter model HI 2211, the mixture was transferred into Teflon-lined stainless steel autoclaves. The static synthesis was carried out for 3 days at 503 K; the products were cooled to room temperature, centrifuged, washed with deionized water, and dried overnight in ambient air at ~343 K.

2.1.2 Analytical Procedures and Equipment

Morphological properties of the all ETS-10 samples were examined by field emission scanning electron microscope (FE-SEM, FEI Quanta 400). Phase identification of all samples was done by X-ray powder diffraction (XRD) using Rigaku-Ultima IV XRD. The diffraction peaks were scanned between 5-40° degrees with scan speed 1°/min. All analyses were done at Central Laboratory, METU.

2.2 Silver Encapsulation of Titanosilicate ETS-10 Crystals

2.2.1 Preparation of Ag⁺-ETS-10 and Ag⁰-ETS-10 Crystals

The silver-exchanged-ETS-10 samples (Ag⁺-ETS-10-*m*, where *m* is wt. % of Ag⁺ loading) were obtained by adding 400 mg of as-synthesized ETS-10 crystals to a 100 mL aqueous AgNO₃ solution of a given concentration. Three different Ag⁺ theoretical loadings (*i.e.* 5, 10, 15 wt. % Ag⁺) were introduced to host ETS-10 crystals. The solution was stirred vigorously for 24 h. After ion exchange, the samples were washed several times by centrifugation and dried at 323 K under ambient air. The modification of ETS-10 into silver nanoparticle containing ones was carried out by reducing Ag⁺-ETS-10-*m* in sodium borohydride (60 mM) suspension at room temperature. Then, the samples were collected by three times centrifugation and dried overnight at 373 K. These samples were denoted as Ag⁰-ETS-10-*m* (where *m* indicates *initial* theoretical wt. % of Ag⁺).

2.2.2 Analytical Procedures and Equipment

Morphological properties of the all ETS-10 samples were examined by field emission scanning electron microscope (FE-SEM, FEI Quanta 400). Specimens for transmission electron microscopy (TEM) and high resolution-transmission electron microscopy (HR-TEM) analyses were prepared through solution-drop method. A small amount of ETS-10 powder was added to methanol solution and sonicated for 5 min. A small droplet of solution was dropped onto a standard holey carbon coated

copper grid. TEM and HR-TEM investigations were performed using a JEOL JEM2100F field emission scanning/transmission electron microscope. Phase identification of all samples was done by X-ray powder diffraction (XRD) using Rigaku-Ultima IV XRD. The diffraction peaks were scanned between 5-40° degrees with scan speed 1°/min. Perkin Elmer Optima 4300DV ICP-OES was used for the elemental analysis. X-ray photoelectron spectroscopy (XPS) analysis was carried out on a PHI 5000 VersaProbe spectrometer with an Al-K α radiation source. The binding energies were referenced to the internal standard C 1s binding energy at 284.5 eV. Diffuse reflectance (DR) UV-vis spectra were recorded using a Shimadzu UV-2450 UV-VIS spectrophotometer. The collected DR-UV-vis spectra were transformed to absorption spectra by using Kubelka-Munk function $[(1-R)^2/2R]$, where the diffuse reflection of the sample (R). Renishaw type Raman microscope was utilized in the Raman spectroscopy analyses, where the excitation wavelength at 532 nm and a power of 0.5-1 mW were chosen for the acquisition. All analyses were done at Central Laboratory, METU.

2.3 Photochromism

2.3.1 Preparation of Ag⁺-ETS-10 Crystals and Ag⁰-ETS-10 Films

Ag⁺ ion-exchanged ETS-10 samples (denoted as Ag⁺-ETS-10) were obtained by adding 500 mg of as-synthesized ETS-10 crystals to a 100 mL aqueous AgNO₃ solution with a concentration of 5.15 mM (5.15 mM corresponding to a maximum theoretical loading of 10 wt. % Ag). The solution was stirred vigorously for 24 h at room temperature. In order to prevent auto-reduction of silver ions, the beaker was covered with parafilm and then with aluminum foil to prevent the solution from sunlight during stirring.

After ion exchange, the samples were washed several times with deionized water, collected by centrifugation and dried at 323 K under ambient air. After ion-exchange, drying temperature was chosen to be low (i.e., 323 K) to prevent auto-reduction of silver ions. The silver content of samples was determined by ICP-OES to be $8.18 \pm$

0.05 wt. %. The Si/Ti molar ratios were 4.57 and 4.40 for as-synthesized ETS-10 and Ag⁺-ETS-10, respectively, which were found to be in correlation with what was reported before [1,2]. Glass substrates used for film preparation (20 mm x 25 mm x 1 mm) were cleaned by successive ultrasonication in acetone, ethanol, and 2-propanol. Each sonication step was carried out for 15 min and followed by 20 min drying in ambient air at 353 K. White colored Ag⁺-ETS-10 films were produced through spin-coating on pre-cleaned glass using an acetone suspension containing 5 wt.% of Ag⁺-ETS-10 crystals. The acetone suspension was sonicated for 30 min before spin-coating to prevent agglomeration of Ag⁺-ETS-10 crystals. Spin-coating of the films with silver ion-exchanged ETS-10 was done in clean room environment under yellow light to prevent samples from UV light. The colors of the silver ion-exchanged samples (i.e., powder and films) were white, which indicates that there was no auto-reduction after treatments. Average film thicknesses were determined to be 1.25 μm from cross sectional FE-SEM analysis (Figure 2.1). Thermal reduction of Ag⁺ ions to Ag⁰ nanoparticles within the ETS-10 films was carried out through calcination at 473 K for 3h in ambient air (i.e., heating from 303 K to 473 K at 5 K/min, isothermal heating at 473 K for 3h, and convective cooling to 303 K). These films with Ag⁰ nanoparticles were denoted as I-Ag⁰-ETS-10.

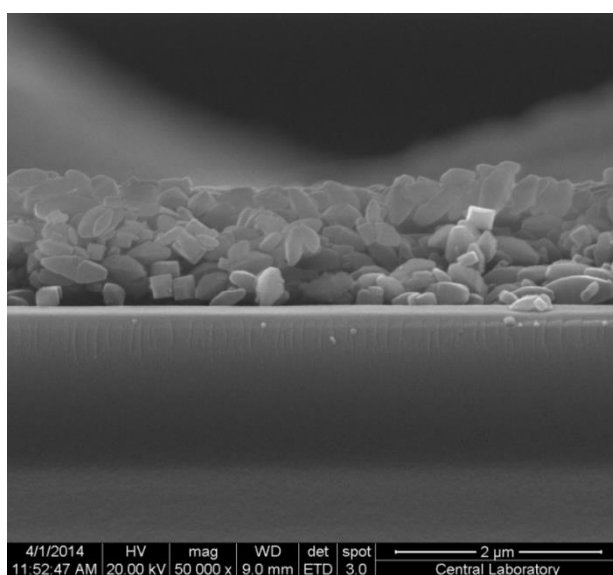


Figure 2.1. Cross-sectional FE-SEM image of films.

2.3.2 Analytical Procedures and Equipment

Morphological properties of the all ETS-10 films were examined by field emission scanning electron microscope (FE-SEM, FEI Quanta 400) SEM at an accelerating voltage of 30 kV. Phase identification of all samples was done by X-ray powder diffraction (XRD) using Rigaku-Ultima IV XRD by using thin-film attachment. The diffraction peaks were scanned between 5-50° with grazing angle of 0.3° with scan speed of 1°/min. Inductively coupled plasma optical emission spectrometry (ICP-OES - Perkin Elmer Optima 4300DV) was used for the elemental analysis. For the relative crystallinity measurements, peak height method was used by using the pure ETS-10 films as a reference. In the literature the peak heights of 2 θ degrees in between 24.65°-27.5° were used for the relative crystallinity measurements of pure ETS-10 crystals [3]. However, in our previous literature report [2] it was shown that when the powder XRD patterns of ETS-10 was compared with XRD pattern of Ag⁺-ETS-10 samples, systematic variations in the relative intensities at certain 2 θ values were observed. As silver loading increased, relative intensities of (200), (204), and (224) reflections increased for Ag⁺-ETS-10-(5, 10, 15 wt. %). Therefore, the relative crystallinity of the samples was calculated according to main Bragg peak, i.e. 2 θ is equal to 24.7°. X-ray photoelectron spectroscopy (XPS) analysis was carried out on a PHI 5000 VersaProbe spectrometer with an Al-K α radiation source. The binding energies were referenced to the internal standard C 1s binding energy at 284.5 eV. The sub-peaks under the high resolution silver and titanium spectra were identified by using PeakFit v4.12. The high resolution spectra of silver and titanium were fitted by Gaussian-Lorentzian functions after removal of the background by choosing two point linear background function. The fitting percentages were adjusted to be 98.99 % and 99.99 % for high resolution spectra of the titanium and silver, respectively. Specimens for high resolution-transmission electron microscopy (HR-TEM) analysis were prepared through solution-drop method. ETS-10 films were scratched through razor blade and a small amount of ETS-10 powder was added into ethanol solution and sonicated for 5 min. A small droplet of solution was dropped onto a standard holey carbon coated copper grid. HR-TEM investigations were performed using a JEOL JEM2100F field emission scanning/transmission electron microscope at an

accelerating voltage of 200 kV. The HR-TEM images (i.e., two different images of the same film) of I-Ag⁰-ETS-10 and 5h-II-Ag⁰-ETS-10 films were examined to estimate size of the silver nanoparticles by using PhotoRuler Manual Version 1.0.0. Around 80 particles were counted for each film from two different areas taken from the same sample. UV-vis spectra were recorded using a Varian Cary EL08083100 UV-Visible spectrophotometer. The analysis range was 290-800 nm, before analysis of the samples, baseline subtraction was performed. The computations employed in Density Functional Theory (DFT) study were done using plane-wave pseudopotential DFT with the generalized gradient approximation (GGA) and ultrasoft pseudopotentials. XCrysDen was used as a visualizer tool. Force threshold for geometric optimization calculations were 0.0025 eV/Å per atom. Kinetic energy cut off was 35 Ryd and charge density cutoff was 350 Ryd for plane-wave basis set. All analyses were done at Central Laboratory, METU.

2.3.3 Testing the Photochromic Activity of Ag⁰-ETS-10 Films

A laser was used to convert metallic silver nanoparticles to their oxidized state in ambient air by exciting the nanoparticles at 532 nm wavelength. These ETS-10 films that were exposed to laser light and oxidized are denoted as LT-ETS-10. The laser source used throughout the study was HIPPO Spectra Physics laser, which is a diode-pumped solid state (DPSS) Q-switched laser. A focused laser beam with beam diameter 80 µm was used to scan an area of 10 mm x 25 mm on the I-Ag⁰-ETS-10 film by moving the laser beam at a constant speed of 600 mm/sec. The parameters of the laser (i.e., output power, repetition rate) were tuned to change the incident power on the sample. Different laser powers were applied to determine the effect of power on the photochromic behavior of the films. Selected intensities which were used in the experiment were 90 W.mm⁻², 100 W.mm⁻², 116 W.mm⁻², and these films were denoted as 90-LT-ETS-10, 100-LT-ETS-10, 116-LT-ETS-10, respectively. In order to investigate the reversible behavior of ETS-10 films after visible laser treatment, thermal treatment was applied for the second time, where LT-ETS-10 samples were gradually calcined in a conventional oven at 473K. During the second thermal treatment, LT-ETS-10

films were kept at 473K for 3h and 5h to see if any changes during Ag^0 formation were going to take place. These samples were denoted as 3h-II- Ag^0 -ETS-10 and 5h-II- Ag^0 -ETS-10, respectively.

2.4 Preparation of ETS-10 Films by using Secondary Growth Method

2.4.1 Preparation of ETS-10 Films

The film preparation procedure consisted of two steps: seed layer formation followed by growth of these seed crystals. In the first step, ETS-10 seed crystals were deposited by spin coating at 5000 rpm for 30 seconds on the ITO glass purchased from Aldrich and α -alumina substrates purchased from CeraQuest, France using an ethanol suspension containing 5 and 7 wt. % of submicrometer-sized ETS-10 crystals. The ITO glass (Nanocs, purity 99%, resistivity 10 ohm/sq) (10 mm \times 25 mm) and α -alumina (10 mm \times 25 mm) substrates were cleaned by successive ultrasonication in acetone, ethanol, and 2-propanol, each sonication step carried out for 15 minutes, followed by 20-minute drying in ambient air at 353 K. Seed crystals were synthesized hydrothermally described in Section 2.1.1. The seeded substrates were heat-treated in ambient air (heating from 303 K to 673 K at 5 °K/min heating-rate, isothermal heating at 673 K for 9h, and convective cooling to RT). In the second step of ETS-10 film preparation, the seed crystals deposited on ITO glass and α -alumina substrates were grown by using the molar composition of 3.4 Na_2O : 1.5 K_2O : TiO_2 : 5.5 SiO_2 : 180 H_2O [1]. In this preparation, NaOH and KF were dissolved in deionized water in a bottle. After dissolving these components, sodium silicate solution was added and hand-shaken for 5 min, forming the Si precursor solution. For preparation of the Ti precursor solution, H_2SO_4 was added to deionized water in another bottle. To this, titanium (III) sulfate $\text{Ti}_2(\text{SO}_4)_3$ (Aldrich) was added and hand-shaken for 5 min. After both precursor solutions were hand-mixed, the Ti precursor solution was poured into the Si precursor solution. The resulting mixture (white, viscous “gel”) was hand-shaken for 5 min. pH of the gel was measured to be pH = 10.6 - 10.8 using a Hanna pH meter model HI 2211. The ITO glass and α -alumina

substrates with seed layers facing downwards were diagonally placed in the Teflon-lined 10 mL stainless steel autoclaves. The substrates were completely submerged in the growth mixture. After 2h to 24h static hydrothermal treatment at 503 K, the contents of the autoclaves were cooled to room temperature in cold water. Some phase separation/settling in the growth mixture was observed after hydrothermal treatment; however, the white structured fluid still covered the substrates. The ETS-10 films supported on the ITO glass and α -alumina substrates were removed from the growth mixture, thoroughly rinsed with 1L deionized water, immediately air-dried using an air gun, and left overnight to dry at room temperature in ambient air. The samples were denoted as shown in Table 2.1.

Table 2.1. ETS-10 films prepared on ITO glass and α -alumina substrates by using secondary growth method.

Sample Code	Concentration of Seed Suspension (wt. %)	# of Spin Coating Step	Reaction Time (hours)	Type of Substrates
5-1S-ITO	5 wt. % of 500 nm-sized-ETS-10 in ethanol suspension	Single	-	ITO glass
7-1S-ITO	7 wt. % of 500 nm-sized-ETS-10 in ethanol suspension	Single	-	ITO glass
7-1S-2h-ITO	7 wt. % of 500 nm-sized-ETS-10 in ethanol suspension	Single	2h	ITO glass
7-1S-4h-ITO	7 wt. % of 500 nm-sized-ETS-10 in ethanol suspension	Single	4h	ITO glass
7-1S-6h-ITO	7 wt. % of 500 nm-sized-ETS-10 in ethanol suspension	Single	6h	ITO glass
7-1S-8h-ITO	7 wt. % of 500 nm-sized-ETS-10 in ethanol suspension	Single	8h	ITO glass
7-1S-10h-ITO	7 wt. % of 500 nm-sized-ETS-10 in ethanol suspension	Single	10h	ITO glass
7-2S-ITO	7 wt. % of 500 nm-sized-ETS-10 in ethanol suspension	Double	-	ITO glass
7-2S-2h-ITO	7 wt. % of 500 nm-sized-ETS-10 in ethanol suspension	Double	2h	ITO glass
7-2S-4h-ITO	7 wt. % of 500 nm-sized-ETS-10 in ethanol suspension	Double	4h	ITO glass
7-2S-6h-ITO	7 wt. % of 500 nm-sized-ETS-10 in ethanol suspension	Double	6h	ITO glass
7-2S-8h-ITO	7 wt. % of 500 nm-sized-ETS-10 in ethanol suspension	Double	8h	ITO glass
7-2S-10h-ITO	7 wt. % of 500 nm-sized-ETS-10 in ethanol suspension	Double	10h	ITO glass
7-2S- α -alumina	7 wt. % of 500 nm-sized-ETS-10 in ethanol suspension	Double	-	α -alumina
7-2S-4h- α -alumina	7 wt. % of 500 nm-sized-ETS-10 in ethanol suspension	Double	4h	α -alumina
7-2S-6h- α -alumina	7 wt. % of 500 nm-sized-ETS-10 in ethanol suspension	Double	6h	α -alumina
7-2S-8h- α -alumina	7 wt. % of 500 nm-sized-ETS-10 in ethanol suspension	Double	8h	α -alumina
7-2S-10h- α -alumina	7 wt. % of 500 nm-sized-ETS-10 in ethanol suspension	Double	10h	α -alumina

2.4.2 Analytical Procedures and Equipment

Morphological properties of the all ETS-10 samples were examined by field emission scanning electron microscope (FE-SEM, FEI Quanta 400). Phase identification of all samples was done by X-ray powder diffraction (XRD) using Rigaku-Ultima IV XRD. The diffraction peaks were scanned between 5-40° degrees with scan speed 1°/min. All analyses were done at Central Laboratory, METU.

2.5 Ionic Conductivity of Zeolites and Zeo-type Materials

2.5.1 Preparation of Titanosilicate ETS-10 Films

The film preparation procedure was described in Section 2.4.1. The hydrothermal reaction at 503 K was conducted for 4 h, 6 h, 8 h, and 10 h in static conditions to achieve ETS-10 films of different thicknesses. The ETS-10 films were removed from the growth mixture, thoroughly rinsed with 1 L deionized water, immediately air-dried using an air gun, and left overnight to dry at room temperature in ambient air.

2.5.2 Preparation of Zeolite Y (FAU) Films

The zeolite Y film preparation procedure consisted of two steps: seed layer formation followed by growth of these seed crystals. In the first step, zeolite Y crystals were deposited by spin coating at 5000 rpm for 30 seconds on α -alumina substrates purchased from France using an ethanol suspension containing 7 wt. % of 100nm-sized zeolite Y crystals. The α -alumina (10 mm \times 25 mm) substrates were cleaned by successive ultrasonication in acetone, ethanol, and 2-propanol, each sonication step carried out for 15 minutes, followed by 20-minute drying in ambient air at 353 K. Seed crystals were synthesized hydrothermally by using the molar composition of $\text{Al}(\text{iPro})_3:2.2\text{TEOS}:2.5\text{TMAOH}:0.19\text{NaOH}:188\text{H}_2\text{O}$. In this preparation, tetramethylammonium hydroxide (25 wt. % TMAOH, Aldrich) and aluminum isopropoxide (98+ %, Aldrich) were dissolved in ultra pure deionized water and stirred for 2h at room temperature. After dissolving these components,

tetraethylortosilicate (99+ % TEOS, Acros) and sodium hydroxide (97 % NaOH, J.T. Baker) were added and viscous gel stirred for 22h at room temperature. The mixture was transferred into 60 mL high density polyethylene (HDPE) bottle. The static synthesis was carried out for 1 day at 373 K; the products were cooled to room temperature, centrifuged, washed with deionized water, and dried overnight in ambient air at ~343 K.

The seeded substrates were heat-treated in ambient air (heating from 303 K to 673 K at 5 °K/min, isothermal heating at 673 K for 9h, and convective cooling to 303 K). In the second step of zeolite Y film preparation, the seed crystals deposited α -alumina substrates were grown by using molar composition of $\text{NaAlO}_2:9.9\text{Na}_2\text{SiO}_3:16.7\text{NaOH}:811\text{H}_2\text{O}$. In this preparation, sodium silicate Na_2SiO_3 (26.5 % SiO_2 , 10.6 % Na_2O , 62.9 % H_2O , Aldrich) was dissolved in ultra pure deionized water and stirred for 1h at room temperature to prepare Si precursor solution. In an another bottle, sodium aluminate NaAlO_2 (50-56 % Al_2O_3 , 40-45 % Na_2O , Fisher Scientific) was dissolved in ultra pure deionized water and stirred for 1h at room temperature to prepare Al precursor solution. Al precursor solution was added to Si precursor solution and stirred for 1h at room temperature. Then, sodium hydroxide NaOH (97 %, Merck) was dissolved in ultra pure deionized water and added to final solution. The resulting viscous gel was stirred for 18h at room temperature to form secondary growth mixture. The α -alumina substrates with seed layers facing downwards were diagonally placed in the conic centrifugation tubes. The substrates were completely submerged in the growth mixture. After 12h static hydrothermal treatment at 373 K, the contents of the centrifugation tube were cooled to room temperature in cold water. Some phase separation/settling in the growth mixture was observed after hydrothermal treatment; however, the white structured fluid still covered the substrates. The zeolite Y films supported on the α -alumina substrates were removed from the growth mixture, thoroughly rinsed with 1L deionized water, immediately air-dried using an air gun, and left overnight to dry at room temperature in ambient air.

2.5.3 Ion-Exchange of Titanosilicate ETS-10 Films

The commercially purchased compounds (i.e., calcium chloride dihydrate, lithium chloride, zinc sulfate hepta hydrtae) used in ion-exchange were received from Merck. Ion-exchange of ETS-10 thin films supported on α -alumina substrates was carried out using homemade Teflon apparatus to place ETS-10 films in solution. ETS-10 films formed on α -alumina substrates were immersed in 1mM $\text{CaCl}_2 \cdot 2\text{H}_2\text{O}$, 1mM, $\text{ZnSO}_4 \cdot 7\text{H}_2\text{O}$ mM and 57.8 μM LiCl aqueous salt solution and stirred vigorously for 4h at room temperature. After ion exchange, ETS-10 films were washed by 1L ultra-pure deionized water (resistivity of 18.18 $\text{M}\Omega\cdot\text{cm}$) and dried at 323 K under ambient air. The Ca^{2+} , Zn^{2+} , and Li^+ -ion-exchanged ETS-10 thin films were denoted as in Table 2.2.

Table 2.2. ETS-10 and M-ETS-10 (where, M= Li⁺, Zn²⁺, and Ca²⁺) films prepared on α -alumina substrates by using secondary growth method.

Sample Code	Concentration of Seed Suspension	# of Spin Coating Step	Reaction Time (hours)	Type of Substrates	Concentration of Ion-Exchange Solution	Ion-Exchange Time (hours)
(Na,K)-4h-ETS-10	7 wt. % of 500 nm-sized-ETS-10 in ethanol suspension	Double	4h	α -alumina	-	-
(Na,K)-6h-ETS-10	7 wt. % of 500 nm-sized-ETS-10 in ethanol suspension	Double	6h	α -alumina	-	-
(Na,K)-8h-ETS-10	7 wt. % of 500 nm-sized-ETS-10 in ethanol suspension	Double	8h	α -alumina	-	-
(Na,K)-10h-ETS-10	7 wt. % of 500 nm-sized-ETS-10 in ethanol suspension	Double	10h	α -alumina	-	-
Li-6h-ETS-10	7 wt. % of 500 nm-sized-ETS-10 in ethanol suspension	Double	6h	α -alumina	57.8 μ M LiCl	4h
Zn-6h-ETS-10	7 wt. % of 500 nm-sized-ETS-10 in ethanol suspension	Double	6h	α -alumina	1mM ZnSO ₄ .7H ₂ O	4h
Ca-6h-ETS-10	7 wt. % of 500 nm-sized-ETS-10 in ethanol suspension	Double	6h	α -alumina	1mM CaCl ₂ .2H ₂ O	4h
Na-Y	7 wt. % of 100 nm-sized-zeolite Y in ethanol suspension	Double	12h	α -alumina	-	-

2.5.4 Analytical Procedures and Equipment

The morphological, compositional and cross-sectional analyses of the all ETS-10 films were examined by field emission scanning electron microscope (FE-SEM, FEI Quanta 400), SEM modulated by energy dispersive X-ray spectroscopy (SEM/EDX). Phase identification of all samples was done by X-ray powder diffraction (XRD) using Rigaku-Ultima IV XRD. The diffraction peaks were scanned between 5° and 40° with scan speed of $1^\circ/\text{min}$. Si/Ti ratio, Na and K concentrations of (Na,K)-6h-ETS-10, Li-6h-ETS-10, Zn-6h-ETS-10 and Ca-6h-ETS-10 films were determined via electron microprobe (EPMA) analysis using the wavelength-dispersive Cameca SX50 electron microprobe. Operating parameters were: 20 kV accelerating voltage, a 25 nA current and a 5 micron spot size. All analyses were done at Central Laboratory, METU.

2.5.5 Design of Conductivity System

The conductivity measurements were carried out by using impedance spectroscopy at Central Laboratory, METU (Figure 2.2).

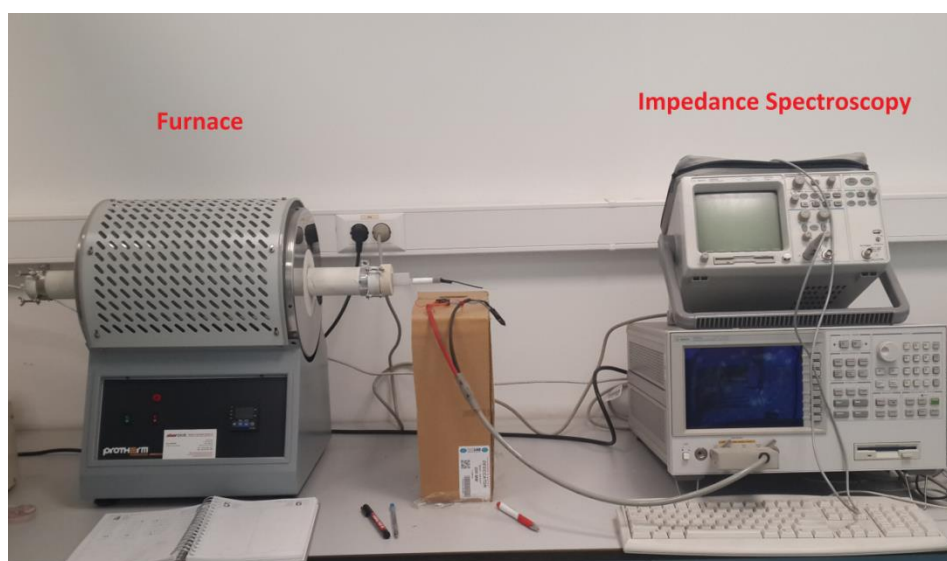


Figure 2.2. Photograph of conductivity system at Central Laboratory, METU.

40 nm gold (99.99 %) electrode contacts were masked on the ETS-10 films prepared via secondary growth method by using Polaron Sputter Coater through homemade silicon-mask with a 1 mm separation. The platinum rod (99.90 %) of 0.3 mm in diameter were attached to gold electrodes using silver paste purchased from DuPont and dried at room temperature for 15 h to dry silver paste properly. One end of the open ended quartz tube (\varnothing : 1 cm, ℓ : 37 cm) was cut to fit ETS-10 films on α -alumina substrate (1 cm \times 2.5 cm). Then, the film was attached to the carved end (\sim 2.5 cm) of the quartz tube. To prevent short circuit, one part of the platinum rod (\sim 50 cm) attached to gold electrode on film was placed in the inner surface of the quartz tube (\varnothing : 2 cm, ℓ : 40 cm) and the other platinum rod (\sim 50 cm) was placed to outside of the quartz tube. The thin film attached to quartz tube (\varnothing : 1 cm, ℓ : 37 cm) was inserted to another open ended quartz tube (\varnothing : 2 cm, ℓ : 40 cm) was cut to fit porous opening of oven (\varnothing : 2.3 cm, ℓ : 60 cm) (Figure 2.3). The whole quartz-tube-setup was arranged and marked to place ETS-10 film in hot zone of the oven in each measurement. One end of the oven was plugged through porous stopper of the oven and the other end of the oven held open to make connection of impedance spectroscopy by platinum rod. An Agilent 4294A Precision Impedance analyzer (40 Hz - 110 MHz) connected to the thin film through platinum wires (\sim 50 cm) was used to measure the impedance of the thin films in between 40 Hz to 1MHz, in combination with the software of the impedance spectroscopy.

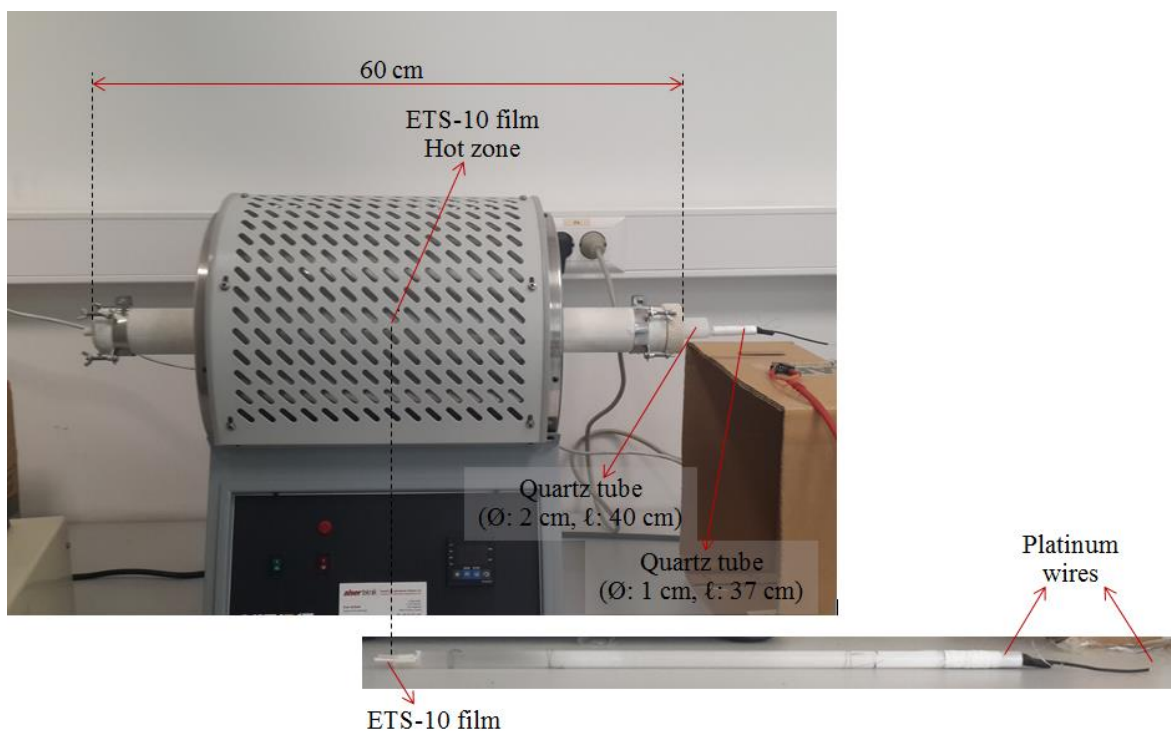


Figure 2.3. Photograph of furnace and tubular quartz system at Central Laboratory, METU.

A typical equivalent circuit model of the parallel combination of a resistor and capacitor for ion transport of the material was chosen from the software of the impedance spectroscopy. Prior to characterization, all samples were heated to 250 °C for at least 12 h to ensure proper dehydration. Measurements were then made in both increasing and decreasing temperature increments with 50 °C at least for three times to observe stability and consistency of the thin films during the measurements. Two sets (i.e., one set contains hydrothermal reaction times: 4 h, 6 h, 8 h, and 10 h) were prepared through identical secondary growth mixtures (i.e., pH of the secondary growth mixtures: 10.56, 10.54) to produce statistics of data collected.

REFERENCES

- [1] L. Lv, F. Su, X.S. Zaho, “A Reinforced Study on the Synthesis of Microporous Titanosilicate ETS-10”, *Micropor. Mesopor. Mater.* 76, 2004, 113-122.
- [2] S. Galioğlu, M. Zahmakıran, Y.E. Kalay, S. Özkar, B. Akata, “Effect of Silver Encapsulation on the Local Structure of Titanosilicate ETS-10”, *Micropor. Mesopor. Mater.* 159 (2012) 1-8.
- [3] T.K. Das, A.J. Chandwadkar, S. Sivasanker, “Preparation, Characterization and Catalytic Properties of the Microporous Titanosilicate, ETS-10”, *Bull. Mater. Sci.* 17, 1994, 1143-1153.

CHAPTER 3

SYNTHESIS OF TITANOSILICATE ETS-10

3.1 Synthesis of Submicrometer-Sized ETS-10 Crystals

Engelhard titanosilicate (ETS-10) is a synthetic microporous (pore dimensions; 4.9 Å and 7.6 Å) crystalline material with a framework built of corner-sharing TiO_6 octahedra and SiO_4 tetrahedra linked through bridging oxygen atoms as shown in Figure 3.1 (Adapted from [1]) [2, 3]. The pore system contains 12-membered rings and displays a considerable degree of disorder due to different stacking sequences, which causes broadening of the ETS-10 pores up to 2 nm [3,4]. These building units are uniquely arranged to form -Ti-O-Ti-O-Ti- chains that run in the crystal *a* and *b* directions as shown in Figure 3.1. These chains are effectively separated from each other by the silica matrix [3], and regarded as a 1-D quantum-confined form of titania with band gap energy, which was shown to be related to the length of the crystals along [110] direction [5]. Each TiO_6 unit incorporates two negative charges, which are compensated by extra framework charge-balancing cations Na^+ and K^+ in the as-synthesized materials as indicated by the ETS-10 stoichiometry $(\text{Na,K})_2\text{TiSi}_5\text{O}_{13}$ [2].

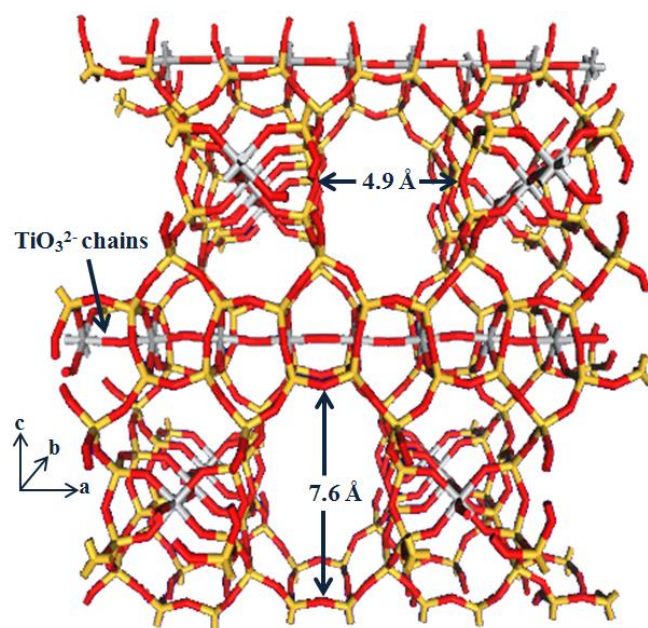


Figure 3.1. Framework connectivity of ETS-10.

In the current thesis, ETS-10 crystals were synthesized by using the molar composition of 3.4 Na₂O: 1.5 K₂O: TiO₂: 5.5 SiO₂: 150 H₂O [6]. In this preparation, NaCl and KCl were dissolved in deionized water in a bottle. After dissolving these components, sodium silicate solution was added and hand-shaken for 5 min, forming the Si precursor solution. For preparation of the Ti precursor solution, H₂SO₄ was added to deionized water in another bottle. To this, P25 TiO₂ was added and hand-shaken for 5 min. After both precursor solutions were hand-mixed, the Ti precursor solution was poured into the Si precursor solution. The resulting mixture (white, viscous “gel”) was hand-shaken for 5 min. The static synthesis was carried out for 3 days at 503 K; the products were cooled to room temperature, centrifuged, washed with deionized water, and dried overnight in ambient air at ~343 K.

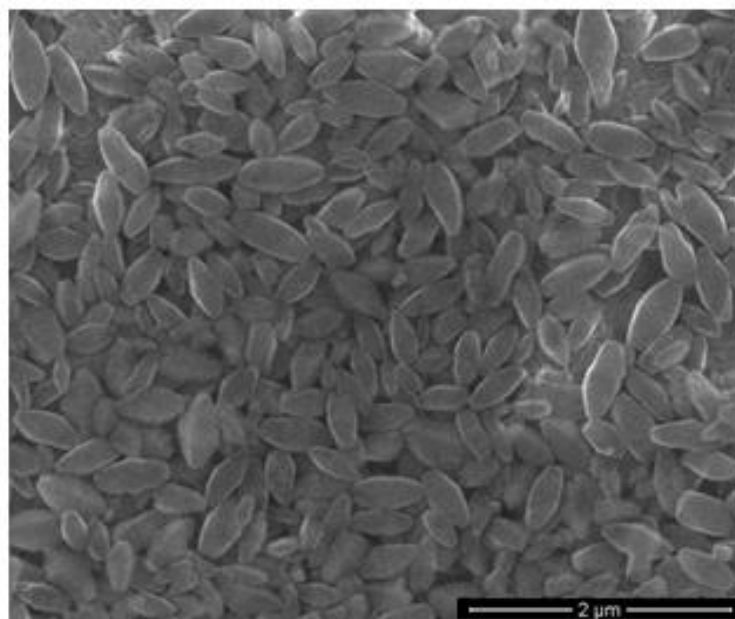


Figure 3.2. FE-SEM image of submicrometer-sized ETS-10 crystals.

It is well known that the use of different titanium sources leads to the formation of ETS-10 crystals with different physical and chemical properties, phase purity, particle morphology, and particle size [7]. The titanosilicate ETS-10 used in this study was prepared starting with the Degussa TiO_2 (P25) as titanium source. The morphological investigation of the as-synthesized titanosilicate ETS-10 crystals was done by FE-SEM. FE-SEM images of ETS-10 (*vide infra*) clearly indicate that the ETS-10 samples synthesized by using P25 are in their typical bipyramidal morphology with an average particle size of less than $0.5\ \mu\text{m}$ (Figure 3.2). The crystalline structure of ETS-10 is in agreement with previous reports explaining this kind of morphological feature typical for ETS-10 growing via a two-dimensional nucleation mechanism [6-8]. As explained in the Section 1.2.2, Ti atoms in P25 are six-coordinated and they act as a structure-directing agent which leads to a rapid nucleation. As a result, a large number of small crystallites with excellent bipyramid morphology as shown in (Figure 3.2) were obtained since ETS-10 microcrystallites were quickly formed in the silica-titania gels via a direct structure reconstruction [6].

3.2 Structural Characterization of Titanosilicate ETS-10 Crystals

The comparison of powder-XRD pattern (*vide infra*) of our ETS-10 samples with that reported in literature [3,7] shows that the samples contain only the pure ETS-10 phase (Figure 3.3). In contrast to the previous results obtained by using TiCl_3 , TiF_4 and $\text{Ti}(\text{NH}_4)_2\text{F}_6$ as Ti sources in the preparation of titanosilicates [6, 9], neither ETS-4 nor quartz phase was found in our ETS-10 samples.

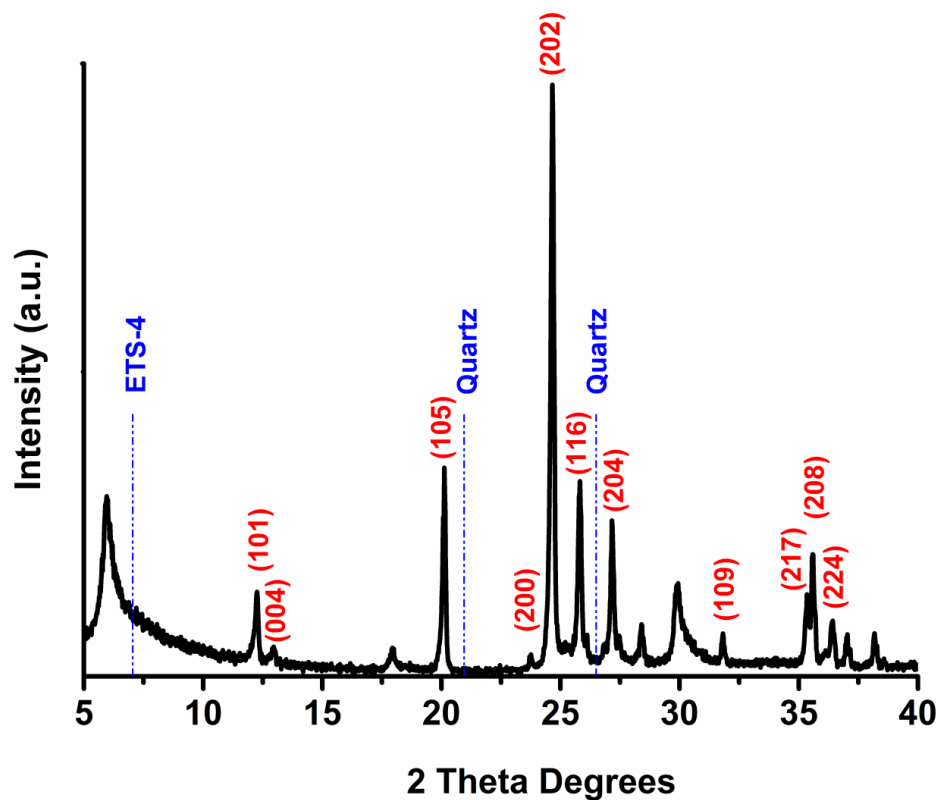


Figure 3.3. XRD pattern of submicrometer-sized ETS-10 crystals.

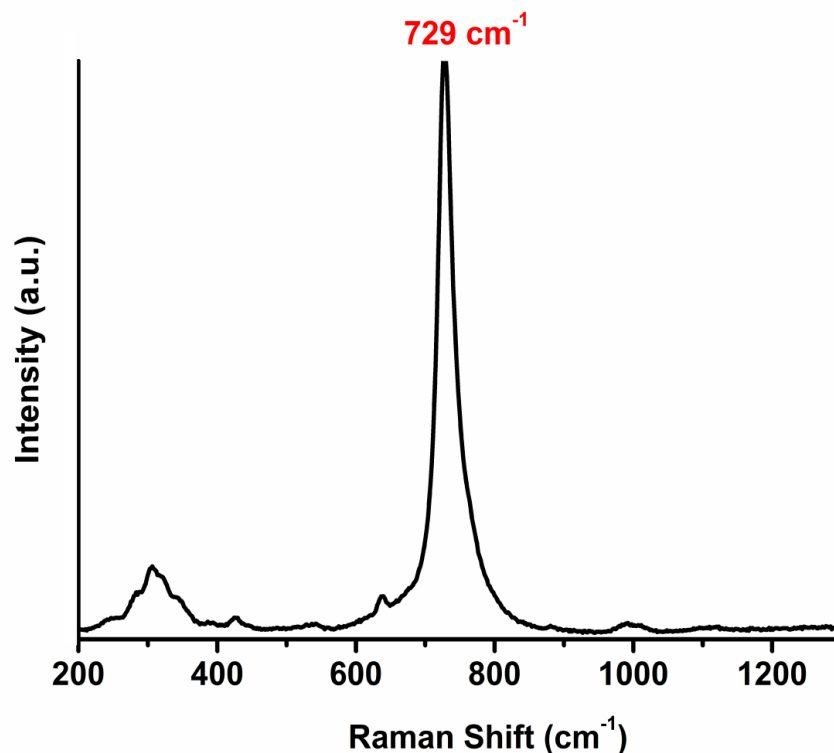


Figure 3.4. Raman spectra of submicrometer-sized ETS-10 crystals.

Raman spectrum of the ETS-10 in Figure 3.4 shows Raman scattering band at 729 cm^{-1} with a bandwidth of 35 cm^{-1} for the Ti-O-Ti stretching of the TiO_3^{2-} quantum wires [10,11]. It is well known that both the position and the width of this band depend on the average -Ti-O-Ti-O-Ti- chain length and concentration of defects. For example, in the Raman spectrum for an ETS-10 sample the Raman scattering band at 724 cm^{-1} with a bandwidth of 24 cm^{-1} has been assigned to titanate quantum wires of $> 50\text{ nm}$ length with very few defects [5], whereas a broader band has been observed at 775 cm^{-1} for a highly defective ETS-10 sample [12]. Similar shifts towards higher frequencies have already been reported in a more defective ETS-10 [4,10,12].

3.3 Conclusions

As a result, FE-SEM images of ETS-10 clearly showed that the ETS-10 samples synthesized by using P25 are in their typical bipyramidal morphology with an average particle size of less than 0.5 μm . The XRD results showed that the samples possess only the pure ETS-10 phase without ETS-4 and/or quartz impurity. Raman spectrum showed typical Raman scattering band at 729 cm^{-1} with a bandwidth of 35 cm^{-1} for the Ti-O-Ti stretching of the TiO_3^{2-} quantum wires. The bandwidth of the obtained samples suggest that the synthesized ETS-10 samples contain mostly unbroken TiO_3^{2-} quantum wires. The synthesized submicrometer-sized ETS-10 crystals were used in silver incorporation to figure out effect of silver encapsulation on the local structure of titanosilicate ETS-10 in Chapter 4. It was used in photochromic application as matrix in Chapter 5. It was also used in film production (i.e., secondary growth method) as seed crystals Chapter 6.

REFERENCES

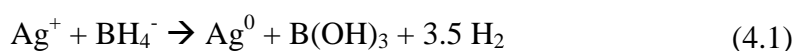
- [1] B. Akata, B. Yilmaz, A. Sacco Jr., J. Porous Mater. 15 (2008) 351.
- [2] S.M. Kuznicki, U.S. Patent 5, 011, 591, (1991).
- [3] M.W. Anderson, O. Terasaki, T. Ohsuna, A. Philippou, S.P. MacKay, A. Ferreira, J. Rocha, S. Lidin, "Structure of the Microporous Titanosilicate ETS-10", Nature, 367, 1994, 347 - 351.
- [4] P.D. Southon, R.F. Howe, "Spectroscopic Studies of Disorder in the Microporous Titanosilicate ETS-10", Chem. Mater. 14, 2002, 4209 - 4218.
- [5] N.C. Jeong, M.H. Lee, K.B. Yoon, "Length-Dependent Band-Gap Shift of TiO_3^{2-} Molecular Wires Embedded in Zeolite ETS-10", Angew. Chem. Int. Ed. 2007, 46, 5868 - 5872.
- [6] L. Lv, F. Su, X.S. Zhao, "A Reinforced Study on the Synthesis of Microporous Titanosilicate ETS-10", Micropor. Mesopor. Mater. 76, 2004, 113 - 122.
- [7] R. Xu, W. Pang, J. Yu, Q. Huo, J. Chen, Chemistry of Zeolites and Related Porous Materials, Wiley, Singapore, 2007.
- [8] S. Galioğlu, M.N. Ismail, J. Warzywoda, A. Sacco Jr., B. Akata, Micropor. Mesopor. Mater. 131 (2010) 401.
- [9] L.L.F. Su, X.S. Zhao, J. Porous Mater. 13 (2006) 263.
- [10] C.C. Pavel, B. Zibrowius, E. Löffler, W. Schmidt, Phys. Chem. Chem. Phys. 9 (2007) 3440.
- [11] Y. Su, M.L. Balmer, J. Phys. Chem. B 104 (2000) 8160.
- [12] L. Lv, J.K. Zhou, F. Su, X.S. Zhao, J. Phys. Chem. C 111 (2007) 773.

CHAPTER 4

EFFECT OF SILVER ENCAPSULATION ON THE LOCAL STRUCTURE OF TITANOSILICATE ETS-10

The ETS-10 samples synthesized by using P25 (Size = $\sim 0.5 \mu\text{m}$) are used to figure out effect of Ag^+ and Ag^0 incorporation on the local 1D TiO_3^{2-} quantum wires. The incorporation of Ag^+ ions into ETS-10 and the reduction of Ag^+ ions forming Ag^0 nanoparticles stabilized by ETS-10 matrix were carried out by using experimental procedure described in Section 2.2.

In order to make silver nanoparticle incorporated ETS-10, Ag^+ -ETS-10-*m* samples were reduced in sodium borohydride (NaBH_4) suspension at room temperature. The reaction for the preparation of nanoscale silver particles by reduction of Ag^+ with NaBH_4 can be written as:



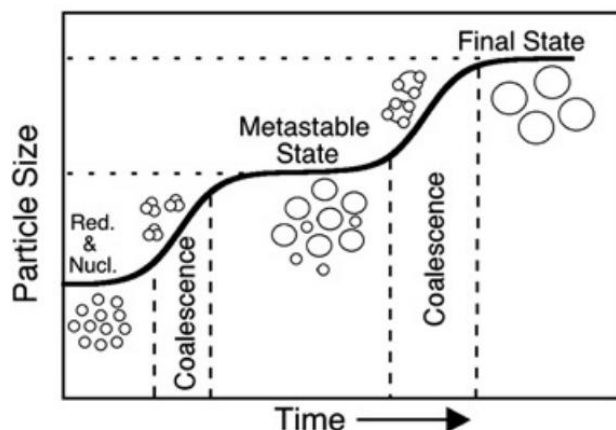


Figure 4.1. Illustration of the growth mechanism for Ag^0 NPs synthesized using NaBH_4 as proposed by Polte et al [1].

“The first step involves reduction (< 200 ms) of Ag^+ into Ag^0 atoms. These atoms form dimers, trimers, etc. clusters. In a second stage (≈ 5 s) the clusters coalesce to generate small particles with a radius of 2-3 nm. This step is followed by a metastable state, where the particles maintain a constant size for around 5-10 min. After this period, a second and last coalescence phase take place (within 30-60 s) to render the final Ag^0 NPs with an average size of 5-8 nm (Figure 4.1)” [1].

4.1 Inductively Coupled Plasma/Optical Emission Spectrometry (ICP-OES)

The ICP-OES-determined Na, K, Ag values (wt. %) in as-synthesized, Ag^+ -ETS-10 and Ag^0 -ETS-10 samples were given in Table 4.1. Furthermore, $(\text{Na}+\text{K}+\text{Ag})/\text{Ti}$ and Si/Ti ratios were given for as-synthesized, Ag^+ -ETS-10 and Ag^0 -ETS-10, respectively. According to Table 4.1, it can be seen that the Na weight percent for reduced samples (Ag^0 -ETS-10) is higher than the ion-exchanged samples (Ag^+ -ETS-10), suggesting the replacement of Na^+ ions to balance the negative charges that were balanced by Ag^+ in Ag^+ -ETS-10 [2].

Table 4.1. The ICP-OES-determined Na, K, Ag values (wt. %) and (Na+K+Ag)/Ti ratios in as-synthesized, Ag⁺-ETS-10 and Ag⁰-ETS-10 samples.

Sample	Na (wt. %)	K (wt. %)	Ag (wt. %)	(Na+K+Ag)/Ti (mole)
ETS-10	5.91 ± 0.03	3.77 ± 0.04	-	1.65
5-Ag ⁺ -ETS-10	4.61 ± 0.08	3.14 ± 0.04	5.00 ± 0.05	1.63
10-Ag ⁺ -ETS-10	3.51 ± 0.04	2.83 ± 0.04	9.64 ± 0.09	1.65
15-Ag ⁺ -ETS-10	2.78 ± 0.06	2.52 ± 0.04	14.89 ± 0.15	1.80
5-Ag ⁰ -ETS-10	5.94 ± 0.12	2.26 ± 0.04	4.28 ± 0.04	1.72
10-Ag ⁰ -ETS-10	5.54 ± 0.12	2.03 ± 0.06	8.01 ± 0.08	1.94
15-Ag ⁰ -ETS-10	5.26 ± 0.32	1.89 ± 0.10	12.4 ± 0.13	2.20

It can also be seen that the silver ions in Ag⁺-ETS-10 were in correlation with the calculated amounts, suggesting an increase in the silver amount with increasing silver loading. Furthermore, the (Na+K+Ag)/Ti and Si/Ti molar ratios for the as-synthesized ETS-10 were in correlation with what was reported before [3,4]. The (Na+K+Ag)/Ti and Si/Ti molar ratios of Ag⁺ and Ag⁰-ETS-10 samples were similar to the as-synthesized ETS-10 in the limits of experimental error except for the Ag⁰-ETS-10-(15 wt. %) sample. For this sample, (Na+K+Ag)/Ti molar ratio (2.20) was higher and Si/Ti molar ratio (3.44) was rather lower than what was found for the as-synthesized ETS-10, which suggests the distortion of local structure of ETS-10 upon ion-exchange and reduction processes at the highest silver loading of 15 wt. %.

4.2 X-Ray Diffraction (XRD)

The as synthesized ETS-10 crystals were used as host material for the guest metal nanoparticles. The XRD patterns of as-synthesized ETS-10, 5, 10 and 15 wt. % Ag⁺ ion-exchanged and 5, 10 and 15 wt. % Ag⁰ nanoparticle incorporated ETS-10 samples are shown in Figure 4.2.

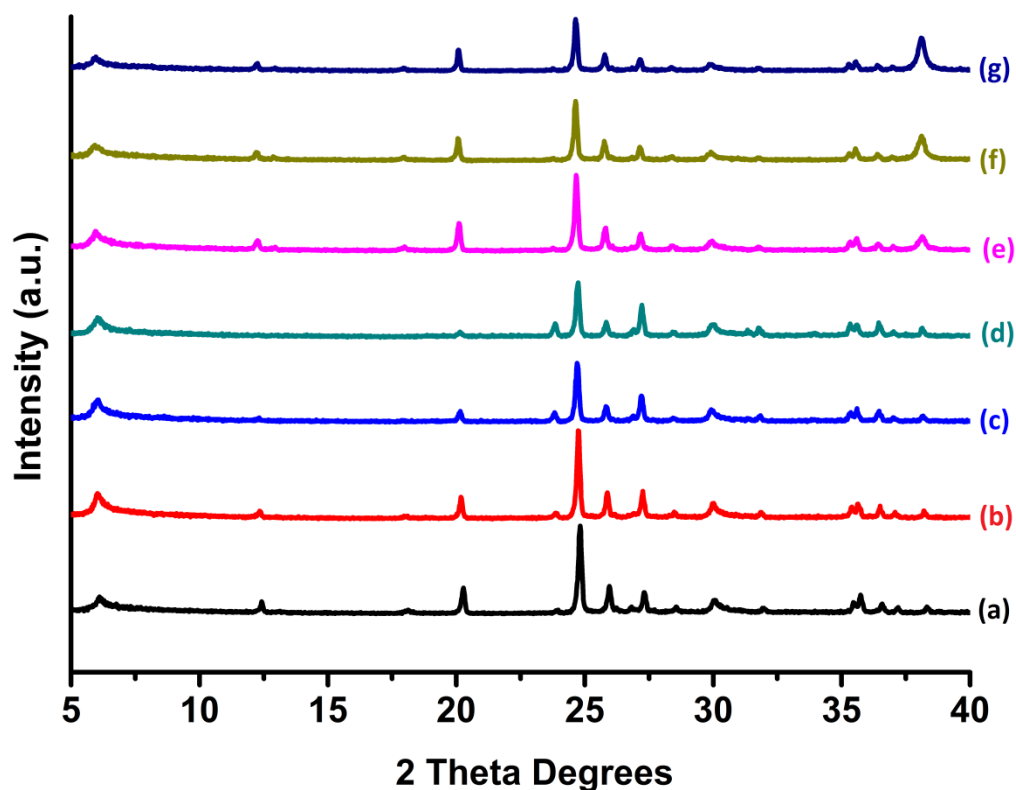


Figure 4.2. X-ray diffraction (XRD) patterns of (a) ETS-10, (b) Ag^+ -ETS-10-(5 wt. %), (c) Ag^+ -ETS-10-(10 wt. %), (d) Ag^+ -ETS-10-(15 wt. %), (e) Ag^0 -ETS-10-(5 wt. %), (f) Ag^0 -ETS-10-(10 wt. %), (g) Ag^0 -ETS-10-(15 wt. %).

As seen from the comparison of the XRD pattern for the as-synthesized ETS-10 and Ag^+ -ETS-10 samples given in Figure 4.2, there is no noticeable change in the positions of the Bragg peaks. Furthermore, no significant peak broadening was detected for the samples with respect to the as-synthesized ETS-10. These XRD results indicate that crystal structure of the samples was not altered upon ion-exchange and reduction. Figure 4.2 also depicts the XRD patterns of the Ag^0 nanoparticles obtained by reduction of Ag^+ ions within the cavities of ETS-10. A comparison of all the XRD patterns clearly gives some insight to the effect of the incorporation of Ag^+ ion into ETS-10 and the reduction of Ag^+ ion forming Ag^0 nanoparticles stabilized by ETS-10 matrix. Compared to the powder XRD patterns of ETS-10, XRD pattern of Ag^+ -ETS-10 samples shows systematic

variations in the relative intensities at certain 2θ values. As silver loading increased, relative intensities of (200), (204), and (224) reflections increased while the intensities of the remaining reflections decreased for Ag^+ -ETS-10-(5, 10, 15 wt. %). Similar results have already been reported and the variation in the intensities of some peaks has been assigned to site selective ion exchange in ETS-10 [3,5,6]. Additionally, in the powder XRD patterns of Ag^0 -ETS-10 samples, the increase in the intensity of Bragg peak at 38.2° with the increase of silver loading, which is attributable to the metallic silver [2,3] is clearly observed. The existence of Ag^0 nanoparticles on the surface of ETS-10 crystals for these samples was also confirmed by their FE-SEM analyses (*vide infra*).

4.3 Field Emission-Scanning Electron Microscopy (FE-SEM) and High Resolution-Transmission Electron Microscopy (HR-TEM)

Morphologies of Ag^0 -ETS-10 in different silver loadings (wt. %) were investigated by FE-SEM, TEM and HR-TEM analyses. Figure 4.3 shows the FE-SEM images of as-synthesized ETS-10 and Ag^0 -ETS-10 samples. At first glance, these images indicate that the method used for the preparation of Ag^0 -ETS-10 samples does not cause any observable defects in the structure of host material ETS-10, a fact which is also supported by XRD results.

TEM images of the samples prepared by borohydride reduction of Ag^+ -ETS-10 with various silver loadings (5, 10, 15 wt. %) were given in Figure 4.4-a-b-c. Within the limitations of bright-field (BF) imaging conditions, the mean sizes of Ag^0 nanoparticles were found to be 3.8, 3.3 and 3.7 nm for Ag^0 -ETS-10 samples with 5, 10, 15 wt. % Ag^+ loadings, respectively. BF images and ICP-OES results (Table 4.1) showed that there is formation of Ag^0 nanoparticles and attributed to their sizes larger than the channel diameter, they exist on the surface of the ETS-10. In order to reveal if any smaller particles were created “in” the channel of ETS-10, specimen was tilted to [110] zone axis where the largest pores within the ETS-10 (Figure 3.1) become parallel to the beam direction.

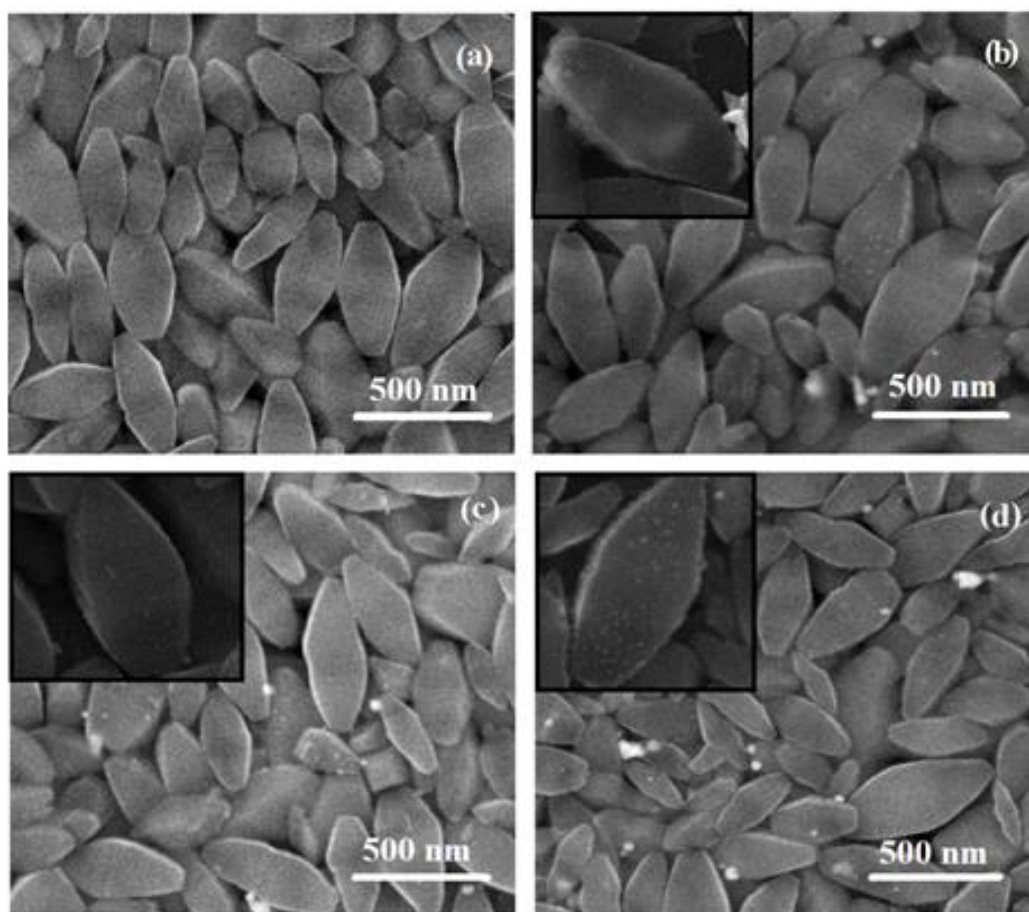


Figure 4.3. Field emission scanning electron microscopy FE-SEM images of (a) ETS-10, (b) Ag⁰-ETS-10-(5 wt. %), (c) Ag⁰-ETS-10-(10 wt. %), (d) Ag⁰-ETS-10-(15 wt. %).

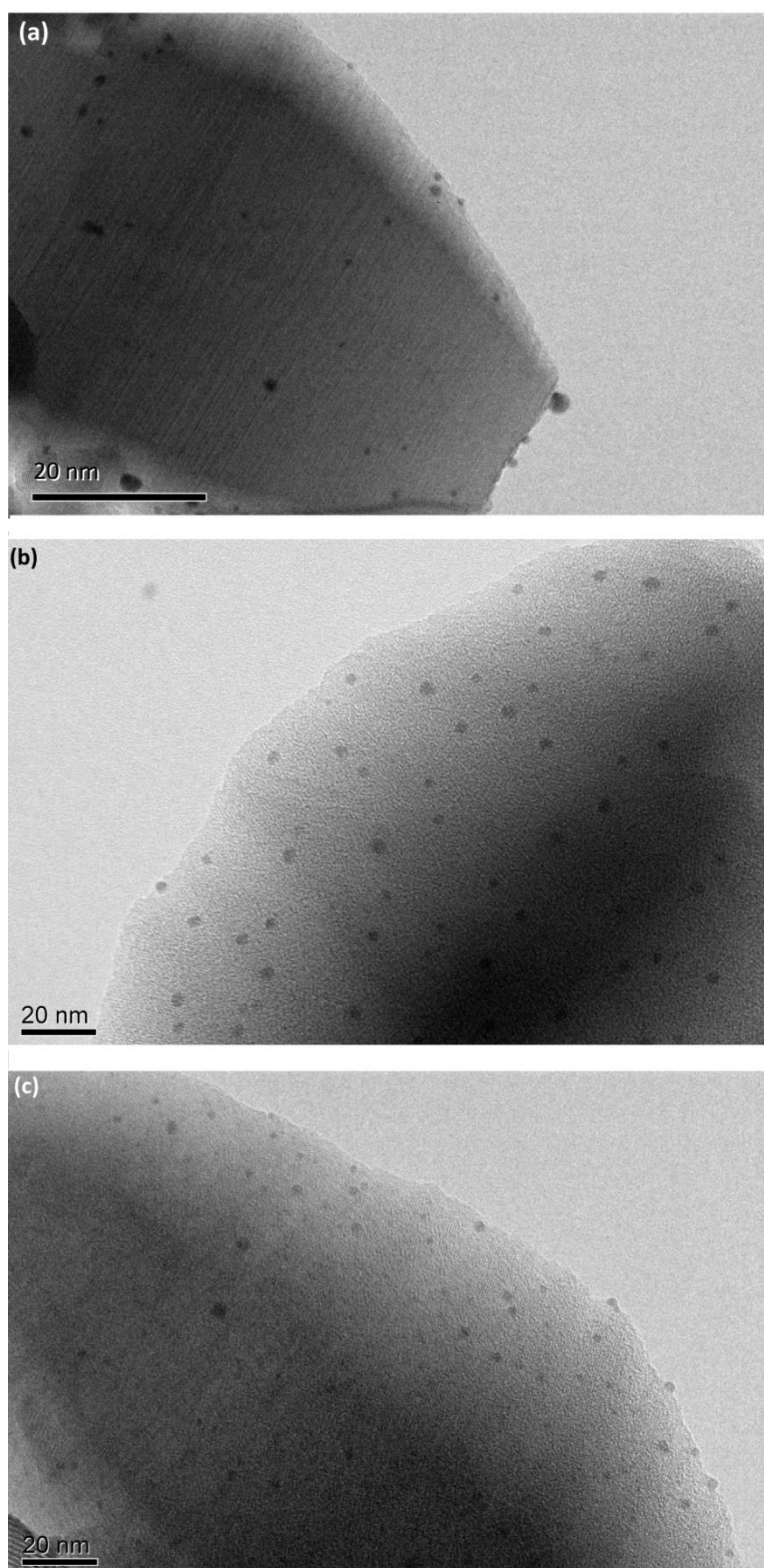


Figure 4.4. Transmission electron microscopy (TEM) image of (a) Ag⁰-ETS-10-(5 wt. %), (b) Ag⁰-ETS-10-(10 wt. %), (c) Ag⁰-ETS-10-(15 wt. %).

HR-TEM images (Figure 4.5-c) along [110] axis clearly show distinctive contrast which may actually indicate the existence of Ag^0 nanoparticles smaller than 2 nm created “in” the channels of ETS-10. Systematic tilting of the specimen has further shown that these features are not surface-attached nanocrystals since their contrast depends on crystallographic directions.

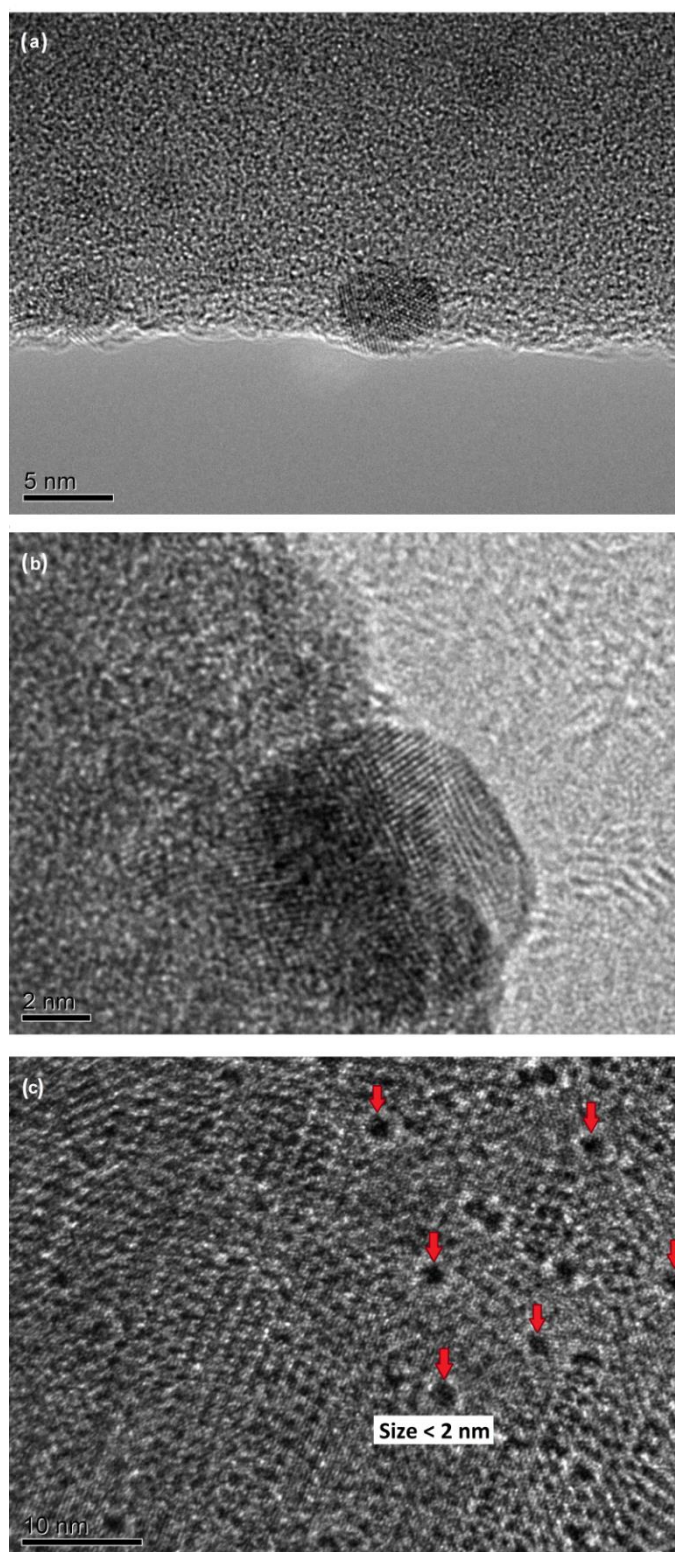


Figure 4.5. (a) and (b) High-resolution TEM (HR-TEM) images of Ag⁰-ETS-10-(10 wt. %) in different magnifications, (c) HR-TEM image of Ag⁰-ETS-10-(10 wt. %) along [110] direction.

According to BF images and the results obtained from nitrogen isotherms (i.e., no mesopore formation), 2 nm Ag^0 nanoparticles may be formed by the attachment of Ag^0 atoms to a mother Ag^0 cluster one by one instead of the formation of small Ag^0 clusters first and their following aggregation, which would have caused different isotherms leading to the possible destruction of the lattice and to mesopore formation. Accordingly, silver nanoparticle formation most likely occurred by the following system: (i) Ag^+ ion-exchange occurred to some extent with the extra framework cations (Na^+ and K^+) of ETS-10 and Ag^+ ions were stabilized in the framework of ETS-10. Then, these Ag^+ ions were reduced through NaBH_4 in the channels of ETS-10 (size < 2 nm); (ii) Remaining Ag^+ ions most probably attached to the surface of ETS-10 and were reduced through NaBH_4 . Since there is no restriction of channel for those that are on the surface, they have diameters of larger than the channel diameter of ETS-10 and aggregated up to 5, 4.8, and 4.5 nm for Ag^0 -ETS-10-(5, 10, 15 wt. %), respectively. Additionally, the representative high resolution TEM (HR-TEM) images of the Ag^0 -ETS-10-(10 wt. %) given in Figure 4.5-a and -b reveal a highly crystalline feature of these Ag^0 nanoparticles located on the surface of ETS-10.

4.4 Diffuse Reflectance - Ultraviolet-visible (DR-UV-vis) Spectroscopy and Nitrogen Adsorption-Desorption Isotherms

The nitrogen adsorption-desorption isotherms of ETS-10 and Ag^0 -ETS-10-(10 wt. %) are given in Figure 4.6. Both isotherms show type I shape, which is a characteristic of microporous materials [7].

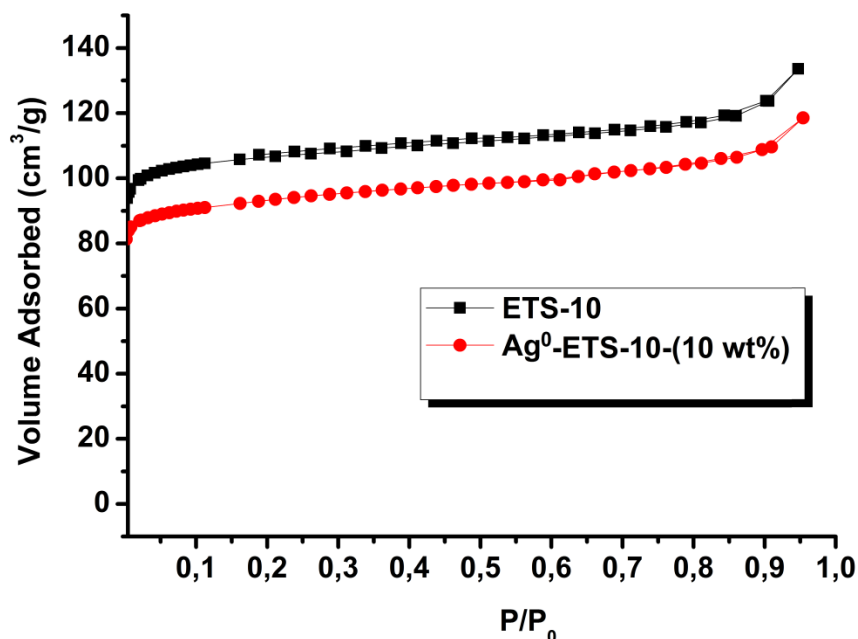


Figure 4.6. Nitrogen adsorption-desorption isotherms of ETS-10 (black) and Ag⁰-ETS-10-(10 wt. %) (red).

Micropore volume and area were determined for ETS-10 and Ag⁰-ETS-10 by *t*-plot method [8]. On passing from ETS-10 to Ag⁰-ETS-10, both micropore volume (from 0.094 to 0.062 cm³/g) and micropore area (from 221 to 141 m²/g) are noticeably reduced. The observed remarkable decrease in the micropore volume and micropore area can be attributed to the encapsulation of Ag⁰ nanoparticles to some extent in the cavities of ETS-10. Furthermore, nitrogen adsorption-desorption isotherms revealed that hysteresis does not exist for Ag⁰-ETS-10 samples, which indicates that there is no mesopore formation after reduction.

DR-UV-vis spectra of the ETS-10 and Ag⁰-ETS-10 samples were depicted in Figure 4.7. It is well known that ETS-10 shows a broad absorption band only in the UV range (250-320 nm) due to the presence of Ti⁴⁺ in octahedral coordination [9]. Therefore, UV spectrum of ETS-10 has no absorption band in the visible region, while UV-vis spectra of the Ag⁰-ETS-10 samples show a distinct absorption in the

visible range centered at around 400 nm. Intensity of this band increases with the increasing silver loading.

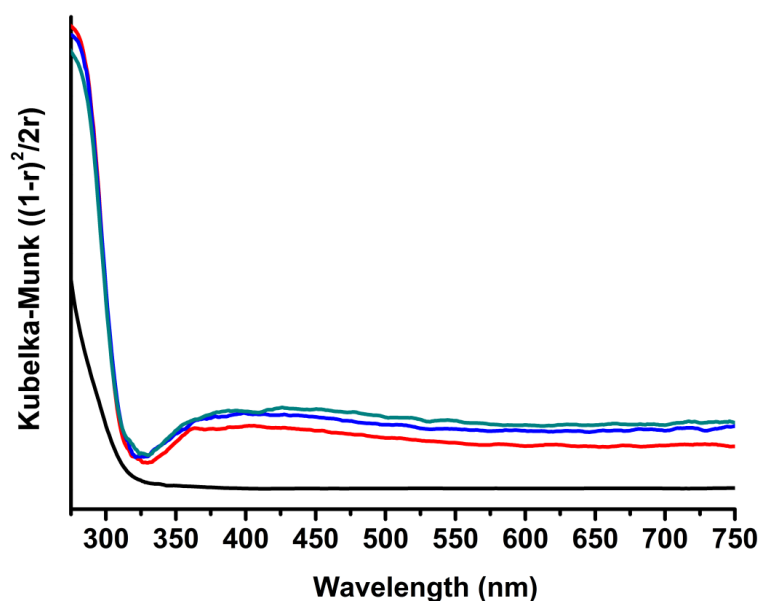


Figure 4.7. Diffuse reflectance-UV-vis spectra (in terms of Kubelka-Munk function) of ETS-10 (black), Ag⁰-ETS-10-(5 wt. %) (red), Ag⁰-ETS-10-(10 wt. %) (blue), Ag⁰-ETS-10-(15 wt. %) (olive).

It is known that the maximum wavelength of the plasmon resonance band increases with the increasing nanoparticle size [10,11]. Agostini [12], Ji [3], and Lv [2] et al., have reported the maximum wavelength of the plasmon resonance of the Ag⁰ nanoparticles in different sizes at 500, 460, and 400 nm, respectively. In the present study, the maximum wavelength and the width of the band at 400 nm do not change with the increasing silver loading. This observation suggests that the size of Ag⁰ nanoparticles does not depend on the silver loading of Ag⁰-ETS-10 samples. In other words, the size of Ag⁰ nanoparticles in the cavities of ETS-10 is restricted by the pore dimension [13].

4.5 X-ray Photoelectron Spectroscopy (XPS)

XPS survey scan of Ag⁰-ETS-10-(10 wt. %) is given in Figure 4.8-a, which exhibits peaks at 576 (Ag 3p), 531 (O 1s), 457 (Ti 2p), 369 (Ag 3d), 155 (Si 2p) and 101 eV (Ag 3s) [14]. High resolution Ag 3d spectra for the samples Ag⁰-ETS-10 with 5, 10 and 15 wt. % (Figure 4.8-b) show doublet for Ag⁰ nanoparticles at 368.0 eV for 3d_{5/2} and 374.0 eV for 3d_{3/2} with a binding energy (BE) separation of 6.0 eV [15]. Furthermore, the Ag 3d doublet was identified at around BEs of 368.3 and 374.3 eV for the samples Ag⁺-ETS-10-(5, 10, 15 wt. %) as shown in Figure 4.8-b in correlation with what was observed by Tiscornia et al. [5]. The BEs of Ag 3d_{5/2} (i.e., 368.3eV) for the Ag⁺-ETS-10 samples were lower than the BEs of AgO and Ag₂O, which are 367.4 and 367.8eV, respectively [3]. Thus, it can be inferred that the silver in Ag⁺-ETS-10-(m wt. %) samples are in their ionic forms.

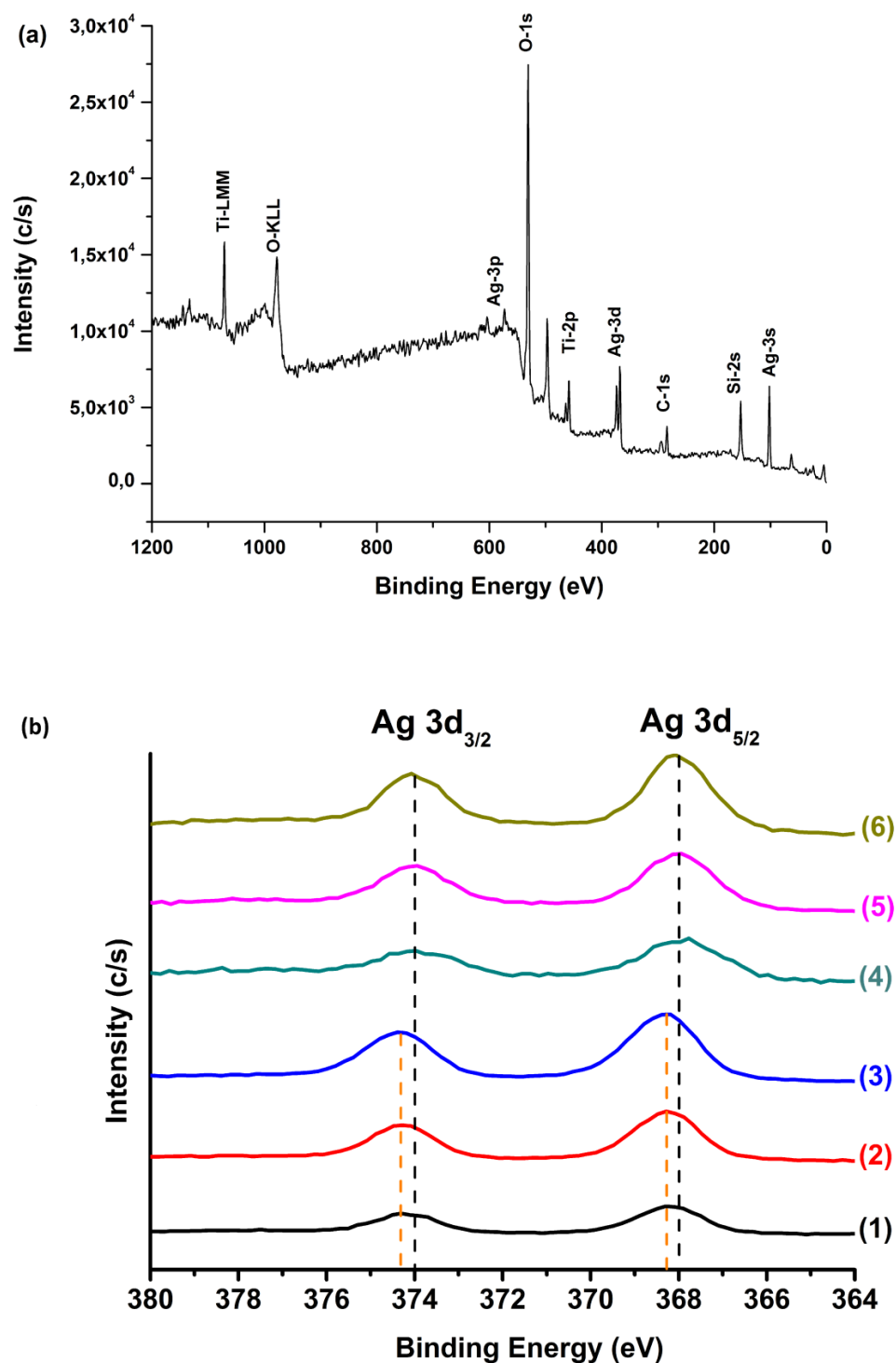


Figure 4.8. (a) XPS survey scan of Ag^0 -ETS-10-(10 wt. %), (b) high resolution Ag 3d spectra of, (1) Ag^+ -ETS-10-(5 wt. %), (2) Ag^+ -ETS-10-(10 wt. %), (3) Ag^+ -ETS-10-(15 wt. %), (4) Ag^0 -ETS-10-(5 wt. %), (5) Ag^0 -ETS-10-(10 wt. %), (6) Ag^0 -ETS-10-(15 wt. %).

4.6 Raman Spectroscopy

Raman spectra of the Ag^+ -ETS-10 and chemically reduced Ag^0 -ETS-10 samples are depicted in Figure 4.9 and 4.10, respectively. As mentioned in Chapter 3 Raman spectrum of the as-synthesized ETS-10 in Figure 4.9-a shows Raman scattering band at 729 cm^{-1} with a bandwidth of 35 cm^{-1} for the Ti-O-Ti stretching of the TiO_3^{2-} quantum wires [16,17]. The position and the width of this band depend on the average -Ti-O-Ti-O-Ti- chain length and concentration of defects.

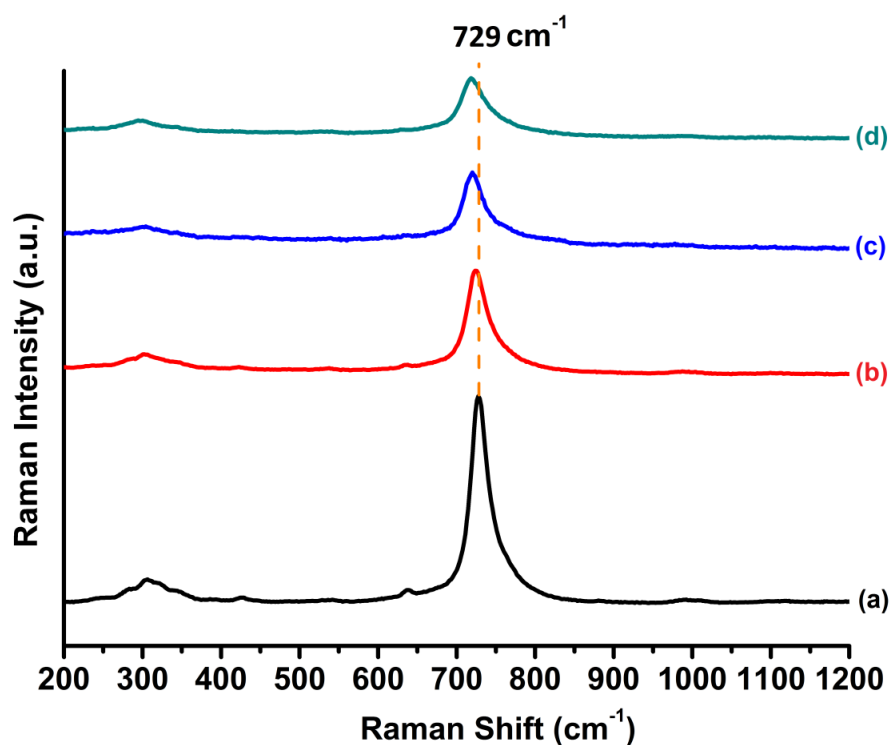


Figure 4.9. Raman spectra of ETS-10 (a), Ag^+ -ETS-10-(5 wt. %) (b), Ag^+ -ETS-10-(10 wt. %) (c), Ag^+ -ETS-10-(15 wt. %) (d).

Upon Ag^+ ion-exchange of ETS-10 samples, the Raman scattering band for the Ti-O-Ti stretching shifts from 729 cm^{-1} to 721 cm^{-1} along with a progressive

increase in the bandwidth. The dependence of the Ti-O-Ti stretching frequency on the size of charge balancing extra framework cation was already shown in the literature; for example, Ti-O-Ti stretching band was observed at 749 cm^{-1} and 796 cm^{-1} for the potassium and ammonium exchanged ETS-10, respectively, along with 80% broadening [16]. In the current study, the incorporation of Ag^+ ions into the ETS-10 did not lead to such significant shifts to higher wavenumbers, but towards slightly lower frequencies (729 cm^{-1} with FWHM: 35.14, 727 cm^{-1} with FWHM: 41.68, 722 cm^{-1} with FWHM: 42.56, 721 cm^{-1} with FWHM: 52.20 with a maximum broadening of 50 % for ETS-10, Ag^+ -ETS-10-(5, 10, 15 wt. %), respectively). In the literature, a gradual shift of the 729 cm^{-1} vibration towards lower frequencies along with a progressive increase in its bandwidth for ETS-10 samples that were ion-exchanged with several different cations (i.e., Na^+ , K^+ , Mg^{2+} , Ca^{2+} , Sr^{2+} , Ba^{2+} , Pb^{2+} , Cd^{2+} , Zn^{2+}) was also observed with varying water content due to the degree of hydration of the sample [18]. Accordingly, one can suggest that the silver loading of ETS-10 up to 15 wt. % Ag^+ does not cause a significant damage in the titanate quantum wire.

The Raman spectra of the Ag^0 -ETS-10 samples given in Figure 4.10 show that, upon chemical reduction of Ag^+ to Ag^0 within the ETS-10 framework, the Ti-O-Ti stretching band shifts to higher frequencies, broadens and loses intensity (729 cm^{-1} with FWHM: 35.14, 739 cm^{-1} with FWHM: 169.48, 739 cm^{-1} with FWHM: 173.06 for ETS-10, Ag^0 -ETS-10-(5, 10 wt. %), respectively).

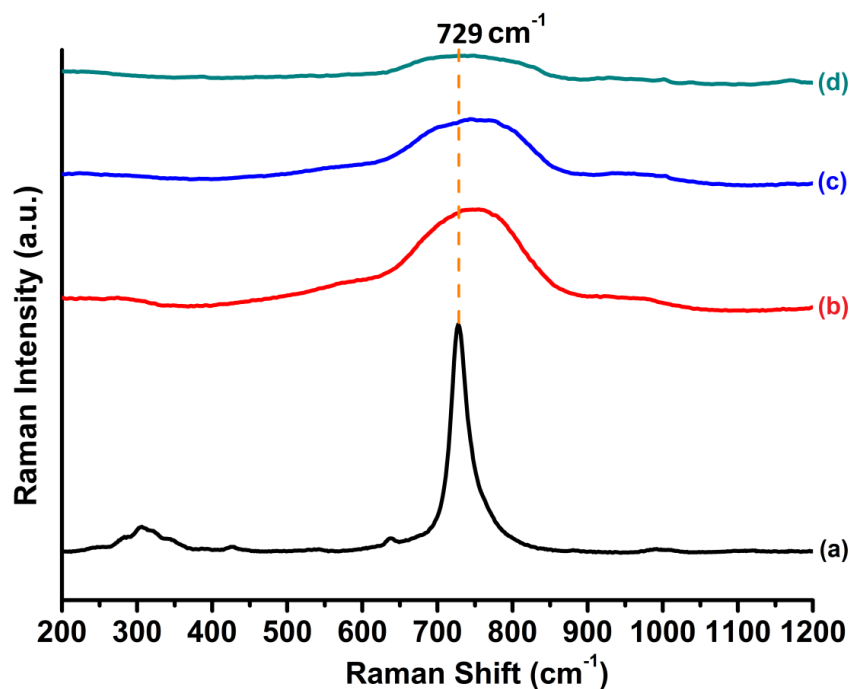


Figure 4.10. Raman spectra of ETS-10 (a), Ag⁰-ETS-10-(5 wt. %) (b), Ag⁰-ETS-10-(10 wt. %) (c), Ag⁰-ETS-10-(15 wt. %) (d).

This result indicates that the formation of Ag⁰ nanoparticles within the framework of ETS-10 causes damage in the titanate quantum wire. The extent of damage increases with the increasing silver loading of ETS-10 sample. In the Raman spectrum of the Ag⁰-ETS-10-(15 wt. %), the Ti-O-Ti stretching band is so broad and flattened that it is barely observable. This implies that the titanate quantum wires are almost collapsed in the ETS-10 sample with high silver loading, which are also in correlation with the measured (Na+K+Ag)/Ti and Si/Ti ratios (Table 4.1).

This study reports, for the first time, the local structural changes in ETS-10 induced by the ion exchange of Ag⁺ ions into the titanosilicate framework and their chemical reduction to Ag⁰ nanoparticles. The FE-SEM images show no significant change in the number and size of the Ag⁰ nanoparticles formed on the external surface of Ag⁰-ETS-10 crystals with increasing silver loading. However,

in the UV-vis spectra, the absorption band at 400 nm due to the plasmon resonance gains intensity with the increasing silver loading. This implies on the formation of more Ag^0 nanoparticles in the cavities of ETS-10 as the silver loading increases. Furthermore, in the Raman spectra one observes a progressive shift of the Ti-O-Ti stretching band at 729 cm^{-1} to higher wavenumbers, broadens and loses intensity with the increasing silver loading.

Taking all the results together, it can be suggested that the formation of Ag^0 nanoparticles within the framework of titanosilicate causes a local structural change in the titanate chains of ETS-10. Although the integrity of titanosilicate is maintained, after the ion exchange of Ag^+ ions within the ETS-10 and their following chemical reduction, Ag^0 nanoparticles are formed within the cavities of titanosilicate, contrary to the previous reports on the formation of Ag^0 particles on the external surface of ETS-10 crystals [3, 12]. The formation of small size Ag^0 nanoparticles within the cavities of titanosilicate, rather than on its external surface, induces a local structural change in the titanate quantum wire. The extent of destruction of the titanate quantum wire increases with the increasing silver loading. The presence of this type of defects has already been shown to be very important for catalytic applications [19,20]. The role of Ag^0 nanoparticles in such systems has also been discussed in terms of their ability to shift the light absorbance of ETS-10 to visible region [3].

4.7 Conclusions

Conclusively, the small size Ag^0 nanoparticles formed within the pores of ETS-10 from the chemical reduction of Ag^+ with sodium borohydride cause defects on the titanate quantum wire, as the presence of Ag^0 nanoparticles causes damage on the titanate chains, which is similar to the defects caused as a result of acid treatment [19,20] or ammonia exchange [16] reported in the literature. As the silver loading of ETS-10 increases, the concentration of defects increases in the titanate wire. This effect can be of great interest in using Ag^0 nanoparticles encapsulated in ETS-10 for future catalytic applications, which might even lead to enhanced

activities due to the combined role of defect formation and Ag^0 nanoparticle inclusion. Accordingly, the results obtained in this study are believed to bring not only the way of enhancement of catalytic activity, but also more insights on the role of the titanate wire in the existing and future applications.

A simple and efficient protocol was applied for the preparation of Ag^0 nanoparticles stabilized by ETS-10 framework at room temperature, which have been characterized by using ICP-OES, XRD, XPS, FE-SEM, TEM, HR-TEM, DR-UV-vis, Raman spectroscopies and N_2 adsorption-desorption technique. Results of these advanced techniques are indicating that this methodology produces highly stable, well-dispersed Ag^0 nanoparticles within the ETS-10 matrix without causing observable defects in the morphology, alteration in ETS-10 lattice, and mesopore formation. The insignificant changes observed on the external surface of the Ag^0 -ETS-10 crystals as a function of increasing silver loading, along with the consistent changes observed in the DR-UV-vis and Raman spectroscopy analysis suggests the formation of Ag^0 nanoparticles within the framework of titanosilicate causing a local structural change in the titanate chains of ETS-10.

REFERENCES

- [1] J. Polte, X. Tuaev, M. Wuithschick, A. Fischer, A.F. Thuenemann, K. Rademann, R. Kraehnert, F. Emmerling, "Formation Mechanism of Colloidal Silver Nanoparticles: Analogies and Differences to the Growth of Gold Nanoparticles", *ACS Nano* 6(7), 2012, 5791 - 5802.
- [2] L. Lv, Y. Luo, W.J. Ng, X.S. Zhao, *Micropor. Mesopor. Mater.* 120, 2009, 304.
- [3] Z. Ji, M.N. Ismail, D.M. Callahan Jr., E. Pandowo, Z. Cai, T.L. Goodrich, K.S. Ziemer, J. Warzywoda, A. Sacco Jr., *Appl. Catal. B: Environ.* 102, 2011, 323.
- [4] L. Lv, F. Su, X.S. Zhao, "A Reinforced Study on the Synthesis of Microporous Titanosilicate ETS-10", *Micropor. Mesopor. Mater.* 76, 2004, 113-122.
- [5] I. Tiscornia, S. Irusta, P. Pradanos, C. Tellez, J. Coronas, J. Santamaria, *J. Phys. Chem. C* 111, 2007, 4702.
- [6] X. Wang, A. Jacobson, *Chem. Commun.*, 1999, 973.
- [7] S. Storck, H. Bretinger, W.F. Maier, *Appl. Catal. A* 174, 1998, 137.
- [8] R.S.H. Mikhail, S. Brunauer, E.E.J. Bodor, *J. Colloid Interf. Sci.* 26, 1968, 45.
- [9] T. Das, A. Chandwadkar, A. Budhkar, S. Belhekar, S. Sivasanker, *Micropor. Mater.* 4, 1995, 195.
- [10] D.D. Evanoff Jr., G. Chumanov, *Chem. Phys. Chem.* 6, 2005, 1221.
- [11] D.D. Evanoff Jr., G. Chumanov, *J. Phys. Chem. B* 108, 2004, 13957.
- [12] G. Agostini, S. Usseglio, E. Groppo, M.J. Uddin, C. Prestipino, S. Bordiga, A. Zecchina, P.L. Solari, C. Lamberti, *Chem. Mater.* 21, 2009, 1343.
- [13] M. Zahmakıran, S. Özkar, *Nanoscale* 3, 2011, 3462.
- [14] C. Wagner, W.M. Riggs, L.E. Davis, J.F. Moulder, G.E. Muilenberg, *Handbook of X-ray Photoelectron Spectroscopy*; Physical Electronic Division, Perkin-Elmer: Waltham, MA, Vol. 55, 1979.
- [15] J.F. Moulder, W.F. Stickle, P.E. Sobol and K.D. Bomben, J. Chastain, Editor, *Handbook of X-ray Photoelectron Spectroscopy*, Perkin Elmer Corporation, Eden Prairie, MN, 1992.

- [16] C.C. Pavel, B. Zibrowius, E. Löffler, W. Schmidt, *Phys. Chem. Chem. Phys.* 9, 2007, 3440.
- [17] Y. Su, M.L. Balmer, *J. Phys. Chem. B* 104, 2000, 8160.
- [18] N. C. Jeong, Y. J. Lee, J. Park, H. Lim, C. Shin, H. Cheong, and K. B. Yoon, *J. of Am. Chem. Soc.* 131, 2009, 13080.
- [19] L. Lv, J.K. Zhou, F. Su, X.S. Zhao, *J. Phys. Chem. C* 111, 2007, 773.
- [20] F.X.L. Xamena, P. Calza, C. Lamberti, C. Prestipino, A. Damin, S. Bordiga, E. Pelizzetti, A. Zecchina, *J. Am. Chem. Soc.* 125, 2003, 2264.

CHAPTER 5

PHOTOCHROMISM

Ag^+ -ETS-10 films were prepared and turned into their Ag^0 nanoparticle form (i.e., I- Ag^0 -ETS-10) according to the procedure described in the experimental Section 2.3. Upon thermal reduction of Ag^+ -ETS-10 films, a color change from white to dark brownish yellow was observed, which was indicative of silver nanoparticles at first glance (Figure 5.1-a and -b). Silver nanoparticles are known to gradually convert to their oxidized state in ambient air, which can be achieved more quickly by exciting the nanoparticles at their SPR frequency (i.e., visible light) [1]. Therefore, I- Ag^0 -ETS-10 films were exposed to a visible laser to achieve the oxidation of metallic silver nanoparticles (i.e., 116-LT-ETS-10). When SPR activity was vanished after visible laser treatment, the film coloration was diminished as can be seen from Figure 5.1-c. As a result, a bleached state corresponding to the colorless form of a photochromic system was achieved.

A second reductive treatment for 5h involving the same protocol of thermal treatment was applied to the 116-LT-ETS-10 films (i.e., 5h-II- Ag^0 -ETS-10) in order to investigate the reversibility of the process after the films were exposed to visible laser. Upon thermal treatment of 116-LT-ETS-10 films, although the original brown color was not fully attained, it was clearly observed that the color of 5h-II- Ag^0 -ETS-10 films was slightly darkened with respect to the initially treated 116-LT-ETS-10 films. Accordingly, partial reversibility was observed in 5h-II- Ag^0 -ETS-10 films (i.e., color darkening) after second thermal treatment (Figure 5.1-d). The films were placed on the logo of Middle East Technical University to distinguish transparency of the films after each treatment (i.e., Figure 5.1-a-d, left). The color of the films was shown more distinctly in Figure 5.1-a-d, right.

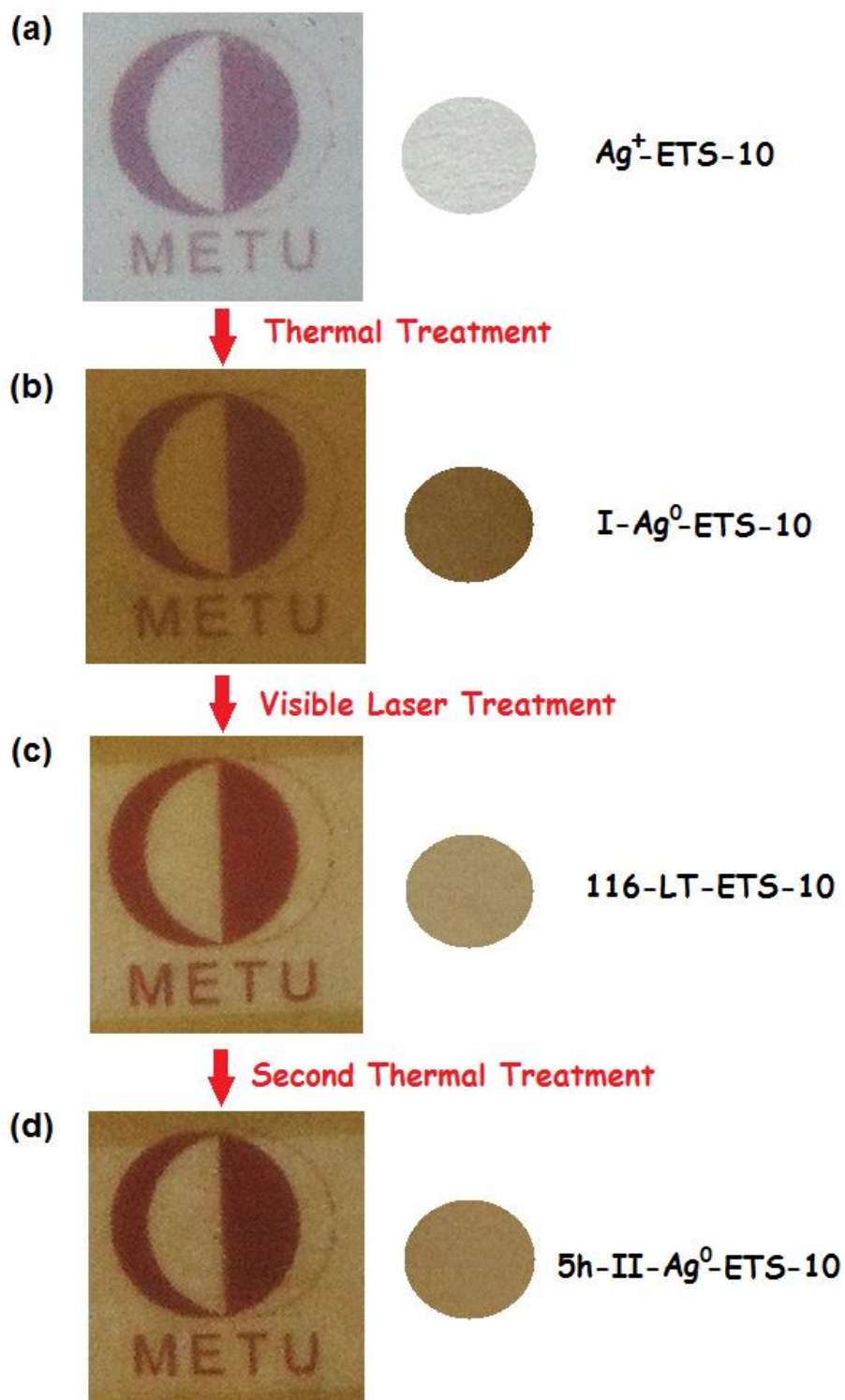


Figure 5.1. Photograph of (a) Ag^+ -ETS-10 films, (b) I- Ag^0 -ETS-10 films, (c) 116-LT-ETS-10 films, (d) 5h-II- Ag^0 -ETS-10 films.

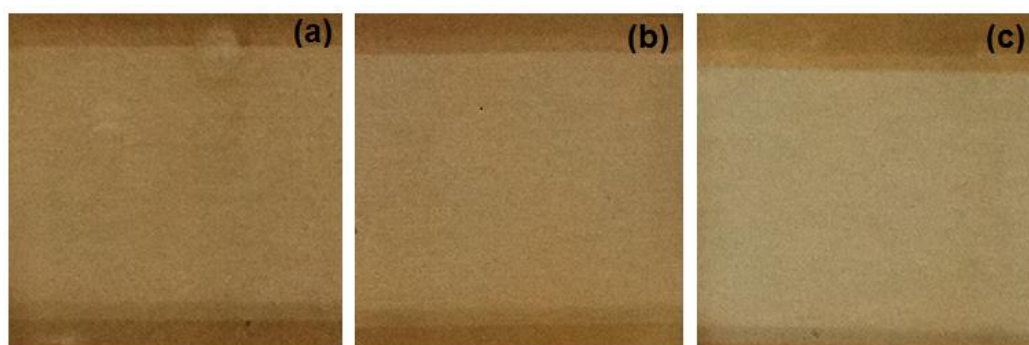


Figure 5.2. Photograph of (a) 90-LT-ETS-10 films, (b) 100-LT-ETS-10 films, (c) 116-LT-ETS-10 films.

It is known that the duration, the spectral width and the irradiance of the visible light exposure have an influence on the final color of the obtained films [2]. Upon achieving a controlled and reversible change in the color of the originally obtained I-Ag⁰-ETS-10 films, it was of interest to investigate the effect of power of the visible laser to see whether a consistent change in the brownish color was going to be attained or not. Accordingly, three different laser powers were applied to I-Ag⁰-ETS-10 films. It was seen that the color of the films bleached more significantly as the power of visible laser increased (Figure 5.2). Consistently, gradient bleaching and color change of the films were also observed in the literature for silver nanoparticle incorporated TiO₂ under visible laser illuminations with different irradiances [2].

5.1 Field Emission-Scanning Electron Microscopy (FE-SEM) and High Resolution-Transmission Electron Microscopy (HR-TEM)

Microporous ETS-10 crystals contain exchangeable extra framework charge-balancing cations (i.e., Na⁺ and K⁺) in the as-synthesized materials. Existence of extra framework cations creates an opportunity of incorporation of desired cations (i.e., Ag⁺) into ETS-10 matrix by ion-exchange and their reduction to nanoparticles within ETS-10 matrix through several reduction techniques [3,4], which leads to the formation of small narrow-sized silver nanoparticles in the inner surface of the

crystals. Morphologies of I-Ag⁰-ETS-10, 116-LT-ETS-10, 5h-II-Ag⁰-ETS-10 films were investigated by FE-SEM and HR-TEM analyses. The formation of Ag⁰ nanoparticles with sizes in the range of 10-20 nm and some 30 nm was observed on the outer surface of ETS-10 crystals as can be seen in Figure 5.3-a and -c. The detailed investigation on the formation of silver nanoparticles at the inner and outer surface of the ETS-10 crystals was discussed in a more detailed way in our previous publication [5]. Silver nanoparticles incorporated into the framework of ETS-10 crystals was more interesting for the current discussion since there should be interaction in between silver nanoparticles and TiO₃²⁻ quantum wires within the ETS-10 framework to observe photochromism. Accordingly, HR-TEM analysis was carried out to examine silver nanoparticles incorporated into the ETS-10 crystals. HR-TEM images revealed that silver nanoparticles were formed upon thermal treatment as well with a mean size of 2.5 nm (Figure 5.3-d). The formation of silver nanoparticles which are smaller than 2 nm was observed inside the channels of ETS-10 by tilting specimen to [110] zone axis where the largest pores within the ETS-10 become parallel to the beam direction in the literature [5]. The observation of the fringes of the pores of zeolitic materials on the incorporated metal nanoparticles is generally accepted as an indicator of formation of metal nanoparticles within the crystals [6,7].

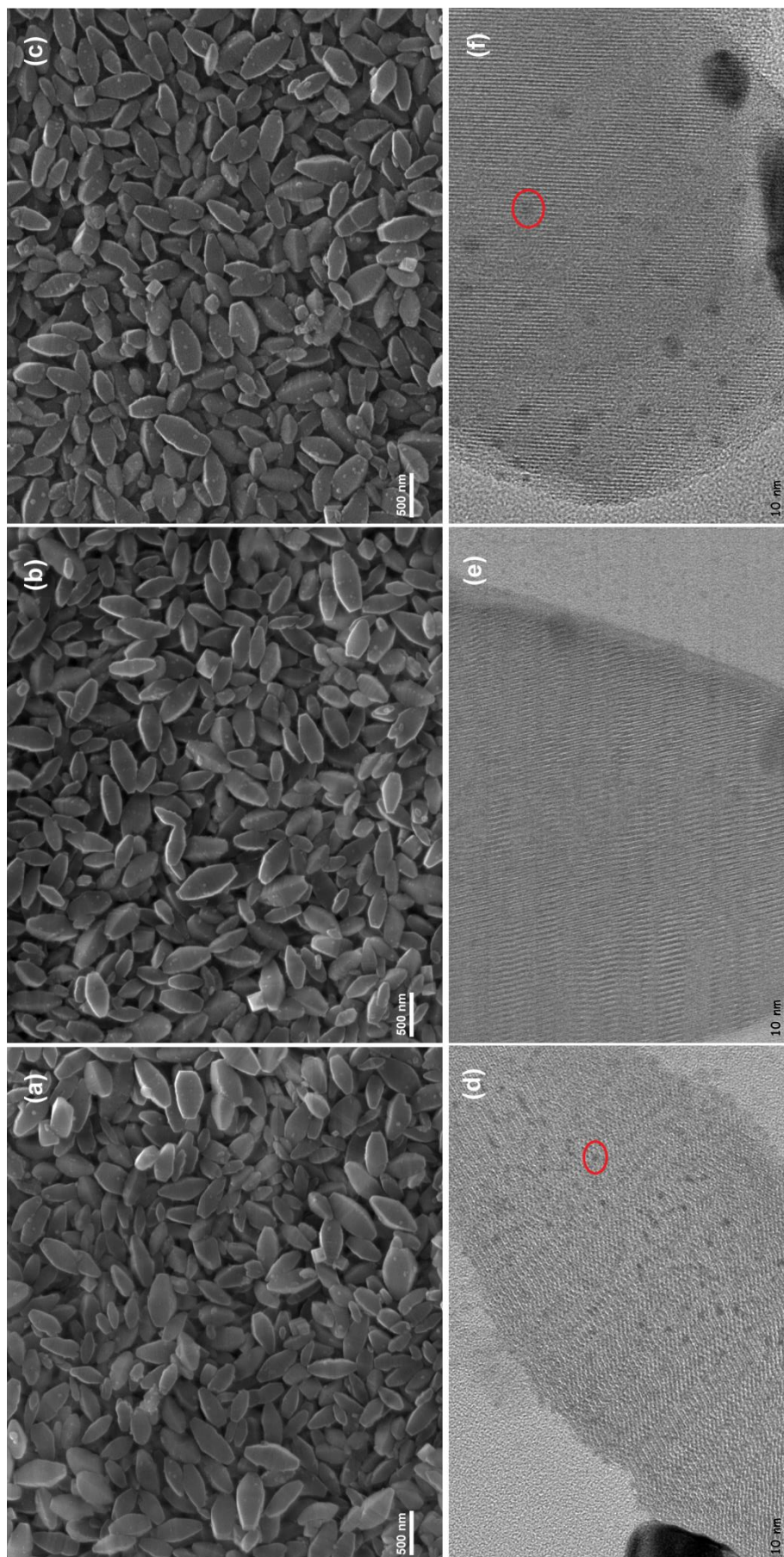


Figure 5.3. Field emission scanning electron microscopy (FE-SEM) images of (a) I-Ag⁰-ETS-10 films, (b) 116-LT-ETS-10 films, (c) 5h-II-Ag⁰-ETS-10 films, high resolution transmission electron microscopy (HR-TEM) images of (d) I-Ag⁰-ETS-10 films, (e) 116-LT-ETS-10 films, (f) 5h-II-Ag⁰-ETS-10 films.

As a result, it is of high possibility that the observed silver nanoparticles in Figure 5.3-d with a mean size of 2.5 nm was within the pores of ETS-10. Although the calculated crystallinity of the I-Ag⁰-ETS-10, 116-LT-ETS-10, 5h-II-Ag⁰-ETS-10 films was decreased to 87, 70 and 77 % for each treatment, respectively (vide infra), FE-SEM and HR-TEM images of the samples revealed that there was no observable structural change (i.e., melting) after any treatment (i.e., reduction, visible laser treatment, or second thermal treatment). The distinction of each treatment was more observable in HR-TEM images (Figure 5.3-e-f). Within the limitations of bright-field (BF) imaging conditions the mean size of nanoparticles formed within the pores of ETS-10 through thermal treatment was found to be 2.5 nm (Figure 5.3-d). It was shown that almost all nanoparticles in the pores of ETS-10 crystals have disappeared after exposure to visible laser at 532 nm through the excitation of the SPR of Ag⁰ nanoparticles (Figure 5.3-e). It is known that at specific size and morphology of Ag⁰ nanoparticles, surface electrons resonate with the incident light at certain wavelength [2,8].

Accordingly, some of the electrons were excited and transferred to ambient oxygen or to the conduction band of ETS-10 [9,10,19,20]. Consequently, the Ag⁰ nanoparticles transformed into Ag⁺ ions and the size of the nanoparticles shrank with respect to initial Ag⁰ nanoparticles. After second reductive treatment, the Ag⁰ nanoparticles reappeared at a mean size of 4 nm, which is slightly larger than the nanoparticles formed by the thermal reduction method as seen in Figure 5.3-f. Such an occurrence was also observed in the literature where it was said that lower thermodynamic energy is needed to reduce ions on the already formed nanoparticles. Therefore, during the second reduction process, nanoparticles could have preferred to contribute to the growth of negligible number of existing nanoparticles (or nuclei) instead of producing separate independent nanoparticles, leading to larger nanoparticle formation [11].

5.2 X-ray Diffraction (XRD)

XRD patterns of as-synthesized ETS-10 and treatment of photochromic cycle (i.e., I-Ag⁰-ETS-10, 116-LT-ETS-10, and 5h-II-Ag⁰-ETS-10 films) can be seen from Figure 5.4.

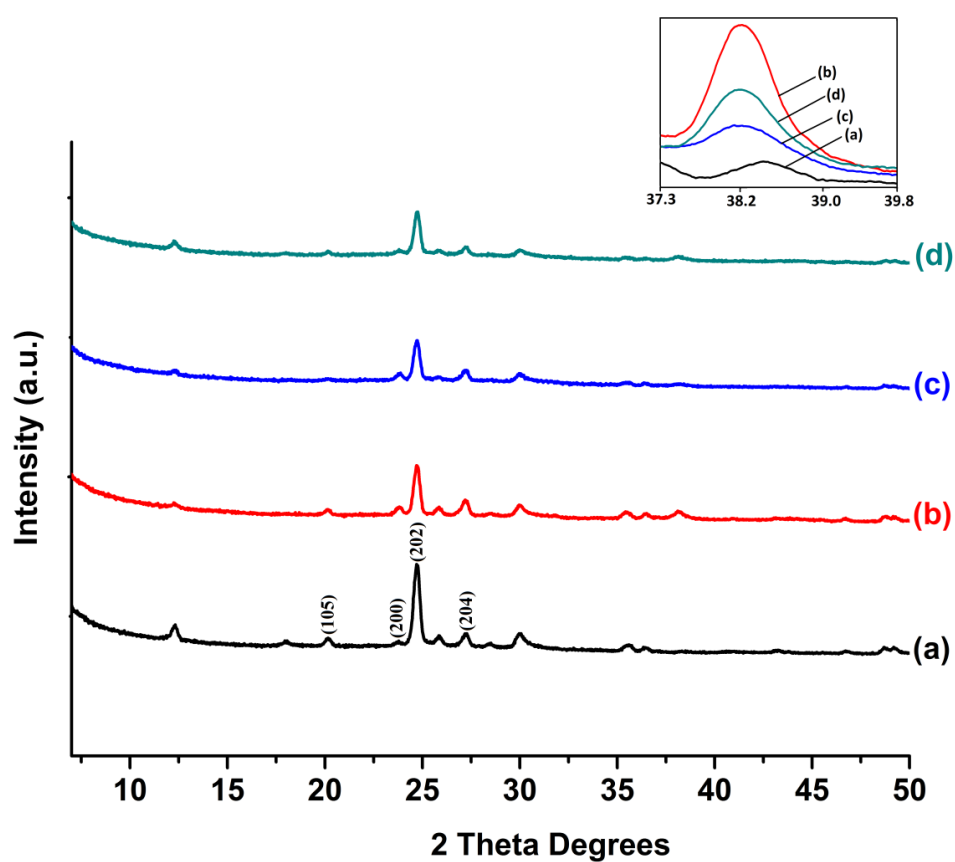


Figure 5.4. X-ray diffraction (XRD) patterns of (a) ETS-10 (black), (b) I-Ag⁰-ETS-10 films (red), (c) 116-LT-ETS-10 films (blue), (d) 5h-II-Ag⁰-ETS-10 films (green).

The HR-TEM results were consistent with XRD results (Figure 5.4, inset). An increase in the intensity of Bragg peak at 38.2° was observed in the XRD patterns of I-Ag⁰-ETS-10 films (Figure 5.4-b), which is representative of the Ag⁰ nanoparticles attributable to the metallic silver in (111) plane [3,4]. Although as-synthesized ETS-10 crystals also have a peak at 2θ degree of 38.4° , a comparison of the relative change in the intensity of Bragg peak at 38.2° clearly gives some insight to the effect of all treatments as can be seen Figure 5.4, inset. The highest intensity was observed for the I-Ag⁰-ETS-10 films; while, 2θ degree of 38.2° noticeably diminished in 116-LT-ETS-10 films with respect to I-Ag⁰-ETS-10 films. After second thermal treatment of the 116-LT-ETS-10 film, although the original peak intensity was not attained, the peak intensity of 38.2° increased again for 5h-II-Ag⁰-ETS-10 films with respect to 116-LT-ETS-10 films.

Furthermore, as seen from the comparison of the XRD patterns for the ETS-10 films given in Figure 5.4, there was no noticeable change in the positions of the Bragg peaks. No significant peak broadening was detected for the samples with respect to the as-synthesized ETS-10 sample as well. The relative crystallinity of the films was calculated to be 87 % for I-Ag⁰-ETS-10 films, while it decreased to 70% after visible laser treatment (i.e., 116-LT-ETS-10). Upon the application of second thermal treatment (i.e., II-Ag⁰-ETS-10), the slight increase in the relative crystallinity was 77%, which can be due to the annealing effect of thermal treatment [12]. Nevertheless, no significant change in the morphology of the crystals as a function of laser or second thermal treatment was observed, which is in correlation with FE-SEM and HR-TEM analyses (Figure 5.3).

5.3 Ultraviolet-visible (UV-vis) Spectroscopy

UV-vis spectra of the ETS-10, I-Ag⁰-ETS-10, 116-LT-ETS-10, and 5h-II-Ag⁰-ETS-10 films are shown in Figure 5.5. ETS-10 shows an absorption band only in the UV range due to the presence of Ti⁴⁺ in octahedral coordination [13]. Therefore, the spectrum of ETS-10 has no absorption band in the visible region, while UV-vis spectra of I-Ag⁰-ETS-10 films show a broad absorption in the visible range. The

broad absorption observed could be due to the large Ag⁰ nanoparticles (i.e., ~15-20 nm) on the outer surface of ETS-10 crystals and/or dielectric medium of the surrounding matrix [14].

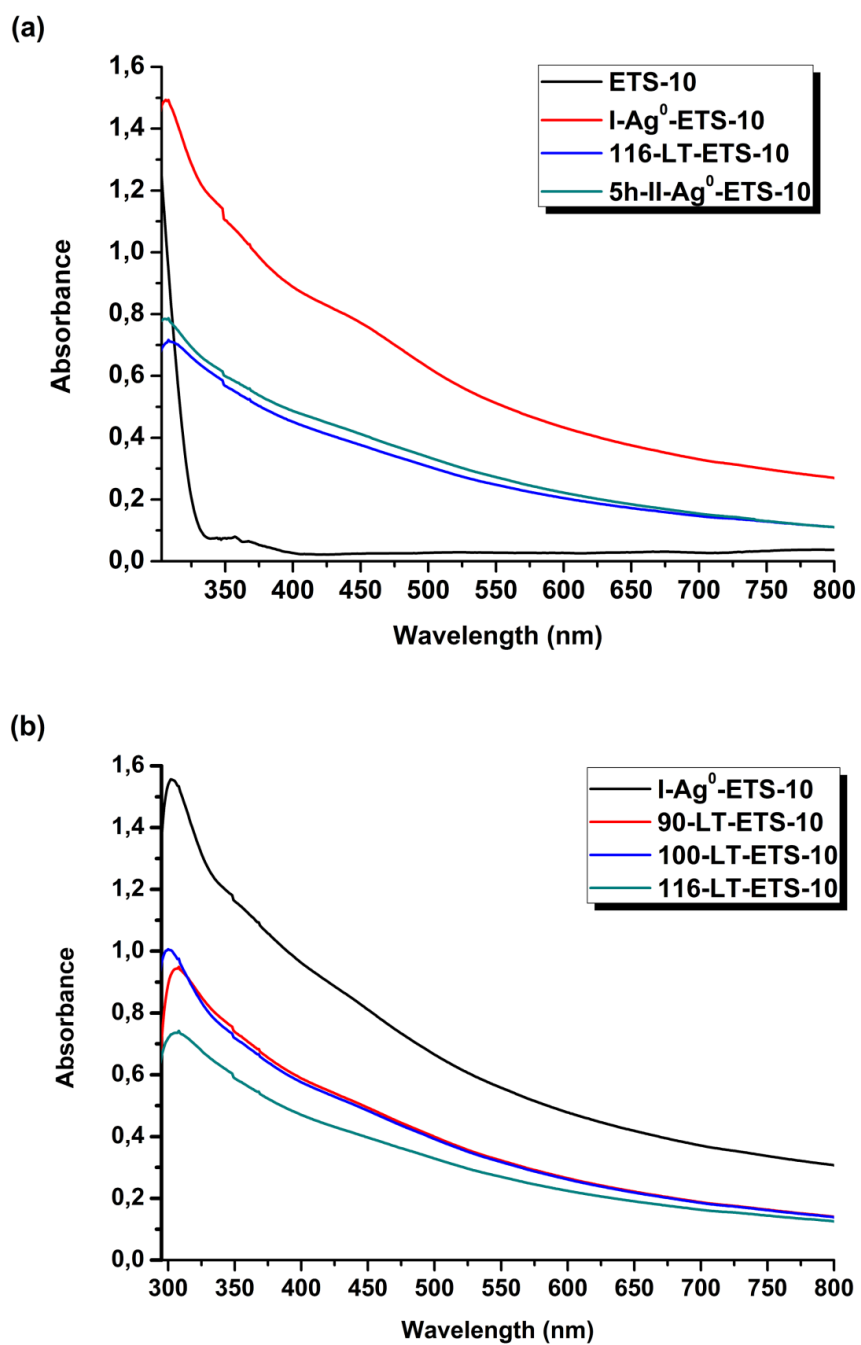


Figure 5.5. UV-vis spectra of (a) ETS-10 (black), I-Ag⁰-ETS-10 films (red), 116-LT-ETS-10 films (blue), 5h-II-Ag⁰-ETS-10 films (green), (b) I-Ag⁰-ETS-10 films (black), 90-LT-ETS-10 films (red), 100-LT-ETS-10 films (blue), 116-LT-ETS-10 films (green).

It seems that the absorption spectrum in the current study is governed by ~ 450 nm peaks, which shows that the generated silver nanoparticles were mostly in the smaller size regime. This is consistent with the HR-TEM results in Figure 5.3-d (Mean size of Ag^0 nanoparticles = 2.5 nm). Accordingly, the absorption around 450 nm can be attributed to small Ag^0 nanoparticles. In order to show the reversibility of the observed photochromism process in ETS-10, a second thermal treatment was performed after the visible laser treatment. After the second thermal treatment of 116-LT-ETS-10 films, the dark yellowish brown color reappeared (Figure 5.1-d). UV-vis spectroscopy showed that second thermal treatment lead to partial restoration (i.e., increase) of the absorption band at around wavelength of 450 nm (Figure 5.5-a), with a slightly more pronounced increase observed upon an increase in the duration of thermal treatment (Figure 5.6). Accordingly, it seems that, although full restoration of the SPR band at 450 nm was not achieved upon thermal treatment, the redox parameters chosen for photochromism process are indeed affecting the state of Ag^+ ions/ Ag^0 nanoparticles within ETS-10.

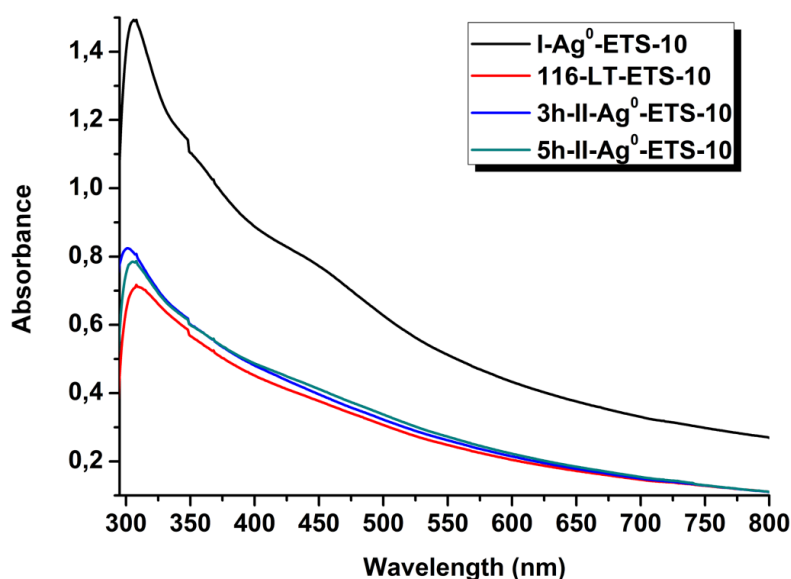


Figure 5.6. I- Ag^0 -ETS-10 films (black), 116-LT-ETS-10 films (red), 3h-II- Ag^0 -ETS-10 films (blue), 5h-II- Ag^0 -ETS-10 films (green).

To elucidate the effect of power on the oxidation (i.e., bleaching state), the power of the visible laser was altered through attenuation filter (i.e., 90 W.mm⁻², 100 W.mm⁻² and 116 W.mm⁻²). It was clear that the original yellowish brown color became consistently lighter as the power of visible laser increased in the oxidation process from 90 W.mm⁻² to 116 W.mm⁻² (Figure 5.2). The UV-vis spectra of the films upon changing power of visible laser are shown in Figure 5.5-b. The SPR activity of the 116-LT-ETS-10 films also noticeably decreased with respect to the 90-LT-ETS-10 films and 100-LT-ETS-10 films. It must be also noted that the film colors were quite stable over time. The color of the 116-LT-ETS-10 film was slightly darkened after few months at room temperature in darkness.

5.4 X-ray Photoelectron Spectroscopy (XPS)

XPS analysis results for I-Ag⁰-ETS-10, 116-LT-ETS-10, 5h-II-Ag⁰-ETS-10 films are shown in Figure 5.7. High resolution Ag 3d spectra for the I-Ag⁰-ETS-10 films in Figure 5.7, show doublet for Ag⁰ nanoparticles at 368.1 eV for 3d_{5/2} and 374.1 eV for 3d_{3/2} with a binding energy (BE) separation of 6.0 eV, which is indicative of Ag⁰ nanoparticles [15]. Compared to the binding energy values of silver metal (i.e., 368.0 eV and 374.0 eV), 0.1 eV shift toward higher values could be attributed to both the quantum size effect and peculiar electronic properties of the ETS-10 matrix [16]. The BEs of Ag 3d_{5/2} (i.e., 368.1 eV) for the I-Ag⁰-ETS-10 films shifted to the BEs of 368.3 eV for both 116-LT-ETS-10 and 5h-II-Ag⁰-ETS-10 films. The shift to metallic form (i.e., shift to BEs of 368.1 eV for Ag 3d_{5/2}) was not observed for 5h-II-Ag⁰-ETS-10 films. Therefore, the high resolution Ag 3d_{5/2} spectrum was deconvoluted into two doublets at 368.1 and 368.5 eV for 5h-II-Ag⁰-ETS-10 film to determine the binding energies accurately. Details of the curve fitting results of the Ag 3d_{5/2} spectra for I-Ag⁰-ETS-10 and 116-LT-ETS-10 films and the corresponding relative sub-peak area ratios (i.e., Ag⁺ / (Ag⁺ + Ag⁰)) were shown in Table 5.1. According to Table 5.1, the ratio of the deconvoluted peak area at 368.5 eV (i.e., Ag⁺) to total area revealed that the ratio of the silver increased from 10.96 to 38.69 % for the cycle of I-Ag⁰-ETS-10 → 116-LT-ETS-10 and decreased from 38.69 to 29.67 % for the cycle of 116-LT-ETS-10 → 5h-II-Ag⁰-ETS-10, which was expected from the

photochromic cycles. When the main Ag 3d_{5/2} peak was considered, the shift to metallic form (i.e., shift to BEs of 368.1 eV for Ag 3d_{5/2}) was not observed for 5h-II-Ag⁰-ETS-10 films. However, detailed identification of the deconvoluted peaks revealed that ionic form of the silver was increased for 116-LT-ETS-10 with respect to I-Ag⁰-ETS-10 and decreased for 5h-II-Ag⁰-ETS-10 with respect to 116-LT-ETS-10, which was in correlation with XRD and UV-vis spectroscopy analyses.

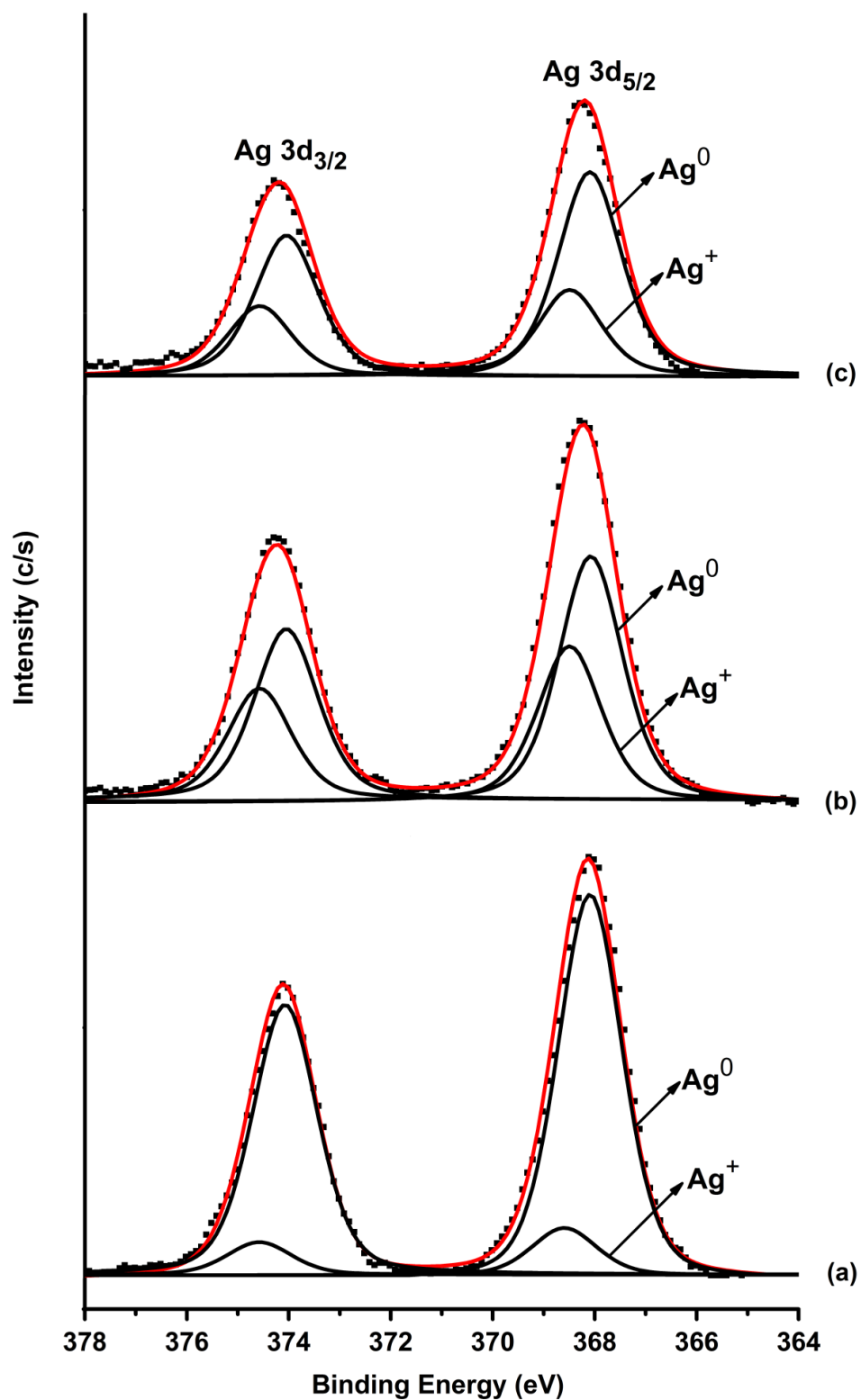


Figure 5.7. X-ray photoelectron spectroscopy (XPS) high resolution Ag 3d spectra of (a) I-Ag⁰-ETS-10 films, (b) 116-LT-ETS-10 films, (c) 5h-II-Ag⁰-ETS-10 films.

High resolution Ti 2p spectra were fitted by Gaussian-Lorentzian functions after removal of the background. Ti 2p spectra of I-Ag⁰-ETS-10, 116-LT-ETS-10 and 5h-II-Ag⁰-ETS-10 films were depicted in Figure 5.8. Details of the curve fitting results of the Ti 2p spectra for the films and the corresponding relative sub-peak area ratios were presented in Table 5.1. The peak in 458.7 eV, related to octahedral Ti species, was observed to shift to 459.1, 458.9, and 459.1 eV for the I-Ag⁰-ETS-10, 116-LT-ETS-10, and 5h-II-Ag⁰-ETS-10, respectively. Similar shifts in the octahedral coordination of Ti species were also observed upon acid treatment in ETS-10 as well [17].

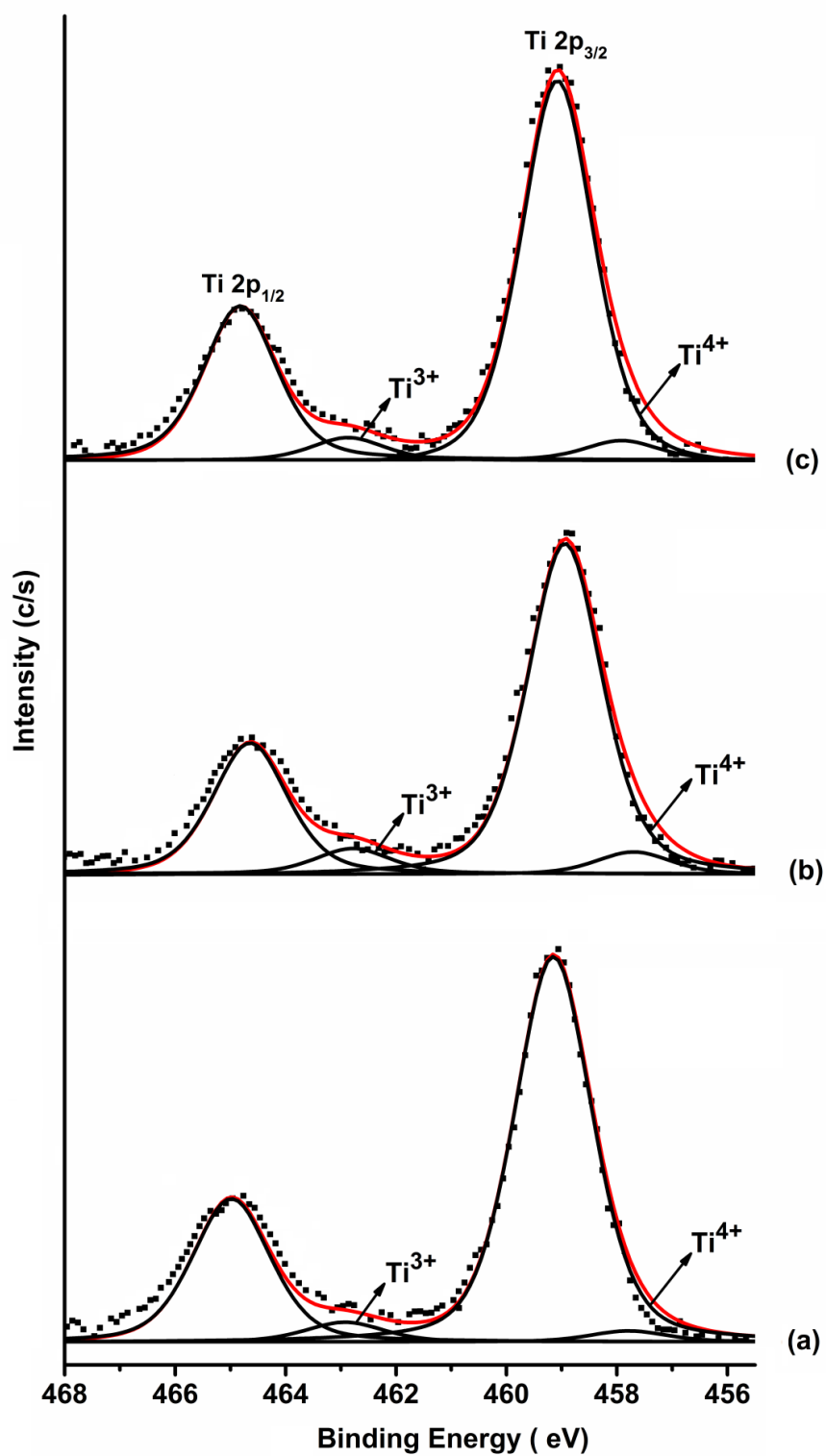
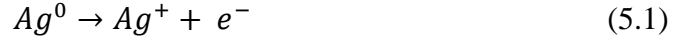


Figure 5.8. X-ray photoelectron spectroscopy (XPS) high resolution Ti 2p spectra of (a) I-Ag⁰-ETS-10 films, (b) 116-LT-ETS-10 films, (c) 5h-II-Ag⁰-ETS-10 films.

The oxidation state of the titanium is expected to shift from Ti^{4+} to Ti^{3+} for the cycle of $I-Ag^0-ETS-10 \rightarrow 116-LT-ETS-10$ and return back from Ti^{3+} to Ti^{4+} for the cycle of $116-LT-ETS-10 \rightarrow 5h-II-Ag^0-ETS-10$ as also shown in the equations below,



According to the XPS database [18], $Ti\ 2p_{3/2} - Ti\ 2p_{1/2}$ of Ti^{3+} Oxide and Ti^{4+} Oxide are given as $457.3 - 462.5 \pm 0.7$ eV and $458.7 - 462.4 \pm 0.2$ eV, respectively. As can be seen from Table 5.1, the relative peak area ratio of $Ti^{3+} / (Ti^{3+} + Ti^{4+})$ was increased from 3.69 to 5.44 % for the cycle of $I-Ag^0-ETS-10 \rightarrow 116-LT-ETS-10$ (Figure 5.8-a vs. -b) while decreased from 5.44 to 4.66 % for the cycle of $116-LT-ETS-10 \rightarrow 5h-II-Ag^0-ETS-10$ (Figure 5.8-b vs. -c). Accordingly, the XPS results proved that the valance state of the titanium shifted from Ti^{4+} to Ti^{3+} and vice versa for the films, which support the photochromic mechanism of the silver incorporated ETS-10 films indisputably in addition to the other results.

Table 5.1. Binding energy of the deconvoluted peaks of the Ti 2p and Ag 3d spectra and the corresponding relative sub-peak area ratios of the films.

Sample	BE of Ti 2p _{1/2} (eV)	BE of Ti 2p _{3/2} (eV)	BE of Ag 3d _{5/2} (eV)	*Area of Ti ³⁺ / (Ti ³⁺ + Ti ⁴⁺) (%)	#Area of Ag ⁺ / (Ag ⁺ + Ag ⁰) (%)	
I-Ag ⁰ -ETS-10	462.9	464.9	457.7	459.1	368.1	
				368.6	3.69	10.96
116-LT-ETS-10	462.7	464.6	457.7	458.9	368.1	368.5
					5.44	38.69
5h-II-Ag ⁰ -ETS-10	462.8	464.8	457.9	459.1	368.1	368.5
					4.66	29.67

*The percentage was calculated according to the ratio of the deconvoluted peak area at 462.9 eV (i.e., Ti³⁺) to total area.

#The percentage was calculated according to the ratio of the deconvoluted peak area at 368.5 eV (i.e., Ag⁺) to total area.

5.5 Mechanism of Photochromic Process of Titanosilicate ETS-10 Films

For reversible photochromic reactions, electron-hole (e^-h^+) pairs generated by electronic transition must react with each reactant in every cycle. For instance, in the structure of Ag^0 nanoparticle incorporated TiO_2 , electronic transition is generated through UV radiation and the created e^-h^+ pairs initiate several reactions for reversible photochromic process [9,10,19-22]. In the case of ETS-10, silica matrix should not contribute to electronic transition. Instead, TiO_3^{2-} quantum wires (i.e., Ti-O-Ti-O-Ti) are considered to be responsible for the electronic transition, which was also discussed in detail in the literature [23,24]. It was shown that the oxygen atoms along the TiO_3^{2-} quantum wires are confined in narrow range of energies, which suggests that electrons are confined in the TiO_6 octahedra [24]. Using DFT modeling of ETS-10 with 132 atoms where two Ti atoms were surrounded by Si and O atoms in one unit cell, band gap energy of ETS-10 was calculated as 3.37 eV [25].

Ag nanoparticles were modeled in a range of 0.9 nm to 2.0 nm, which varies in a range of about 20 to 300 atoms. Relaxation computations were completed for the eligible models (i.e. up to 150 atoms) under vacuum condition. Density functional theory (DFT) calculations within the gradient-corrected approximation (GGA) have been carried out on ETS-10 and silver nanoparticles with the aim to elucidate the effect of geometric optimization of particles and ETS-10 together. All interactions between atoms (i.e., the interaction between Ag and Si, O or Ti) were included in these calculations. 20-atom sized (i.e., 0.9 nm) silver nanoparticle was used for the DFT calculations instead of 300-atom sized (i.e., 2.0 nm) silver nanoparticle, since calculations did not converge due to quiet high number of atoms in one unit cell for a DFT input (i.e., total 432 atoms for 2.0 nm-sized nanoparticle). Relaxation calculations were completed under absolute temperature at vacuum level. The results suggest that ETS-10 had robust geometry and incorporation of the silver nanoparticles had minimal effect on the structure. However, in order to investigate the interactions in more detail, Molecular Dynamics (MD) simulations should be performed with temperature parameters. The Fermi level of the silver nanoparticles consisting of 20 Ag atoms in one unit cell (at size of ~ 0.9 nm) and conduction band

edge of ETS-10 were calculated to be -3.19 eV and -0.8 eV, respectively (Figure 5.9-a). Within the limitation of DFT study to find Fermi level accurately, it could be speculated that the Fermi level of the silver nanoparticles consisting of 20 Ag atoms matches with the band gap energy of ETS-10, which could enable transfer in redox reactions.

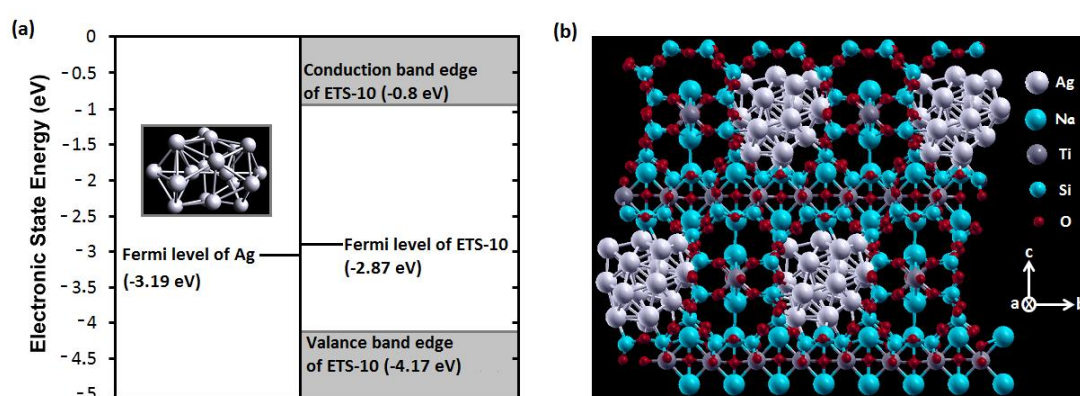


Figure 5.9. (a) Comparison between the position of the Fermi level of silver nanoparticles consisting of 20 atoms (~ 0.9 nm) and band gap energy of the ETS-10, (b) The silver nanoparticles consisting of 20 atoms that place within the ETS-10 pores.

Size of the silver nanoparticles formed affects the photochromic process due to the size dependent redox potential (or Fermi level) of silver nanoparticles. This is known to influence both thermodynamics and kinetics of the photoinduced dissolution of Ag^0 nanoparticles [26]. Han *et al.*, calculated that Ag^0 nanoparticles of a few nanometer sizes are subject to easier oxidation than those of over 20 nm in the viewpoint of thermodynamics [26]. In the case of zeolites, the cages and channels of zeolites provide a novel environment for molecular and nanoparticle assembly for photochemical reactions [27]. Dutta *et al.* showed that, zeolites can be active participants in reactions with photoexcited entrapped molecules as electron donors and acceptors [27]. As a result, the porous structure of the zeolites prevents

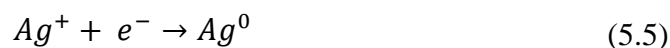
recombination of the charge-separated species. Accordingly, since the created Ag^0 nanoparticles are smaller due to the confining effect of the pores of ETS-10 matrix, they can be oxidized easily (Figure 5.7).

The proposed mechanism of photochromic process for ETS-10 films is given as following. The reduced metallic state is formed through thermal treatment. In the absence of thermal treatment (or after visible light radiation), the metallic Ag^0 nanoparticles gradually transform into oxidized state. The visible light accelerates oxidation process through photo-excitation of electrons of Ag^0 nanoparticles. The suggested reactions for the reversible photochromic process for Ag^0 nanoparticle incorporated ETS-10 is shown in the equations below.

The main reaction;



In the presence of thermal energy;



In the absence of thermal energy (or visible light radiation);



5.6 Conclusions

The photochromic behavior of Ag^0 nanoparticle incorporated ETS-10 and the possible role of the unique TiO_3^{2-} quantum wires in the photochromic mechanism were comprehensively investigated for the first time. For that purpose, Ag^+ ions were incorporated into ETS-10 matrix by ion-exchange of extra framework cations (i.e., Na^+ and K^+) to form Ag^+ ion-exchanged ETS-10. The redox process, which contains

colored form (i.e., activated state) of the photochromic system / colorless form (i.e., bleached state) of the photochromic system of Ag^0 nanoparticle incorporated ETS-10 films, was achieved through thermal reduction of the films and exposure of them to visible laser at wavelength of 532 nm, respectively. XRD, HR-TEM and UV-vis spectroscopy results showed that photochromic cycle was obtained for Ag^0 nanoparticle incorporated ETS-10 films. According to XPS results, the ratio of the deconvoluted peak area at 368.5 eV (i.e., Ag^+) to total area revealed that the ratio of the silver increased from 10.96 to 38.69 % for the cycle of I- Ag^0 -ETS-10 \rightarrow 116-LT-ETS-10 and decreased from 38.69 to 29.67 % for the cycle of 116-LT-ETS-10 \rightarrow 5h-II- Ag^0 -ETS-10, which was expected from the photochromic cycles. Furthermore, the XPS results proved that the valance state of the titanium shifted from Ti^{4+} to Ti^{3+} and vice versa for the films, which support the photochromic mechanism of the silver incorporated ETS-10 films indisputably in addition to the other results.

REFERENCES

- [1] N. Crespo-Monteiro, N. Destouches, L. Bois, F. Chassagneux, S. Reynaud, T. Fournel, *Adv. Mater.* 22 (29) (2010) 3166-3170.
- [2] N. Crespo-Monteiro, N. Destouches, L. Nadar, S. Reynaud, F. Vocanson, J.Y. Michalon, *Appl. Phys. Lett.* 99 (2011), 173106-3.
- [3] Z. Ji, M.N. Ismail, D.M. Callahan Jr., E. Pandowo, Z. Cai, T.L. Goodrich, K.S. Ziemer, J. Warzywoda, A. Sacco Jr., *Appl. Catal. B: Environ.* 102 (2011) 323-333.
- [4] G. Agostini, S. Usseglio, E. Groppo, M.J. Uddin, C. Prestipino, S. Bordiga, A. Zecchina, P.L. Solari, C. Lamberti, *Chem. Mater.* 21 (2009) 1343-1353.
- [5] S. Galioğlu, M. Zahmakıran, Y.E. Kalay, S. Özkar, B. Akata, *Micropor. Mesopor. Mater.* 159 (2012) 1-8.
- [6] Zahmakıran, M., Özkar, S., *Langmuir* 24 (2008) 7065-7067.
- [7] Zahmakıran, M., Özkar, S., *J. Mater. Chem.* 19 (2009) 7112-7118.
- [8] K. Matsubara, T. Tatsuma, *Adv. Mater.* 19 (2007) 2802-2806.
- [9] K. Kawahara, K. Suzuki, Y. Ohko, T. Tatsuma, *Phys. Chem. Chem. Phys.* 7 (2005) 3851-3855.
- [10] K. Naoi, Y. Ohko, T. Tatsuma, *Chem. Commun.* 10 (2005) 1288-1290.
- [11] Crespo-Monteiro et al. *Appl. Phys. Lett.* 99, (2011)173106.
- [12] C.C. Pavel, D. Vuono, L. Catanzaro, P. De Luca, N. Bilba, A. Nastro, J.B. Nagy, *Micropor. Mesopor. Mater.* 56 (2002) 227-239.
- [13] T. Das, A. Chandwadkar, A. Budhkar, S. Belhekar, S. Sivasanker, *Micropor. Mater.* 4 (1995) 195-203.
- [14] L. Bois, F. Chassagneux, Y. Battie, F. Bessueille, L. Mollet, S. Parola, N. Destouches, N. Toulhoat, N. Moncoffre, *Langmuir* 26(2) (2010) 1199-1206.
- [15] J.F. Moulder, *Handbook of X-ray Photoelectron Spectroscopy: A Reference Book of Standard Spectra for Identification & Interpretation of XPS Data*, Perkin Elmer Corporation: Eden Prairie, MN, 1992.
- [16] M. Zahmakıran, S. Özkar, *Langmuir* 25 (2009) 2667-2678.

- [17] L. Lv, F.Y. Lee, J. Zhou, F. Su, X.S. Zhao, *Micropor. Mesopor. Mater.* 96 (2006) 270-275.
- [18] C.D. Wagner, A.V. Naumkin, A. Kraut-Vass, J.W. Allison, C.J. Powell, J.R. Jr. Rumble, NIST Standard Reference Database 20, Version 3.4 (web version) (<http://srdata.nist.gov/xps/>) 2003.
- [19] Y. Ohko, T. Tatsuma, T. Fujii, K. Naoi, C. Niwa, Y. Kubota, A. Fujishima, *Nat. Mater.* 2 (2003) 29-31.
- [20] K. Naoi, Y. Ohko, T. Tatsuma, *J. Am. Chem. Soc.* 126 (2004) 3664-3668.
- [21] L. Nadar, R. Sayah, F. Vocanson, N. Crespo-Monteiro, A. Boukenter, S. Sao Joao, N. Destouches, *Photochem. Photobiol. Sci.* 10 (2011) 1810-1816.
- [22] A. Kafizas, C.W. Dunnill, I.P. Parkin, *Phys. Chem. Chem. Phys.* 13 (2011) 13827-13838.
- [23] A.M. Shough, D. Doren, *Chem. Mater.* 21 (2009) 1232-1241.
- [24] A. Damin, F.X.L. Xamena, C. Lamberti, B. Civalleri, C.M. Zicovich-Wilson, A. Zecchina *J. Phys. Chem. B* 108 (2004) 1328-1336.
- [25] M. Koc, S. Galioglu, D. Toffoli, H. Toffoli, B. Akata, in press.
- [26] R. Han, X. Zhang, L. Wang, R. Dai, Y. Liu, *Appl. Phys. Lett.* 98 (2011) 221905-3.
- [27] P.K. Dutta, M. Severance, *J. Phys. Chem. Lett.* 2 (2011) 467-476.

CHAPTER 6

PREPARATION OF ETS-10 FILMS BY USING SECONDARY GROWTH METHOD

6.1 Parameters that affect Microstructure of Titanosilicate ETS-10 Films

In the current thesis study, one of the objectives was to enhance the film formation methods in order to obtain continuous, well-intergrown ETS-10 films with columnar grain structure. For that reason, spin coating method was preferred with the intention to obtain thinner seed layered structures on ITO and α -alumina substrates as explained in Section 2.4. The following parameters affecting the microstructure of the ETS-10 films were studied:

- Concentration of ETS-10 seed crystals
- Number of spin coating step
- Reaction time of secondary growth
- Type of substrate

6.1.1 Effect of Seed Concentration and Number of Spin Coating Step

In the literature [1,2] and our previous study [3], suspensions containing 5 wt. % of 500 nm-sized ETS-10 crystals were dip-coated on substrates. In our previous study, single, double, and triple dip-coating steps were applied to obtain full coverage of seed crystals. The effect of dip-coating step on the preferred orientation of films was investigated. The results revealed that the thinnest film obtained by single dip-coating possessed the highest $a(b)$ -out-of-plane preferred orientation. Accordingly, in the current thesis study, instead of dip-coating, spin-coating method was chosen to form thinner seed layers. Based on the literature [1,2] and our previous studies [3],

the effect of seed concentration and the number of applied spin-coating steps were investigated to find out the parameters leading to the thinnest seed layer resulting in its full coverage over the chosen substrate of choice. This is crucial to obtain continuous, well-intergrown, defect- and crack-free films [1, 4-7].

For the above mentioned reasons, 5 wt. % ETS-10 was the starting concentration to be investigated. It was found that even if the number of spin-coating steps were increased, full coverage was very hard to obtain leaving apparent blank spots on substrates. Thus, 7 wt. % was the next concentration to investigate and examine whether continuous, crack free films were going to be obtained or not.

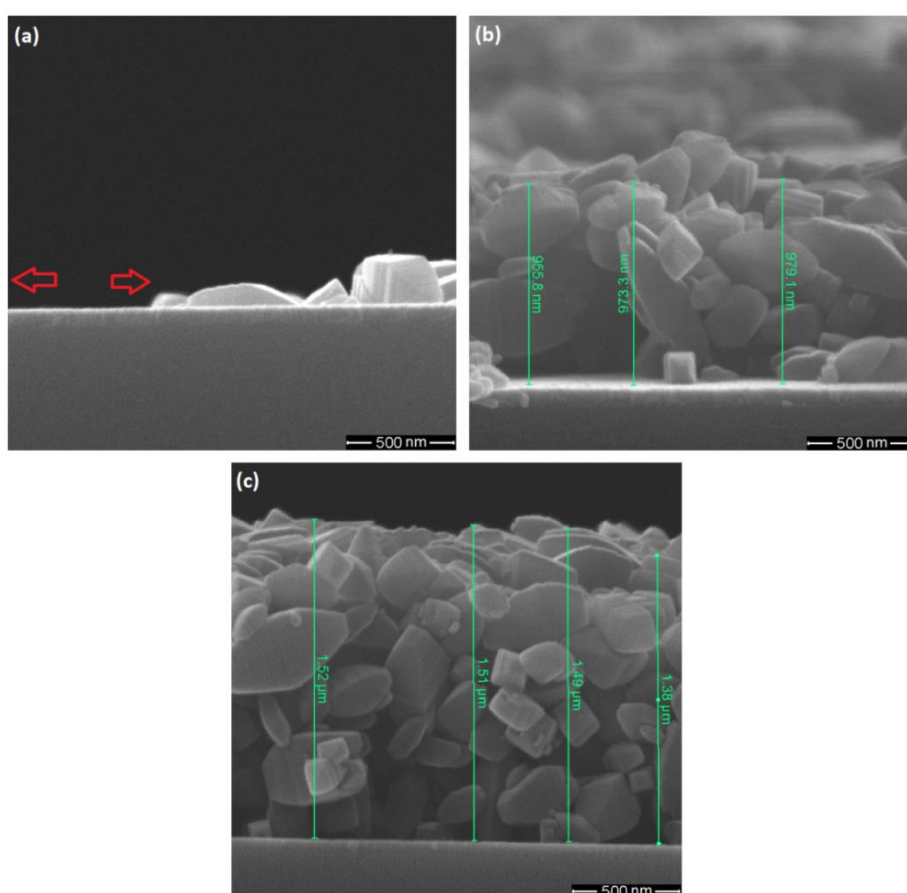


Figure 6.1. Cross sectional FE-SEM images of seed layers (a) 5-1S-ITO, (b) 7-1S-ITO, and (c) 7-2S-ITO.

Comparison of the Figure 1.15 [3] and Figure 6.1 shows that spin-coating method had been more sufficient with respect to dip-coating method to obtain thinner (i.e., 0.38 ± 0.03 and 0.50 ± 0.15 μm for single spin-coating and dip-coating, relatively) seed layer by applying 5 wt. % ETS-10 suspension. However, there were some noteworthy intercrystalline gaps between the seed crystals that can affect the final film microstructure (Figure 6.1-a). Secondary growth of seed crystals denoted as 5-1S-ITO (see Table 2.1 for denotation) was carried out to figure out effect of intercrystalline gaps between seed crystals as can be seen from Figure 6.2.

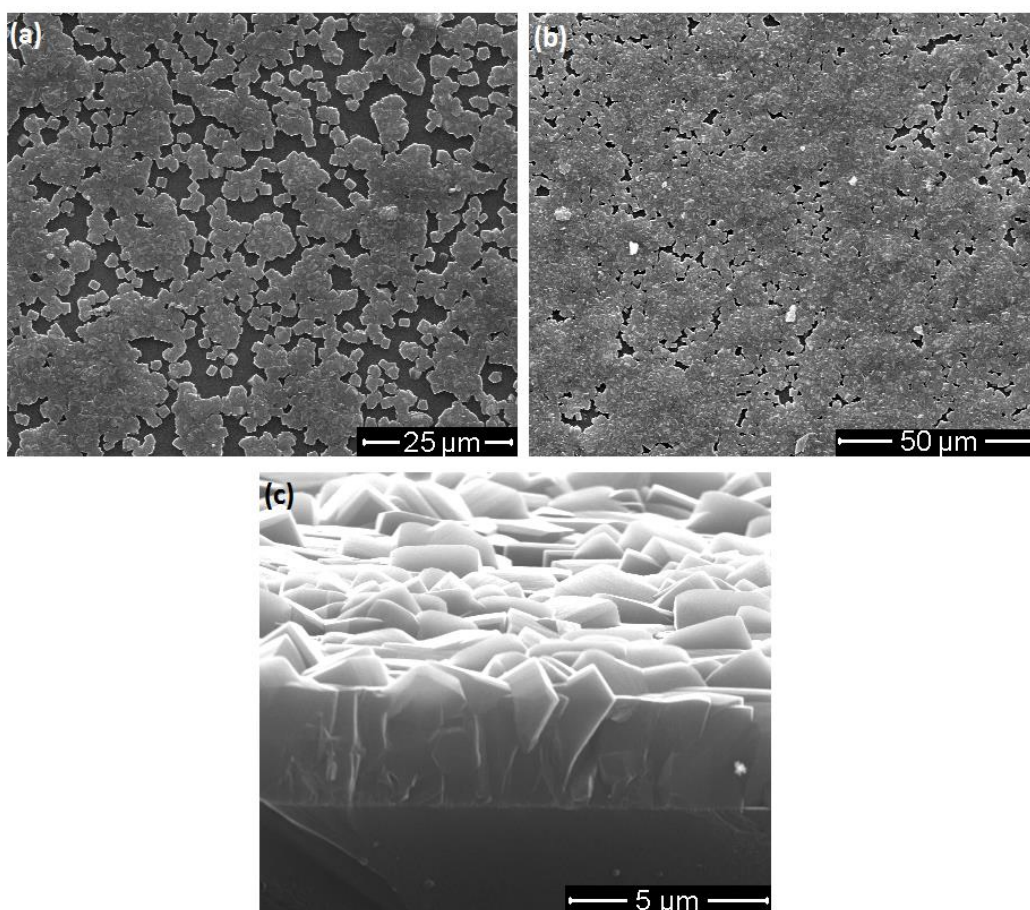


Figure 6.2. Top-view FE-SEM image of ETS-10 films (a) 5-1S-4h-ITO, (b) 5-1S-10h-ITO and (c) cross-sectional FE-SEM image of 5-1S-10h-ITO.

Figure 6.2-a displays ETS-10 films prepared on ITO glass using secondary growth of seed crystals formed by using single spin-coating step of 5 wt. % ETS-10 suspension, which shows well-grown columnar grain structure (*vide infra*). The reaction time of secondary growth was 4 hours. When the reaction time of secondary growth was increased from 4 hours to 10 hours, the intercrystalline gaps between the seed crystals were filled relatively (Figure 6.2-a vs. -b). However, even though in-plane growth was enhanced by increasing reaction time, it was not sufficient to fill the intercrystalline gaps between the seed crystals. In our previous study, after 4h-growth the obtained films were continuous (i.e., without intercrystalline gaps) even after single dip-coating step [3] (see Figure 1.15). However, 4 hours-secondary-growth of 5-1S-ITO seed layer was not adequate to obtain gap-free and continuous film since in-plane growth rate was not sufficient to fill the intercrystalline gaps between the seed crystals.

The top- (Figure 6.2) and cross-section-view FE-SEM images (Figure 6.1-a) showed that the concentration of the 5 wt. % ETS-10 ethanol suspension used to form seed layer was not sufficient to cover entire surface of the ITO glass substrate with seed crystals. Thus, the concentration of ETS-10 suspension was increased from 5 wt. % to 7 wt. % to enhance the coverage of seed crystals. The seed layer formed by single spin-coating step using 7 wt. % ETS-10 suspension (7-1S-ITO) was not sufficient to obtain full coverage as well. Therefore, number of spin coating step was increased from single (7-1S-ITO) to double to obtain full seed coverage (7-2S-ITO). Afterwards, the effect of reaction time was investigated for both 7-1S-ITO and 7-2S-ITO seed layers in order to obtain crack-free, continuous ETS-10 films.

The thicknesses of ETS-10 seed layers were 0.38 ± 0.03 , 0.90 ± 0.04 , and 1.12 ± 0.10 μm for 5-1S-ITO, 7-1S-ITO, and 7-2S-ITO, respectively. The thicknesses of the ETS-10 films were determined from at least twenty different spots of three cross sectional FE-SEM images. The average thicknesses of the films were determined and standard deviations were calculated to define margin of error. The thickness of seed layer prepared on ITO glass substrates via single spin-coating of 5 wt. % ETS-10 suspension (5-1S-ITO) was in the range of single ETS-10 crystal (i.e., 300-500 nm)

which in turn can enhance preferred orientation of the final film obtained through secondary growth method [3]. The cross-sectional-view FE-SEM images of 7-1S-ITO, and 7-2S-ITO displayed that the formed seed layers by using spin-coating method were randomly oriented (Figure 6.1).

For conductivity measurements (Chapter 7), ETS-10 films should be formed on non-conducting substrates such as; regular glass or α -alumina substrates. Unlike the films grown on ITO glass, the films prepared on regular glass peeled off the substrate during drying. ETS-10 film grown on the ITO glass was ultrasonicated in deionized water for up to 60 min, and there were no obvious differences in the substrate coverage of the film during the whole testing duration. This result is similar to the results of Yoon et al., who, using the secondary growth method were able to prepare zeolite Y films, which were more strongly attached on the ITO glass than on regular glass and fused silica substrates [8]. Thus, the reason for stronger bonding of zeolite/zeotype films to the ITO surface than to the glass/fused silica surfaces may be related more to the physical (e.g., contact area between crystals and the substrate) than the chemical (i.e., crystal/substrate surface termination) nature of the crystal/substrate interface [3]. When not completely covered with ETS-10 crystals covalently bonded to the fiber surface, fused silica fibers partially dissolved upon hydrothermal treatment in the secondary growth mixture, and crystals fell off the fibers [2]. Therefore, ETS-10 films were prepared on non-conducting α -alumina substrates using secondary growth method for conductivity investigation.

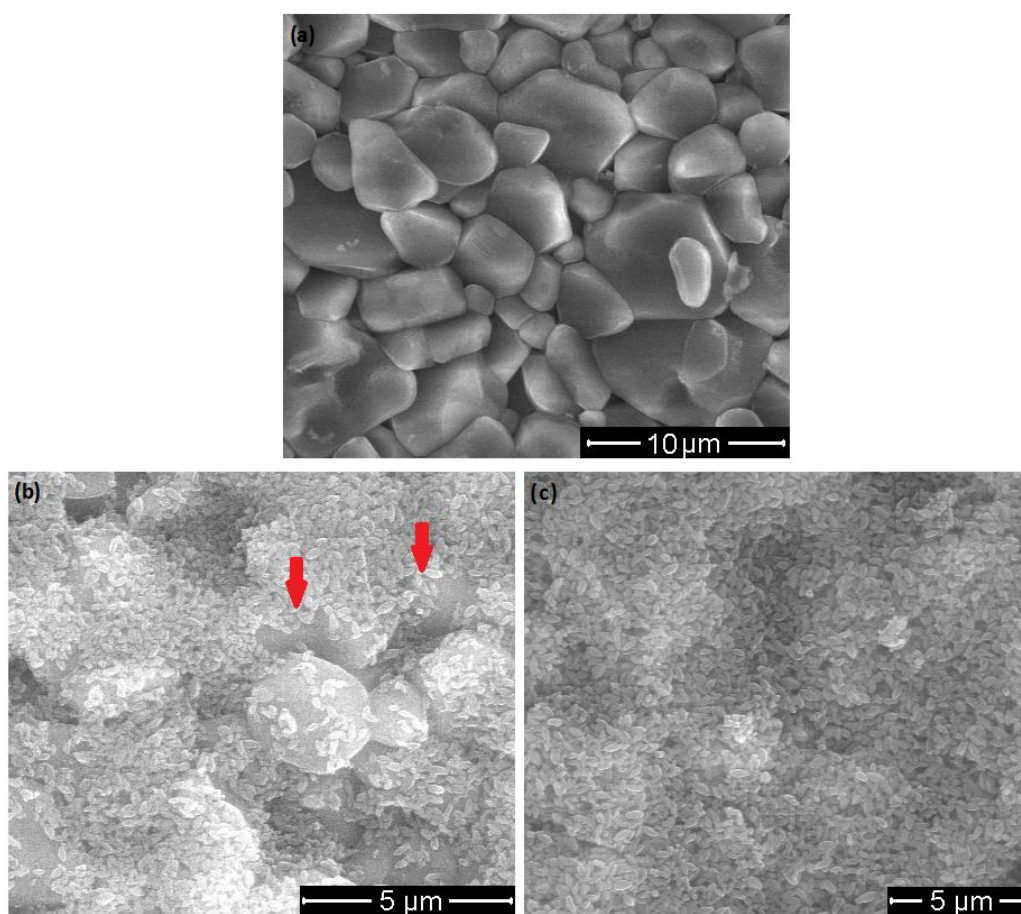


Figure 6.3. FE-SEM images of (a) bare α -alumina substrate, ETS-10 seed layers on α -alumina substrates (b) 7-1S- α -alumina and (c) 7-2S- α -alumina.

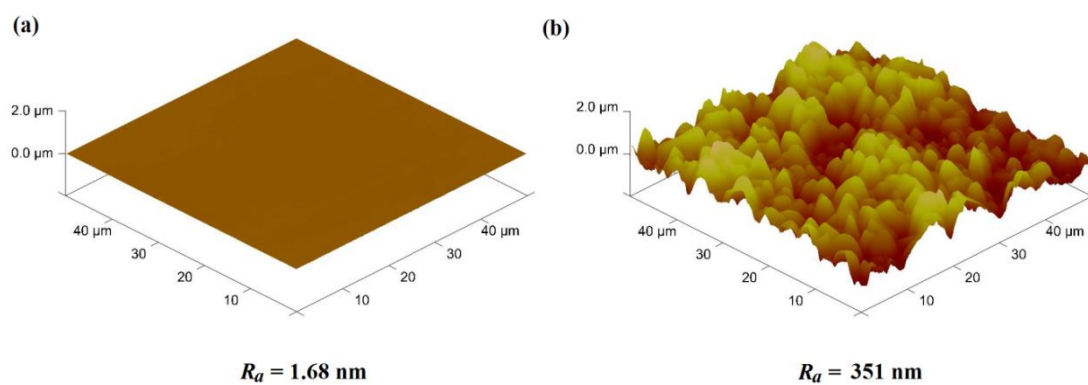


Figure 6.4. AFM images of bare (a) ITO glass and (b) α -alumina substrates.

The surface roughness of α -alumina substrates is high compared to ITO glass substrates (Figure 6.3-a and 6.4). Although ETS-10 seed layer prepared on ITO glass via single spin coating step of 7 wt. % ETS-10 suspension (7-1S-ITO) was not completely sufficient to obtain full coverage of seed crystal, the intercrystalline gaps between seed crystals were insignificant which could have been filled with in-plane growth (*vide infra*). In the case of α -alumina substrate, single (7-1S- α -alumina) and double (7-2S- α -alumina) spin coating steps were applied by using ethanol suspension containing 7 wt. % of ETS-10 as well. As can be seen from Figure 6.3-b the film coated via single spin coating step possess some noteworthy gaps, which in turn influence intergrowth of the final film negatively. Therefore, in the current thesis study the film coated via double spin coating step (7-2S- α -alumina) was investigated to obtain gap-free continuous films by using secondary growth method.

6.1.2 Effect of Reaction Time and Substrate Type

2-hours and 24-hours-growth were conducted to investigate minimum and maximum reaction time for secondary growth to obtain continuous, well-intergrown ETS-10 films with columnar grain structure. As can be seen from Figure 6.5-a and -b, 2-hours-reaction was not sufficient to obtain intergrown titanosilicate ETS-10 films. After 2-hours-reaction the morphology of the crystals on the substrate was identical to the initial seed crystals. The cross section FE-SEM image showed that the columnar grain structure was not formed in 2-hours-growth. Therefore, reaction times of 4-, 6-, 8- and 10-hours were also investigated.

Above mentioned problem was not observed for 4-, 6-, 8- and 10-hours-growth as shown in Figure 6.6. Further increase of the reaction time from 10 hours to 24 hours resulted in cracking and peeling off the film, which was shown in Figure 6.5-c.

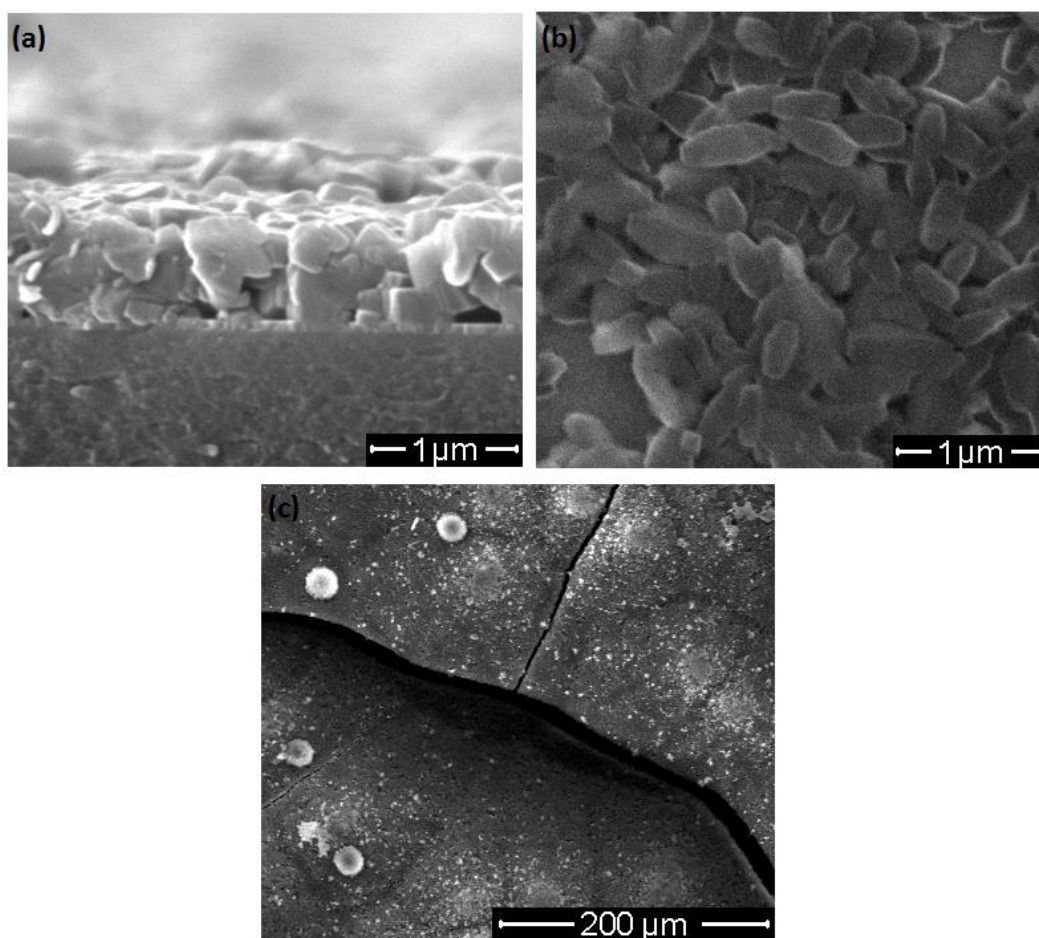


Figure 6.5. FE-SEM images of ETS-10 films (a) cross section of 7-1S-2h-ITO and top-view of (b) 7-1S-2h-ITO, and (c) 7-1S-24h-ITO.

FE-SEM analysis showed that full seed coverage cannot be obtained on ITO glass substrates after single spin-coating step using a suspension of 7 wt. % ETS-10, that is, some intercrystalline gaps existed between seed crystals. Nevertheless, in-plane growth rate was observed to be mostly sufficient to fill the gaps between seed crystals even after 4h-reaction although some gaps existed as shown in Figure 6.6-a (red arrows). The columnar grain structure of the films increased with increasing reaction time from 2h to 10h. According to the cross section FE-SEM images, columnar grain structure was not formed in 2-hours-growth, whereas it was successfully obtained for 4-, 6-, 8-, and 10-hours-growth (Figure 6.6).

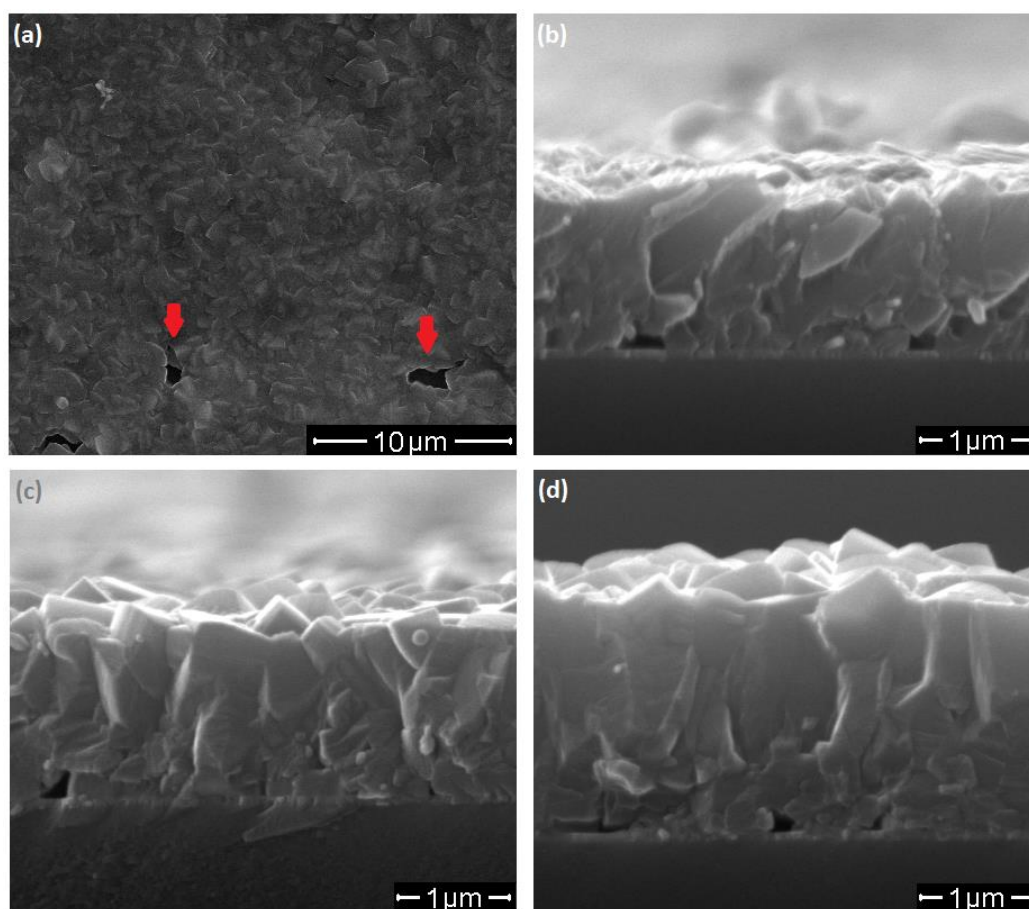


Figure 6.6. FE-SEM images of ETS-10 films prepared via secondary growth method (a) top-view of 7-1S-4h-ITO and cross section of, (b) 7-1S-4h-ITO, (c) 7-1S-6h-ITO, (d) 7-1S-8h-ITO.

Figure 6.6 vs. 6.2-c show the effect of orientation and thickness of seed layer on the final film microstructure. Upon using 5 wt. % ETS-10 suspension with single spin-coating, it was seen that only a single layer of ETS-10 seed crystal was formed on ITO glass with a seemingly better orientation with respect to 7 wt. % trials (Figure 6.1). Furthermore, the columnar grain structure seemed to be formed directly on the ITO layer (Figure 6.2-c). On the other hand, oriented columnar grain structures were obtained after $\sim 0.9 - 1 \mu\text{m}$ thickness from ITO layer for the secondary growth of 7-1S-ITO films according to the cross section FE-SEM images. This observed thickness of $\sim 0.9 - 1 \mu\text{m}$ correlates with the thickness of randomly oriented seed

layer (i.e., $0.90 \pm 0.04 \mu\text{m}$) (Table 6.1). Furthermore, some small gaps were observed between ITO layer and bottom of the grown film that cannot be filled (Figure 6.6), which could be due to “randomly oriented” seed layer.

The thickness of the columnar grain structure increased when the reaction time increased from 4h to 10h. The thicknesses of 0.64 ± 0.02 , 1.33 ± 0.03 , 1.41 ± 0.03 , 1.96 ± 0.02 , and 2.48 ± 0.03 were obtained for 7-1S-2h-ITO, 7-1S-4h-ITO, 7-1S-6h-ITO, 7-1S-8h-ITO, and 7-1S-10h-ITO samples, respectively (Table 6.1). The trend of ETS-10-film-thickness with respect to seed layer formation was discussed in the Section 6.2.

Table 6.1. Thicknesses of ETS-10 films prepared on ITO glass substrates using secondary growth of seed crystals 7-1S-ITO.

Sample	Reaction Time (Hours)	Thickness (μm)
7-1S-ITO	-	0.90 ± 0.04
7-1S-2h-ITO	2h	0.64 ± 0.02
7-1S-4h-ITO	4h	1.33 ± 0.03
7-1S-6h-ITO	6h	1.41 ± 0.03
7-1S-8h-ITO	8h	1.96 ± 0.02
7-1S-10h-ITO	10h	2.48 ± 0.03

Figure 6.7 shows XRD patterns of ETS-10 crystals in the powder form and ETS-10 films prepared on ITO glass substrates using secondary growth of seed crystals 7-1S-ITO. The characteristic ETS-10 pattern was obtained for the films grown through 2h, 4h-, 6h-, 8h-, and 10h-reaction. The XRD patterns revealed that the produced ETS-10 films do not contain impurities of TiO_2 , quartz or ETS-4 that is usually obtained in the synthesis of ETS-10. The peaks were broader for ETS-10 films compared to ETS-10 powder. For the powder form of ETS-10, standard powder attachment was

used with focusing beam (Bragg-Brentano) geometry, whereas for the film analysis, thin-film attachment with parallel beam geometry was used. The obtained peaks with Bragg Brentano geometry are sharper compared to parallel beam one due to geometry differences [9].

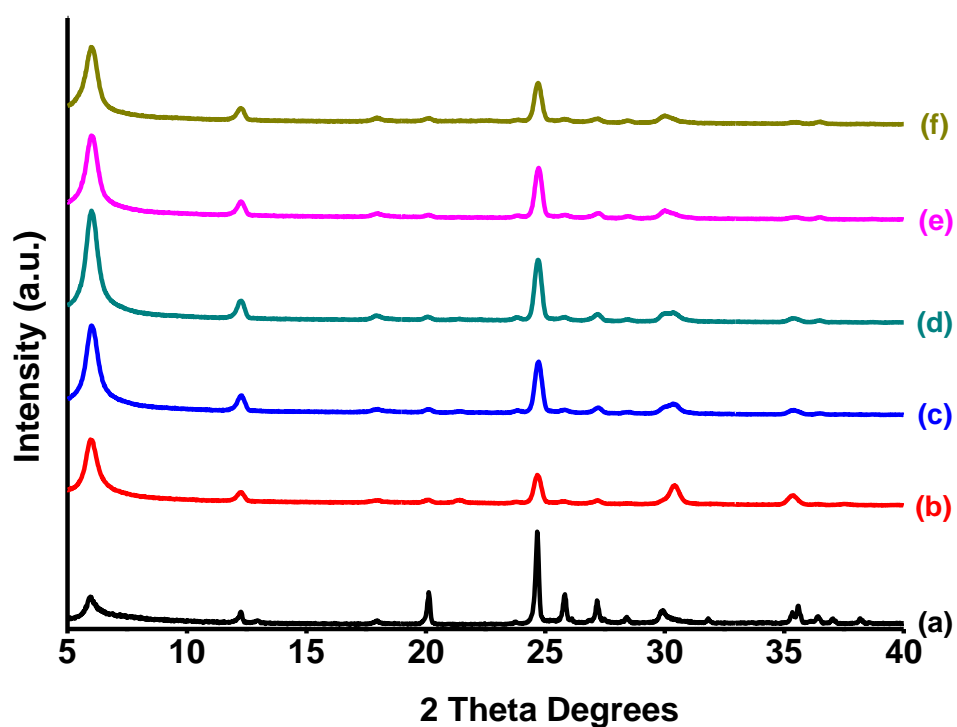


Figure 6.7. XRD patterns of (a) ETS-10 crystals in the powder form and ETS-10 films (b) 7-1S-2h-ITO, (c) 7-1S-4h-ITO, (d) 7-1S-6h-ITO, (e) 7-1S-8h-ITO, (f) 7-1S-10h-ITO.

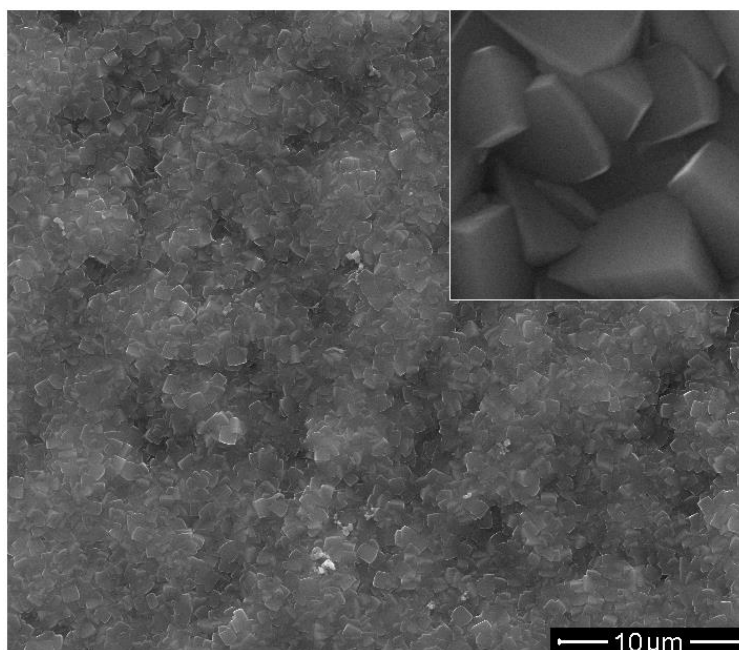


Figure 6.8. Top-view FE-SEM image of 7-2S-4h-ITO.

Fully covered, crack- and defect-free films were obtained after secondary growth of 7-2S-ITO seed layer (Figure 6.8). The inset shows interconnected ETS-10 seed crystals after secondary growth step. The cross sectional FE-SEM images showed that the fully-grown columnar grain structure was not formed after 4-hours-growth, where it was obtained for 6-, 8-, and 10-hours-growth (Figure 6.9). Similar to ETS-10 films prepared on ITO glass substrates using secondary growth of 7-1S-ITO seed crystals, some small gaps were observed between ITO layer and bottom of the grown film. The thickness of the columnar grain structure was increased when the reaction time increased from 4h to 10h (Figure 6.9). The thicknesses of 1.15 ± 0.03 , 1.45 ± 0.06 , 1.61 ± 0.03 , 2.40 ± 0.01 , and 3.43 ± 0.06 were obtained for 7-2S-2h-ITO, 7-2S-4h-ITO, 7-2S-6h-ITO, 7-2S-8h-ITO, and 7-2S-10h-ITO samples, respectively (Table 6.2). The high magnification FE-SEM image of ETS-10 film (i.e., 10h-reaction) displays uniformity of the intergrown film by using secondary growth method (Figure 6.9-a).

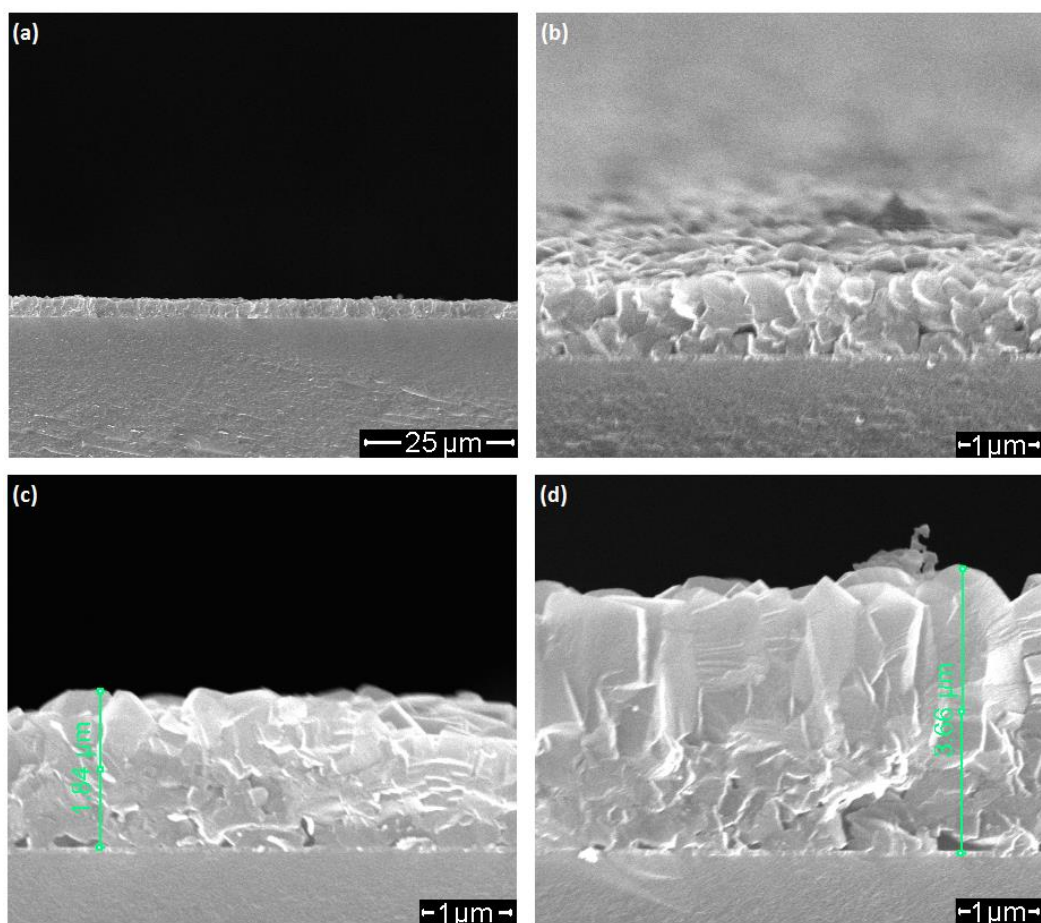


Figure 6.9. FE-SEM images of ETS-10 films prepared via secondary growth method (a) and (d) cross section view of 7-2S-10h-ITO, (b) 7-2S-4h-ITO, and (c) 7-2S-6h-ITO.

Table 6.2. Thickness of ETS-10 films prepared on ITO glass substrates using secondary growth of seed crystals 7-2S-ITO.

Sample	Reaction Time (Hours)	Thickness (μm)
7-2S-ITO	-	1.12 ± 0.10
7-2S-2h-ITO	2h	1.15 ± 0.03
7-2S-4h-ITO	4h	1.45 ± 0.06
7-2S-6h-ITO	6h	1.61 ± 0.03
7-2S-8h-ITO	8h	2.40 ± 0.01
7-2S-10h-ITO	10h	3.43 ± 0.06

In order to test these materials' conductivity in the application field and also to investigate the effect of substrate on ETS-10 film growth, α -alumina substrates were used instead of ITO glass to grow the films with similar experimental parameters. XRD patterns of ETS-10 crystals in the powder form and ETS-10 films prepared on α -alumina substrates using secondary growth of seed crystals formed via double spin-coating of 7 wt. % ETS-10 suspension are shown in Figure 6.10. As shown in Figure 6.10, the characteristic ETS-10 pattern was obtained for the films grown through 4h-, 6h-, 8h-, and 10h-reaction. Accordingly, ETS-10 films were successfully obtained on α -alumina substrates.

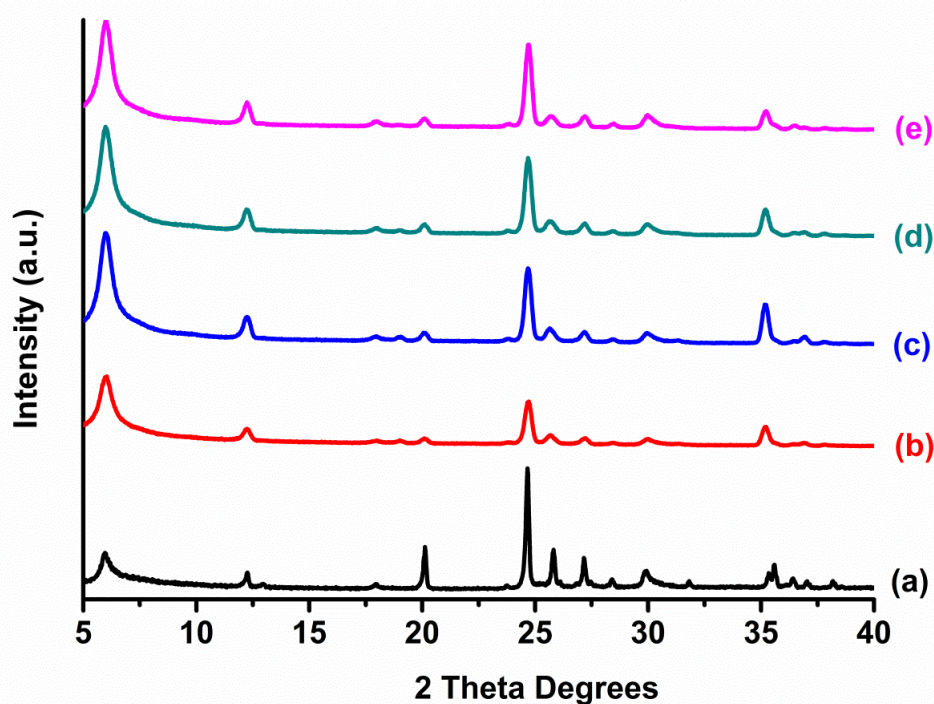


Figure 6.10. XRD patterns of (a) ETS-10 crystals in the powder form and ETS-10 films (b) 7-2S-2h- α -alumina, (c) 7-2S-4h- α -alumina, (d) 7-2S-6h- α -alumina, (e) 7-2S-8h- α -alumina, (f) 7-2S-10h- α -alumina.

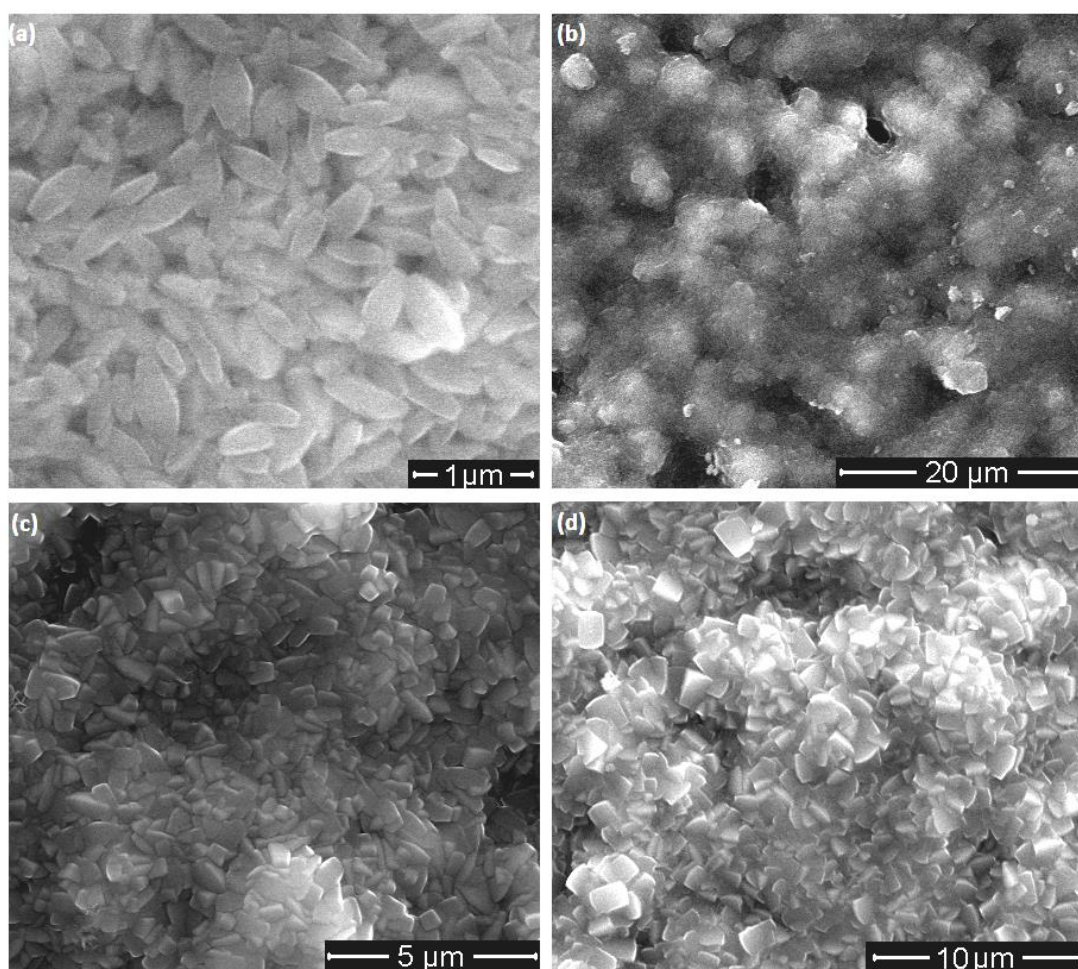


Figure 6.11. Top-view FE-SEM images of ETS-10 films prepared via secondary growth method, (a) 7-2S-2h- α -alumina, (b) 7-2S-4h- α -alumina, (c) 7-2S-6h- α -alumina and (d) 7-2S-10h- α -alumina.

The results of the effect of increased reaction time are shown in Figure 6.10. Top-view FE-SEM image of the 2h-reaction showed that 2h-reaction was not sufficient to obtain an intergrown film (Figure 6.11-a). Furthermore, the typical morphology of the intergrown film (i.e., in-plane grain dimensions) was not observed for 4h-growth on α -alumina unlike ETS-10 films prepared on ITO glass substrates (Figure 6.11-b). However, cross section FE-SEM image of 4h-growth showed well-grown and gap-free columnar grain structure (Figure 6.12-a). The well-grown columnar grain structure was also observed for 6h-, 8h-, and 10h-reaction times (Figure 6.12). The

thicknesses of 2.00 ± 0.08 , 2.19 ± 0.06 , 2.60 ± 0.05 , and 4.26 ± 0.07 were obtained for 7-2S-4h- α -alumina, 7-2S-6h- α -alumina, 7-2S-8h- α -alumina, and 7-2S-10h- α -alumina samples, respectively (Table 6.3). The trend of ETS-10-film-thickness with respect to seed layer formation was discussed in the Section 6.2. Due to high surface roughness of the α -alumina substrate (Figure 6.3-a), it was almost impossible to determine the thickness of the seed layer from cross section FE-SEM views.

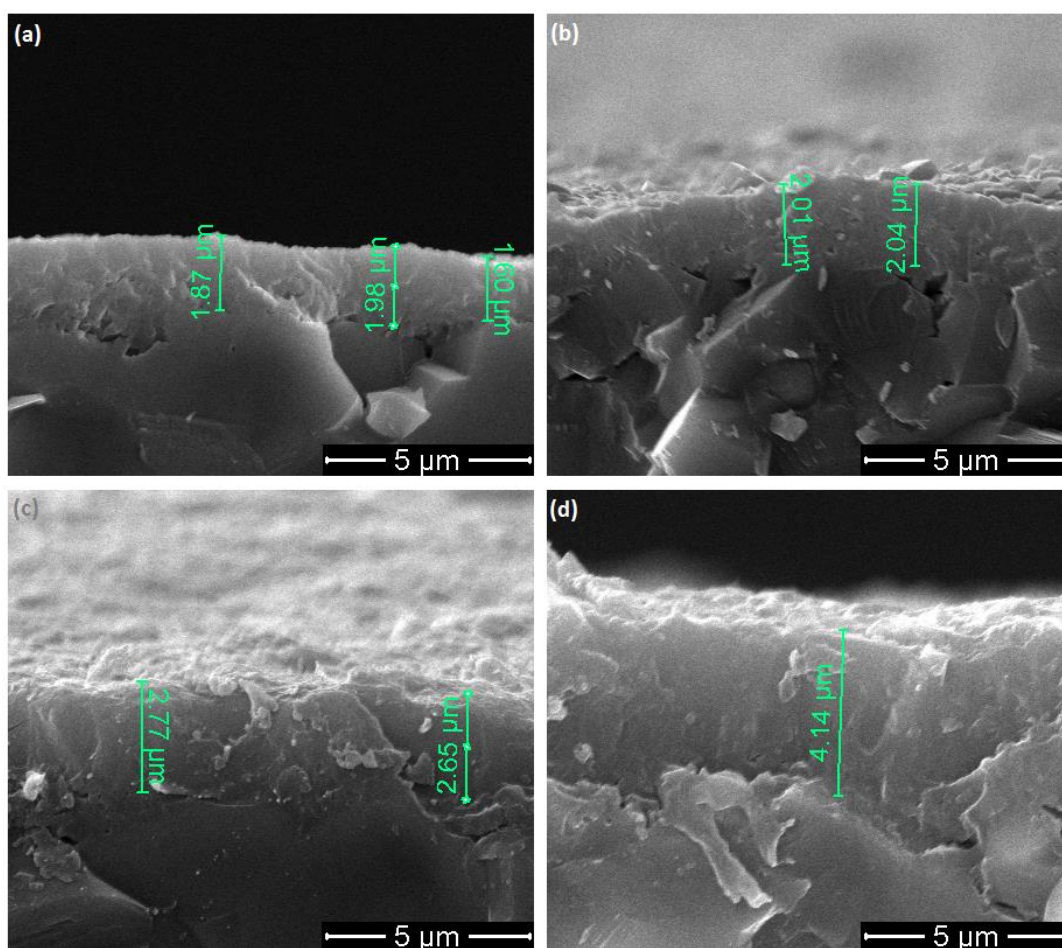


Figure 6.12. Cross section FE-SEM images of ETS-10 films prepared via secondary growth method, (a) 7-2S-4h- α -alumina, (b) 7-2S-6h- α -alumina, (c) 7-2S-8h- α -alumina and (d) 7-2S-10h- α -alumina.

Table 6.3. Thickness of ETS-10 films prepared on α -alumina substrates using secondary growth of seed crystals 7-2S- α -alumina.

Sample	Reaction Time (Hours)	Thickness (μm)
7-2S- α -alumina	-	-
7-2S-4h- α -alumina	4h	2.00 ± 0.08
7-2S-6h- α -alumina	6h	2.19 ± 0.06
7-2S-8h- α -alumina	8h	2.60 ± 0.05
7-2S-10h- α -alumina	10h	4.26 ± 0.07

6.2. Discussion

The thicknesses of the ETS-10 films were given in Table 6.4. In our previous study [3] single, double and triple dip-coating method was applied to obtain seed layers. 4h static hydrothermal reaction (i.e., secondary growth) was carried out at 200 °C. The most preferred oriented one was the thinnest ETS-10 film prepared by using single dip-coating step of 5 wt. % ETS-10 suspension (5-1D-4h-ITO). In the current thesis study, 2h to 10h static hydrothermal reactions (i.e., secondary growth) was carried out at 230 °C. As can be seen from Table 6.4, the thickness of the seed layer prepared on ITO glass by using single spin-coating step of 5 wt. % ETS-10 suspension was thinner compared to dip-coated films (5-1D-ITO vs. 5-1S-ITO).

Although identical secondary growth parameters were applied to obtain ETS-10 films, the thicknesses of the ETS-10 films prepared on α -alumina substrates using secondary growth of 7-2S- α -alumina seed crystals were higher than the films prepared on ITO glass substrates using secondary growth of 7-2S-ITO. The surface roughness of the α -alumina substrates was higher with respect to ITO glass substrates ($R_a = 351$ and 1.68 nm for α -alumina and ITO glass substrate, respectively). It seems that the surface roughness of the substrate was found to be a crucial parameter for

altering thickness of the films. The thickness of the columnar grain structure was increased when the reaction time increased from 4h to 10h.

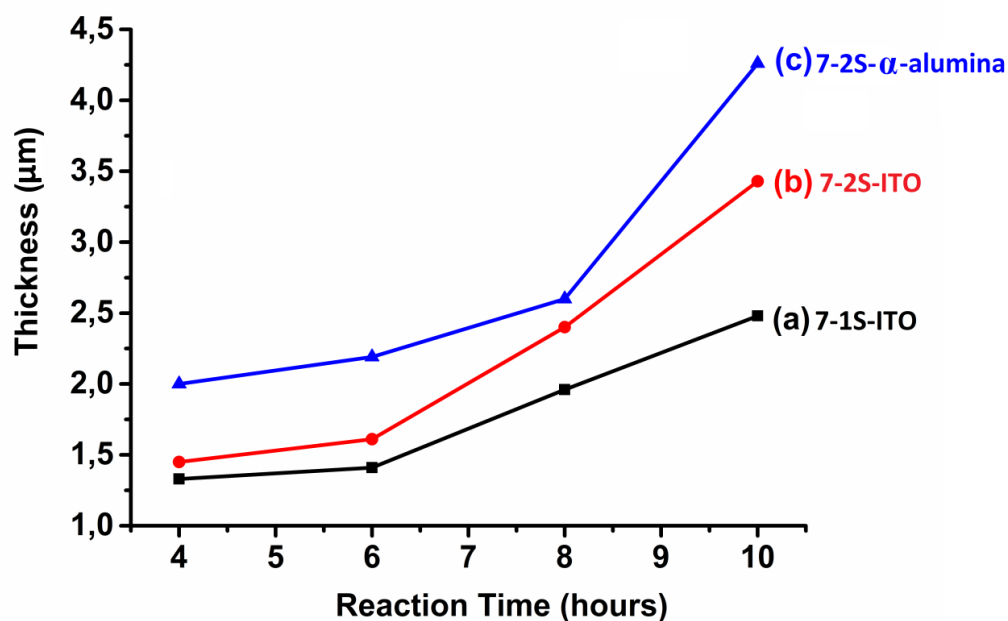


Figure 6.13. Comparison of ETS-10-film-thickness related to reaction time, (a) ETS-10 films prepared on ITO glass substrates using secondary growth of 7-1S-ITO seed crystals, (b) ETS-10 films prepared on ITO glass substrates using secondary growth of 7-2S-ITO seed crystals, (c) ETS-10 films prepared on α -alumina substrates using secondary growth of 7-2S- α -alumina seed crystals.

Table 6.4. Comparison of ETS-10-film-thickness related to reaction time.

Sample	Reaction Time (hours)	Thickness (μm)	Ref.
5-1D-ITO*	-	0.50 ± 0.15	[3]
5-2D-ITO*	-	0.60 ± 0.20	[3]
5-3D-ITO*	-	0.75 ± 0.25	[3]
5-1D-4h-ITO*	4h	1.50 ± 0.15	[3]
5-2D-4h-ITO*	4h	1.60 ± 0.20	[3]
5-3D-4h-ITO*	4h	1.75 ± 0.25	[3]
5-1S-ITO	-	0.38 ± 0.03	This study
7-1S-ITO	-	0.90 ± 0.04	This study
7-1S-2h-ITO	2h	0.64 ± 0.02	This study
7-1S-4h-ITO	4h	1.33 ± 0.03	This study
7-1S-6h-ITO	6h	1.41 ± 0.03	This study
7-1S-8h-ITO	8h	1.96 ± 0.02	This study
7-1S-10h-ITO	10h	2.48 ± 0.03	This study
7-2S-ITO	-	1.12 ± 0.10	This study
7-2S-2h-ITO	2h	1.15 ± 0.03	This study
7-2S-4h-ITO	4h	1.45 ± 0.06	This study
7-2S-6h-ITO	6h	1.61 ± 0.03	This study
7-2S-8h-ITO	8h	2.40 ± 0.01	This study
7-2S-10h-ITO	10h	3.43 ± 0.06	This study
7-2S- α -alumina	-	-	This study
7-2S-4h- α -alumina	4h	2.00 ± 0.08	This study
7-2S-6h- α -alumina	6h	2.19 ± 0.06	This study
7-2S-8h- α -alumina	8h	2.60 ± 0.05	This study
7-2S-10h- α -alumina	10h	4.26 ± 0.07	This study

* 5-1D-ITO, 5-2D-ITO , and 5-3D-ITO represent ETS-10 seed layers prepared on ITO glass using 1, 2, and 3 dip coating steps of ethanol suspension containing 5 wt.% of 500nm-sized ETS-10 crystals, respectively. 5-1D-4h-ITO, 5-2D-4h-ITO, and 5-3D-4h-ITO show ETS-10 films prepared on ITO glass via secondary growth (4h reaction) of those ETS-10 seed layers deposited using 1, 2, and 3 dip coating steps, respectively.

As explained in experimental Section 2.1.1 and 2.4.1, ETS-10 seed crystals were synthesized by using Degussa P25 TiO_2 as Ti source in the synthesis system of 3.4 Na_2O : 1.5 K_2O : TiO_2 : 5.5 SiO_2 : 150 H_2O (System I); whereas, titanium (III) sulfate ($\text{Ti}_2(\text{SO}_4)_3$) (Aldrich) was used as Ti source in the synthesis system of 3.4 Na_2O : 1.5 K_2O : TiO_2 : 5.5 SiO_2 : 180 H_2O (System II) [10] for secondary growth of seed crystals. The use of different titanium sources leads to the formation of ETS-10 crystals with different phase purity, particle morphology, and particle size [11]. As shown in Figure 1.4, the crystals displayed bipyramid morphology when P25 was used as Ti source; whereas, they showed truncated bipyramid morphology when TiCl_3 was used [10]. Different morphology of the crystals was explained by different rates of nucleation and crystal growth as Ti sources were altered [10]. When TiCl_3 was used as the Ti source, the rates of nucleation and crystal growth are slow since the step of oxidation of is very slow (the rate-limiting step), leading smooth and large crystals with a truncated bipyramid morphology [10]. Although titanium (III) sulfate ($\text{Ti}_2(\text{SO}_4)_3$) was used in our study as Ti source in the secondary growth of seed crystals instead of TiCl_3 , similar trend was observed, that is, the seed crystals displayed bipyramid morphology when P25 was used as Ti source; whereas, they showed truncated bipyramid morphology when titanium (III) sulfate ($\text{Ti}_2(\text{SO}_4)_3$) was used. Truncated bipyramid morphology of ETS-10 crystals was also observed in the literature when titanium (III) sulfate ($\text{Ti}_2(\text{SO}_4)_3$) was used as Ti source [12].

As mentioned in the Section 1.2.2, synthesis of titanosilicate ETS-10 is very sensitive to source materials, pH of synthesis gel, contents of water, Na^+ and K^+ ions in the synthesis gels, $\text{SiO}_2/\text{TiO}_2$ molar ratios, and temperature on the crystallization of ETS-10 [10]. The effect of different Ti sources was discussed above. The other parameters except water content were same for System I (i.e., seed crystals synthesis) and System II (i.e., secondary growth). The water content was increased in System II. In the literature [13], increasing water content in the ETS-10 synthesis utilizing titanium sulfate (TS-992) as Ti source resulted in relatively increased average a dimension than the average c dimension. The aspect ratio ($R = c \text{ dimension} / a \text{ dimension}$) of the crystals were 0.41 ± 0.01 and 0.25 ± 0.01 when water amount was 300 and 900 mol, respectively. When water amount was increased in the synthesis system, larger

degree of development of the square faces compared to trapezoidal faces was observed, which was attributed to the suppressed crystal nucleation and decreased crystallization rate in diluted synthesis mixtures [14]. In our synthesis system, both changing Ti source from P25 to titanium (III) sulfate ($\text{Ti}_2(\text{SO}_4)_3$) and increasing water amount of the synthesis mixture lead to more truncated bipyramid morphology and higher growth rate along their a and b directions.

Figure 6.14 shows effect of secondary growth gel parameters (i.e., different Ti source and increased amount of water in synthesis system) on the final film structure. The morphology of initial seed crystals was bipyramidal where the grown crystals in film were more equiaxed than the seed crystals. The growth rate of seed crystals was faster along their a and b directions as can be seen in Figure 6.14 (red arrow) since the secondary growth gel was chosen to have higher crystal growth rate in the a and b directions to that in the c direction with respect to the gel used to synthesize the seed crystals [3].

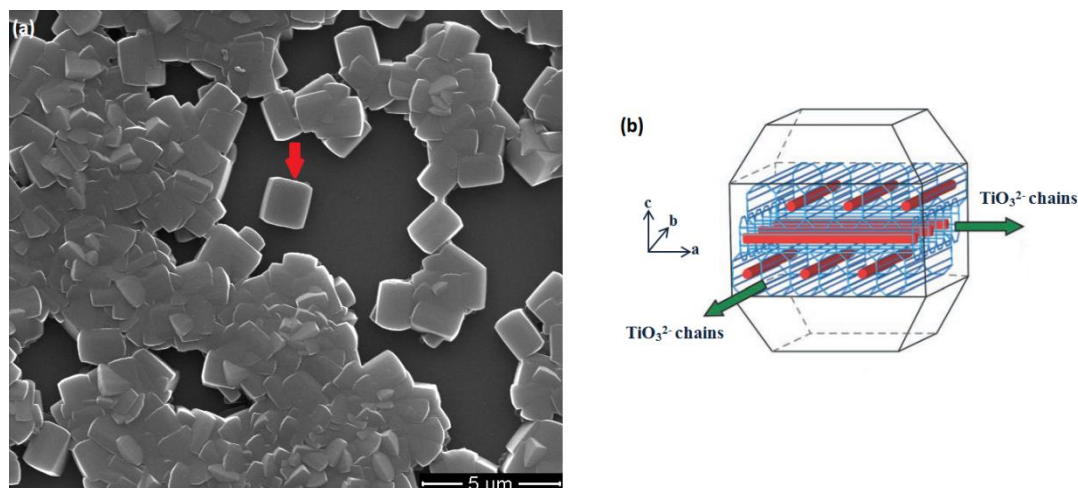


Figure 6.14. (a) Top-view FE-SEM image of 5-1S-4h-ITO, (b) Schematic view adapted from [15].

The van der Drift growth model, competitive growth of adjacent seed crystals, can be considered in the titanosilicate ETS-4 and ETS-10 film production on the substrates [3,6,7,16]. It is a competitive growth between crystallites that have different texture orientation and growth velocities. The crystals are randomly oriented in the beginning of the growth. However, with increasing reaction time, “crystallites having the most rapid growth direction perpendicular to the substrate (for example, {110} direction) will gradually overgrow their neighboring slowly growing grains and hence develop a columnar structure with a preferential orientation {110} normal to the substrate [17]”.

“In this faceted growth model, each crystal grows with facets moving with their characteristic normal growth rates until a facet meets the face of adjacent growing crystal. As the immobile grain boundary is formed upon adjacent crystals impingement, the crystals whose orientation is such that the fastest growing direction is perpendicular to the substrate will out-grow the neighboring crystals with other orientations. This implies that during the secondary growth step, the ETS-10 crystals on the surface of the seed layers grew directly by epitaxy (i.e., oriented overlayers) [3]”.

6.3 Conclusions

The current thesis study shows production of continuous, defect- and crack-free ETS-10 films by seeded hydrothermal synthesis (i.e., secondary growth) on ITO glass and α -alumina substrates. The synthesis parameters (reaction time, seeding procedure, seed concentration) have been investigated. The XRD patterns revealed that the produced ETS-10 films do not contain impurities of TiO_2 , quartz or ETS-4 that usually obtained in the synthesis ETS-10 crystals. FE-SEM images showed well-intergrown and 1.3 - 4.3 μm thick ETS-10 films with columnar grain structure. 4 hours-secondary-growth of the 5-1S-ITO seed layer was not enough to obtain continuous (i.e., without intercrystalline gap) film since in-plane growth rate was not sufficient to fill the gaps between the seed crystals. In-plane growth was relatively enhanced by increasing reaction time from 4h to 10h. However, when large distances

exist between the adjacent seed crystals (5-1S-ITO), increasing concentration of ETS-10 seed suspension (7-1S-ITO) and number of spin-coating step (7-2S-ITO and 7-2S- α -alumina) seems to be superior to increasing reaction time of secondary growth to obtain continuous films. According to FE-SEM analyses the van der Drift growth model, competitive growth of adjacent seed crystals, can be considered in the titanosilicate ETS-10 film production on the ITO glass and α -alumina substrates.

REFERENCES

- [1] Z. Lin, J. Rocha, A. Navajas, C. Tellez, J. Coronas, J. Santamaria, "Synthesis and Characterization of Titanosilicate ETS-10 Membranes", *Micropor. Mesopor. Mater.* 67, 2004, 79-86.
- [2] Z. Ji, J. Warzywoda, A. Sacco Jr., "Titanosilicate ETS-10 Thin Film Preparation on Fused Silica Optical Fibers", *Micropor. Mesopor. Mater.* 101, 2007, 279-287.
- [3] S. Galioğlu, M.N. Ismail, J. Warzywoda, A. Sacco Jr., B. Akata, "Preparation and Microstructural Characterization of Oriented Titanosilicate ETS-10 Thin Films on Indium Tin Oxide Surfaces", *Micropor. Mesopor. Mater.*, 131, 2010, 401-406.
- [4] C.M. Braunbarth, L.C. Boudreau, M. Tsapatsis, "Synthesis of ETS-4/TiO₂ Composite Membranes and their Pervaporation Performance", *J. Membrane Sci.* 174, 2000, 31-42.
- [5] B. Yilmaz, K.G. Shattuck, J. Warzywoda, A. Sacco Jr., "Controlling Crystal Orientation in Microporous Titanosilicate ETS-4 Films by Secondary Growth Method", *J. Mater. Sci.*, 2006, 41, 3135-3138.
- [6] B. Yilmaz, K.G. Shattuck, J. Warzywoda, A. Sacco, Jr., "Oriented Growth of ETS-4 Films Using the Method of Secondary Growth", *Chem. Mater.* 2006, 18, 1107-1112.
- [7] H. Jeong, J. Krohn, K. Sujaoti, M. Tsapatsis, "Oriented Molecular Sieve Membranes by Heteroepitaxial Growth", *J. Am. Chem. Soc.*, 2002, 124, 12966-12968.
- [8] H.S. Kim, M.H. Lee, N.C. Jeong, S.M. Lee, B.K. Rhee, K.B. Yoon, "Very High Third-Order Nonlinear Optical Activities of Intrazeolite PbS Quantum Dots", *J. Am. Chem. Soc.* 128, 2006, 15070-15071.
- [9] S. Mobilio, F. Boscherini, C. Meneghini, "Synchrotron Radiation: Basics, Methods and Applications", Springer-Verlag Berlin Heidelberg, 2015.
- [10] L. Lv, F. Su, X.S. Zaho, "A Reinforced Study on the Synthesis of Microporous Titanosilicate ETS-10", *Micropor. Mesopor. Mater.* 76, 2004, 113-122.

- [11] R. Xu, W. Pang, J. Yu, Q. Huo, J. Chen, "Chemistry of Zeolites and Related Porous Materials", Wiley, Singapore, 2007.
- [12] C.C. Pavel, I.V. Asaftei, Gh. Iofcea, P. DeLuca, D. Vuono, J.B. Nagy, A. Nastro, N. Bilba, in: E.W.J. vanSteen, L.H. Callanan, M. Claeys, C.T. OConnor (Eds.), Proceedings: 14th International Zeolite Conference, ISBN: 0-958-46636-X, p. 770.
- [13] Z. Ji, J. Warzywoda, A. Sacco Jr., "Synthesis and Morphological Control of Large Titanosilicate ETS-10 Crystals", Micropor. Mesopor. Mater. 109, 2008, 1-11.
- [14] Z. Ji, B. Yilmaz, J. Warzywoda, A. Sacco Jr., "Hydrothermal Synthesis of Titanosilicate ETS-10 using $\text{Ti}(\text{SO}_4)_2$ ", Micropor. Mesopor. Mater. 81, 2005, 1 - 10.
- [15] N.C. Jeong, M.H. Lee, K.B. Yoon, "Length-Dependent Band-Gap Shift of TiO_3^{2-} Molecular Wires Embedded in Zeolite ETS-10", Angew. Chem. Int. Ed. 2007, 46, 5868 - 5872].
- [16] B. Yilmaz, K. G. Shattuck, J. Warzywoda, A. Sacco Jr., "Controlling Crystal Orientation in Microporous Titanosilicate ETS-4 Films by Secondary Growth Method", J. Mater. Sci. 41, 2006, 3135-3138.
- [17] H. Fecht, K. Bruhne, P. Gluche, "Carbon-Based Nanomaterials and Hybrids: Synthesis, Properties, and Commercial Applications", Taylor & Francis Group, U.S., 2014, pp. 19.

CHAPTER 7

IONIC CONDUCTIVITY OF ZEOLITES AND ZEO-TYPE MATERIALS

The firmly-attached, defect- and crack-free ETS-10 films on conducting ITO glass and non-conducting α -alumina substrates were formed by using secondary growth of seed crystals. Several parameters affecting the microstructure of the ETS-10 films were investigated comprehensively in Chapter 6. In the last part of the current thesis study, the electrical properties of (i.e., ionic conductivity) of titanosilicate ETS-10 films prepared on α -alumina substrates via secondary growth method was investigated by using impedance spectroscopy at Central Laboratory, METU. A special furnace, Protherm, was purchased and a tubular quartz system was designed to study the ionic conductivity of microporous titanosilicate ETS-10 films in the temperature range of 25 to 500 °C by using impedance spectroscopy. Furthermore, Na^+ and K^+ ions within the framework of as-synthesized ETS-10 films were ion-exchanged with Li^+ , Ca^{2+} , and Zn^{2+} ions through homemade Teflon apparatus to figure out the effect of cation site occupancy on conduction. The long-range ionic conductivity of titanosilicate ETS-10 films prepared by secondary growth method was discussed in the following sections. Following parameters affecting the long-range ionic conductivity of ETS-10 films were studied:

- Hydration state (i.e., effect of temperature),
- Grain boundary structure (i.e., comparison of intergrown film versus powder samples),
- Cation site occupancy (i.e., effect of ion-exchange).

7.1 Measurement Methods

When conductivity of a material is ionic or mixed (i.e., electronic and ionic), impedance spectroscopy is the preferred tool in conductivity measurements. Accordingly, the response of the system to a periodic small ac signal was collected over varying ac frequencies (typically 10 Hz - 10 MHz). The analysis of the response detected can give insight information about sample [1]. Complex notation was used to simplify the calculations of impedances. To write complex impedance data, equivalent circuits were used in which R stands for resistance, $1/j\omega C$ for capacitance and $j\omega L$ for inductance (Section 1.2.6.2).

The equivalent circuit of the system was chosen to be combined combination of resistor and capacitor. Impedance plane plot (Argand diagram) can be obtained as a function of frequency. The low frequency intercept of the semicircle with the Z' (real) axis was used to calculate conductivity of the sample [2].

When impedance data were collected as a function of temperature, activation energy for transport, E_A , could be calculated by fitting conductivity data to equation below, where k is Boltzmann's constant, E_A is the activation energy, σ is the conductivity, σ_0 is the pre-exponential factor, and T is the temperature in Kelvin [2].

$$\sigma = (\sigma_0 / T) \exp (-E_A / kT) \quad (7.1)$$

$$\text{slope} = -E_A / k \quad (7.2)$$

Conductivity can be found from the equation below,

$$\rho = \frac{RA}{\ell} \quad (7.3)$$

$$\sigma = \frac{1}{\rho} \quad (7.4)$$

where, ρ is resistivity, R is the electrical resistance of a uniform specimen of the material (measured in ohms, Ω , from impedance spectroscopy), ℓ is the length of the piece of material (measured in centimeters, cm, $\ell = 0.1$ cm), A is the cross-sectional area of the specimen (measured in square centimeters, cm^2 , $A = 1.3$ cm x Film thickness (cm)) and σ is the conductivity ($\Omega^{-1}\text{cm}^{-1}$) (Figure 7.1).

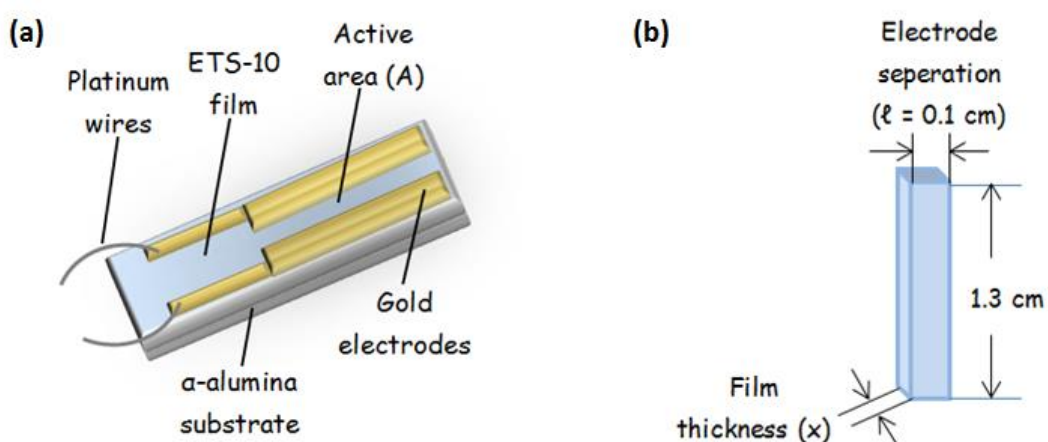


Figure 7.1. Representation of (a) ETS-10 film and gold electrodes, (b) active area of the film where conductivity is measured.

7.2 Ionic Conductivity of (Na^+ , K^+)-ETS-10 and FAU Films

As mentioned in Section 1.2.6.1, the conductivity values of the dehydrated zeolites can be located in the middle range with respect to the typical solid state electrolytes [3]. Though the intrinsic conductivity of the zeolites is restricted by their structure, ionic conductivity can be increased by using defect-free zeolite film since films possess noticeably lower electrical resistance than the compressed pellets usually that have been typically used in conductivity measurements. Therefore, engineering the microstructure and orientation of the zeolite film provide an advantage to improve conductivity of zeolites and zeo-type materials [4].

In the literature, ionic conductivity of pressed pellet of zeolite Y powder has been widely investigated [5-8]. Studies about ionic conductivity of zeolite membrane/film are limited. Dutta et al. studied ionic conductivity of zeolite Y membrane and they proposed that the use of zeolite membrane will improve response of sensors and lead to design of miniaturized sensors [9].

Accordingly, zeolite Y film (framework type FAU) was synthesized according to the procedure described in Section 2.5.2. The XRD data of zeolite Y film revealed that zeolite Y was the only phase without presence of any unknown phase. The reflections were matched with the database data of zeolite Y (Figure 7.2). Intergrown, crack-free zeolite Y film with columnar grain structure was obtained after 12h reaction as can be seen from Figure 7.3-a. The cross-section SEM images revealed that the average thickness of the films was $4.44 \pm 0.11 \mu\text{m}$ (Figure 7.3-b). The thicknesses of the zeolite Y films were determined from at least twenty different spots of three cross-section FE-SEM images. The average thicknesses of the films were determined and standard deviations were calculated to define margin of error. Si/Al ratio and Na concentration of the zeolite Y was determined to be 1.51 ± 0.01 and 14.90 ± 0.41 wt. % from energy dispersive X-ray spectroscopy (EDX) detector attached to the FE-SEM (accelerating voltage 10 kV).

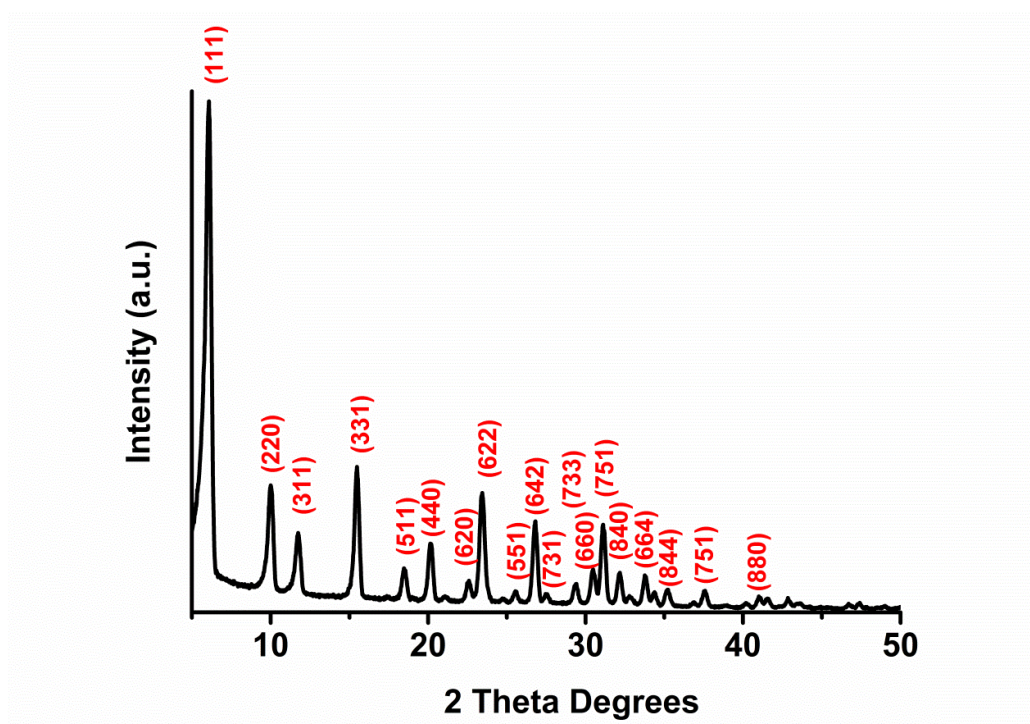


Figure 7.2. XRD pattern of zeolite Y films prepared via secondary growth method.

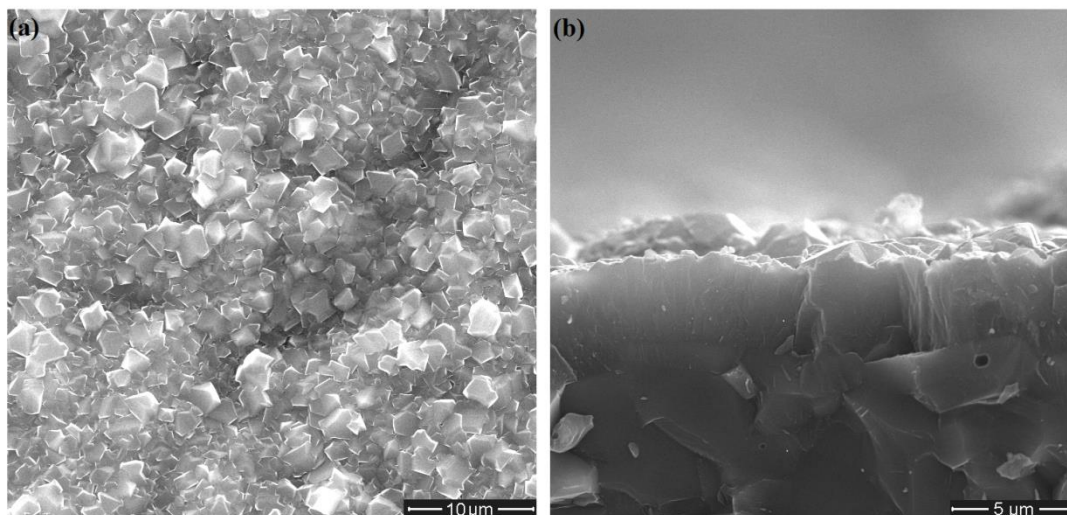


Figure 7.3. (a) Top-view and (b) cross-section FE-SEM images of zeolite Y films prepared on α -alumina substrates via secondary growth method.

The impedance of the all samples was collected in between 40 Hz to 1MHz in conjunction with the software of the impedance spectroscopy. The impedance data of the hydrated films was collected over the temperature range of 25 - 250 °C. For dehydrated films, all films were heated up to 250 °C for at least 12 h to ensure proper dehydration prior to characterization. Measurements of dehydrated samples were then taken in both increasing and decreasing temperature increments of 50 °C at least for two times.

7.2.1 Ionic Conductivity of Hydrated (Na^+ , K^+)-ETS-10 and FAU Films

Figure 7.4 and 7.5 display Arrhenius plot of conductivity of ETS-10 and zeolite Y films in the temperature range of 25 - 500 °C, respectively. The behavior of the film can be divided into three parts: (i) hydrated (~ 20 - 100 °C); (ii) desorption (~ 100 - 220 °C); (iii) dehydrated (~ 220 - 500 °C). Except the data collected at 25 °C for ETS-10 film, an increase in conductivity was observed with the degree of hydration. The sorption of various molecules on a zeolite affects state of cations and conductivity of the zeolite. It was found that the electrical conductivity of zeolites increases when there is water adsorption (i.e., hydrated samples) [7,10]. In the hydrated state, the cations are coordinated by water molecules, leading to a weaker interaction with the negatively charged lattice. Thus, the probability to move through the lattice is increased, i.e., the conductivity increases with the degree of hydration [7] (Figure 1.29).

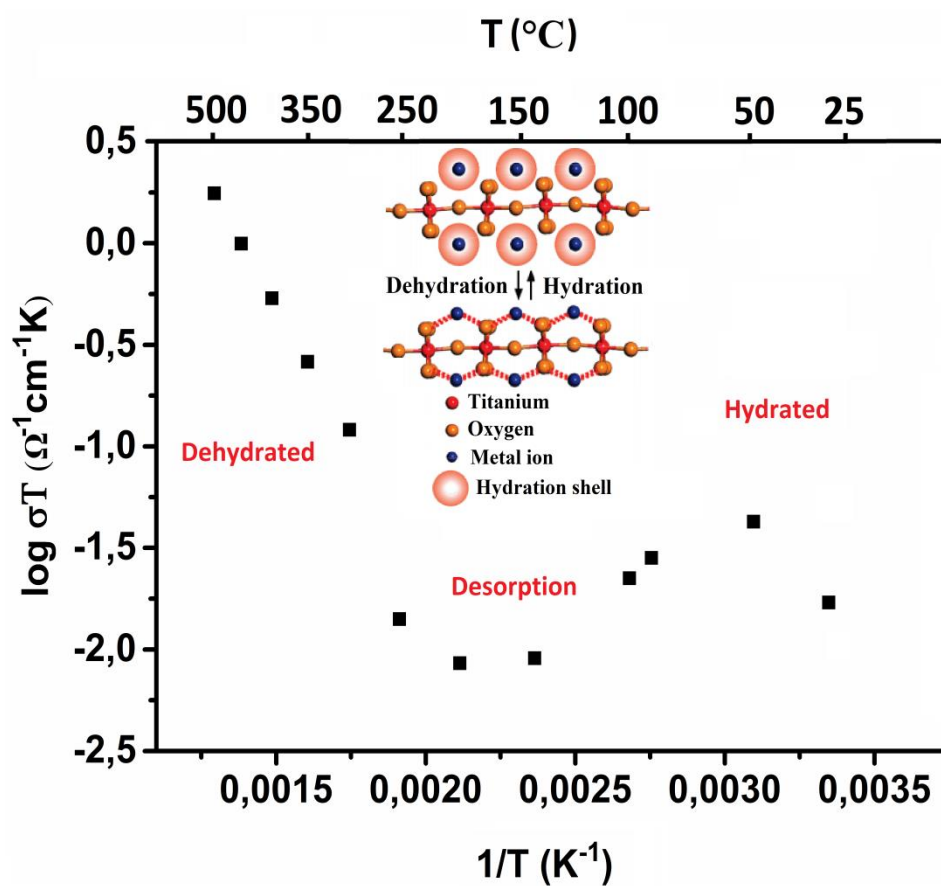


Figure 7.4. Arrhenius plot of conductivity for (Na,K)-8h-ETS-10 films, the inset figure is adapted from Yoon et al. [11].

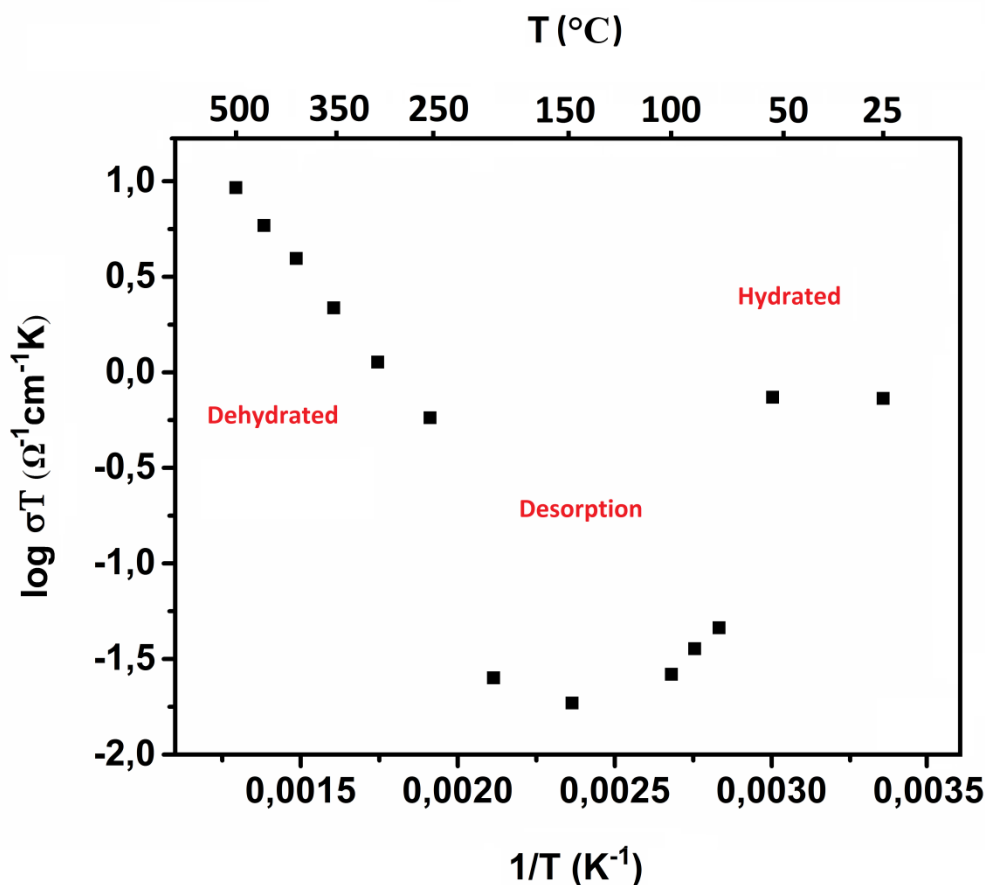


Figure 7.5. Arrhenius plot of conductivity for Na-Y films prepared by 12h-reaction.

In the desorption range, water is evaporated and cations are no longer coordinated by water molecules. Therefore, probability to move through the lattice is decreased; as a result conductivity is decreased. The extraframework cations in zeolite and zeo-type materials become mobilized by further increase temperature from 200 to 500 °C. Collecting impedance data of the films in their hydrated state can be misleading due to the variable hydration state of the films, because presence of water molecules modify the potential barriers for site hopping of cations leading to fluctuating conductivity values [4]. Accordingly, in the current thesis study, zeolite and zeo-type films in their dehydrated states were used to collect impedance data as a function of temperature and to calculate corresponding activation energy for transport. For that purpose, all films were heated up to 250 °C for at least 12 h to ensure proper dehydration prior to characterization. Measurements of dehydrated samples were

then taken in both increasing and decreasing temperature increments of 50 °C at least for two times.

7.2.2 Ionic Conductivity of Dehydrated (Na^+ , K^+)-ETS-10 and FAU Films

Characteristic impedance data for (Na,K)-ETS was displayed in an Argand diagram in Figure 7.6. The impedance spectra show a semicircle as a function of frequency. These spectra may be understood in terms of equivalent circuit models (Section 1.2.6.2). The semicircle of (Na,K)-ETS-10 becomes wider as the temperature is decreased, showing the decreased ionic conductivity (i.e., increased $Z' \approx$ resistance R).

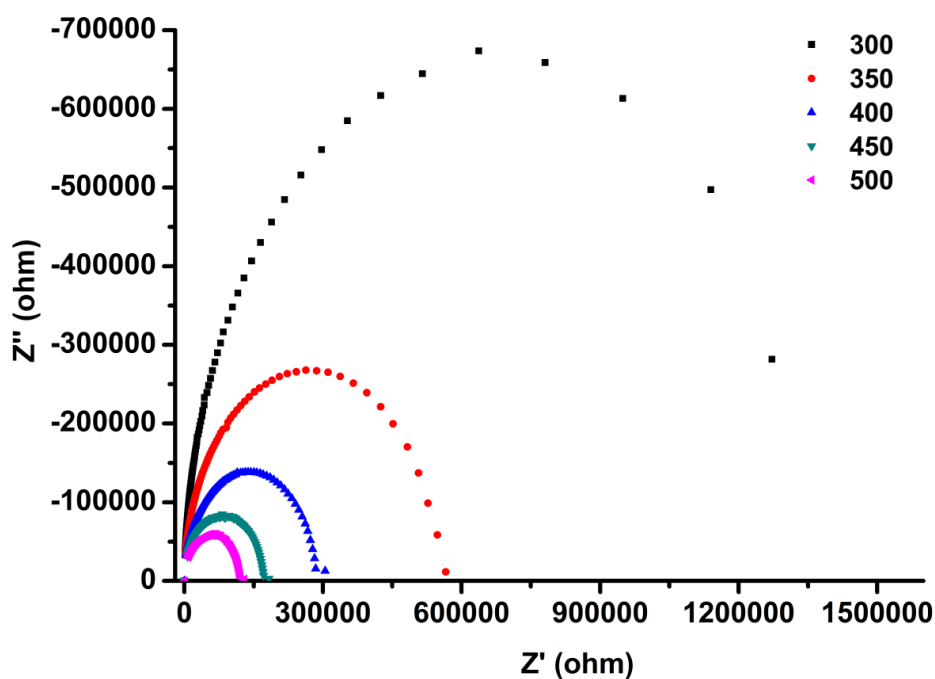


Figure 7.6. Argand diagram (plot of imaginary part of the impedance Z'' versus real part of the impedance Z' plotted parametrically as a function of frequency) of (Na,K)-6h-ETS-10 films.

The low frequency intercept of the semicircle with the Z' (real) axis (See Figure 1.20-b) was used to calculate the conductivity of the films by using equations 7.3 and 7.4. Then activation energy for transport (E_A) was calculated by using equation 7.1 (See Appendix A for an example). Figure 7.7 displays the Arrhenius plots of ionic conductivities for Na-Y films and (Na,K)-ETS-10 prepared by 6h-reaction. The activation energy of Na-Y film was calculated to be 38.4 kJ mol^{-1} (0.4 eV), which was lower compared to the result reported by Dutta et al. [12]. They concluded that activation energies increased with increasing Si/Al ratio for the membrane, commercial micrometer, submicrometer, nano, and synthetic micrometer zeolite Y with Si/Al ratios of 2.58, 2.5, 1.75, 1.68, and 1.48 have E_A of 93, 83, 78, 66, and 51 kJ mol^{-1} (i.e., 1, 0.9, 0.8, 0.7 and 0.5 eV), respectively since with lower Si/Al ratios there are more cations within the framework, and the cation-cation repulsion facilitates motion. The reported activation energy for pressed pellets of synthetic micrometer powder zeolite Y ($E_A = 51 \text{ kJ mol}^{-1}$, 0.5 eV) [12] can be compared with the activation energy of zeolite Na-Y film prepared in the current thesis study since Si/Al ratio of the samples was 1.5. The decreased activation energy (i.e., 51 kJ mol^{-1} to 38.4 kJ mol^{-1}) could be attributed to the decreased grain boundary obstacles in intergrown zeolite Y film with respect to the pressed pellets of powder zeolite Y.

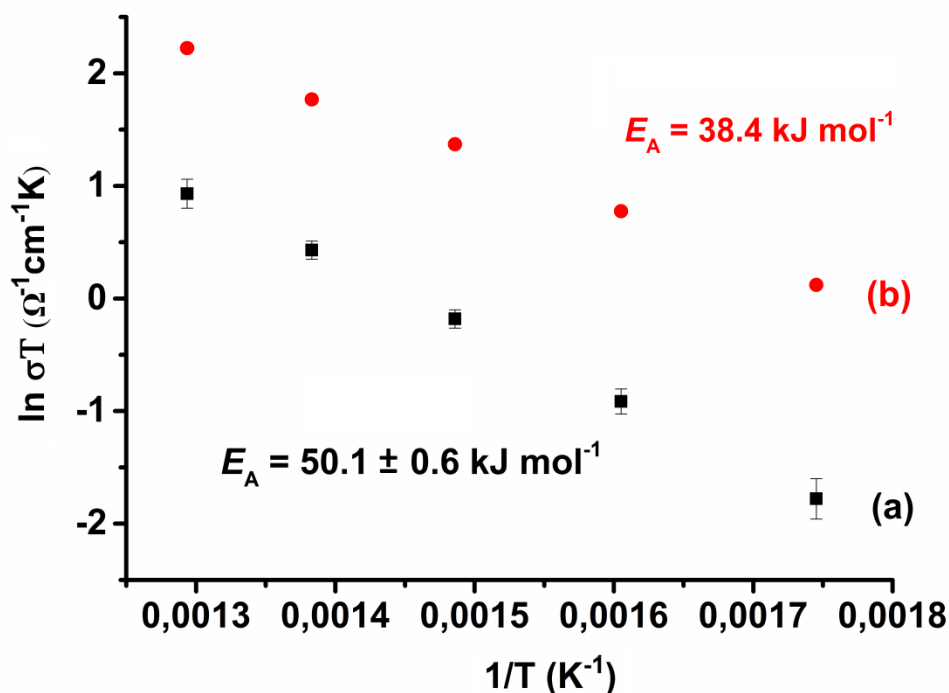


Figure 7.7. Arrhenius plots of ionic conductivities for (a) (Na,K)-6h-ETS-10 ($E_A = 50.1 \pm 0.6 \text{ kJ mol}^{-1}$) and (b) Na-Y films ($E_A = 38.4 \text{ kJ mol}^{-1}$).

Although zeolite Y had been widely investigated for its conductivity in the literature, to the best of our knowledge, there is only one literature report about the ionic conductivity of unmodified ETS-10 crystals [13]. ETS-10 has totally different in terms of structural properties, such as higher ion-exchange capacity due to its -2 net charge in its unit cell, channel like structure, and TiO_3^{2-} wires leading to special interest to investigate its electronic properties. In the literature, surface modified titanosilicate ETS-10 crystals were used, where the protonic conductivity of ETS-10 was tested for fuel cell applications [14]. Wei et al. [13] used pressed pellets of powder Na-ETS-10 to measure ionic conductivity of ETS-10 by using impedance spectroscopy. There are limited studies investigating conductivity of zeolites in their film form [12,15] and none for ETS-10 thin films in the literature.

In the current study, the activation energy of (Na,K)-ETS-10 films prepared by 6h reaction was measured and calculated to be $50.1 \pm 0.6 \text{ kJ mol}^{-1}$ (0.5 eV) (Figure 7.7).

The error bars were added from three independent impedance measurements of (Na,K)-6h-ETS-10 films. The pH of the secondary growth gels was 10.54, 10.50, and 10.57. It was found to have a lower activation energy for ion conduction and higher dc conductivity than that of Na-ETS-10 powder samples reported in the literature by Wei et al. [13], $50.1 \pm 0.6 \text{ kJ mol}^{-1}$ vs. 58.5 kJ mol^{-1} (i.e., 0.5 vs. 0.6 eV). The lower activation energy of the defect-free, intergrown ETS-10 film with respect to pressed pellets could be attributed to noticeably lower electrical resistance than the compressed pellets due to increased ionic current (flux) [4].

Si/Ti ratio and Na + K concentrations of (Na,K)-ETS-10 film prepared by 6h reaction (6h-(Na,K)-ETS-10) was determined via electron microprobe (EPMA) analysis using the wavelength-dispersive Cameca SX50 electron microprobe at Central Laboratory, METU. Si/Ti ratio, Na + K concentrations were found to be 5.08 ± 0.09 and $7.21 \pm 0.44 \text{ wt. \%}$ respectively as expected. Although both ETS-10 and zeolite Y were grown on α -alumina substrates using the same methodology resulting into continuous, intergrown films with columnar grain structure, still direct comparison of zeolite Na-Y films with (Na,K)-ETS-10 films would not be appropriate. This is due to the following parameters affecting ionic conductivity of the films, which were different: (i) pore structure (cages and channels for zeolite Y and zeo-type ETS-10, respectively), (ii) type of carriers (Na and Na + K for zeolite Y and zeo-type ETS-10, respectively), and (iii) concentration of carriers ($14.90 \pm 0.41 \text{ wt. \%}$ and $7.21 \pm 0.44 \text{ wt. \%}$ for zeolite Y and zeo-type ETS-10, respectively). The purpose of investigating conductivity of zeolite Na-Y film was to test our system design for conductivity measurement by using a well-known zeolite type. We were able to synthesize nano Y crystals, containing complex and difficult synthesis procedure, as seed crystals and to produce zeolite Y films on α -alumina substrates by using secondary growth method.

Conductivity measurements of both Na-Y and (Na,K)-ETS-10 films revealed that, although the intrinsic conductivity of the zeolites and zeo-type materials were restricted by their structure, their ionic conductivity was increased upon successful formation of their thin film forms by using structurally intergrown, defect-free

zeolite films. This can be due to the films' possessing noticeably lower electrical resistance than the pressed pellets, which are typically used in conductivity measurements [4].

7.2.2.1 Ionic Conductivity of Dehydrated (Na⁺, K⁺)-ETS-10 Films as a Function of Film Thickness

In Chapter 6, production of continuous, defect- and crack-free ETS-10 films by using seeded hydrothermal synthesis (i.e., secondary growth) on ITO glass and α -alumina substrates was discussed. Upon investigating the synthesis parameters (reaction time, seeding procedure, seed concentration), it was shown that the thickness of the columnar grain structure can be increased when the reaction time of secondary growth increased from 4h to 10h. To figure out the effect of grain boundary on ionic conduction, ETS-10 possessing different thicknesses of columnar grain structure (i.e., films prepared via 4h- to 10h-growth) was tested and the results are shown in Figure 7.8. The conductivity of the samples at 450 °C was in the range of $\sim 10^{-3} \Omega^{-1} \text{cm}^{-1}$ (Table 7.1). However, activation energy of the films decreased from 52.8 to 47.3 kJ mol⁻¹ (i.e., 0.6 to 0.5 eV) for 4h-(Na,K)-ETS-10 to 10h-(Na,K)-ETS-10 films (Table 7.1).

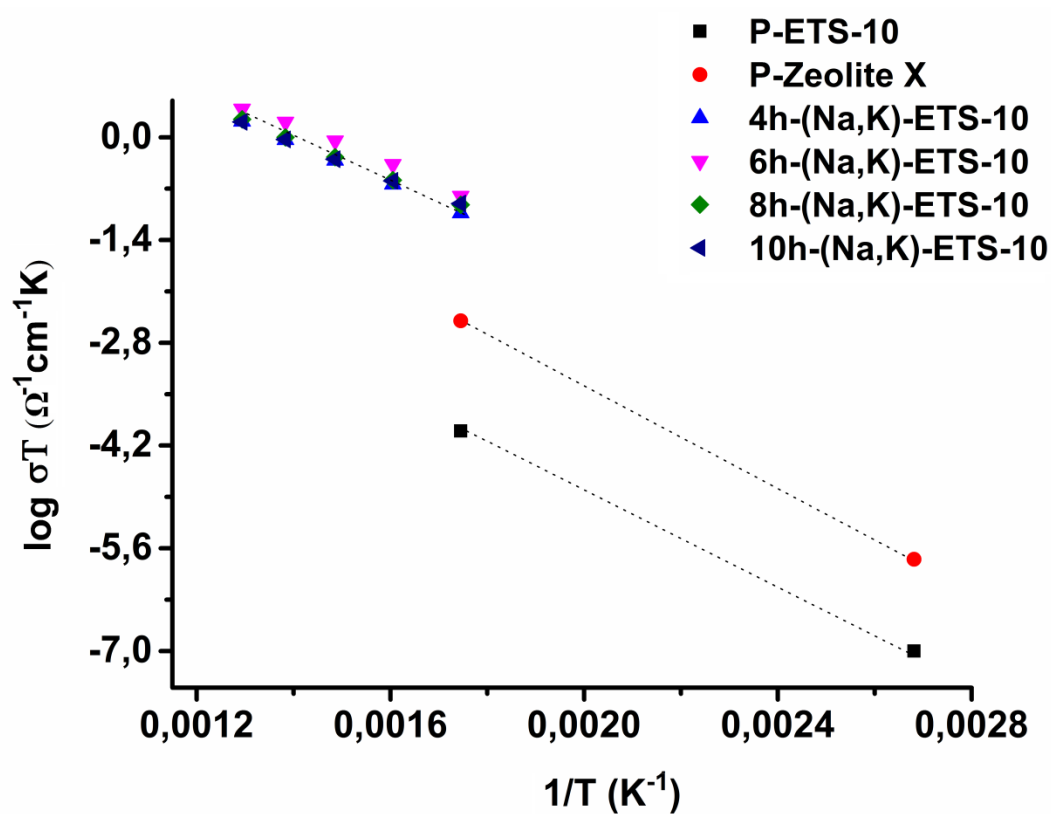


Figure 7.8. Arrhenius plots of ionic conductivities for (black) pressed pellets of powder ETS-10 (data was taken from literature [13]), (red) pressed pellets of powder zeolite X (data was taken from literature [13]), (blue) 4h-(Na,K)-ETS-10, (pink) 6h-(Na,K)-ETS-10, (green) 8h-(Na,K)-ETS-10, (purple) 10h-(Na,K)-ETS-10.

Table 7.1. Thickness, activation energy of transport (E_A), and conductivity values at 300, 450 and 500 °C for ETS-10 films.

Sample	Thickness (μm)	Activation Energy E_A (kJ mol^{-1})	Conductivity at 300 °C ($\Omega^{-1}\text{cm}^{-1}$)	Conductivity at 450 °C ($\Omega^{-1}\text{cm}^{-1}$)	Conductivity at 500 °C ($\Omega^{-1}\text{cm}^{-1}$)
(Na,K)-4h-ETS-10	2.00 ± 0.08	52.8	1.4×10^{-4}	1.1×10^{-3}	1.8×10^{-3}
(Na,K)-6h-ETS-10	2.19 ± 0.06	50.1	2.9×10^{-4}	2.1×10^{-3}	3.3×10^{-3}
(Na,K)-8h-ETS-10	2.60 ± 0.05	49.4	2.1×10^{-4}	1.4×10^{-3}	2.3×10^{-3}
(Na,K)-10h-ETS-10	4.26 ± 0.07	47.3	2.2×10^{-4}	1.3×10^{-3}	2.1×10^{-3}

As mentioned in the Chapter 6, the thickness of the connected columnar grain structure was increased when reaction time of secondary growth increased from 4h to 10h. The decreased activation energy from 4h-(Na,K)-ETS-10 to 10h-(Na,K)-ETS-10 films could be explained by increased columnar grain structure. Although activation energy of the transport was decreased, the conductivity of the films at 450 °C was not increased (i.e., $10^{-3} \Omega^{-1}\text{cm}^{-1}$), which could be explained by the unchanging concentration of charge carriers within the films (Na + K). Furthermore, the slope of the literature data [13] for powder pressed pellets of ETS-10 was in the same range of our ETS-10 films, which once again suggest our system design was appropriate for conductivity measurement of film samples.

All ETS-10 films prepared by using secondary growth method was found to have lower activation energy for ion conduction and higher dc conductivity than that of pressed pellets of powder ETS-10 and zeolite X (framework type FAU) samples reported in the literature.

7.2.3 Ionic Conductivity of Dehydrated M-ETS-10 (where, M = Li⁺, Zn²⁺, Ca²⁺) Films

Effect of charge-radius of extra-framework cations on ionic conductivity were extensively studied in the literature (Section 1.2.6.3.2). The coulombic attraction decreases between the counter ion and its site as the cation becomes larger; therefore, the activation energy E_A decreases with increasing monovalent-cation radius (r) for many Y-type faujasites. The activation energies of divalent cation-exchanged zeolite X- and Y-type faujasites increased with increasing ionic radius [3,6-8]. Based on the literature studies, conductivity of dehydrated M-ETS-10 (where, M = Li⁺, Zn²⁺, Ca²⁺) films prepared by 6h-growth were studied to figure out the effect of cation site occupancy on conduction as shown in Figure 7.9. First, exchangeable extraframework cations of Na⁺ and K⁺ in the framework of ETS-10 films were ion-exchanged with monovalent Li⁺ and divalent Ca²⁺ and Zn²⁺ cations by using LiCl, CaCl₂·2H₂O and ZnSO₄·7H₂O salt solutions. Arrhenius plots of ionic conductivities

for (Na,K)-6h-ETS-10, Li-6h-ETS-10, Zn-6h-ETS-10, and Ca-6h-ETS-10 films were shown in Figure 7.9-a, -b, -c, and -d, respectively.

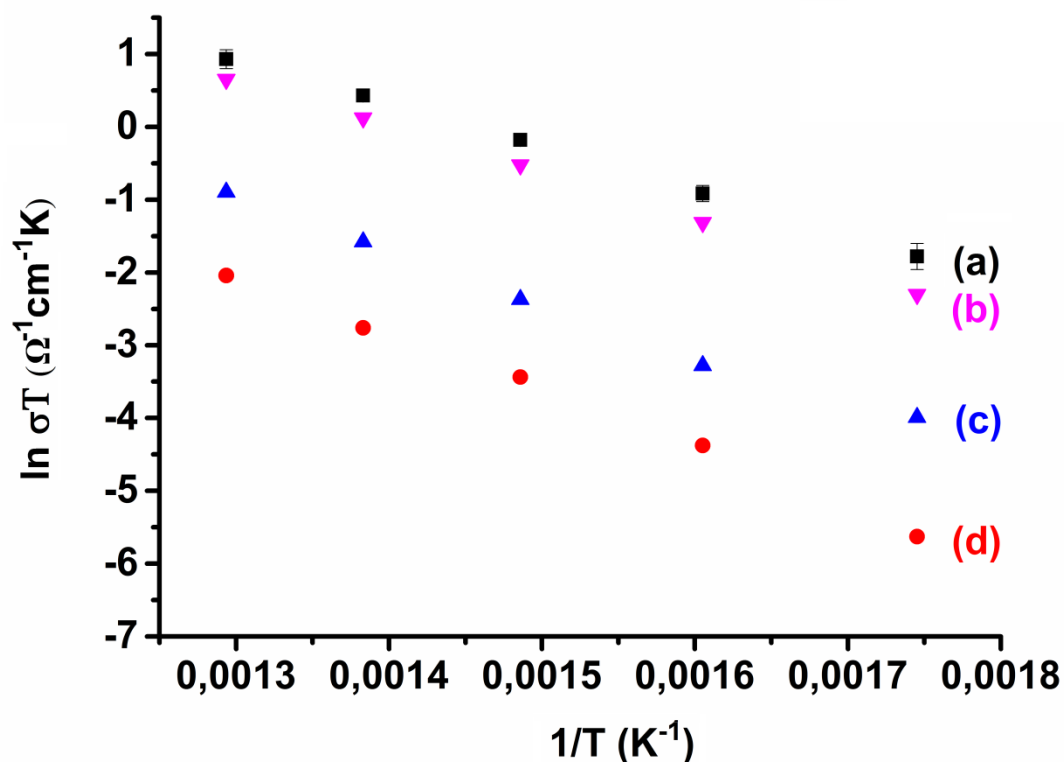


Figure 7.9. Arrhenius plots of ionic conductivities for (a) (Na,K)-6h-ETS-10, (b) Li-6h-ETS-10, (c) Zn-6h-ETS-10, and (d) Ca-6h-ETS-10 films.

For monovalent cations (Na^+ , K^+ , Li^+ etc.), the activation energy E_A decreases with increasing monovalent-cation radius (r) for many Y-type faujasites. The cation radius of K^+ , Na^+ , and Li^+ ions are 133, 97, and 68 pm, respectively [16,17]. The $E_A(r)$ behaviour of Li-6h-ETS-10 films going from Li^+ to (Na^+ , K^+) can be seen better in Figure 7.10 as the coulombic interaction decreases with increasing cation radius. The activation energies of Li-6h-ETS-10 and (Na,K)-6h-ETS-10 films were 54.5 and $50.1 \pm 0.6 \text{ kJ mol}^{-1}$ (i.e., 0.6 and 0.5 eV), respectively. In all type of zeolites (i.e., zeolite

X, Y and A), Li^+ -forms have high activation energy and subsequently low conductivity values. The small-sized Li^+ ions can penetrate into the tetrahedral structure and form covalent bonds with the tetrahedral oxygens [3,8], which cause a strong interaction with anionic framework. As a result, the total energy barrier for ion migration includes an additional term, i.e., *disassociation energy* [3]. The concentration of carriers, activation energy and conductivity values at 300, 450 and 500 °C for M-ETS-10 films can be found in Table 7.2.

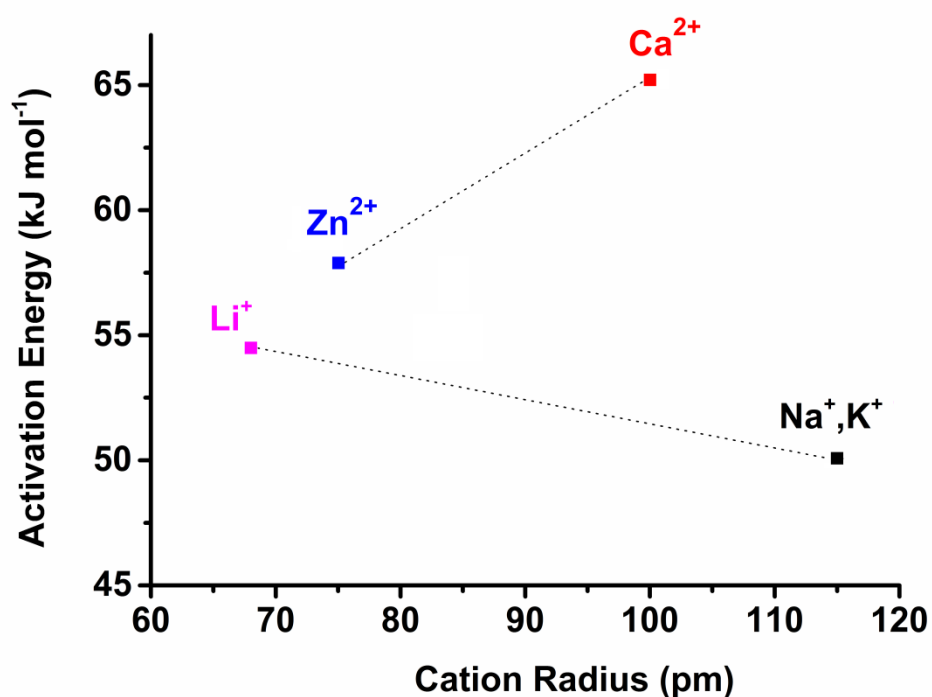


Figure 7.10. Relationship of activation energy (E_A) with cation radius (r) within the as-synthesized (Na,K)-6h-ETS-10 and partly ion-exchanged M-6h-ETS-10 films, where $M = \text{Li}^+$, Ca^{2+} , and Zn^{2+} .

The activation energies of divalent cation-exchanged zeolite X- and Y-type faujasites increased with increasing ionic radius [3,6-8]. Same trend was also observed for divalent cation-exchanged ETS-10 films. The cation radius of Ca^{2+} and Zn^{2+} ions are

100 and 75 pm, respectively [6]. The activation energy of the as-synthesized (Na,K)-6h-ETS-10 films ($50.1 \pm 0.6 \text{ kJ mol}^{-1}$) was increased from 57.9 to 65.2 kJ mol^{-1} (i.e., 0.6 to 0.7 eV) for Zn-6h-ETS-10 and Ca-6h-ETS-10 films, respectively (Table 7.2). The two sites of negative charge in the lattice are associated with each divalent cation. The calcium ion takes place between two relatively widely separated negative charges and the bond strength diminishes significantly. Sharp increase in E_A with increasing cation size indicates the greater ease of bonding to two crystallographically separated sites for the larger cations [8].

Table 7.2. Thickness, activation energy of transport (E_A), and conductivity values at 300, 450 and 500 °C for partly ion-exchanged M-ETS-10 films, where M = Li⁺, Zn²⁺, and Ca²⁺.

Sample	^Δ Concentration of (Na ⁺ + K ⁺) (mol)	^Δ Concentration of Li ⁺ , Zn ²⁺ , Ca ²⁺ (mol)	Si/Ti Ratios (mol)	Activation Energy E_A (kJ mol ⁻¹)	Conductivity at 300 °C ($\Omega^{-1}\text{cm}^{-1}$)	Conductivity at 450 °C ($\Omega^{-1}\text{cm}^{-1}$)	Conductivity at 500 °C ($\Omega^{-1}\text{cm}^{-1}$)
(Na,K)-6h-ETS-10	1.71 ± 0.06	-	5.1 ± 0.1	50.1	2.9 x 10 ⁻⁴	2.1 x 10 ⁻³	3.3 x 10 ⁻³
*Li-6h-ETS-10	0.74 ± 0.02	-	5.6 ± 0.2	54.5	1.7 x 10 ⁻⁴	1.6 x 10 ⁻³	2.5 x 10 ⁻³
Zn-6h-ETS-10	1.17 ± 0.04	0.08 ± 0.04	5.8 ± 0.2	57.9	3.2 x 10 ⁻⁵	2.9 x 10 ⁻⁴	5.2 x 10 ⁻⁴
Ca-6h-ETS-10	0.90 ± 0.04	0.14 ± 0.02	5.2 ± 0.2	65.2	6.3 x 10 ⁻⁶	8.8 x 10 ⁻⁵	1.7 x 10 ⁻⁴

*The concentration of Li cannot be determined from EPMA analysis.

^ΔThe values of wt. % were converted to mol based on stoichiometry of ETS-10 (Na,K)₂TiSi₅O₁₃.

Si/Ti ratios of the ETS-10 films were in the range of 5.1 - 5.8, which is 5 in an ideal ETS-10 crystals according to the stoichiometry of ETS-10 $(\text{Na,K})_2\text{TiSi}_5\text{O}_{13}$. The Si/Ti ratios revealed that the framework was disturbed by ion-exchange procedure; however, it was not altered significantly. Total exchangeable cations of ETS-10 crystals are 2 mol. Table 7.2 showed that Na+K value of (Na,K)-6h-ETS-10 films was 1.71 ± 0.06 mol, which could be accepted in an experimental error. Both monovalent (Li^+) and divalent (Zn^{2+} , Ca^{2+}) ion-exchanges were carried out for (Na,K)-6h-ETS-10 films, to measure conductivity of M-ETS-10, where $\text{M} = \text{Li}^+$, Zn^{2+} , Ca^{2+} . The concentration of monovalent Li cannot be determined from EPMA analysis. However, concentration of Zn-6h-ETS-10 and Ca-6h-ETS-10 films were determined to be 0.08 ± 0.04 and 0.14 ± 0.02 mol, respectively. Ion-exchange of (Na,K)-6h-ETS-10 films were carried out only 4h in 1mM salt solution to prevent peeling off the films from substrate. The results showed that, partial ion-exchange was achieved for the films. Although small amount of $\text{Na}^+ + \text{K}^+$ ions were ion-exchanged with Ca^{2+} and Zn^{2+} , similar trend in ionic conductivity with divalent cation-exchanged zeolite X- and Y-type faujasites was observed, that is, activation energy increased with increasing ionic radius (Figure 7.9 and 7.10). Activation energies of Zn-6h-ETS-10 and Ca-6h-ETS-10 films increased from 57.9 to 65.2 kJ mol⁻¹ (i.e., 0.6 to 0.7 eV) as ionic radius increased from 75 to 100 pm, respectively.

Both monovalent and divalent cation-exchanged (Na,K)-6h-ETS-10 films exhibited higher activation energies and lower conductivities in the temperature range of 300 - 500 °C with respect to as-synthesized (Na,K)-6h-ETS-10 films (Table 7.2). Furthermore, dc conductivities of zeo-type (Na,K)-6h-ETS-10 films ($\sim 10^{-3} \Omega^{-1}\text{cm}^{-1}$) were higher than that of pressed pellets of powder zeolite Y and zeolite X ($\sim 10^{-4} - 10^{-6} \Omega^{-1}\text{cm}^{-1}$) reported in the literature. As known from literature, zeolites are promising material to be used as an ion conductor due to well defined pores and mobile exchangeable cations which have been tested for many years. However, conductivity of zeolites is low (or middle range) with respect to the other ionic conductors. Two reasons are proposed: (i) the electrostatic interaction between negatively charged framework of zeolites and extraframework cations is strong, which hinders ion migration; (ii) the size of channels or cages of the zeolites is so

large that the mobile ions are trapped on the walls of the channels or cages that have sites with relatively high potential energy depths; therefore, the cations become partly immobilized [18]. Therefore to improve ionic conductivity of zeolites and zeo-type materials, the ion-channel size should be matched and the interaction between the anionic framework and the cations should be diminished. To investigate these effects, ionic conductivity of zeo-type crystalline materials has been examined in the literature [2,13,18]. Our results showed that dc conductivities of zeo-type (Na,K)-6h-ETS-10 films ($\sim 10^{-3} \Omega^{-1}\text{cm}^{-1}$) were higher than that of pressed pellets of zeo-type cation-exchanged powder sodium hydrogen germanate ($\sim 10^{-3} - 10^{-4} \Omega^{-1}\text{cm}^{-1}$) and zincosilicate VPI-9 ($\sim 10^{-4} - 10^{-7} \Omega^{-1}\text{cm}^{-1}$) (See Table 1.6 and 1.7).

7.3 Conclusions

Impedance spectroscopy was used to investigate the long-range ionic conductivity of microporous titanosilicate ETS-10 films prepared through secondary growth method. (Na,K)-ETS-10 films were found to have lower activation energies for ion conduction than that of powder Na-ETS-10 and zeolite X reported in the literature. Furthermore, dc conductivities of zeo-type (Na,K)-6h-ETS-10 films ($\sim 10^{-3} \Omega^{-1}\text{cm}^{-1}$) at 450 °C were higher than that of pressed pellets of zeo-type cation-exchanged powder sodium hydrogen germanate ($\sim 10^{-3} - 10^{-4} \Omega^{-1}\text{cm}^{-1}$) and powder zincosilicate VPI-9 ($\sim 10^{-4} - 10^{-7} \Omega^{-1}\text{cm}^{-1}$). Both monovalent and divalent cation-exchanged (Na,K)-6h-ETS-10 films exhibited higher activation energies and lower conductivities in the temperature range of 300 - 500 °C with respect to as-synthesized (Na,K)-6h-ETS-10 films. For monovalent cations (Li^+), the activation energy E_A decreased with increasing monovalent-cation radius while it increased with increasing ionic radius for divalent cations which was in correlation with the literature. Overall results showed that ionic conductivity of intergrown (Na,K)-6h-ETS-10 and M-ETS-10 films were significantly enhanced with respect to pressed pellets of powders zeolite and zeo-type materials reported in the literature. Ionic conductivity was increased by using intergrown, defect-free zeolite film since films possess noticeably lower electrical resistance than the compressed pellets usually used in conductivity measurements, which implies importance of engineering the

microstructure of the zeolite film to improve conductivity of zeolites and zeo-type materials. The current study shows ionic conductivity of titanosilicate “ETS-10 films” for the first time in the literature which can be important for ion-exchange, fuel cells, and sensor applications.

REFERENCES

- [1] A. Lasia, *Electrochemical Impedance Spectroscopy and Its Applications, Modern Aspects of Electrochemistry*, B. E. Conway, J. Bockris, and R.E. White, Edts., Kluwer Academic/Plenum Publishers, New York, 1999, Vol. 32, p. 143-248.
- [2] J.C. McKeen, M. E. Davis, "Conductivity of Mono- and Divalent Cations in the Microporous Zincosilicate VPI-9", *J. Phys. Chem. C* 2009, 113, 9870-9877.
- [3] I.M. Kalogeras, A. Vassilikou-Dova, "Electrical Properties of Zeolitic Catalysts", *Defect and Diffusion Forum*, 164, 1998, 1-36.
- [4] S.M. Aurbach, K.A. Carrado, P.K. Dutta, "Handbook of Zeolite Science and Technology", Marcel Dekker, Inc., 2003, Chapter 17.
- [5] U. Simon, U. Flesch, "Cation-Cation Interaction in Dehydrated Zeolites X and Y Monitored by Modulus Spectroscopy", *J. Porous Mater.* 1999, 6, 33-40.
- [6] W.J. Mortier, R.A. Schoonheydt, "Surface and Solid State Chemistry of Zeolites", *Prog. Solid State Chem.* 16 (1985) 1-125.
- [7] U. Simon, M.E. Franke, "Electrical Properties of Nanoscaled Host/Guest Compounds", *Micropor. Mesopor. Mater.* 41 (2000) 1-36.
- [8] D.C. Freeman and D. N. Stamires, "Electrical Conductivity of Synthetic Crystalline Zeolites", *Chem. Phys.* 35 (1961), 799-806.
- [9] Y. Zheng, X. Li, P.K. Dutta, "Exploitation of Unique Properties of Zeolites in the Development of Gas Sensors", *Sensors* 2012, 12, 5170-5194.
- [10] D. Vucelic , N. Juranic, "The Effect of Sorption on the Ionic Conductivity of Zeolites", *J. Inorg. Nucl. Chem.*, 1976, 38, 2091-2095.
- [11] N.C. Jeong, Y.J. Lee, J. Park, H. Lim, C. Shin, H. Cheong, K.B. Yoon, "New Insights into ETS-10 and Titanate Quantum Wire: A Comprehensive Characterization", *J. Am. Chem. Soc.* 131, 2009, 13080-13092.
- [12] M. Severance, Y. Zheng, E. Heck, P.K. Dutta, "Influence of Crystallite Size on Cation Conductivity in Faujasitic Zeolites", *J. Phys. Chem. A* 2013, 117, 13704-13711.

- [13] T. Wei, H.W. Hillhouse, "Ion Transport in the Microporous Titanosilicate ETS-10", *J. Phys. Chem. B*, 2006, 110, 13728-13733.
- [14] A. Eguizabal, J. Lemus, V. Roda, M. Urbiztondo, F. Barreras, M.P. Pina, "Nanostructured Electrolyte Membranes based on Zeotypes, Protic Ionic Liquids and Porous PBI membranes: Preparation, Characterization and MEA Testing", *Int. J. Hydrogen Energy*, 37, 2012, 7221-7234.
- [15] J. Zhang, X. Li, J. White, P.K. Dutta, "Effects of Surface and Morphological Properties of Zeolite on Impedance Spectroscopy-Based Sensing Performance", *Sensors* 2012, 12, 13284-13294.
- [16] G. Sethia, R.S. Somani, H.C. Bajaj, "Sorption of Methane and Nitrogen on Cesium Exchanged Zeolite-X: Structure, Cation Position and Adsorption Relationship", *Ind. Eng. Chem. Res.*
- [17] WEB: "Sorption of CO, CH₄, and N₂ on Alkali and Alkaline Earth Metal Ion Exchanged Zeolite-X", Chapter 2, http://shodhganga.inflibnet.ac.in:8080/jspui/bitstream/10603/8402/8/08_chapter%202.pdf, 06.04.2015.
- [18] S. Feng, M. Greenblatt, "Preparation, Characterization, and Ionic Conductivity of Novel Crystalline, Microporous Germanates, M₃HGe₇O₁₆.xH₂O, M, = NH₄⁺, Li⁺, K⁺, Rb⁺, Cs⁺; x = 4 - 6.2", *Chem. Mater.* 1992, 4, 462-468.

CHAPTER 8

SUMMARY, CONCLUSION AND FURTHER SUGGESTIONS

As a final chapter, structural and optical properties of as-synthesized and silver incorporated zeo-type titanosilicate ETS-10, preparation of titanosilicate ETS-10 films by secondary method, and the significance of the exploring electric properties of titanosilicate ETS-10 films prepared by secondary method will be summarized and concluded.

8.1 Synthesis of ETS-10 Crystals

Submicrometer-sized ETS-10 crystals were synthesized by using the molar composition of 3.4 Na₂O: 1.5 K₂O: TiO₂: 5.5 SiO₂: 150 H₂O [1].

1. FE-SEM analysis of ETS-10 (*vide infra*) clearly showed that the ETS-10 samples synthesized by using P25 are in their typical bipyramidal morphology with an average particle size of less than 0.5 μm .
2. The XRD analysis showed that the samples possess only the pure ETS-10 phase without ETS-4 and/or quartz impurity.
3. Raman analysis showed typical Raman scattering band at 729 cm^{-1} with a bandwidth of 35 cm^{-1} for the Ti-O-Ti stretching of the TiO_3^{2-} quantum wires. The bandwidth of the obtained samples suggest that the synthesized ETS-10 samples contain mostly unbroken TiO_3^{2-} quantum wires.

The synthesized submicrometer-sized ETS-10 crystals were used in silver incorporation to figure out effect of silver encapsulation on the local structure of titanosilicate ETS-10 in Chapter 4. It was used in photochromic application as matrix

in Chapter 5. It was also used in film production (i.e., secondary growth method) as seed crystals Chapter 6.

8.2 Silver Incorporation into Titanosilicate ETS-10

The preparation of Ag^0 nanoparticles within the framework of ETS-10 (Ag^0 -ETS-10) was reported following an established method, which involves the incorporation of Ag^+ ions into ETS-10 matrix by ion-exchange with extra framework ETS-10 cations (Na^+ and K^+) forming Ag^+ -ETS-10 and their reduction within ETS-10 matrix with sodium borohydride in aqueous medium at room temperature.

The resulting Ag^0 nanoparticle incorporated ETS-10 framework were isolated as solid powder and characterized by ICP-OES, XRD, XPS, FE-SEM, TEM, HR-TEM, DR-UV-vis, Raman spectroscopies and N_2 adsorption-desorption technique. The study also includes the results obtained from investigation of the changes in the local structure of ETS-10 upon its modification by Ag^+ ion-exchange and following chemical reduction plus the extent of destruction as a function of silver loading (Chapter 4).

1. Results of these advanced techniques are indicating that this methodology produces highly stable, well-dispersed Ag^0 nanoparticles within the ETS-10 matrix without causing observable defects in the morphology, alteration in ETS-10 lattice, and mesopore formation.
2. Raman spectroscopy analysis suggests the formation of Ag^0 nanoparticles within the framework of titanosilicate causing a local structural change in the titanate chains of ETS-10.
3. As the silver loading of ETS-10 increases, the concentration of defects increases in the titanate wire. This effect can be of great interest in using Ag^0 nanoparticles encapsulated in ETS-10 for future catalytic applications,

which might even lead to enhanced activities due to the combined role of defect formation and Ag^0 nanoparticle inclusion.

4. The results obtained in this study are believed to bring not only the way of enhancement of catalytic activity, but also more insights on the role of the titanate wire in the existing and future applications.

8.3 Photochromism

Silver doped titania has been studied extensively as a photochromic inorganic material in the literature [2-7]. In the structure of Ag^0 nanoparticle incorporated TiO_2 , electronic transition is generated through UV radiation and the created e^- - h^+ pairs initiate several reactions for reversible photochromic process.

The Ag^0 nanoparticles incorporated into the insulating silica matrix were found not to exhibit photochromism, whereas semiconductor TiO_2 is needed for electron transport [2]. Microporous zeolites are insulators (i.e., wide bandgap materials). Therefore, insulating silica matrix should not contribute to electronic transition in the case of microporous titanosilicate ETS-10. Instead, TiO_3^{2-} quantum wires (i.e., Ti-O-Ti-O-Ti) are considered to be responsible for the electronic transition. Accordingly, photochromic behavior of Ag^0 nanoparticle incorporated titanosilicate ETS-10 films was studied to show role of 1-D TiO_3^{2-} quantum wires in the ETS-10 crystals (Chapter 5).

1. The photochromic behavior of Ag^0 nanoparticle incorporated ETS-10 and the possible role of the unique TiO_3^{2-} quantum wires in the photochromic mechanism were comprehensively investigated for the first time.
2. Ag^+ ions were incorporated into ETS-10 matrix by ion-exchange of extra framework cations (i.e., Na^+ and K^+) to form Ag^+ ion-exchanged ETS-10. The redox process, which contains colored form (i.e., activated state) of the photochromic system / colorless form (i.e., bleached state) of the

photochromic system of Ag^0 nanoparticle incorporated ETS-10 films, was achieved through thermal reduction of the films and exposure of them to visible laser at wavelength of 532 nm, respectively. XRD, HR-TEM and UV-vis spectroscopy results showed that photochromic cycle was obtained for Ag^0 nanoparticle incorporated ETS-10 films.

3. According to XPS results, the ratio of the deconvoluted peak area at 368.5 eV (i.e., Ag^+) to total area revealed that the ratio of the silver increased from 10.96 to 38.69 % for the cycle of $\text{I-Ag}^0\text{-ETS-10} \rightarrow 116\text{-LT-ETS-10}$ and decreased from 38.69 to 29.67 % for the cycle of $116\text{-LT-ETS-10} \rightarrow 5\text{h-II-Ag}^0\text{-ETS-10}$, which was expected from the photochromic cycles.
4. The XPS results proved that the valance state of the titanium shifted from Ti^{4+} to Ti^{3+} and vice versa for the films, which support the photochromic mechanism of the silver incorporated ETS-10 films indisputably in addition to the other results.

8.4 Preparation of ETS-10 Films by using Secondary Growth Method

Zeolite and zeo-type films/membranes are typically used in catalysis or separation applications. Various type of application areas showed that preferred-oriented, defect- and crack-free intergrown films/membranes are superior to the randomly oriented films/membranes.

There are some advantages of zeo-type microporous Engelhard titanosilicate (i.e., ETS-4 and ETS-10) membranes compared to conventional zeolite membranes: (i) there is no need to use expensive structure directing agents which leads to application of calcination step that usually forms defects in the films; (ii) the films are generally prepared under comparatively mild pH conditions (i.e., $\sim 10\text{-}11$ vs. $\sim 12\text{-}13$), decreasing the chemical attack on the substrate surfaces; (iii) the existence of TiO_6 octahedra- SiO_4 tetrahedra oxides provides a possibility to make framework substitution such as aluminum, gallium, zirconium, tin etc. In this way, the catalytic

and adsorption properties of the microporous titanosilicate membranes can be adjusted [8]. Although there are several advantages of titanosilicate materials discussed above, limited studies exist in the literature about production of ETS-10 film/membrane. ETS-10 films were produced on conductive ITO glass substrates for the first time by our group [9]. In the current thesis study, defect- and crack- free intergrown ETS-10 films/membranes with columnar grain structure were produced on ITO glass and α -alumina substrates by using secondary growth method and secondary growth parameters were investigated comprehensively. The production of well-intergrown and well-adhered titanosilicate ETS-10 films on ITO glass and α -alumina substrates led us to investigate conductivity of ETS-10 for the first time in the scope of the current thesis study (Chapter 7).

One of the objectives was to enhance the film formation methods in order to obtain continuous, well-intergrown ETS-10 films with columnar grain structure. The following parameters affecting the microstructure of the ETS-10 films were studied:

- Concentration of ETS-10 seed crystals
 - Number of spin coating step
 - Reaction time of secondary growth
 - Type of substrate
1. Continuous, defect- and crack-free ETS-10 films by seeded hydrothermal synthesis (i.e., secondary growth) on ITO glass and α -alumina substrates. The synthesis parameters (reaction time, seeding procedure, seed concentration) have been investigated.
 2. The XRD analysis revealed that the produced ETS-10 films do not contain impurities of TiO_2 , quartz or ETS-4 that usually obtained in the synthesis ETS-10 crystals.

3. FE-SEM images showed well-intergrown and 1.3 - 4.3 μm thick ETS-10 films with columnar grain structure.
4. When large distances exist between the adjacent seed crystals, increasing concentration of ETS-10 seed suspension and number of spin-coating step seems to be superior to increasing reaction time of secondary growth to obtain continuous films.
5. According to FE-SEM analyses the van der Drift growth model, competitive growth of adjacent seed crystals, can be considered in the titanosilicate ETS-10 film production on the ITO glass and α -alumina substrates.

8.5 Ionic Conductivity of Zeolites and Zeo-Type Materials

To the best of our knowledge, only Dutta et al. [10,11] studied “film” form of zeolites prepared by secondary growth method in conductivity measurements instead of pressed pellets of powder. They proposed that use of zeolite membrane will improve response of sensors and lead to design miniaturized sensors [12].

In the current thesis study, long-range ionic conductivities of zeo-type titanosilicate ETS-10 and zeolite Y films prepared via secondary growth method were investigated. A system design was carried out to study ionic conductivity of microporous titanosilicate ETS-10 films in the temperature range of 25 to 500 $^{\circ}\text{C}$ by using impedance spectroscopy at Central Laboratory, METU. The Na^{+} and K^{+} ions within the framework of as-synthesized ETS-10 films were ion-exchanged with Li^{+} , Ca^{2+} , and Zn^{2+} ions to figure out effect of cation site occupancy on conduction. The following parameters affecting the long-range ionic conductivity of the ETS-10 films were studied:

- Hydration state,
- Grain boundary structure,
- Cation site occupancy.

1. Impedance spectroscopy was used to investigate the long-range ionic conductivity of microporous titanosilicate ETS-10 films prepared through secondary growth method. (Na,K)-ETS-10 films were found to have lower activation energies for ion conduction than that of powder Na-ETS-10 and zeolite X reported in the literature.
2. Furthermore, dc conductivities of zeo-type (Na,K)-6h-ETS-10 films ($\sim 10^{-3} \Omega^{-1}\text{cm}^{-1}$) were higher than that of pressed pellets of zeo-type cation-exchanged powder sodium hydrogen germanate ($\sim 10^{-3} - 10^{-4} \Omega^{-1}\text{cm}^{-1}$) and powder zincosilicate VPI-9 ($\sim 10^{-4} - 10^{-7} \Omega^{-1}\text{cm}^{-1}$). Both monovalent and divalent cation-exchanged (Na,K)-6h-ETS-10 films exhibited higher activation energies and lower conductivities in the temperature range of 300 - 500 °C with respect to as-synthesized (Na,K)-6h-ETS-10 films.
3. For partly ion-exchanged monovalent cations (Li^+), the activation energy E_A decreased with increasing monovalent-cation radius while it increased with increasing ionic radius for divalent cations which was in correlation with the literature.
4. Overall results showed that ionic conductivity of intergrown (Na,K)-6h-ETS-10 and M-ETS-10 films were significantly enhanced with respect to pressed pellets of powders zeolite and zeo-type materials reported in the literature. Ionic conductivity was increased by using intergrown, defect-free zeolite film since films possess noticeably lower electrical resistance than the compressed pellets usually used in conductivity measurements, which implies importance of engineering the microstructure of the zeolite film to improve conductivity of zeolites and zeo-type materials.
5. The current study shows ionic conductivity of titanosilicate “ETS-10 films” comprehensively for the first time which can be important for ion-exchange, fuel cells, and sensor applications.

8.6 Outlook for the Future Work

In Chapter 5, the photochromic behavior of Ag^0 nanoparticle incorporated ETS-10 and the possible role of the unique TiO_3^{2-} quantum wires in the photochromic mechanism were comprehensively investigated for the first time. Further studies can be carried out to investigate photochromic properties of other type of zeolite and/or zeo-type materials that contain titania (i.e., zeo-type titanosilicate ETS-4 or zeolite titanium beta) to compare silver incorporated titanosilicate ETS-10.

In the Chapter 6, the film formation method was enhanced in order to obtain continuous, well-intergrown titanosilicate ETS-10 films with columnar grain structure. The following parameters affecting the microstructure of the ETS-10 films were studied: (i) concentration of ETS-10 seed crystals; (ii) number of spin coating step; (iii) reaction time of secondary growth; (iv) type of substrate. Preferred orientation of the prepared films could be investigated by using XRD analysis to obtain quantitative data.

In Chapter 7, long-range ionic conductivities of zeo-type titanosilicate ETS-10 and zeolite Y films prepared via secondary growth method were investigated. A system design was carried out to study ionic conductivity of microporous titanosilicate ETS-10 films in the temperature range of 25 to 500 °C by using impedance spectroscopy. The Na^+ and K^+ ions within the framework of as-synthesized ETS-10 films were ion-exchanged with Li^+ , Ca^{2+} , and Zn^{2+} ions to figure out effect of cation site occupancy on conduction. The following parameters affecting the long-range ionic conductivity of the ETS-10 films were studied: (i) hydration state, (ii) grain boundary structure, (iii) cation site occupancy. Further studies can be done to obtain fully ion-exchanged ETS-10 films and other monovalent (i.e., K^+) and divalent cations (Mg^{2+}) can be also investigated to prove trend of activation energy. Resistive type humidity sensors can be designed by using titanosilicate ETS-10 films prepared via secondary growth method.

REFERENCES

- [1] L. Lv, F. Su, X.S. Zaho, "A Reinforced Study on the Synthesis of Microporous Titanosilicate ETS-10", *Micropor. Mesopor. Mater.* 76, 2004, 113-122.
- [2] K. Kawahara, K. Suzuki, Y. Ohko, T. Tatsuma, *Phys. Chem. Chem. Phys.* 7, 2005, 3851-3855.
- [3] Y. Ohko, T. Tatsuma, T. Fujii, K. Naoi, C. Niwa, Y. Kubota, A. Fujishima, *Nat. Mater.* 2, 2003, 29-31.
- [4] K. Naoi, Y. Ohko, T. Tatsuma, *J. Am. Chem. Soc.* 126, 2004, 3664 - 3668.
- [5] K. Naoi, Y. Ohko, T. Tatsuma, *Chem. Commun.* 10, 2005, 1288-1290.
- [6] L. Nadar, R. Sayah, F. Vocanson, N. Crespo-Monteiro, A. Boukenter, S. Sao Joao, N. Destouches, *Photochem. Photobiol. Sci.* 10, 2011, 1810-1816.
- [7] A. Kafizas, C.W. Dunnill, I.P. Parkin, *Phys. Chem. Chem. Phys.* 13, 2011, 13827-13838.
- [8] Z. Lin, J. Rocha, A. Navajas, C. Tellez, J. Coronas, J. Santamaria, "Synthesis and Characterization of Titanosilicate ETS-10 Membranes", *Micropor. Mesopor. Mater.* 67, 2004, 79-86.
- [9] S. Galioglu, M.N. Ismail, J. Warzywoda, A. Sacco Jr., B. Akata, "Preparation and microstructural characterization of oriented titanosilicate ETS-10 thin films on indium tin oxide surfaces", *Microporous and Mesoporous Materials* 131, 2010, 401-406.
- [10] M. Severance, Y. Zheng, E. Heck, P.K. Dutta, "Influence of Crystallite Size on Cation Conductivity in Faujasitic Zeolites", *J. Phys. Chem. A* 117, 2013, 13704-13711.
- [11] J. Zhang, X. Li, J. White, P.K. Dutta, "Effects of Surface and Morphological Properties of Zeolite on Impedance Spectroscopy-Based Sensing Performance", *Sensors* 12, 2012, 13284-13294.
- [12] Y. Zheng, X. Li, P.K. Dutta, "Exploitation of Unique Properties of Zeolites in the Development of Gas Sensors", *Sensors*, 12, 2012, 5170-5194.

APPENDICES

Appendix A : Calculation of Activation Energy

Impedance plane plot (Argand diagram) was obtained as a function of frequency. The low frequency intercept of the semicircle with the Z' (real) axis (i.e., R in Table A.1) was used to calculate conductivity of the sample.

Conductivity can be found from the equation below,

$$\rho = \frac{RA}{\ell} \quad (\text{A.1})$$

$$\sigma = \frac{1}{\rho} \quad (\text{A.2})$$

where, ρ is resistivity, R is the electrical resistance of a uniform specimen of the material (measured in ohms, Ω , from impedance spectroscopy), ℓ is the length of the piece of material (measured in centimeters, cm, $\ell = 0.1$ cm), A is the cross-sectional area of the specimen (measured in square centimeters, cm^2 , $A = 1.3$ cm x Film thickness (cm)) and σ is the conductivity ($\Omega^{-1}\text{cm}^{-1}$) (Figure 7.1). For example, calculation of conductivity values for (Na,K)-4h-ETS-10 films were given below:

Conductivity of the film at 573 K can be written as:

$$\sigma = 0.1 \text{ cm} / (2738000 \Omega * 1.3 \text{ cm} * 0.0002 \text{ cm})$$

$$\sigma = 0,000140473 \Omega^{-1}\text{cm}^{-1}$$

$$\sigma = 1,4 \times 10^{-4} \Omega^{-1}\text{cm}^{-1}$$

R is the electrical resistance at 573 K (measured in ohms, Ω , from impedance spectroscopy) (Table A.1), ℓ is the length of the piece of material (measured in centimeters, cm, $\ell = 0.1$ cm), A is the cross-sectional area of the specimen (measured in square centimeters, cm^2 , $A = 1.3$ cm x Film thickness (cm)) and σ is the conductivity ($\Omega^{-1}\text{cm}^{-1}$). Film thickness of (Na,K)-4h-ETS-10 was 2.00 ± 0.08 μm (See Table 6.3).

When impedance data were collected as a function of temperature, activation energy for transport, E_A , could be calculated by fitting conductivity data to equation below, where k is Boltzmann's constant, E_A is the activation energy, σ is the conductivity, σ_0 is the pre-exponential factor, and T is the temperature in Kelvin.

$$\sigma = (\sigma_0 / T) \exp (-E_A / kT) \quad (\text{A.3})$$

$$\sigma T = \sigma_0 \exp (-E_A / kT) \quad (\text{A.4})$$

$$\ln (\sigma T) = \ln \sigma_0 + (-E_A / kT) \quad (\text{A.5})$$

$$\ln (\sigma T) = (- E_A / k) 1/T \quad (\text{A.6})$$

$$\text{slope} = -E_A / k \quad (\text{A.7})$$

Table A.1. Conductivity values of (Na,K)-4h-ETS-10 films.

T (°C)	T (K)	1/T (K)	R (Ω)	σ ($\Omega^{-1}\text{cm}^{-1}$)	$\ln \sigma T$ ($\Omega^{-1}\text{cm}^{-1}\text{K}$)
300	573	0.001745	2738000	0.000140473	-2.51961
350	623	0.001605	1210000	0.000317864	-1.61934
400	673	0.001486	618000	0.000622355	-0.87025
450	723	0.001383	347000	0.001108402	-0.22143

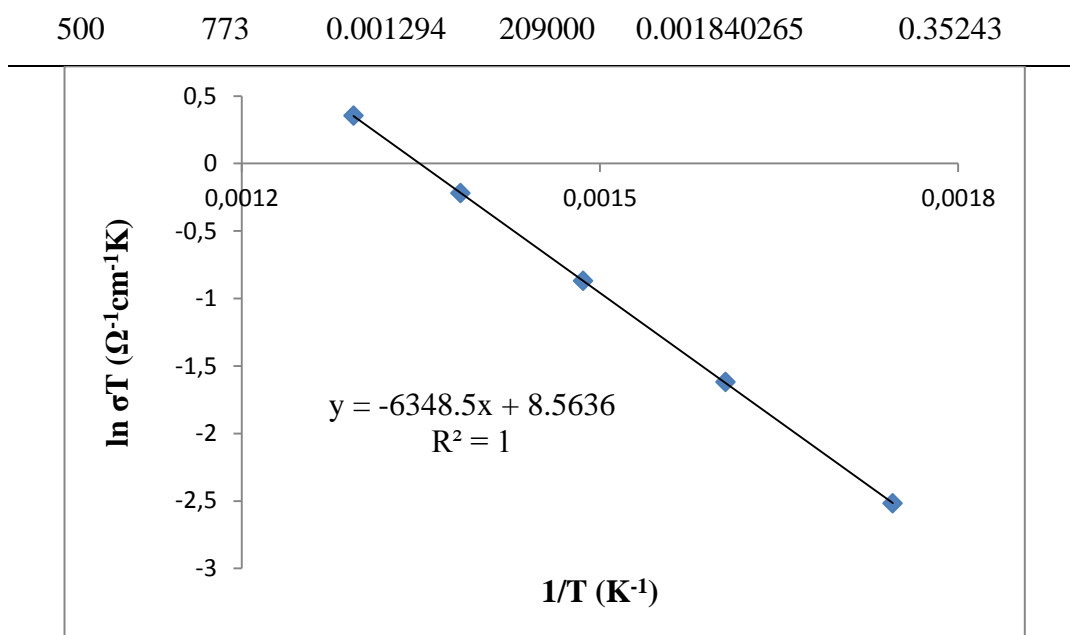


Figure A.1. Arrhenius plot of ionic conductivity for (Na,K)-4h-ETS-10,

First of all, a line was plotted to connect each data point obtained in the temperature range of 300 - 500 °C ($\ln \sigma T$ vs. $1/T$) and equation of the line was defined. Then, the slope of the line (6348.5) was multiplied by the gas constant R ($R = 8.314 \text{ J mol}^{-1}\text{K}^{-1}$) to find the activation energy of the film ($52.78 \text{ kJ mol}^{-1} = 0.6 \text{ eV}$).

CURRICULUM VITAE

PERSONAL INFORMATION

Surname, Name: GALİOĞLU ÖZALTUĞ, Sezin

Nationality: Turkish

Date and Place of Birth: 1983, Hatay

Phone: +90 312 210 7417-6459

Fax: +90 312 210 7433

e-mail: sezingalioglu@gmail.com

EDUCATION

Degree	Institution	Year of Graduation
M.Sc.	METU, Micro & Nano Technology Dept.	2010
B.Sc.	Ankara University, Physics Engineering Dept.	2006

WORK EXPERIENCE

Year	Place	Enrollment
2012 - 2013	NUROL AR-GE Müh. San. Tic. A.Ş.	R & D Engineer

FOREIGN LANGUAGES

English (Advanced)

PUBLICATIONS

A. Thesis

1. Sezin Galioglu, M.Sc. Thesis, June 2010.

Synthesis and Characterization of Titanosilicate ETS-10 for Potential Photovoltaic Applications

B. Journal Articles

1. Mehmet Koç, Sezin Galioglu, Daniele Toffoli, Hande Ustunel, Burcu Akata, “Understanding the Effects of Ion-Exchange in Titanosilicate ETS-10: A Joint Theoretical and Experimental Study”, J. Phys. Chem. C 118, (2014), 27281-27291.

2. Mehmet Koç, Sezin Galioglu, Daniele Toffoli, Hande Üstünel, and Burcu Akata, “Effect of Ion-Exchange on Structural, Electronic, and Vibrational Properties of the -O-Ti-O-Ti-O- Quantum Wires in ETS-10”, MRS Proceedings (2014), 1704, mrss14-1704-qq04-02 doi:10.1557/opl.2014.796.

3. Sezin Galioglu, Melda Isler, Zeynep Demircioglu, Mehmet Koc, Francis Vocanson, Nathalie Destouches, Raşit Turan, Burcu Akata, “Photochromic Behavior of Silver Nanoparticle Incorporated Titanosilicate ETS-10 Films”, Microporous and Mesoporous Materials 196, (2014), 136-144.

4. Esin Soy, Sezin Galioglu, Oleksandr O. Soldatkin, Sergei V. Dzyadevych, Juliusz Warzywoda, Albert Sacco Jr., Burcu Akata, “Direct Evidence of Advantage of Using Nanosized Zeolite Beta for ISFET-Based Biosensor Construction”, Journal of Nanoparticle Research 15, (2013), 1645.

5. Sezin Galioglu, Mehmet Zahmakıran, Y. Eren Kalay, Saim Özkar, Burcu Akata, "Effect of Silver Encapsulation on the Local Structure of Titanosilicate ETS-10", *Microporous and Mesoporous Materials* 159, (2012), 1-8.
6. Sezin Galioglu, N. Mariam Ismail, Juliusz Warzywoda, Albert Sacco Jr., Burcu Akata, "Preparation and microstructural characterization of oriented titanosilicate ETS-10 thin films on indium tin oxide surfaces", *Microporous and Mesoporous Materials* 131, (2010), 401-406.

C. Conference and Meeting Presentations

1. Sezin Galioglu, Melda İşler, Zeynep Demircioğlu, Mehmet Koç, Francis Vocanson, Natalie Destouches, Raşit Turan, Burcu Akata, "Photochromic Behavior of Silver Nanoparticle Incorporated Titanosilicate ETS-10 Films", 4th International Conference on Multifunctional, Hybrid and Nanomaterials, Sitges (Near Barcelona), Spain, March 9-13, 2015 (Poster Presentation).
2. Sezin Galioglu, Ibrahim Cam, Burcu Akata, "Conductivity of Microporous Titanosilicate ETS-10 Films", 4th International Conference on Multifunctional, Hybrid and Nanomaterials, Sitges (Near Barcelona), Spain, March 9-13, 2015 (Poster Presentation).
3. Duygu Kuzyaka, Sezin Galioglu, Burcu Akata, "Secondary Growth of Microporous Vanadosilicate Films", 4th International Conference on Multifunctional, Hybrid and Nanomaterials, Sitges (Near Barcelona), Spain, March 9-13, 2015.
4. Sezin Galioglu, Melda İşler, Zeynep Demircioğlu, Raşit Turan, Burcu Akata, "Photochromic Behavior of Titanosilicate ETS-10", 17th International Zeolite Conference (17th IZC), Moscow, Russia, July 7-12, 2013 (Poster Presentation).
5. Melda Isler, Sezin Galioglu, Burcu Akata, 17th International Zeolite Conference (17th IZC), "Ruthenium Nanoparticles Encapsulated Disordered Titanosilicate ETS-10", Moscow, Russia, July 7-12, 2013.

6. Sezin Galioglu, Melda İşler, Zeynep Demircioğlu, Raşit Turan, Burcu Akata, “Photochromic Behavior of Silver Nanoparticle Incorporated Titanosilicate ETS-10 Films”, International Porous and Powders Materials Symposium and Exhibition, Izmir, Turkey, June 3-6, 2013 (Oral Presentation).
7. Melda Isler, Sezin Galioglu, Burcu Akata, “Ruthenium Nanoparticle Encapsulated Disordered Titanosilicate ETS-10”, International Porous and Powders Materials Symposium and Exhibition, İzmir, Turkey, June 3-6, 2013.
8. Melda Isler, Sezin Galioglu, Burcu Akata, “Incorporation of Ruthenium Nanoparticles into Titanosilicate ETS-10: Preparation, Characterization and Photocatalytic Properties”, Materials Research Society (MRS) Fall Meeting, December 1-6, 2013.
9. Sezin Galioglu, Mehmet Zahmakıran, Yunus Eren Kalay, Saim Özkar, Burcu Akata, “Effect of Silver Encapsulation on the Local Structure of Titanosilicate ETS-10”, 8th Nanoscience and Nanotechnology Conference, Ankara, Turkey, June 25-28, 2012 (Oral Presentation).
10. Sezin Galioglu, Burcu Akata, “Structural Characterization of Titanosilicate ETS-10”, Second International Conference on Multifunctional, Hybrid and Nanomaterials, Strasbourg, France, March 6-10, 2011 (Oral Presentation).
11. Sezin Galioglu, Mariam N. Ismail, Juliusz Warzywoda, Albert Sacco Jr., Burcu Akata, “Preparation and Microstructural Characterization of Oriented Titanosilicate ETS-10 Thin Films on Indium Tin Oxide Surfaces”, 6th Nanoscience and Nanotechnology Conference, Izmir, Turkey, June 15-18, 2010 (Oral Presentation).

RESEARCH ACTIVITIES

1. Visiting Researcher, Texas Tech University, Edward E. Whitacre Jr. College of Engineering, Lubbock Texas, U.S.A, October-December, **2014**.
2. Visiting Researcher, CNRS à l'Institut des Sciences Analytiques de l'Université Claude Bernard-Lyon 1, Lyon, France, April-June, **2014**.
3. Visiting Researcher, Hubert Curien Laboratory, Université Jean Monnet, Saint Etienne, France, March-April, **2011** and October-November, **2011**.
4. Visiting Researcher, Center for Advanced Microgravity Materials Processing (CAMMP), Northeastern University, Boston, U.S.A, July-September, **2009** and February-May, **2010**.
5. Visiting Researcher, Center for Microcrystal Assembly, Sogang University, Seoul, South Korea, April-June, **2009**.

AWARDS

2007-2008 Academic Year METU Graduate Courses Performance Award.